Experimental campaign on Reinforced Concrete buildings typical of the Groningen region

Dynamic testing of a full-scale two-storey Reinforced Concrete precast wall-slab-wall structure representative of the Groningen building stock (EUC-BUILD5).

Eucentre

Brunesi E., Peloso S., Pinho R. and Nascimbene R.

General Introduction

The experimental and study program into the seismic response of buildings initially focussed on masonry buildings (Ref. 1 to 8), with many tests and experiments on masonry building material, walls and full-scale buildings. Both a terraced house and a detached house have been tested by EUcentre in Pavia (Italy), with follow-up experiments on the first floor and roof of the terraced house by LNEC in Lisbon (Portugal).

However, in Groningen, many buildings have been constructed using pre-cast concrete elements. Often these buildings are not easily recognized as the pre-cast concrete elements making up the structural system are behind masonry veneers, giving the building a masonry appearance.

To better understand the seismic behaviour of the precast concrete panels commonly used in construction in The Netherlands (e.g. Heembeton and Alvon panels and Dycore floors) experiments were conducted. Especially, the connections between the panels are important to understand the seismic response of a pre-cast concrete building (Ref. 9).

The current report describes experimental dynamic testing of a full-scale two-storey one-bay reinforced precast concrete prototype. The test structure (EUC-BUILD5 specimen) was designed to combine several common features of this type of structures and it was built directly on the shaking table of EUCENTRE laboratory by a Dutch contractor. In an earlier report the cyclic testing of a precast specimen is discussed (Ref. 10)

This document describes the testing campaign performed at EUCENTRE laboratory in 2017, executed in collaboration with the DICAr Laboratory of the University of Pavia (UNIPV). The experimental programme included thus:

- Characterisation testing of concrete samples (compression tests);
- Characterisation testing of mortar samples (compression tests, flexural tests);
- Characterisation testing of mortar specimens (triplet tests, bond wrench tests);
- Characterisation testing of felt material (cyclic tests);
- Component testing of three-way connections (cyclic tests);
- Dynamic testing of a full-scale specimen in as-built configuration (shake-table test).

The results of these experiments are used in the preparation of fragility curves for these buildings (Ref. 11).

References

1. Eucentre Shake-table Test of Terraced House Modelling Predictions and Analysis Cross Validation, staff from ARUP, Eucentre (Pavia) and TU Delft, November 2015 [this document also includes; (1) Instruments full-scale test-house Eucentre Laboratory, (2) Protocol for Shaking Table Test on Full Scale Building (Eucentre) V_1, and (3) Selection of Acceleration Time-Series for Shake Table Testing of Groningen Masonry Building at the EUCENTRE, Pavia, all three by staff from Eucentre (Pavia)],

2. Collapse shake-table testing of terraced house (LNEC-BUILD1), Eucentre and LNEC (U. Tomassetti, A. A. Correia, F. Graziotti, A.I. Marques, M. Mandirola, P.X. Candeias), 1st September 2017.

3. LNEC-BUILD1: Modelling predictions and analysis cross-validation, ARUP, TU Delft, Eucentre and Mosayk (several staff members from all four institutions), 8th September 2017.

4. Using the Applied Element Method to model the collapse shake-table testing of a URM cavity wall structure (LNEC-BUILD1), Mosayk (D. Malomo, R. Pinho), 31st October 2017.

5. Using the Applied Element Method to model the collapse shake-table testing of a terraced house roof substructure (LNEC-BUILD2), Mosayk (D. Malomo, R. Pinho), 31st October 2017.

6. Experimental campaign on a clay URM full-scale specimen representative of the Groningen building stock (EUC-BUILD2), Eucentre (F. Graziotti, U. Tomassetti, A. Rossi, B. Marchesi, S. Kallioras, M. Mandirola, A. Fragomeli, E. Mellia, S. Peloso, F. Cuppari, G. Guerrini, A. Penna, G. Magenes, G), 20th July 2016.

7. EUC-BUILD2: Modelling predictions and analysis cross-validation of detached single-storey URM Building, ARUP, TU Delft, Eucentre and Arcadis (several staff members from all four institutions), 30th September 2016

8. Shake-table test up to collapse on a roof substructure of a Dutch terraced house (LNEC-BUILD2), Eucentre and LNEC (A.A. Correia, A.I. Marques, V. Bernardo, L. Grottoli, U. Tomassetti, F. Graziotti), 31st October 2017.

9. Cyclic testing of precast panel connections for RC precast wall-slab-wall structures representative of the Groningen building stock. Eucentre (E. Brunesi, R. Nascimbene), 22nd October 2015.

10. Experimental campaign on Reinforced Concrete buildings typical of the Groningen region, Cyclic testing of a full-scale two-storey Reinforced Concrete precast wall-slab-wall structure representative of the Groningen building stock (EUC-BUILD4), EUCentre, Brunesi E., Peloso S., Pinho R. and Nascimbene R., June 2017.

11. Report on the v5 fragility and consequence models for the Groningen Field, H. Crowley and R. Pinho, 31st October 2017.

NAM

Title	Experimental campaign on Reinforced Concrete buildings typical of the Groningen region **Dynamic testing of a full-scale two-storey Reinforced Concrete precast wall-slab-wall structure representative of the Groningen building stock (EUC-BUILD5).**		Date	October 2017
			Initiator	NAM
Autor(s)	**Brunesi E., Peloso S., Pinho R. and Nascimbene R.**	**Editors**	Jan van Elk and Dirk Doornhof	
Organisation	EUCentre	**Organisation**	NAM	
Place in the Study and Data Acquisition Plan	Study Theme: Seismic Response Buildings Comment: The experimental and study program into the seismic response of buildings initially focussed on masonry buildings (Ref. 1 to 8), with many tests and experiments on masonry building material, walls and full-scale buildings. Both a terraced house and a detached house have been tested by EUcentre in Pavia (Italy), with follow-up experiments on the first floor and roof of the terraced house by LNEC in Lisbon (Portugal). However, in Groningen, many buildings have been constructed using pre-cast concrete elements. Often these buildings are not easily recognized as the pre-cast concrete elements making up the structural system are behind masonry veneers, giving the building a masonry appearance. To better understand the seismic behaviour of the precast concrete panels commonly used in construction in The Netherlands (e.g. Heembeton and Alvon panels and Dycore floors) experiments were conducted. Especially, the connections between the panels are important to understand the seismic response of a pre-cast concrete building (Ref. 9). The current report describes experimental dynamic testing of a full-scale two-storey one-bay reinforced precast concrete prototype. The test structure (EUC-BUILD5 specimen) was designed to combine several common features of this type of structures and it was built directly on the shaking table of EUCENTRE laboratory by a Dutch contractor. In an earlier report the cyclic testing of a precast specimen is discussed (Ref. 10) This document describes the testing campaign performed at EUCENTRE laboratory in 2017, executed in collaboration with the DICAr Laboratory of the University of Pavia (UNIPV). The experimental programme included thus: ▪ Characterisation testing of concrete samples (compression tests); ▪ Characterisation testing of mortar samples (compression tests, flexural tests); ▪ Characterisation testing of mortar specimens (triplet tests, bond wrench tests); ▪ Characterisation testing of felt material (cyclic tests); ▪ Component testing of three-way connections (cyclic tests);			

	▪ Dynamic testing of a full-scale specimen in as-built configuration (shake-table test). The results of these experiments are used in the preparation of fragility curves for these buildings (Ref. 11).
Directliy linked research	(1) Shake Table Tests (2) Risk Assessment
Used data	Full experimental and Modelling program into seismic response URM & non-URM buildings.
Associated organisation	NAM
Assurance	Independent Assurance Panel

Nederlandse Aardolie Maatschappij B.V.

Schepersmaat 2, Postbus 28000, 9400 HH Assen

Experimental campaign on RC buildings typical of the Groningen region: dynamic testing of a precast specimen

EUCENTRE
FOR YOUR SAFETY.

Via Ferrata 1, 27100 Pavia, Italy
Tel. +39.0382.516911 Fax. +39.0382.529131
http://www.eucentre.it
email: info@eucentre.it

LAB AND TESTS RESPONSIBLE	DOCUMENT AUTHOR	REVIEWER
Filippo Dacarro	Emanuele Brunesi	Rui Pinho
Signature	Signature	Signature

	Document type:	
Issue: 30/10/2017		File name: EUC_BUILD5-test_campaign_report.pdf
Revision: 19/12/2017	**Technical report**	
Revision:	pages: 364	Protocol 215/2017U
Revision:		

Cite as:

Brunesi E., Peloso S., Pinho R., Nascimbene R. (2017). *Dynamic testing of a full-scale two-storey RC precast wall-slab-wall structure representative of the Groningen building stock*. Report EUC215/2017U, European Centre for Training and Research in Earthquake Engineering (EUCENTRE), Pavia, Italy.

According to Italian law, EUCENTRE Foundation trademark cannot be reproduced, copied or utilised, without the written permission of the EUCENTRE Foundation, which is the owner, except in accordance with established contract conditions pertaining to the production of this document.

This report, produced by the EUCENTRE Foundation, may be reproduced and/or released only in its entirety. Any partial reproduction must be authorised with the written consent by the Eucentre responsible of the project.

Table of contents

1 Preamble

As discussed in Arup report *229746_031_NOT2008_Rev0.05_Issue EUC-BUILD-4 Prototype building description*, reinforced concrete buildings in the Groningen region largely consist of what are herein termed wall-slab-wall structures, featuring no columns or beams, but only slabs and walls.

These structures can be found in both cast-in-place (tunnel construction or not) as well as precast configurations, and this report deals with the experimental programme aimed at dynamically testing the latter (please refer to Arup report *229746_031.0_DRW2007_Rev0.05_Issue_EUC-BUILD-4_5 SWb Specimen drawings* for construction details on the selected prototype structure).

Cyclic testing of another precast specimen (EUC-BUILD4) and cyclic testing of a cast-in-place prototype (EUC-BUILD3) are described in two separate companion reports.

2 Introduction

2.1 Description of test programme

This report describes experimental testing activities that were undertaken within the framework of the research programme for hazard and risk of induced seismicity in Groningen sponsored by the Nederlandse Aardolie Maatschappij BV. As part of NAM data acquisition and analysis programme aimed at developing a seismic hazard and risk model for induced seismicity in the Groningen area, dynamic tests were performed on a full-scale reinforced precast concrete wall-slab-wall structure, representative of a building typology that was found to be relatively common in the region. Auxiliary characterization tests were carried out as well.

Laboratory tests were thus performed on a full-scale two-storey one-bay reinforced precast concrete prototype, which was adapted to the needs imposed by laboratory constraints. The test structure, namely EUC-BUILD5 specimen, was designed to combine several common features of this type of structures (please refer to Arup report: *229746_031_NOT2008_Rev0.05_Issue EUC-BUILD-4 Prototype building description* for details on the selected design concept) and it was built directly on the shaking table of EUCENTRE laboratory by a Dutch contractor.

This document describes the testing campaign performed at EUCENTRE laboratory in 2017, execute also in collaboration with the DICAr Laboratory of the University of Pavia (UNIPV). The experimental programme included thus:

- Characterisation testing of concrete samples (compression tests);
- Characterisation testing of mortar samples (compression tests, flexural tests);
- Characterisation testing of mortar specimens (triplet tests, bond wrench tests);
- Characterisation testing of felt material (cyclic tests);
- Component testing of three-way connections (cyclic tests);
- Dynamic testing of a full-scale specimen in as-built configuration (shake-table test).

The complete list of the tests carried out at EUCENTRE laboratory is reported in Table 1.

Table 1. Summary table of tests and dates.

Laboratory	Activity name	Test type	Day of test
UNIPV	Concrete samples	Compression – Characterisation	Jun 21, 2017
UNIPV	Concrete samples	Compression – Characterisation	Jul 31, 2017
UNIPV	Mortar samples	Compression – Characterisation	Aug 03, 2017
UNIPV	Mortar samples (gap)	Compression – Characterisation	Aug 01, 2017
UNIPV	Mortar samples	Flexural – Characterisation	Aug 03, 2017
UNIPV	Mortar samples (gap)	Flexural – Characterisation	Aug 01, 2017
UNIPV	Mortar (specimens)	Triplet – Characterisation	Jul 24-26, 2017
UNIPV	Mortar (specimens)	Bond wrench – Characterisation	Jul 26, 2017
UNIPV	Felt material (cyclic)	Cyclic/friction – Characterisation	Nov 2-30, 2017

| UNIPV | Three-way joint (cyclic) | Cyclic – Component | Nov 10-21, 2017 |
| EUCENTRE | EUC-BUILD5 | Dynamic full-scale (shake-table) | Jul 31-Aug 02, 2017 |

3   Nomenclature

Symbol	Definition
Application: triplet tests for characterisation of mortar – Section 4.2	
μ	Static friction coefficient of mortar bed-joint (triplet specimen)
σ	Compressive stress applied to triplet specimen
τ	Shear stress of mortar computed by means of triplet test results
τ_0	Cohesion (or adhesion stress) of mortar computed by means of triplet tests
A_l	Lateral surface of triplet specimens, parallel to the vertical shear force
F_H	Horizontal force applied to triplet specimen
F_V	Vertical force imposed to triplet specimen and measured during testing
R^2	Coefficient of determination of the regression curve for triplet test results
Application: bond wrench tests for characterisation of mortar – Section 4.3	
h	Height of the specimen for bond wrench testing
e_1	Distance from the applied load to the tension face of the specimen
e_2	Distance from the centre of gravity of the lever and upper clamp to the tension face
W	Weight of masonry/concrete unit pulled of the specimen and any adherent mortar
F_1	Applied load
F_2	Weight of the bond wrench
f_w	Bond strength
d	Mean depth of the specimen for wrench testing
b	Mean width of the bed-joint tested
Z	Section modulus of the projected plan area of the failure surface

4   Auxiliary material characterisation and component tests

As normally foreseen during all experimental campaigns, auxiliary material tests were performed to characterise the behaviour of concrete, mortar and fabric felts. In more detail:

- Cubic concrete samples underwent standard tests for determining the compressive resistance of concrete. Tests were performed on concrete cubes delivered by the producer of precast wall and slab panels;
- Mortar samples underwent standard tests for determining compressive and tensile resistance of the mortar used for both the wet connections between the precast wall panels and the wet joints between the precast wall panels and the slabs or foundations underneath them;
- Triplet tests were performed for determining the cohesion and friction coefficient of mortar under three different levels of axial load that were selected to be representative of the range of axial load values present in EUC-BUILD5 specimen;
- Bond wrench tests were performed for determining the bond strength of the mortar used for construction of EUC-BUILD5 specimen. These set of tests was carried out in accordance with the European Norm EN 1052-5;
- Cyclic tests were performed to evaluate the frictional/mechanical properties of felt material, as well as any type of eventual strength degradation. Tests were carried out under different levels of axial load representative of those present in EUC-BUILD5 specimen.

Additionally, a set of component tests aimed at investigating the cyclic response of three-way panel connections present in the full-scale building under consideration was carried out, with a view to evaluate the behaviour of wet connection systems of this type. Specimens built according to the design concept of EUC-BUILD4 and EUC-BUILD5 prototypes were thus prepared and tested cyclically, in pseudostatic fashion, allowing the determination of key response parameters for these joints. The specimens consisted of two concrete blocks that resemble details of joint arrangement as well as typical concrete thickness of these precast panels.

Indeed, notwithstanding the fact that the set of characterisation tests already performed and documented in the EUC-BUILD4 test report had provided useful data on the monotonic behaviour of the steel connectors themselves, it was felt that it would be beneficial to obtain cyclic response curves that capture the resistance of an entire joint, as well as any type of in-cycle and between-cycle strength degradation. Cyclic loads were applied by means of an actuator working in displacement-controlled mode, so as to allow the capturing of any eventual response softening. Specific details regarding reinforcement layout of precast panel stripes, arrangement and execution of the three-way joint, and test procedure will be presented in Section 4.5, but it can be anticipated that this series of tests provided valuable information for better understanding of the full-scale test and numerical modelling of the full-scale building mock-up, since the latter's response at ultimate condition was affected by the cyclic behaviour of its three-way connections (please refer to Section 6 of this report and also to its EUC-BUILD4 companion document: *Cyclic testing of a full-scale two-storey RC precast wall-slab-wall structure representative of the Groningen building stock*).

4.1 Tests for material characterisation of concrete and mortar

Concrete class C35/45 (according to Eurocode 2) was nominally used for the precast concrete walls of EUC-BUILD5 specimen, whilst concrete class C53/65 was adopted for the hollow core slabs of this building mock-up. The mechanical properties of concrete and mortar were then experimentally verified by means of characterisation tests performed in compliance with current European standards (UNI EN 12390-3-4-7), even if, it is noted, concrete compressive strength values have little bearing on the response of the full-scale building, which is instead dominated by issues of connection behaviour (see Chapter 6).

Furthermore, it is also noted that, as more extensively discussed in Section 5.3, at the end of the construction of specimen EUCBUILD5 it was noticed that a conspicuous gap was present between the stability walls and the slabs, and hence a mortar joint was executed between the precast wall and slab panels (seemingly in accordance with what is customarily done in practice, in such cases), thus increasing the relevance and interest on the characteristics of the mortar used for this intervention.

4.1.1 Compressive strength of concrete

Standard compressive tests (UNI EN 12390-3-4-7) were performed on sixteen concrete cubes shipped to Pavia by the construction company, after a minimum 28 days curing period so that one can characterise the full compressive resistance of the concrete pertaining to the wall panels of the full-scale specimen.

In particular, three concrete cubes delivered by the producer of the precast wall panels were tested on June 21st (i.e. after 30 days of casting of the full-scale specimen, hence roughly 60 days after the casting of the precast panels (which took place in the second half of May)), whilst another thirteen cubes were tested on July 31st (i.e. the first day of testing of EUC-BUILD5 specimen).

Figure 1 shows the testing machine employed for such characterisation tests, the obtained compression resistance values are reported in Table 2 and Table 3. It is noted that the latter values refer to the actual resistance measured on those cubes (i.e. applied force divided by the area of the concrete cube), and not to their cylindrical equivalent, which is instead typically estimated by multiplying the cubic strength with a reduction factor in the 0.80-0.85 range. It is also noted that that "S" stands for satisfactory failure mode.

Figure 1. Testing apparatus for characterisation of compressive strength of concrete cubes.

Table 2. Concrete material characterisation tests: cubic samples tested on June 21st – wall panels.

ID	Label on sample	Size [mm³]	Mass [kg]	Mass/Vol. [kg/m³]	Load [kN]	Max stress [N/mm²]	Type of failure
1	5/17/2017	150.5 x 150.1 x 150.2	7.84	2311	1422	62.97	S
2	5/18/2017	150.5 x 149.8 x 149.9	7.97	2358	1373	60.92	S
3	5/23/2017	148.8 x 149.5 x 149.5	8.00	2405	1570	70.56	S

Table 3. Concrete material characterisation tests: cubic samples tested on July 31st – wall panels.

ID	Label on sample	Size [mm³]	Mass [kg]	Mass/Vol. [kg/m³]	Load [kN]	Max stress [N/mm²]	Type of failure
1	5/17/2017	150 x 150 x 150	7.90	2341	1354	60.2	S
2	5/17/2017	150 x 150 x 150	7.65	2267	1403	62.3	S
3	5/17/2017	150 x 150 x 150	7.78	2305	1472	65.4	S
4	5/18/2017	150 x 150 x 150	7.89	2338	1442	64.1	S
5	5/18/2017	150 x 150 x 150	7.87	2332	1354	60.2	S
6	5/18/2017	150 x 150 x 150	7.74	2293	1324	58.9	S
7	5/23/2017	150 x 150 x 150	7.90	2341	1481	65.8	S
8	5/23/2017	150 x 150 x 150	7.95	2356	1501	66.7	S
9	5/23/2017	150 x 150 x 150	7.88	2335	1422	63.2	S
10	5/24/2017	150 x 150 x 150	7.86	2329	1570	69.8	S
11	5/24/2017	150 x 150 x 150	7.57	2243	1383	61.5	S
12	5/24/2017	150 x 150 x 150	7.81	2314	1550	68.9	S
13	6/13/2017	150 x 150 x 150	7.63	2261	1795	79.8	S

The average compressive resistance is equal to 65.1 MPa, with a standard deviation of about 5.5 MPa, and whilst the above set of results seems to imply a certain degree of variation in the resistance values of the concrete, it should be kept in mind that, independently of their variability, the results in question indicate in any case a very reassuringly high compression resistance. Furthermore, the compression resistance of the concrete is anyway of very modest relevance to the test results of the full-scale building, and hence also to the modelling efforts, given that the response of the specimen is instead governed by the deformation of the steel connectors and the resistance of the mortar joint executed to fill the gap between the stability wall and the slab panels (see Section 5.3).

4.1.2 Compressive and tensile strength of mortar

As previously noticed and extensively discussed in Section 5.3, EUC-BUILD5 full-scale specimen underwent a "repairing" intervention after it was observed that, a gap was present between the stability wall and the slab panels. As typically done in Dutch construction practice, the layer of fabric felt material underneath the precast slab panel was removed and the gap filled with mortar, so as to restore the contact between the vertical and lateral load-bearing elements. Hence, compressive and tensile strength of the mortar adopted for gap-filling is of foremost importance, since the response of this mortar joint affects the overall behaviour of the full-scale specimen under consideration.

Standard compression and three-point flexural testing of mortar samples was carried out, as shown in the following figures (Figure 2 to Figure 5). Six specimens were prepared during the gap-filling intervention that was executed on the full-scale specimen, on July 21st. More in detail, three samples were prepared per each mortar supply, one for the first-storey slab gap and the other for the second-storey slab gap. It is worth noting that a total of nine tests per each supply of mortar were carried out because after the execution of the flexural test each rectangular specimen resulted to be split into two almost identical parts that were subsequently tested in compression. The setup for compression testing is presented in Figure 2, whilst the one used for three-points bending tests is shown in Figure 3. Considering that the test results are meant to be representative of the mechanical properties of the mortar joints that the full-scale specimen would exploit during the dynamic testing, the characterisation tests were executed in contemporaneous fashion to the shake-table testing itself (1st August 2017, at the first sign of damage that was detected in the mortar joints of EUC-BUILD5 specimen). The curing period was thus 10 days. Test results are reported in Table 4.

Table 4. Material characterisation tests of mortar for gap-filling – Samples tested on August 1st.

Label	Origin	Tensile strength [MPa]	Compressive strength [MPa]	
			Sample 1 of 2	Sample 2 of 2
P1_G	Upper slab gap 21/07/2017	6.07	24.89	24.95
P2_G	Upper slab gap 21/07/2017	4.83	24.28	23.97
P3_G	Upper slab gap 21/07/2017	5.24	24.77	20.36
P4_G	Lower slab gap 21/07/2017	4.41	19.93	21.21
P5_G	Lower slab gap 21/07/2017	4.64	19.37	20.05
P6_G	Lower slab gap 21/07/2017	4.28	20.66	19.74
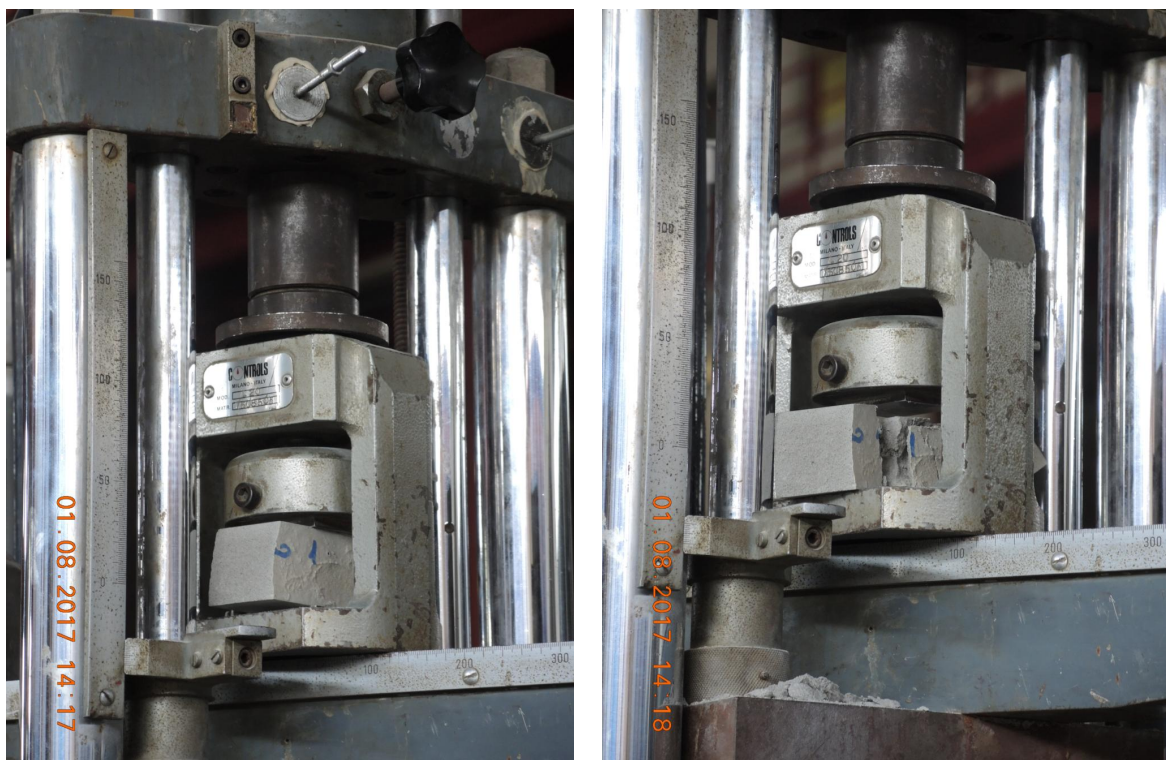
Figure 2. Compression test for characterisation of gap-filling mortar – Setup and failure of a specimen.

Figure 3. Three-points flexural testing for characterisation of gap-filling mortar – Experimental setup.

Figure 4. Three-points flexural testing for characterisation of gap-filling mortar – Failure mode of a specimen.

Figure 5. Failure mode of specimens at the end of three-points flexural testing of gap-filling mortar samples.

The results summarised in Table 4 seem to indicate a relatively moderate degree of variation in the resistance values of the mortar employed for gap-filling purposes. A tensile strength value of about 5.38 and 4.45 MPa was obtained, on average, for the mortar used at the upper and lower slab gaps, respectively. Relatively low values of coefficient of variation can be also computed from these results, particularly if those pertaining to upper and lower slabs are considered separately (i.e. 4 and 12%).

In addition to material characterisation testing of the mortar employed for the wet joint between the stability wall and the slab panels at both the first and second storeys of EUC-BUILD5 specimen, it is worth mentioning that other two sets of tests were performed to characterise the mortar (i) for the two- or three-way panel-to-panel connections, and (ii) for the wall base joints. Results of the former and latter series of tests are collected in Table 5 and Table 6, respectively. Needless to say that the same scheme and criteria used before were extended to the two experimental activities discussed in what follows. The only minor difference is that nine samples (instead of six) were prepared for each set of tests, which implies that a total of twenty-seven tests were performed for each supply of mortar. Eighteen of them were compression tests and the other nine were three-point flexural tests for the characterisation of tensile resistance of mortar. As discussed later on, the obtained results indicate a certain degree of variation in the resistance values of both types of mortar.

Table 5. Characterisation tests of mortar for two- and three-way joints – Samples tested on August 3rd.

Label	Origin	Tensile strength [MPa]	Compressive strength [MPa]	
			Sample 1 of 2	Sample 2 of 2
P1_C	Mortar for connectors	7.86	76.64	74.80
P2_C	Mortar for connectors	7.54	77.25	83.39
P3_C	Mortar for connectors	8.69	79.71	81.55
P4_C	Mortar for connectors	9.04	75.41	71.12
P5_C	Mortar for connectors	8.90	81.55	76.64
P6_C	Mortar for connectors	8.74	73.58	76.64
P7_C	Mortar for connectors	7.31	81.55	81.55
P8_C	Mortar for connectors	7.52	79.09	79.71
P9_C	Mortar for connectors	8.78	82.16	80.32

Table 6. Characterisation tests of mortar underneath precast panels – Samples tested on August 3rd.

Label	Origin	Tensile strength [MPa]	Compressive strength [MPa]	
			Sample 1 of 2	Sample 2 of 2
P1_P	Mortar under panels	9.31	92.58	90.74
P2_P	Mortar under panels	8.05	83.39	82.16
P3_P	Mortar under panels	9.66	85.84	83.39
P4_P	Mortar under panels	8.74	83.39	82.77
P5_P	Mortar under panels	9.20	84.61	85.84
P6_P	Mortar under panels	8.39	87.68	88.29
P7_P	Mortar under panels	9.52	85.22	86.76
P8_P	Mortar under panels	9.20	80.93	77.25
P9_P	Mortar under panels	8.62	88.29	88.29

The average compressive resistance of the mortar used for panel-to-panel connections and joints at the base of the precast wall panels was 78.5 and 85.4 MPa, respectively; the average tensile strength of the former type of mortar was 8.26 MPa, whilst that of the latter one was 8.96 MPa. In both cases under consideration, the coefficient of variation of the tensile resistance was higher than that of the compressive one (6-8% versus 4%).

4.2 Triplet tests for characterisation of mortar

The mortar material was object of further investigation, with a view to characterise other mechanical properties, such as cohesion and friction coefficient as well as the bond strength. Two types of specimen were thus prepared, one for triplet tests and the other one for bond wrench tests. The former test typology is presented hereafter, whereas a separate section (i.e. Section 4.3) describes the main aspects of the latter.

In addition to previous characterisation tests, nine triplet specimens such as the one shown in Figure 6, were each tested under three different levels of axial load, so as to estimate, with a good level of confidence, the cohesion and frictional resistance of mortar. It is again worth noting that in the full-scale specimen, like in several existing buildings of this type, no steel rebars connect the first with the second-story walls through the floor, and the same applies to the wall-to-foundation connection at the base of the structure. Precast wall-elements are simply resting on the foundations without any

starter rebars that protrude from the foundation into the wall panel. This implies that the entire lateral-force resisting system relies only on the shear resistance of mortar, and justifies the need of further testing aimed at studying cohesion and frictional properties of the mortar itself.

Figure 6. Testing apparatus for triplet specimens – Characterisation of cohesion and friction of mortar.

In light of this, nine triplet specimens consisting of concrete bricks and layers of mortar of the same thickness as the one used for the full-scale specimen were each tested under three different levels of axial load. Such an approach was meant to assess variations in the shear resistance as a consequence of changes in the imposed axial/horizontal load, which was in any case selected to be representative of the range of axial load values present in the walls of EUC-BUILD5 specimen. Furthermore, it is noted that different sequences of axial force were applied to try to evaluate any possible sensitivity to theis aspect as well.

Despite the fact that testing of triplets is based on well-known and established methods, it is mostly applied to the case of masonry structures. As such, some key aspects of both experimental setup and procedure are presented in the following as background information for interested readers. The full set of experimental results is reported in Section 4.2.2, along with a summary of key data and trends derived (i.e. cohesion and static friction coefficient of mortar).

As shown in Figure 6, each triplet specimen consists of three concrete blocks and two mortar layers placed in-between them; the specimen is set in the testing apparatus between two steel plates, while it is supported by roller bearings. A compression force is then applied at the two lateral faces of the specimen, before the application of the vertical force by means of an actuator in displacement control. The horizontal/axial load is kept constant during each single test and the vertical shear force is applied to the central concrete block. It is clear that the only aim of triplet tests is to

determine the level of shear force that can be resisted by the mortar, which in turn allows to determine cohesion and friction coefficients.

4.2.1 Experimental setup and procedure

Figure 7 depicts a triplet test setup, which in the present context consists of three concrete bricks and two layers of mortar placed in-between them. The specimen is supported by roller bearings and is post-tensioned by means of steel rods and plates. Figure 8 and Figure 9 present photos of the testing apparatus and details of the adopted experimental setup. The horizontal/axial load is kept constant during each single test and the vertical force is applied, in displacement control, to the central concrete block by means of an actuator.
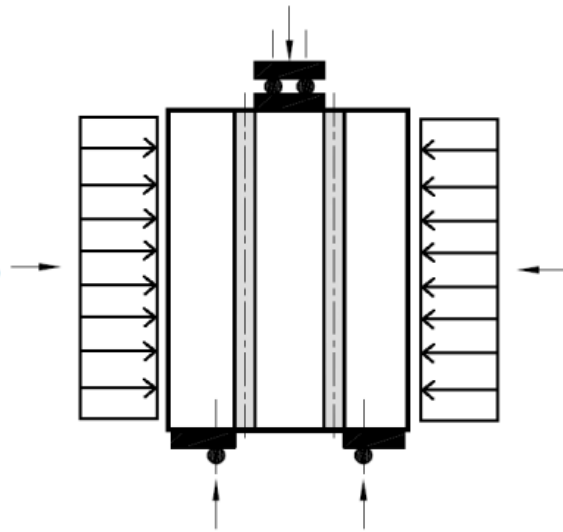
Figure 7. Triplet testing of mortar: application of horizontal and vertical forces.

As previously mentioned, three levels of horizontal/axial load, corresponding to 0.2 MPa, 0.6 MPa and 1.0 MPa, were selected for each triplet specimen, with the sequence of their application being also varied from one test to the other. The compressive load is meant to be uniformly distributed on the faces of the specimen and the vertical force is applied with a very low velocity. The horizontal force (F_H) and the vertical force (F_V) were measured during the tests and allowed one to determine the shear stress (τ), for a given compressive stress (σ).

Figure 8. Experimental setup for friction testing of felt material.

Figure 9. Testing apparatus and installed/assembled triplet specimen.

Figure 10. Examples of relative block-to-block sliding mechanism during one of the triplet tests.

The shear stress τ, for a given compressive stress σ (imposed by the lateral load on the specimen, F_H), can be expressed as:

$$\tau = \frac{F_V}{2A_l}$$

where A_l is the lateral surface of the specimens parallel to the vertical shear force, and which was equal to 195 x 95 mm^2. The imposed compressive stress σ is equal to:

$$\sigma = \frac{F_H}{A_l}$$

4.2.2 Test results

Figure 11 presents the vertical shear force-pseudotime response of triplet specimens #01, #02 and #03, the testing of which was carried out imposing increasing levels of horizontal/axial force that correspond to 0.2 MPa, 0.6 MPa and 1.0 MPa. Response plots such as the one shown in Figure 11 allow one to identify the drops in strength corresponding to the activation of sliding (see Figure 10). Figure 12 and Figure 13 show the vertical force-pseudotime-history of the other specimens (i.e. triplet specimen #04 to triplet specimen #09).
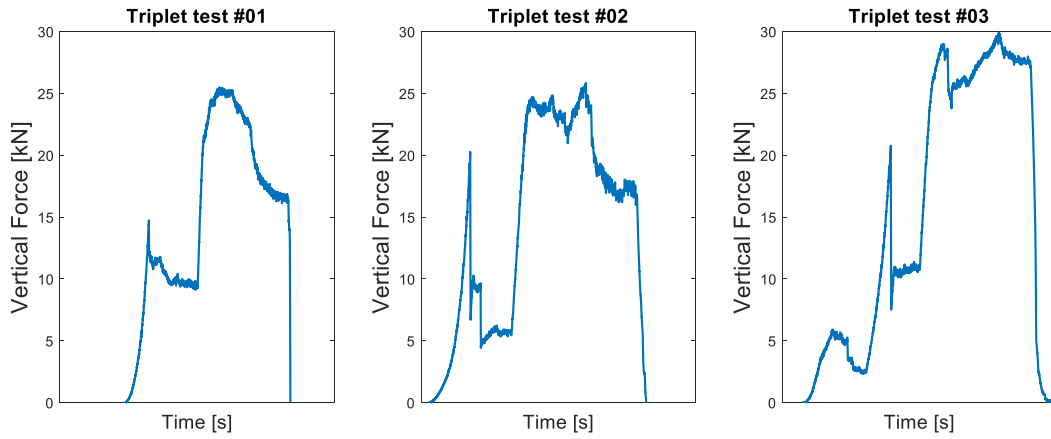
Figure 11. Triplet tests #01, #02 and #03: vertical force-pseudotime response – σ = 0.2 - 0.6 – 1.0 MPa.
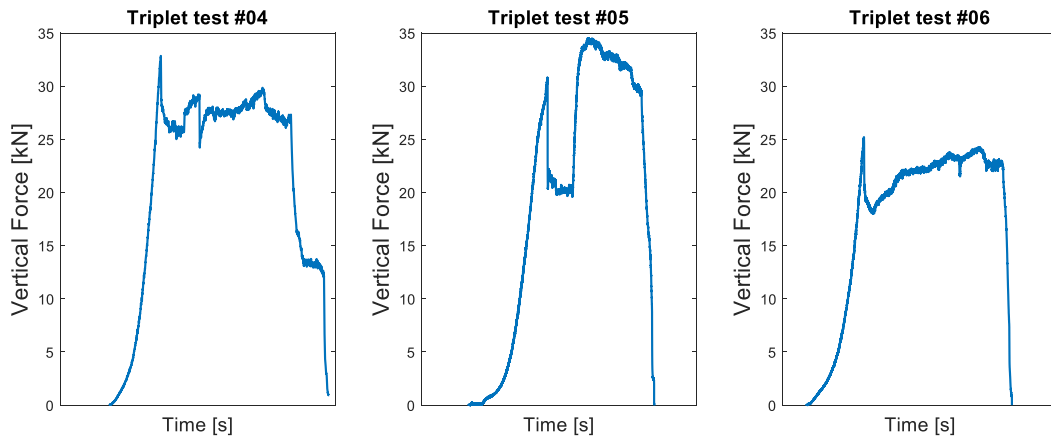
Figure 12. Triplet test #04, #05 and #06: vertical force-pseudotime response – σ = 0.6 – 1.0 - 0.2 MPa.
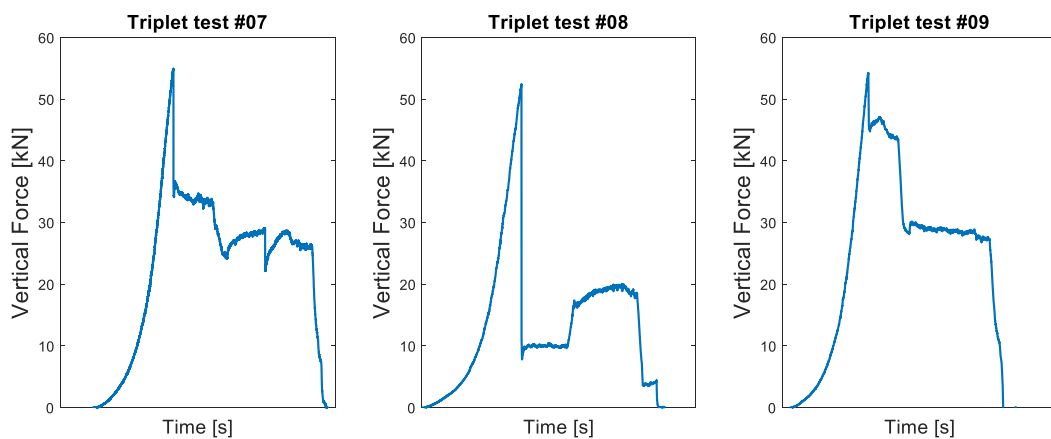
Figure 13. Triplet test #07, #08 and #09: vertical force-pseudotime response – σ = 1.0 - 0.6 - 0.2 MPa.

Key values obtained from the force-time plots reported above (Figure 11 to Figure 13) are collected in Table 7, which summarises the couples (σ, τ) and (F_H, F_V).

Table 7. Triplet test results: axial load/stress and shear force/stress.

Triplet label	Axial load [kN]	Axial stress [MPa]	Shear force [kN]	Shear stress [MPa]
#01	3.7	0.201	14.7	0.398
#02	3.5	0.190	20.3	0.547
#03	3.9	0.209	20.8	0.561
#04	11.8	0.639	32.8	0.887
#05	12.0	0.649	30.8	0.832
#06	11.8	0.637	25.2	0.681
#07	18.6	1.001	55.0	1.483
#08	18.3	0.986	52.5	1.416
#09	19.2	1.038	54.3	1.464

By plotting the couples (σ,τ), it is possible to obtain a graph such as the one shown in Figure 14.
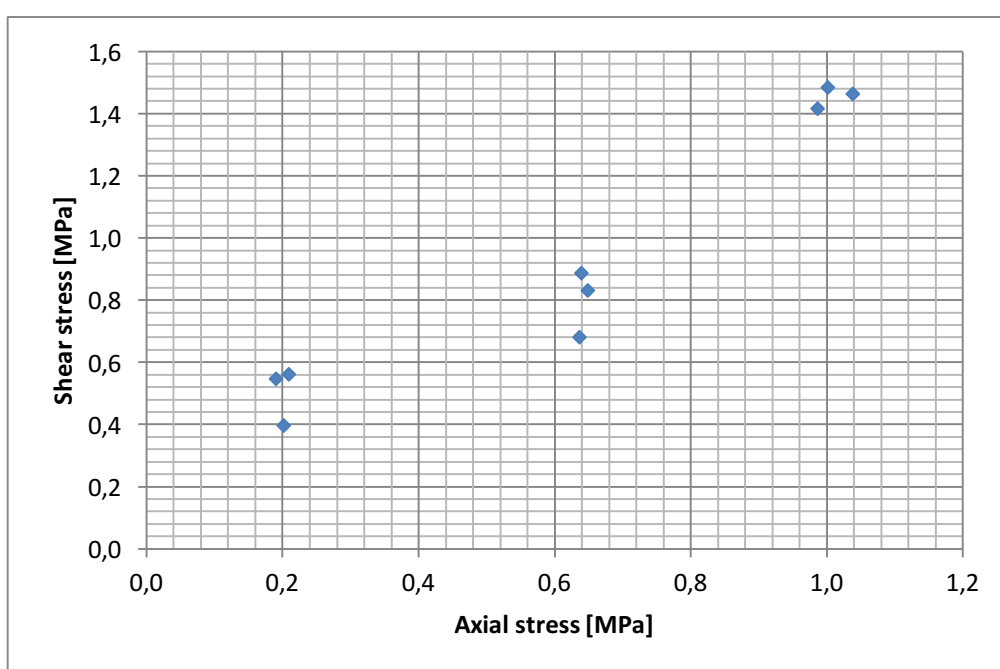
Figure 14. Triplet test results – Axial stress vs. shear stress.

It was felt that the Coulomb's law can be used for a readily interpretation of the obtained results. In detail, the shear strength τ of the mortar bedjoints of the specimens depends on three parameters that are the cohesion τ_0, the static friction coefficient μ, and the transversal compression σ. The cohesion (or adhesion stress) contributes to the resistance only if the mortar bedjoints are not cracked, whilst the friction force acts also after the formations of fractures, for as long as the concrete blocks and the mortar are in contact. According to Coulomb's law, which was found to be representative of the results, the shear strength τ is linearly dependent on the imposed axial compression σ, as expressed below:

$$\tau = \tau_0 + \mu\sigma$$

Regression analysis was thus performed and the obtained regression curve is presented in Figure 15, together with all (σ, τ) couples. It is worthwhile to mention that the couples reported herein refer to the maximum value of shear strength of mortar, which is given by both cohesion and friction force, as the specimen is uncracked before the test is performed.
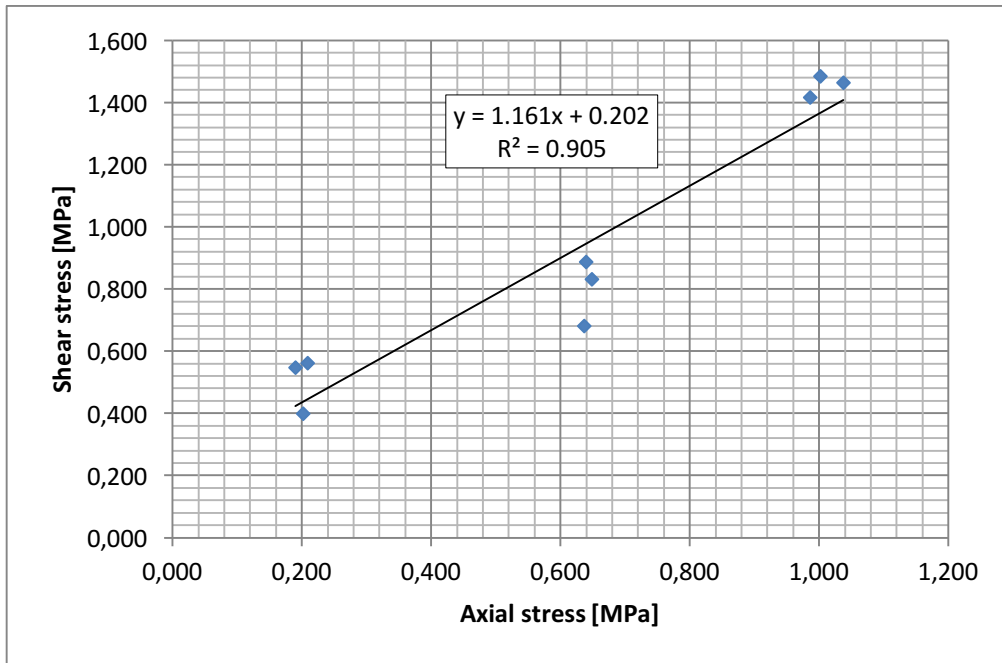
Figure 15. Triplet test results – (σ, τ) couples and regression envelope.

The regression curve plotted in Figure 15 can be expressed as:

$$\tau = \tau_0 + \mu\sigma = 0.202 + 1.161\sigma \quad - \quad R^2 = 0.905$$

It can be concluded that the proposed curve shows a good fit with the obtained experimental results, given that the coefficient of determination of the regression R^2 is equal to 0.905; the cohesion τ_0 (i.e. the Y-intercept of the linear regression line) is 0.202, whereas the coefficient of friction μ (i.e. the slope of the linear regression line) is 1.161.

4.3 Bond wrench tests for characterisation of mortar

As anticipated in Section 4.2, a set of bond wrench tests on concrete-mortar specimens was carried out to characterise the bond strength of the latter material, which forms the horizontal bedjoint of a two-concrete-bricks specimen. Bond wrench testing was executed in accordance with the European Norm EN 1052-5. Although this type of test is based on a well-known and established approach, it is mostly applied to the case of masonry structures. As such, some key aspects of both the experimental setup and the testing procedure are reported in the following as background information for interested readers. The full set of experimental results is presented in Section 4.3.2, along with a summary of key data and trends that were derived.

4.3.1 Experimental setup and procedure

Figure 16 shows the type of specimen that is used for these tests, whereas the test layout is depicted by the drawing of Figure 17. The specimen, which consists of two concrete bricks connected by a bed-joint, is subjected to a bending moment and a compressive force because of the application of two forces in accordance with the loading scheme presented in Figure 17.

Figure 16. Example of concrete-mortar specimen for bond wrench testing – Geometrical characteristics.
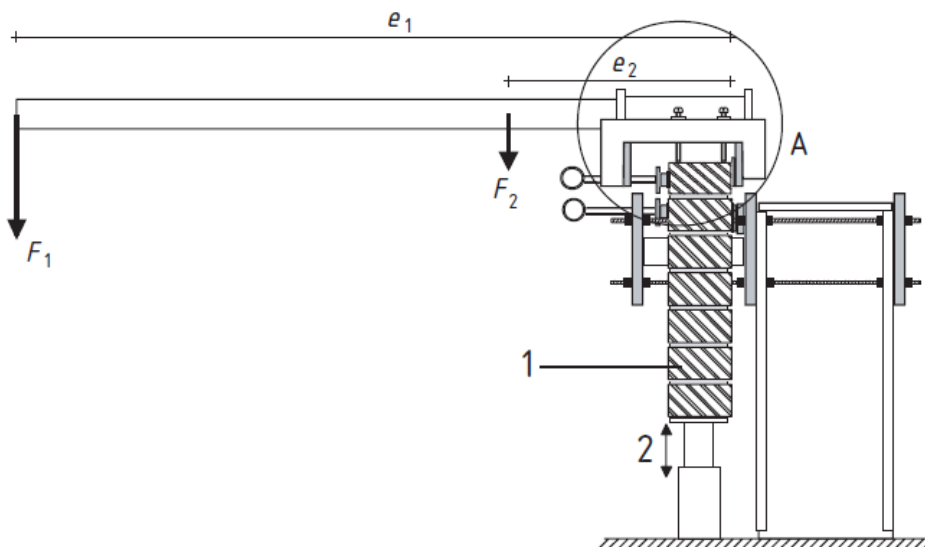
Figure 17. Bond wrench testing of mortar: setup and application of forces.

The list of symbols according to EN 1052-5 is reported below, whereas the acceptable types of bed-joint failure can be observed in Figure 18. Finally, Table 8 summarises key geometrical parameters of the testing apparatus and its weight.

h height of the specimen

e_1 distance from the applied load to the tension face of the specimen

e_2 distance from the centre of gravity of the lever and upper clamp to the tension face

W weight of masonry/concrete unit pulled of the specimen and any adherent mortar

F_1 applied load

F_2 weight of the bond wrench

f_w bond strength

d mean depth of the specimen

b mean width of the bed joint tested

Z section modulus of the projected plan area of the failure surface
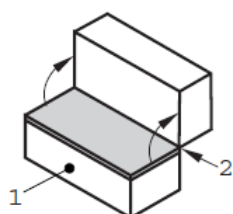
Figure A.1 — Failure at interface between mortar and upper unit
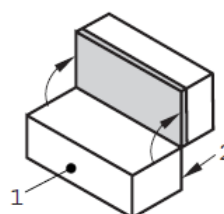
Figure A.2 — Failure at interface between mortar and lower unit
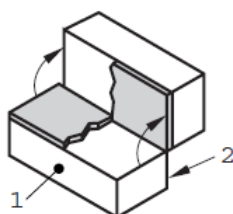
Figure A.3 — Failure at interface between mortar and both units
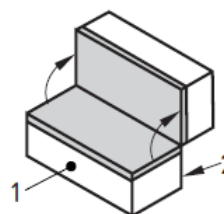
Figure A.4 — Tension failure within mortar bed

Figure 18. Bond wrench testing – Type of acceptable failures according to EN 1052-5.

Table 8. Bond wrench testing: geometry and weight of the apparatus.

b	195	[mm]
d	95	[mm]
Z	293312.5	[mm^3]
e_1	1327	[mm]
e_2	298.13	[mm]
F_2	122.53	[N]

As can be gathered from Figure 17, the test brick (i.e. the top one) is subjected to a bending moment and a compressive force, due to the two forces F_1 and F_2, whilst the remaining of the specimen is clamped. The test was performed twice on the same specimen with the failure of the second mortar bed-joint. In what follows, the main results obtained from this series of testing are summarised.

4.3.2 Test results

The following figures (i.e. Figure 19 to Figure 23) show examples of the experimental setup, as well as of the two failure modes observed (i.e. A1 and A2); Figure 21 shows the former, whilst Figure 22 and Figure 23 present the latter. Indeed, all specimens failed according to the A1 or A2 type of failure described in EN 1052-5 (see Figure 18) and no intermediate modes of failure were observed. Table 9 summarises all test results.

Figure 19. Testing apparatus for bond wrench tests – Boundary conditions and application of loads.

Figure 20. Bond wrench testing: Geometry and apparatus for base-campling.

Figure 21. Bond wrench testing: first test, bed-joint #01 – Observed failure mode (A1).

Figure 22. Bond wrench testing: third test, bed-joint #03 – Observed failure mode (A2).

Figure 23. Bond wrench testing: third test, bed-joint #03 – Detailed view of the observed failure mode.

Table 9. Bond wrench testing: bond strength and observed failure mode.

Bedjoint	W [N]	F$_1$ [N]	M$_{max}$ [Nm]	f$_w$ [MPa]	Way of failure
#01	30.02	203.47	270	0.973	A1
#02	31.97	188.39	250	0.908	A1
#03	36.68	271.29	360	1.265	A2
#04	30.53	278.82	370	1.298	A1
#05	37.12	331.57	440	1.525	A2
#06	31.09	195.93	260	0.941	A1
#07	30.61	180.86	240	0.876	A1
#08	31.45	173.32	230	0.843	A1
#09	31.01	241.15	320	1.135	A1

The bond strength was found to range approximately from 0.843 MPa to 1.525 MPa, and the mean value of this parameter was computed to be 1.085 MPa, as reported in Table 10. Standard deviation and coefficient of variation (CoV) are 0.235 MPa and 21.6%, respectively.

Table 10. Bond wrench testing: bond strength – mean value, standard deviation and CoV.

f$_w$	
Mean [MPa]	1.085
St. dev. [MPa]	0.235
CoV [%]	21.63

4.4 Cyclic tests for characterisation of fabric felt material

Notwithstanding the fact that fabric felt triplet tests have already been carried out as part of the material characterisation testing for EUC-BUILD4 specimen (please refer to Eucentre report *Cyclic testing of a full-scale two-storey RC precast wall-slab-wall structure representative of the Groningen building stock*), providing data on the frictional force transfer that can be exerted by this type of material, it was felt that it would be beneficial to try to obtain cyclic response curves that might capture any type of eventual in-cycle and between-cycle strength degradation of this response parameter. Therefore, a material characterisation cyclic test setup of the type shown in Figure 24 has been designed and undertaken as part of the characterisation/companion tests for EUC-BUILD5 specimen.

It is worthwhile to note that although the full-scale specimen under consideration herein (i.e. EUC-BUILD5) underwent removal of the felt material and subsequent mortar-filling of the conspicuous wall-slab gaps present at both storeys after its erection (see Section 5.3), the plan to cyclically test the felt material was not abandoned, since it would provide valuable information for the numerical modelling of all those precast buildings where no such wall-slab gap exists after construction, and thus where their seismic response may be governed by issues of sliding on felt. For instance, the experimental response of EUC-BUILD4 specimen is clearly a noteworthy example of such a behaviour, as sliding was observed for relatively low levels of force and storey drifts (refer to Eucentre report *Cyclic testing of a full-scale two-storey RC precast wall-slab-wall structure*

representative of the Groningen building stock for details on the observed response of this specimen).
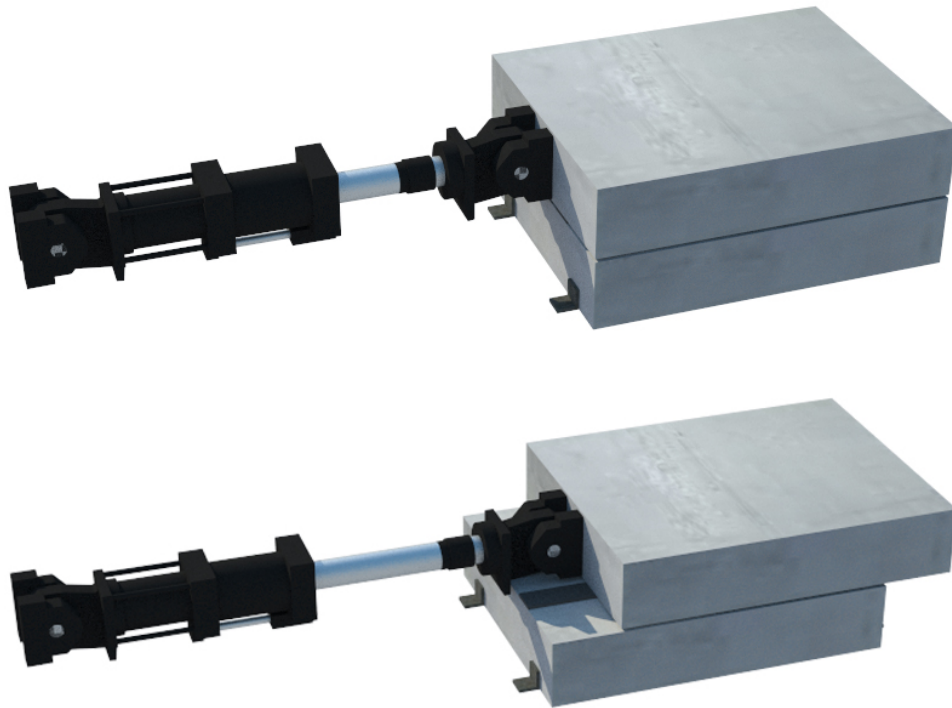
Figure 24. Setup for friction testing of felt material in cyclic fashion.

In what follows, construction details of the specimens are presented as background information for interested readers. In Section 4.4.2, key aspects of both experimental setup and procedure are illustrated. The full set of experimental results is then reported in Section 4.4.3, together with the main trends observed.

4.4.1 Construction process of the specimens

Each test specimen consists of two concrete blocks in-between which the fabric felt material is lodged. Details regarding the construction process of these blocks are shown hereafter (see Figure 25 to Figure 33). As can be gathered from Figure 25 to Figure 28, longitudinal and transversal reinforcing rebars as well as plastic tubes were arranged in the formworks, which were then grouted up by concrete. Figure 29 to Figure 31 show details of concrete casting, whilst Figure 32 and Figure 33 present the concrete blocks after that the formworks have been dismantled. Note that the above-mentioned plastic tubes were provided in such way that the concrete blocks feature properly-conceived holes that permit laboratory technicians to assemble the specimen and to attach the test rig to it.

Figure 25. Details of the formworks and reinforcement arrangement.

Figure 26. Arrangement of steel rebars and plastic tubes.

Figure 27. Top view of longitudinal and transversal reinforcing rebars.

Figure 28. Enlarged view of longitudinal and transversal reinforcing rebars.

Figure 29. Casting of concrete blocks – Detail 1.

Figure 30. Casting of concrete blocks – Detail 2.

Figure 31. Detail of concrete blocks after casting.

Figure 32. Concrete blocks for friction testing of felt material after removal of the formwork.

Figure 33. Detail of a concrete block after removal of the formwork.

4.4.2 Experimental setup and procedure

Figure 34 shows the specimen and the experimental setup for cyclic testing, whilst the position and size of the pieces of felt can be gathered from Figure 35. It is noted that each one of those pieces consisted of three layers of felt, which were first glued together and then lodeged at the top surface of the bottom concrete block in correspondence to the four corners (initial testing attempts using a single layer of felt proved unsuccessful since after the very first loading cycles the felt material would quickly get "wrinkled or partially disintegrated" and concrete-on-concrete contact would start occurring – see Appendix C). As shown in Figure 36, Figure 37 and Figure 38, three vertical load configurations were considered to be representative of low, medium and high vertical pressure conditions, namely 0.2 MPa, 0.4 MPa and 0.6 MPa. It is worthwhile to recall that these values are representative of those present in the walls of the full-scale test specimen.

Each set of felts was tested under the three above-mentioned vertical load configurations, which implies that the specimen was dismantled at every three tests in order to substitute the four pieces of felt. Furthermore, the loading sequence was changed from a triplet to another in such way that each set of intact pieces of felt underwent the first test of the three under low vertical pressure, medium vertical pressure and high vertical pressure. Each one of those combinations was tackled twice by starting the testing first by pushing and then by pulling.

The same loading protocol was considered for all tests and it consisted of two push/pull cycles at a maximum absolute displacement of 30 mm. The adopted instrumentation can be seen in Figure 34 and Figure 36. More in detail, two potentiometers were installed to measure any eventual sliding of the bottom concrete block and other two potentiometers were used to take track of the displacement

of top concrete block with respect to an external reference (i.e. the strong floor of the laboratory). Torsion was also traced by using other two instruments installed on the two sides of the specimen.

Figure 34. Experimental setup and instrumentation for cyclic testing of felt material.

Figure 35. Position and size of the portions of felt in-between the two concrete blocks.

Figure 36. Vertical loading configurations – Configuration #1, low vertical pressure (0.2 MPa).

Figure 37. Vertical loading configurations – Configuration #2, medium vertical pressure (0.4 MPa).

Figure 38. Vertical loading configurations – Configuration #3, high vertical pressure (0.6 MPa).

For what concerns the setup, the actuator was attached to the top concrete block of the specimen by means of steel plates and steel cables that were post-tensioned through steel beams. Other two stiff steel beams, each of which was restrained by two concrete masses, were used to prevent the base of the specimen from sliding on the strong floor of the laboratory (see Figure 38). Displacements associated with such a mechanism were, in any case, measured and were found to be negligibly small.

4.4.3 Test results

First of all, experimental data were processed so as to obtain the force-displacement response curve of each test, which permits assessment of the static and dynamic friction coefficients of the material under study.

Figure 39 presents an example of the hysteretic force-displacement response curve for one case of testing under high vertical pressure, whereas Figure 40 collects all responses distinguishing between low, mid and high vertical pressure conditions. As can be gathered from Figure 39 and Figure 40, a fairly rigid-plastic response was obtained for all tests, regardless of the imposed vertical pressure. It should be nonetheless noted that the initial branch of the response deviates from a "perfectly-rigid" behaviour due to the fact that three felt layers glued together were tested (as described in Section 4.4.2), which inevitably implies some initial shear/horizontal distortion of such felt assembly. The transition zone between static (curve initial peak) and dynamic (curve flatter plateau) friction was evident as well (see Figure 39 and Figure 40). A value of 10 mm was conventionally identified to differentiate between the two abovementioned phases.
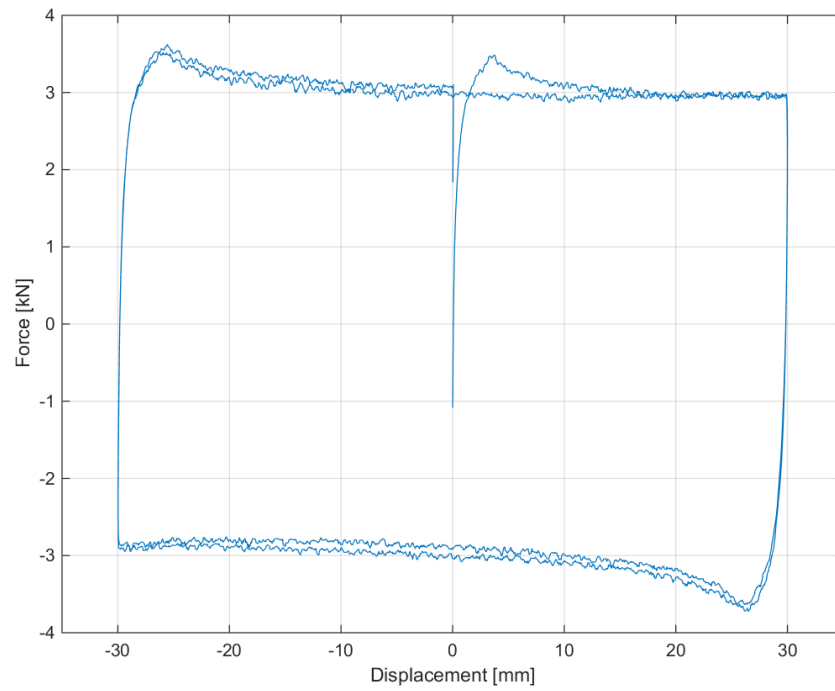
Figure 39. Example of force-displacement response during cyclic friction testing.
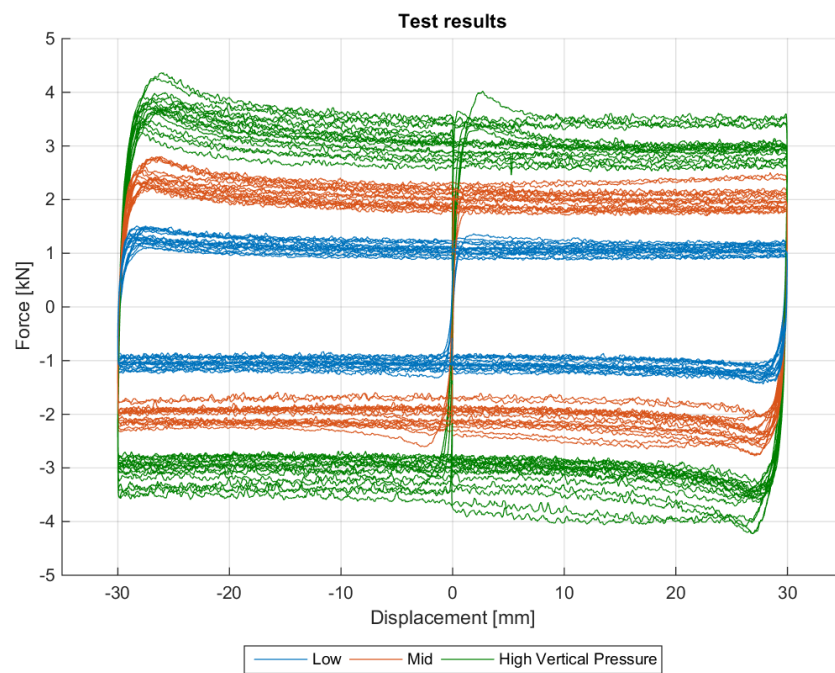
Figure 40. Comparison between the three sets of response curves for different levels of vertical pressure.

The horizontal force measured/imposed by the actuator was then normalised to the applied vertical force so as to determine the coefficient of friction of the fabric felt material, as shown in Figure 41, Figure 42 and Figure 43, which present the series of friction coefficient-displacement response curves under low, mid and high vertical pressure, respectively. As can be seen therein, the curves from each individual test are plotted along with their statistics, namely mean and mean plus/minus one standard deviation. Note that the latter curves were derived (i) by neglecting the aforediscussed initial shear deformability of the felt layers assembly, that is by assuming a rigid behaviour for both the initial and unloading stiffnesses, and (ii) by taking as dynamic friction the value after a displacement of 10 mm is exceeded.

Furthermore, use was made of the series of estimates shown in Figure 41, Figure 42 and Figure 43 to plot charts that systematically report the variability of the static and dynamic friction coefficients under the three levels of vertical pressure under consideration (see Figure 44 to Figure 52). More in detail, Figure 44 compares the set of static and dynamic coefficients of friction obtained for the case of low vertical pressure, whereas Figure 45 and Figure 46 present them separately together with the mean value and the mean value plus and minus one standard deviation. Information of similar type can gathered from Figure 47 to Figure 49 and from Figure 50 to Figure 52 for the cases of medium and high vertical pressure, respectively. Finally, Table 11 reports a summary of the mean static and dynamic friction coefficients under low, mid and high vertical pressure. The coefficient of variation (CoV) was also computed, revealing that higher variability can be associated with the static friction coefficient. In this case, the CoV is found to range from approximately 10.5% to 11.6%, the higher value corresponding to the lower vertical pressure. Such trend is reversed as far as dynamic friction is concerned, considering that the CoV is in the range 8.6-9.3%, the higher value corresponding to the higher vertical pressure (i.e. 0.6 MPa).
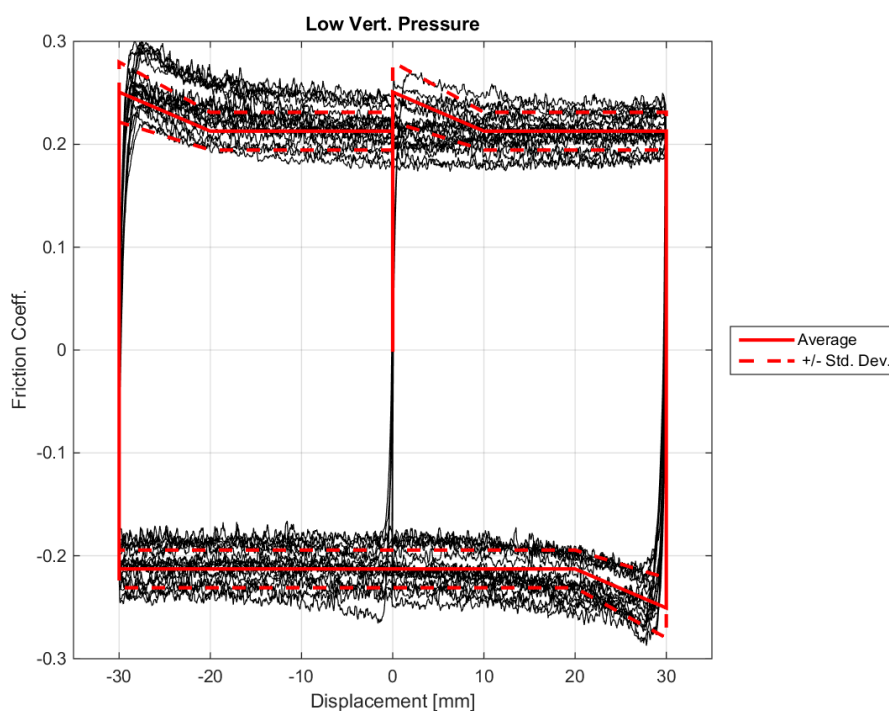
Figure 41. Friction coefficient versus displacement response curves – Low vertical pressure.
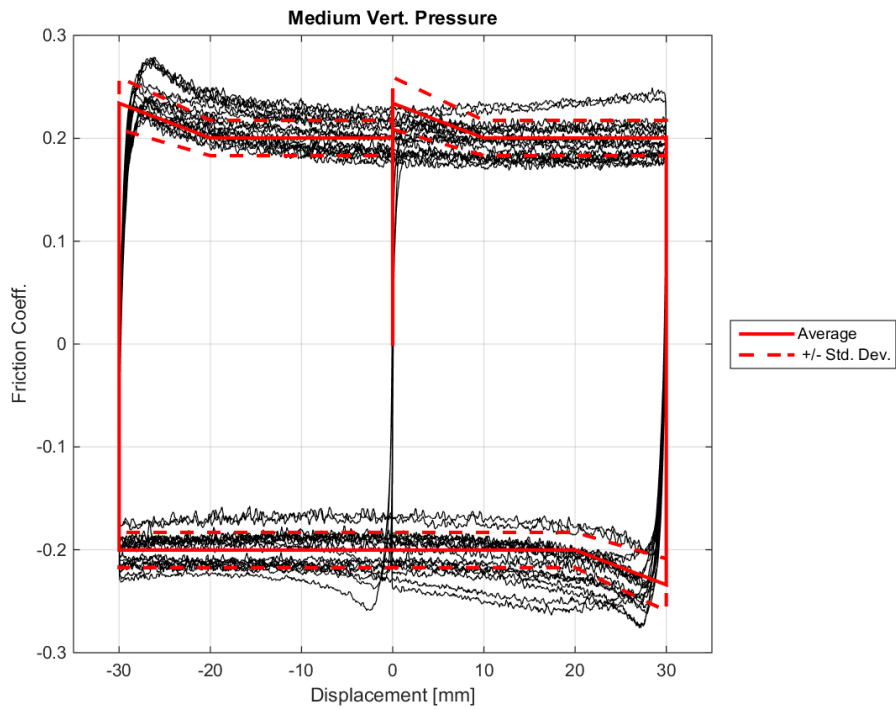
Figure 42. Friction coefficient versus displacement response curves – Medium vertical pressure.
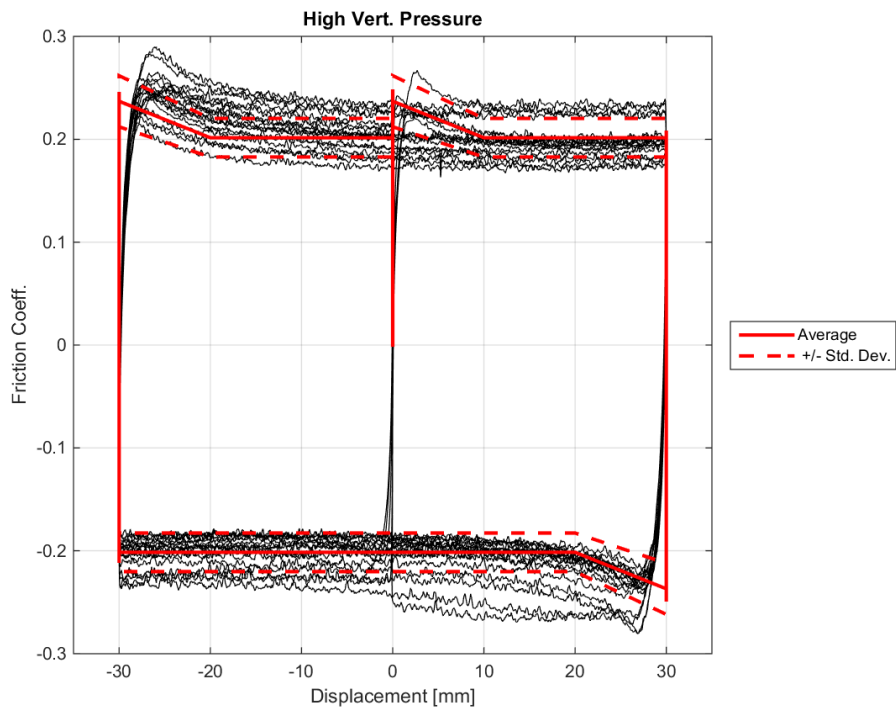
Figure 43. Friction coefficient versus displacement response curves – High vertical pressure.
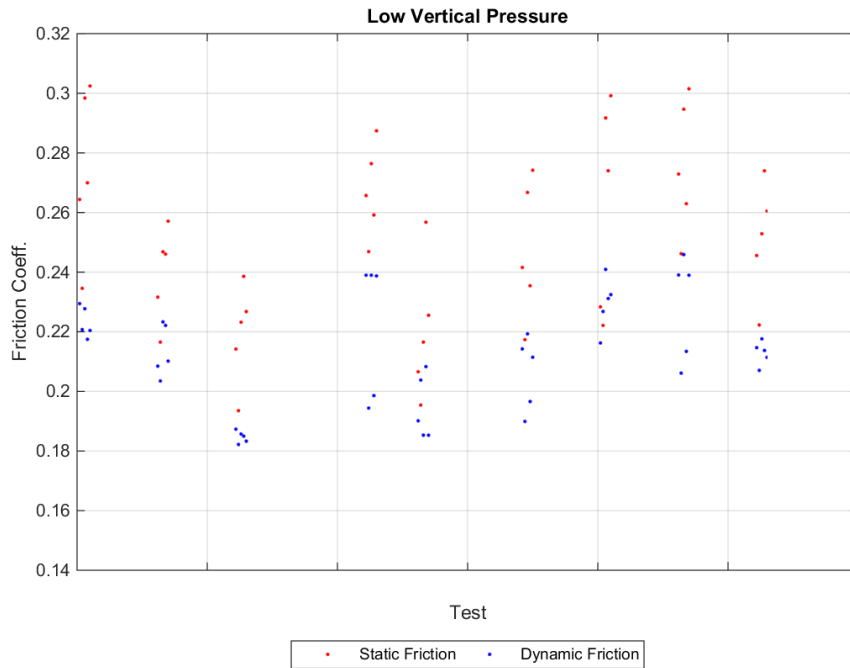
Figure 44. Comparison between static and dynamic friction coefficients – Low vertical pressure.
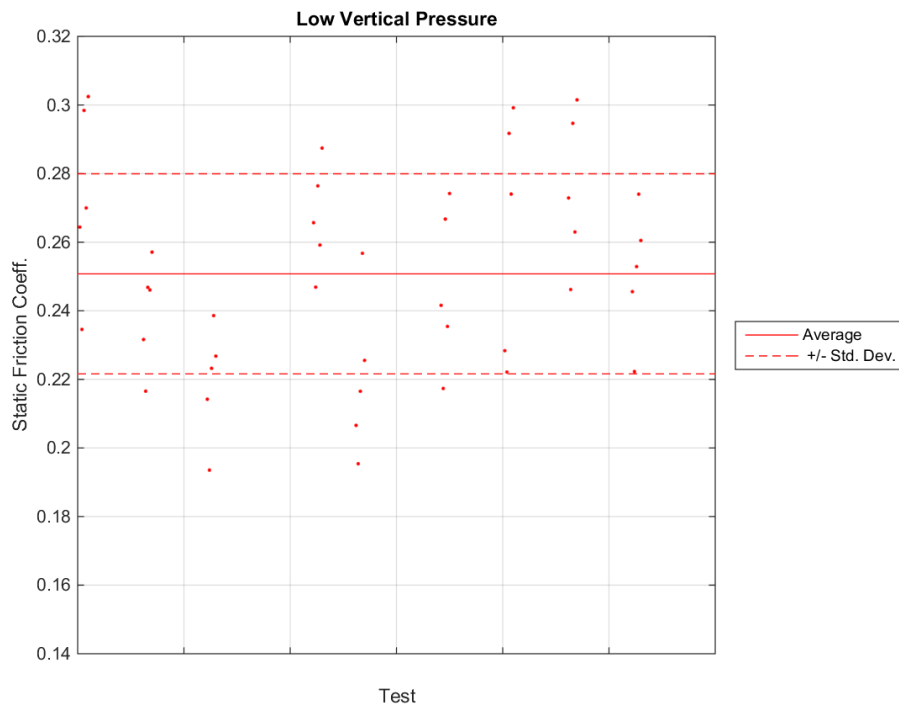
Figure 45. Static friction coefficient (individual estimates and statistics) – Low vertical pressure.
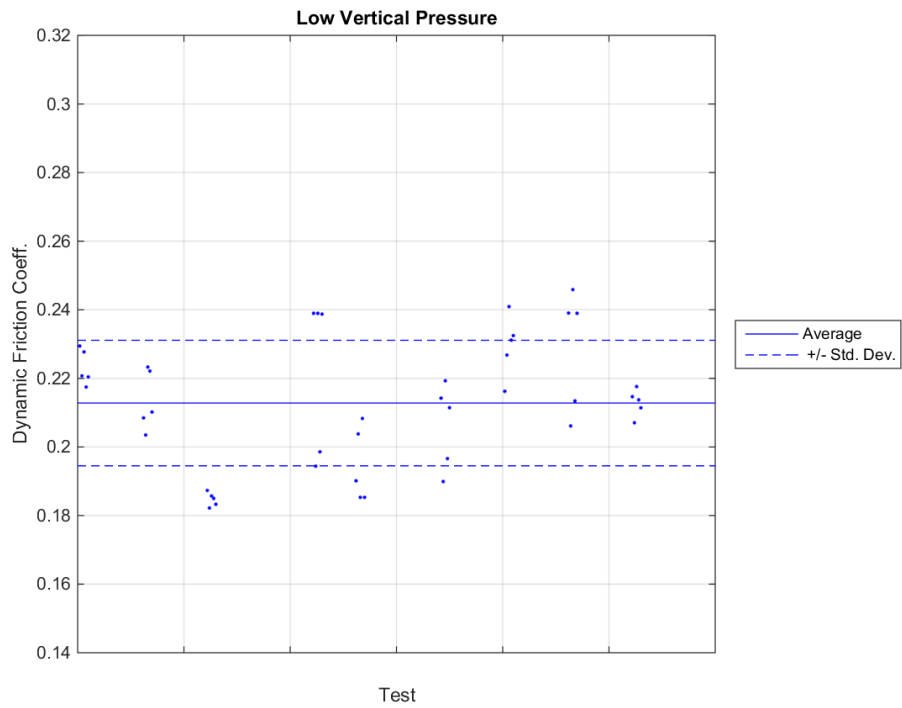
Figure 46. Dynamic friction coefficient (individual estimates and statistics) – Low vertical pressure.
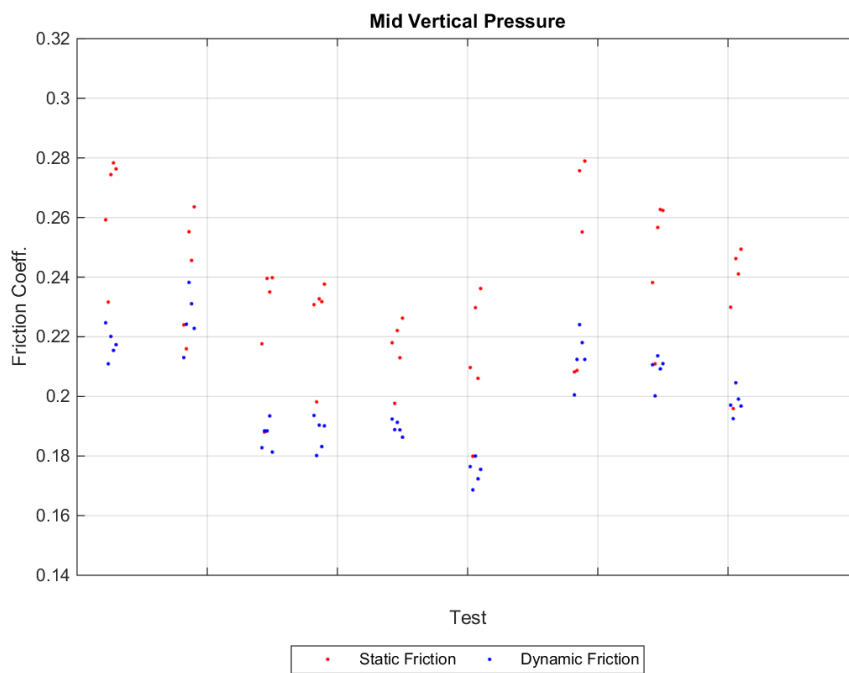
Figure 47. Comparison between static and dynamic friction coefficients – Medium vertical pressure.
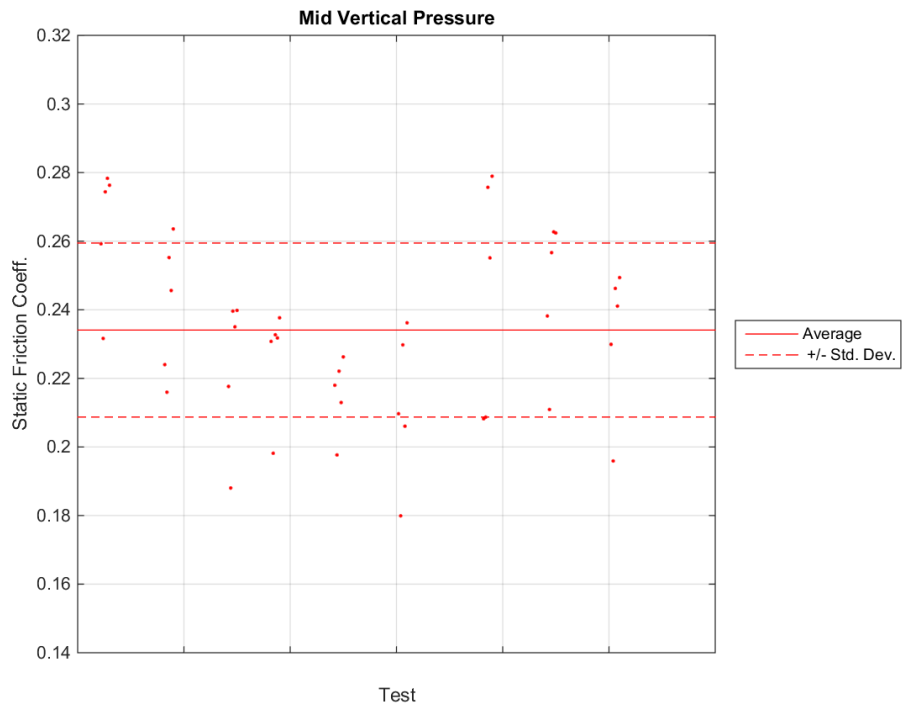
Figure 48. Static friction coefficient (individual estimates and statistics) – Medium vertical pressure.
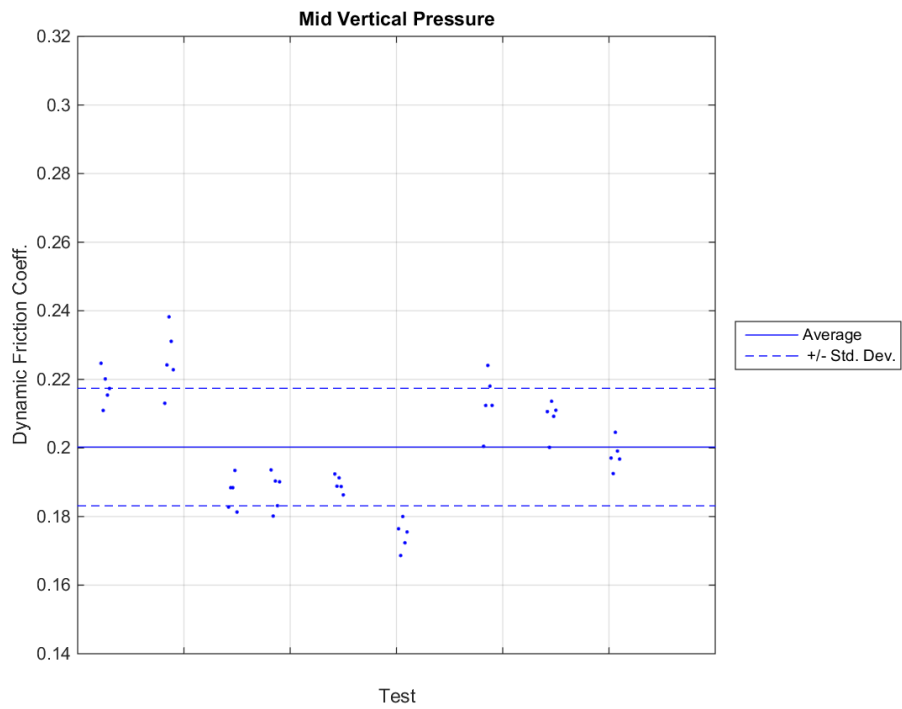
Figure 49. Dynamic friction coefficient (individual estimates and statistics) – Medium vertical pressure.
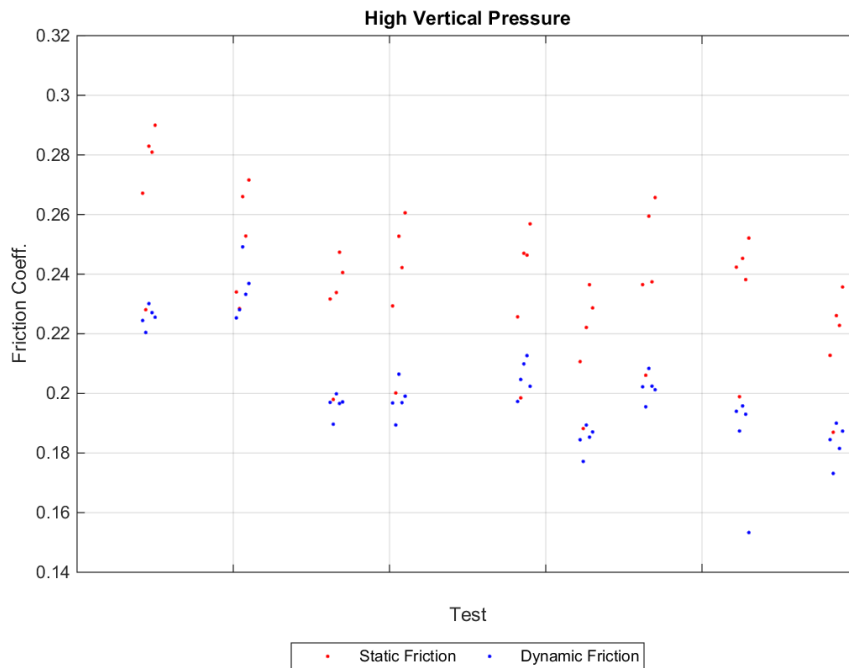
Figure 50. Comparison between static and dynamic friction coefficients – High vertical pressure.
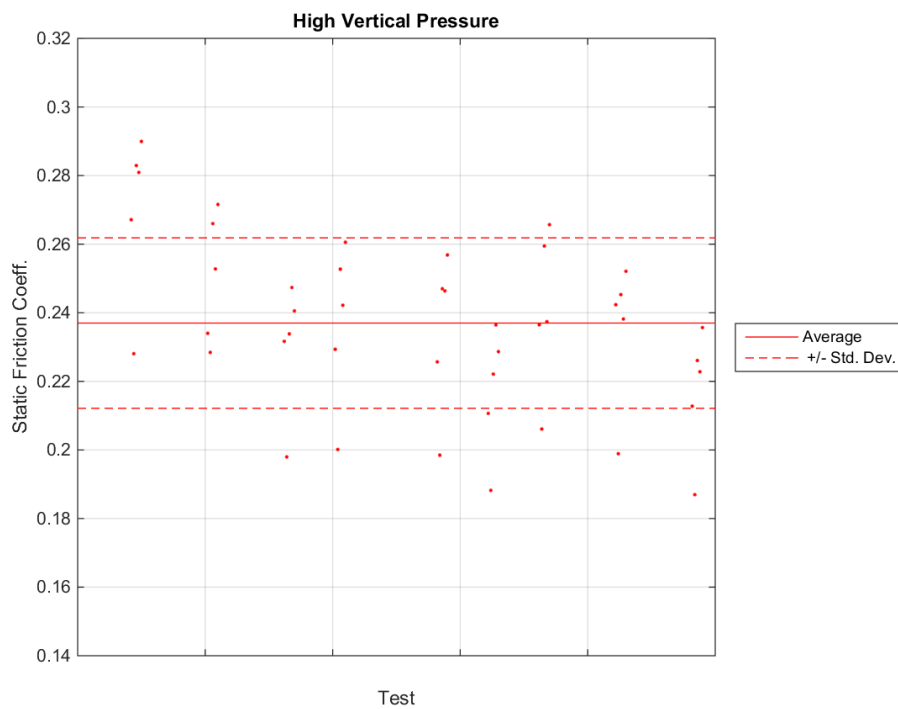
Figure 51. Static friction coefficient (individual estimates and statistics) – High vertical pressure.
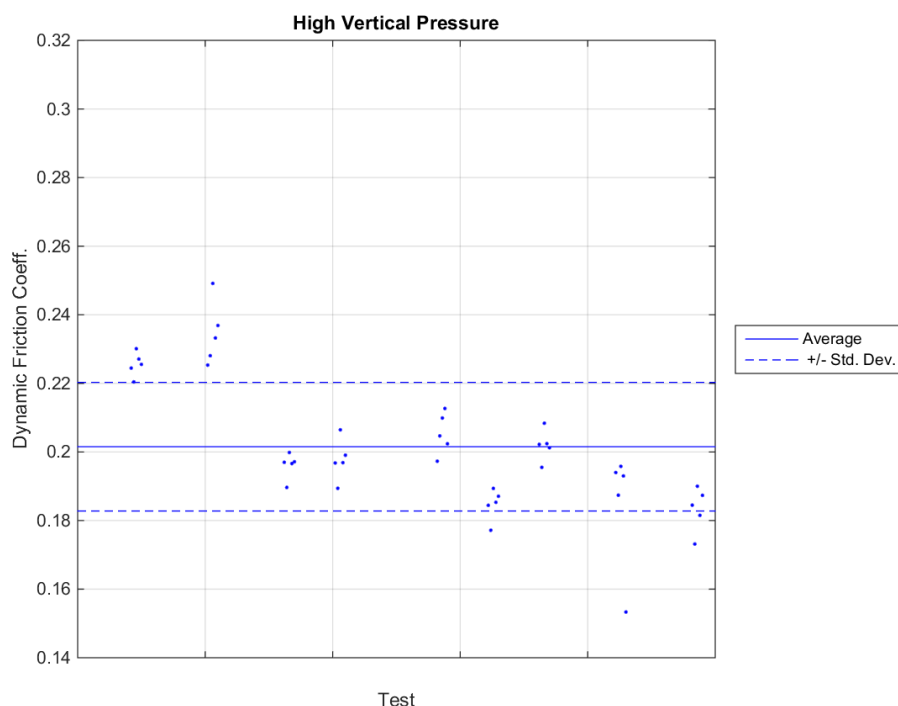
Figure 52. Dynamic friction coefficient (individual estimates and statistics) – High vertical pressure.

Table 11. Summary of static and dynamic friction coefficients – mean value, standard deviation and CoV.

Friction coefficient	Static friction			Dynamic friction		
	0.2 MPa	**0.4 MPa**	**0.6 MPa**	**0.2 MPa**	**0.4 MPa**	**0.6 MPa**
Mean [-]	0.251	0.234	0.237	0.213	0.200	0.202
St. dev. [-]	0.029	0.025	0.025	0.018	0.017	0.019
CoV [%]	11.6	10.9	10.5	8.6	8.6	9.3

In closing, it can be inferred that the friction values from these cyclic tests (in the 0.20-0.25 range) appear to be much lower than what had been obtained with the (necessarily monotonic) triplet tests (where an average value of 0.37 was obtained); interested readers may find more exhaustive information on the triplet testing carried out as material characterisation tests for EUC-BUILD4 specimen in the Eucentre report *Cyclic testing of a full-scale two-storey RC precast wall-slab-wall structure representative of the Groningen building stock*. In this respect, and also with regards to implications for the numerical modelling of existing buildings featuring joints made up of felt material, it should be pointed out that:

- these felt cyclic tests results can be considered to be referring to the response of the felt material alone (see Section 4.4.2 for further details on how this was achieved);
- however, in actual structures the friction between the wall and slab precast elements is not conditioned only by the felt, but also by the concrete, since soon after the first sliding movements, concrete-to-concrete contact occurs as well, as observed in the first attempts of

these material characterisation tests (as discussed in Section 4.4.2) and also during the cyclic testing of EUC-BUILD4 specimen, where one could clearly hear the sound of concrete grinding;

- in other words, if one would want to explicitly include, in a precast house numerical model, the felt's cyclic constitutive law, then the latter should be complemented with something that takes also into account the concrete-to-concrete friction that will inevitably be occurring as well;

- thus, and in short, the original value of 0.37 would still be recommended as the friction coefficient to use for analysis of similar structures, not only for the reasons outlined above, but also because it was noticed during the construction of the test specimens that the precast panels edges are never perfectly flat and smooth, and hence there is never a perfectly laid felt layer in-between the wall and slab precast elements.

4.5   Component tests of three-way panel connections

Precast concrete technology in the Netherlands (and worldwide) is highly-standardised, in terms of both the building system and the construction process. The same applies to the connections between the elements, which, in this construction system, are primarily constituted by mortar and welded joints (conforming to NEN-EN 287-1), as well as felts and mechanical anchors (refer to Arup report: *229746_031_NOT2008_Rev0.05_Issue EUC-BUILD-4 Prototype building description* for details on the selected design concept and to Eucentre report: *NAM_Project-precast_panels_testing_report – EUC319/2015U*). In particular, wall-to-wall joints are constituted by mechanical connections that can be either two-way or three-way anchorages, depending on if two contiguous panels are linked or not with a perpendicular stability/shear wall.

Small niches are usually created in correspondence to the inner edge of each wall segment in order to arrange the panel-to-panel connections at different positions up to the height of the wall. The anchoring system of mechanical connectors is composed of bolts and steel plates that are typically used to fasten the hook reinforcement to the external longitudinal rebar of each panel segment. Photographs are shown in Section 4.5.1. After the anchors are lodged into the niches, high-strength mortar is adopted for the injection grout (Section 4.1.2).

Of paramount importance is therefore the characterisation of mechanical properties of those anchors that were observed to fail, by a flexural mechanism, during the testing of EUC-BUILD4 specimen. As can be gathered from the results shown in Section 6, the failure mode observed during dynamic shake-table testing was very much aligned with that ascertained during cyclic pseudostatic testing, thus confirming that cyclic testing of panel connections are needed for better understanding (please also refer to Eucentre report EUC173/2017U for tests on steel connectors).

A drawing of the testing apparatus for these complementary tests on three-way panel connections is shown in Figure 53, whilst the main construction details adopted for the specimens are discussed later in this Section and are also highlighted in Section 4.5.1 by means of a photographic sequence.
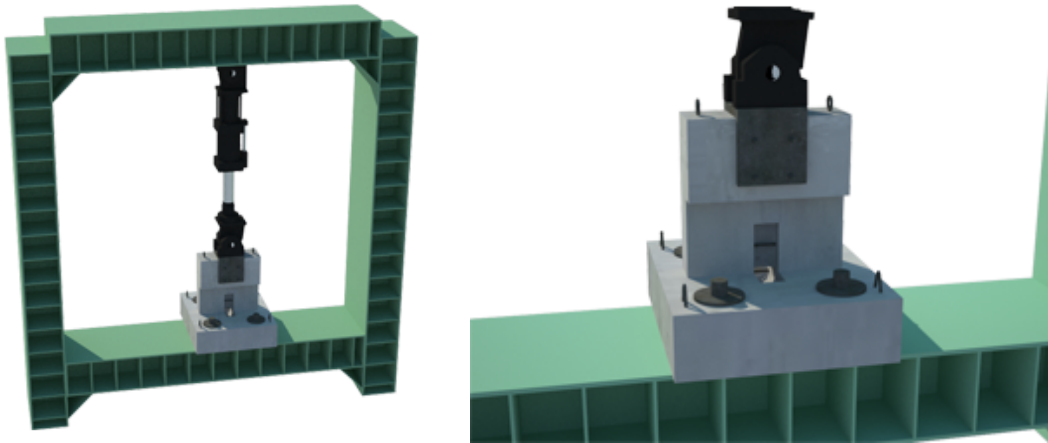
Figure 53. Testing apparatus for cyclic testing of three-way panel connections.

In order to be able to prepare the specimens for the cyclic testing of the panel connections, it was felt that further knowledge on their exact detailing should have been gained, for which reason it was decided to remove the concrete cover on some of the wall panels of the EUC-BUILD4 specimen (as per design specs, they should be identical to those of EUC-BUILD5). It was realised that:

- the steel mesh installed on the wall panels does not feature a spacing of 250 mm (as indicated in the design drawings), but rather a spacing of 180 mm in the vertical direction and 250 mm in the horizontal direction.
- the 10 mm vertical bar to which the connectors then hook into is embedded at a distance of 40 from the wall surface (in the original drawings these dimensions could not be readily identified).

These observations coming from the dismantling of the EUC-BUILD4 specimen were implemented to design the specimens for the investigation reported in this section. It is worth noting that this further set of component tests was aimed at testing only the three-way connection between the stability and lateral walls, since the damage patterns of EUC-BUILD4 specimen (please refer to Eucentre report *Cyclic testing of a full-scale two-storey RC precast wall-slab-wall structure representative of the Groningen building stock* for details on the set of damage patterns collected after each test run) and EUC-BUILD5 specimen (please refer to Section 6.5 of this report), confirmed that two-way joints between the transversal wall panels remained almost intact.

To evaluate the response of this type of wet connection, specimens consisting of portions of concrete panels that resemble details of joint arrangement as well as typical concrete thickness of the ones used for the full-scale buildings were thus prepared and tested by applying cyclic loads through a displacement-controlled actuator.

In what follows, construction details of the specimens are presented as background information for interested readers. In Section 4.5.2, key aspects of both the experimental setup and the testing procedure are illustrated. The full set of experimental results is then reported in Section 4.5.3, along with the main trends derived from the additional series of component tests.

4.5.1 Construction process of the specimens

Each test specimen consists of two concrete wall stripes featuring reinforcement arrangement and construction details typical of those used for the precast wall panels of EUC-BUILD5 specimen (see Section 4.5). Details regarding the construction process of these blocks are shown hereafter (see Figure 54 to Figure 70). As can be gathered from Figure 54 to Figure 57, longitudinal and transversal reinforcing rebars as well as plastic tubes and polystyrene blocks were arranged in the formworks, which were then grouted up by concrete. Note that the above-mentioned plastic tubes and polystyrene blocks were provided in such way that the horizontal and vertical concrete panels of the specimen feature properly-conceived holes that permit laboratory technicians to assemble the specimen, lodging the steel connectors in their sockets. Figure 58 and Figure 59 show details of concrete casting of one of the five horizontal panels manufactured by laboratory technicians, whilst Figure 60 and Figure 61 illustrate the same process for a vertical panel. Furthermore, Figure 62 to Figure 64 present one of the wall stripes before and after that the formworks have been dismantled and the block of polystyrene has been removed. Vertical and horizontal panels were then lifted up and moved to the laboratory, where the technicians assembled the five specimens (see Figure 65). It can be seen from Figure 66 to Figure 68 that the steel connector was firstly lodged in the socket of the horizontal panel and that the vertical panel was then seated onto the horizontal one so as to permit the arrangement of the other steel connector in the niche of the vertical panel. Finally, Figure 69 and Figure 70 show the specimens after mortar grout and curing.

Figure 54. Arrangement of reinforcing rebars in one of the wall stripes.

Figure 55. Detail of reinforcing rebars and polystyrene block in one of the wall stripes – Horizontal panel.

Figure 56. Detail of reinforcing rebars and polystyrene block in one of the wall stripes – Vertical panel.

Figure 57. Detail of reinforcing rebars and plastic tubes in one of the wall stripes – Vertical panel.
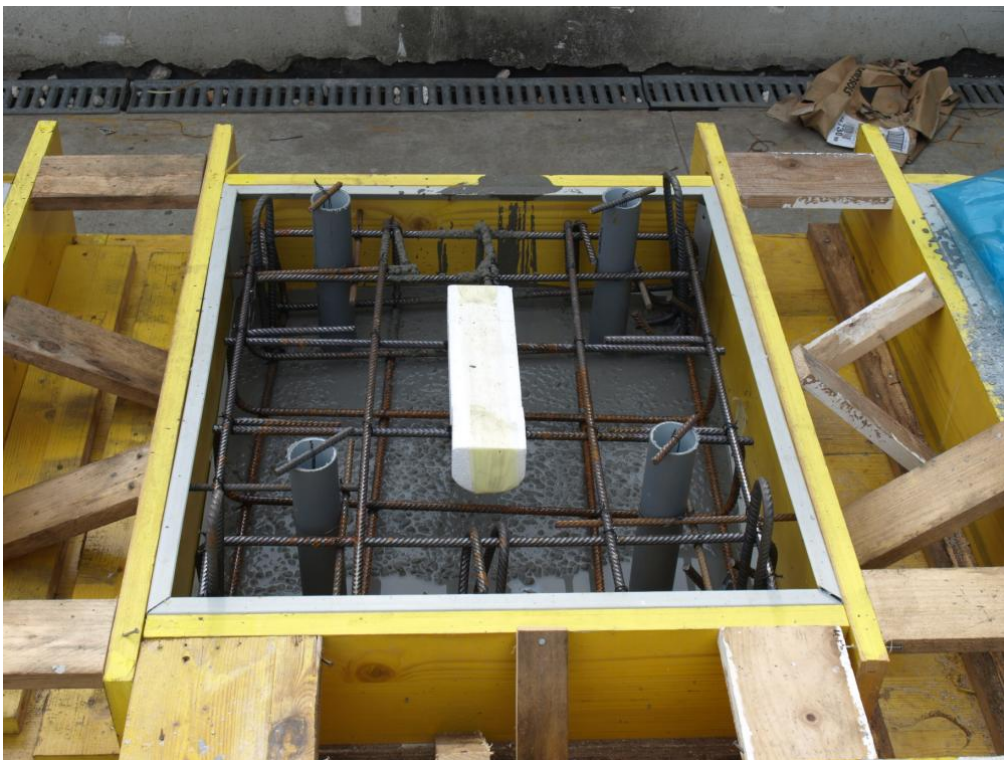
Figure 58. Casting of concrete – Horizontal panel (featuring characteristics of the lateral walls).

Figure 59. Detail of one horizontal panel after casting of concrete.

Figure 60. Casting of concrete – Vertical panel (featuring characteristics of the stability walls).

Figure 61. Detail of one vertical panel after casting of concrete.

Figure 62. Detail of one horizontal panel before removal of the formworks.

Figure 63. Detail of one horizontal panel after removal of the formworks and polystyrene.

Figure 64. Removal of polystyrene in one horizontal panel and detail of the connector socket.

Figure 65. Assembling of the specimens – Uplift of vertical panel.

Figure 66. Arrangement of hook reinforcement in the connector socket – Horizontal panel.

Figure 67. Lodgement of the steel connector in one horizontal panel.

Figure 68. Detail of wood spacers and mortar grout in the connector socket.

Figure 69. View of the five specimens after assembling and mortar grout.

Figure 70. Detail of a specimen after mortar grout and curing.

4.5.2 Experimental setup and procedure

Five specimens were tested in pseudostatic fashion, one of them monotonically so as to identify the most suitable loading protocol for cyclic testing of the other four specimens and to verify any effect due to the nature/type of loading, namely to compare monotonic and cyclic response/performance. Figure 71 presents the experimental setup used for testing of the three-way connectors, whereas a detail of the specimen mounted on the testing apparatus and instrumented for testing can be seen in Figure 72. A more systematic picture of the instrumentation is provided in Figure 73, in which drawings of top and lateral views of the specimen are collected so as to permit the identification of the type and position of the seven potentiometers.

As far as the instrumentation is concerned, it can be understood from Figure 72 and Figure 73 that two 100 mm-stroke potentiometers were symmetrically installed on the two short edges of the specimen and that four 50 mm-stroke potentiometers were mounted at the corners of the two long edges of it. Also in this case, potentiometers were symmetrically arranged in order to monitor displacements in different portions of the specimen and check for any eventual uneven deformation. Other two 50 mm-stroke potentiometers were installed on the steel plate to which the actuator was attached so as to measure any possible displacements in this zone as well.

As can be gathered from Figure 72, use was made of four steel plates and rods to seat the specimen on a base plate that was fixed to the testing apparatus. Plates and rods were stiff enough to avoid any relative displacement at the base of the specimen. Another C-shaped steel plate was used to attach the actuator to the specimen so as to apply loads in monotonic and cyclic fashion.

Figure 71. Global view of the experimental setup for cyclic testing of three-way panel connections.

Figure 72. Detail of the typical instrumentation assumed for testing.

Top view
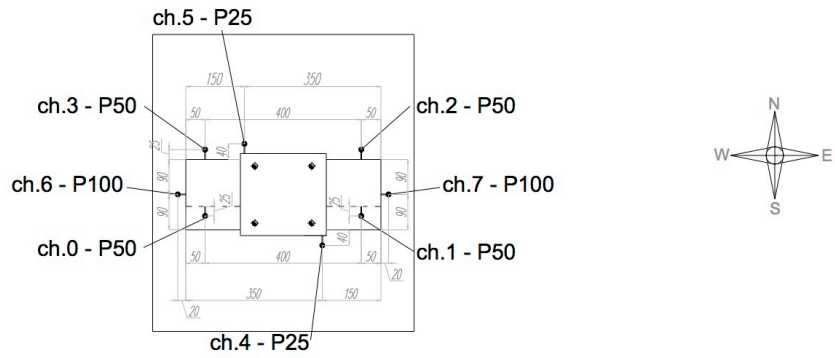
South
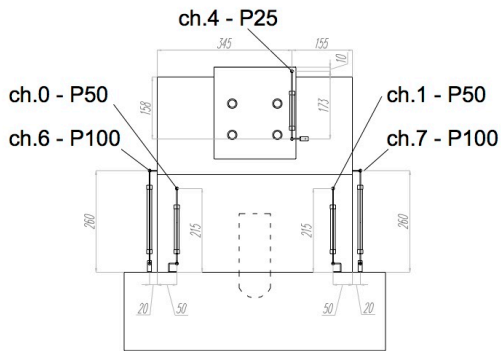
North
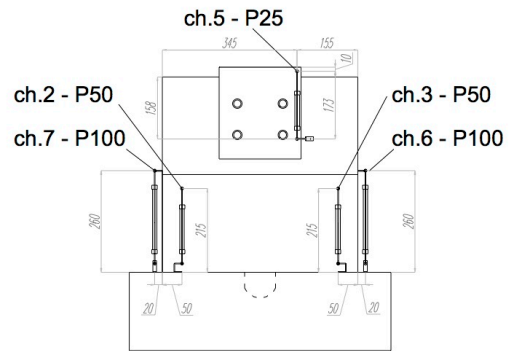
West
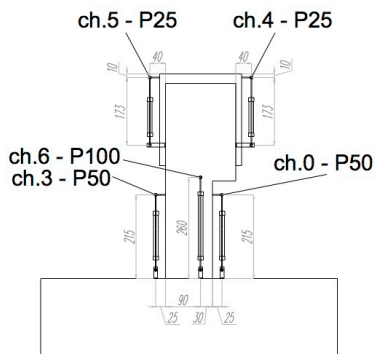
East
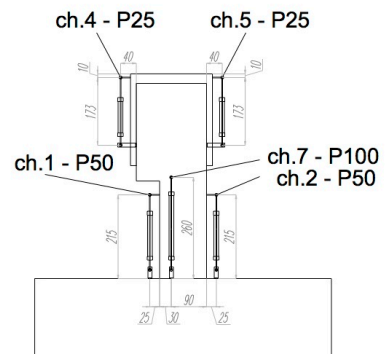
Figure 73. Type and position of the adopted potentiometers – Top and lateral views.

As previously mentioned, the first specimen was tested monotonically by applying the axial load in displacement control mode. Such test results were then used to define the cyclic loading protocol, which consisted of a necessarily asymmetric loading history; after the application of two force-controlled half cycles at 5 kN and 10 kN, the testing was carried out in displacement control mode imposing seven displacement levels: 0.5 mm, 1.0 mm, 2.0 mm, 4.0 mm, 8.0 mm, 16.0 mm and 24.0 mm. Two half cycles per amplitude were performed by pulling up the specimen (i.e. positive displacement). It is noted that the testing was concluded with an additional monotonic ramp up to failure.

4.5.3 Test results

Figure 74 presents the axial force-axial displacement response curve obtained by the monotonic testing of specimen #1, whereas Figure 75 illustrates the type and level of damage for an imposed vertical displacement of 24 mm. It results evident that, after initial cracking, the two portions of the specimen were completely detached, apart from the mechanical connection or continuity ensured by the permanently bent steel connector lodged in the niche of the base portion of the specimen. A photograph showing the flexural failure mode of the upwardly-bent steel connector at the end of the test can be seen in Figure 76. It is worth specifying that this latter photo was taken after the removal of grout, when the steel connector had been already cut.

The specimen resisted a vertical force of about 13 kN for a displacement of 2 mm, after which value a drop in strength can be observed, since the force resisted at 5 mm was approximately equal to 10 kN. Due to a sort of catenary action mobilised by the steel connector, the resistance increased as the displacement was increased, and the specimen reached its maximum load-carrying capacity, which was slightly higher than 14 kN (for an imposed vertical displacement of about 23 mm). Once this displacement level was exceeded, softening started being observed because of the extensive damage (i.e. permanent flexural deformation) of the steel connector in the base connector socket.
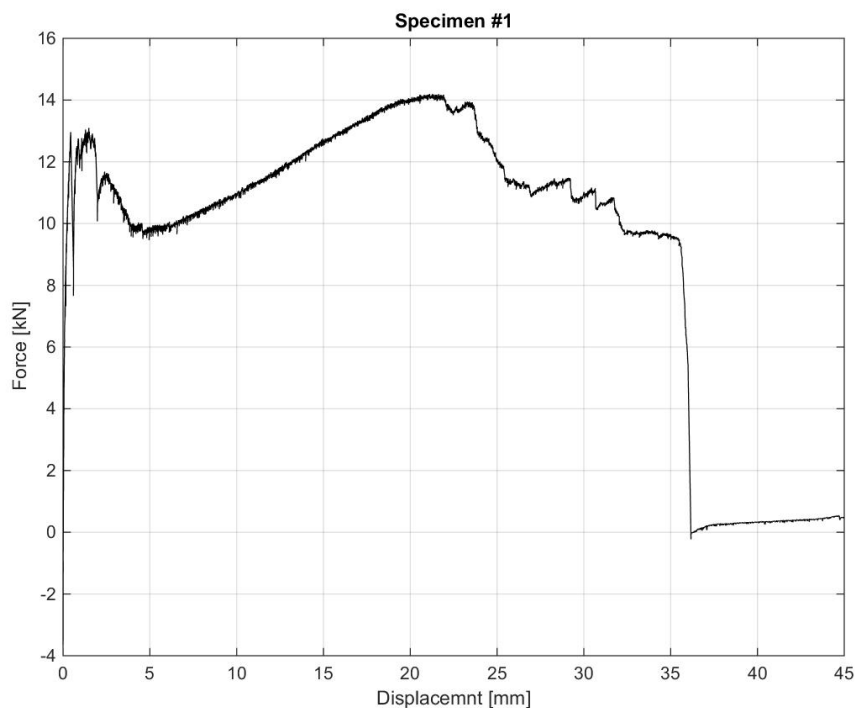
Figure 74. Axial force-displacement response of specimen #1 – Monotonic testing.

Figure 75. Damage and detachment of the two portions of the specimen.

Figure 76. Failure mechanism of the steel connector at the end of the test (after cutting and removal of grout).

Cyclic testing of specimens #2 to #5 was undertaken imposing the previously described asymmetric loading history, which is summarised also in Table 12.

Table 12. Asymmetric loading protocol for cyclic testing of three-way steel connectors.

Test run #	Test Name	Main DoF	Control Type	Ampl.	Load Shape	Cycles
			(Force or Displ.)	[kN] [mm]		[#]
01	Step#01-FC	Long	Force	5	triang.	2
02	Step#02-FC	Long	Force	10	triang.	2
03	Step#03-DC	Long	Displ.	0.5	triang.	2
04	Step#04-DC	Long	Displ.	1.0	triang.	2
05	Step#05-DC	Long	Displ.	2.0	triang.	2
06	Step#06-DC	Long	Displ.	4.0	triang.	2
07	Step#07-DC	Long	Displ.	8.0	triang.	2
08	Step#08-DC	Long	Displ.	16.0	triang.	2
09	Step#09-DC	Long	Displ.	24.0	triang.	2
10	Step#10-DC	Long	Displ.	50.0	ramp	-

Figure 77 shows the cyclic force-displacement response curve of specimen #2, whereas the flexural failure mechanism of the steel connector is presented in Figure 78.
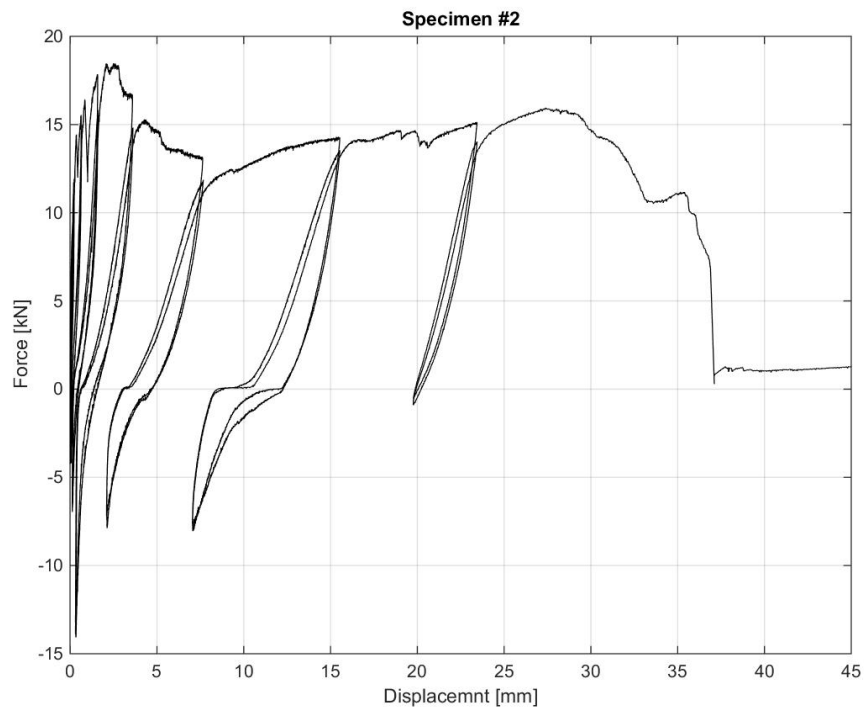
Figure 77. Axial force-displacement response of specimen #2 – Cyclic testing.

Figure 78. Flexural failure mode of the steel connector – Specimen #2.

Figure 79 shows the cyclic force-displacement response curve of specimen #3, whereas the flexural failure mechanism of the steel connector is presented in Figure 80.
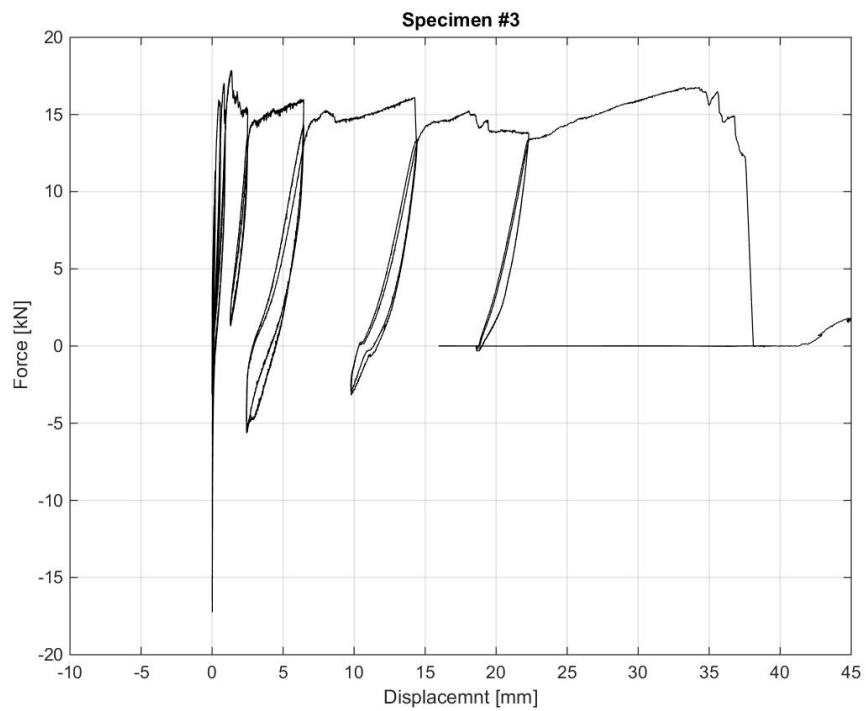
Figure 79. Axial force-displacement response of specimen #3 – Cyclic testing.

Figure 80. Deformed shape of the two steel connectors at the end of the test – Specimen #3.

Figure 81 shows the cyclic force-displacement response curve of specimen #4, whereas the flexural failure mechanism of the steel connector is presented in Figure 82.
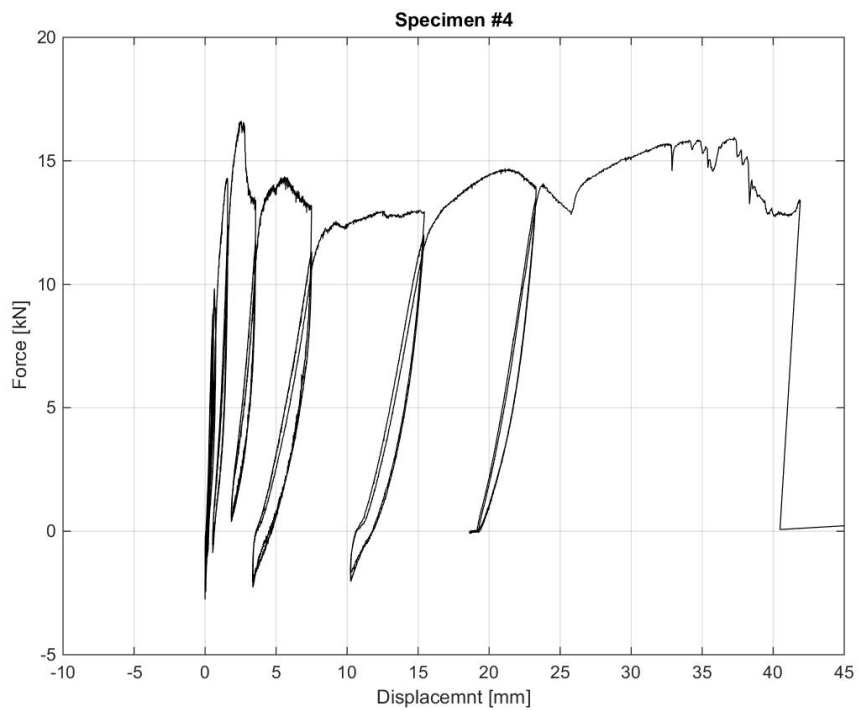
Figure 81. Axial force-displacement response of specimen #4 – Cyclic testing.

Figure 82. Bending of the steel connector embedded in the bottom connector's socket – Specimen #4.

Figure 83 shows the cyclic force-displacement response curve of specimen #5, whereas the flexural failure mechanism of the steel connector is presented in Figure 84.
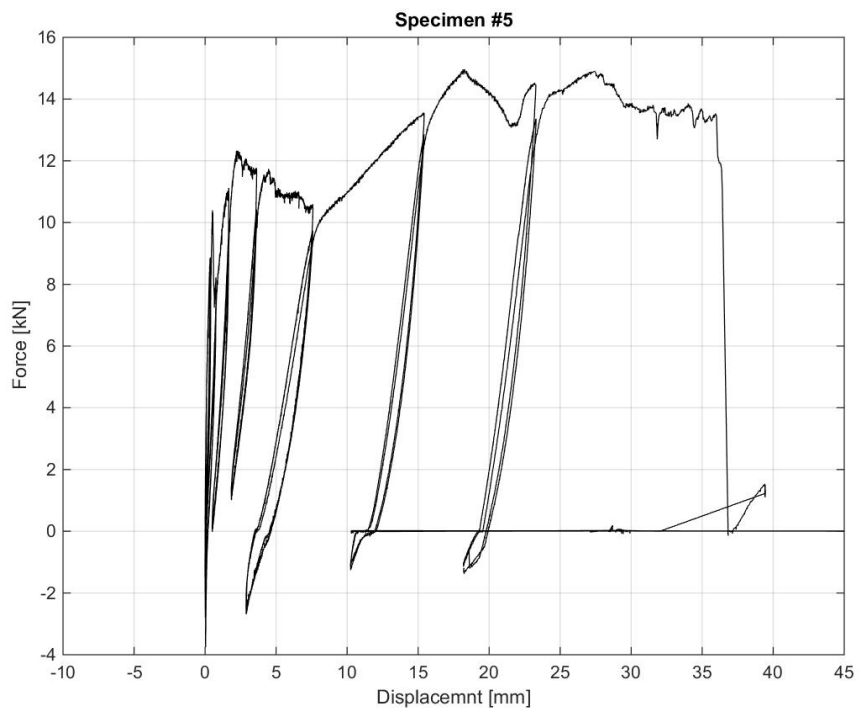
Figure 83. Axial force-displacement response of specimen #5 – Cyclic testing.

Figure 84. Bending of the steel connector in correspondence to the anchoring region of the hook.

The envelope of the hysteretic response curves of specimens #2 to #5 was then obtained, as shown in Figure 85, Figure 86, Figure 87 and Figure 88. The comparison between the monotonic response of specimen #1 and the envelope curves pertaining to the cyclically tested specimens is presented in Figure 89, whereas the mean response computed by using the monotonic curve and the envelopes of the four cyclic tests is provided in Figure 90, where the five experimental response curves and their analytically computed counterpart are superimposed.

Whilst the observed flexural failure mechanisms were very similar in form and type (see Figure 76, Figure 78, Figure 80, Figure 82 and Figure 84), the resistance was found to vary significantly, as far as the response of a specimen is compared to that of the other ones, and, in addition to that, the five curves had different variability for different levels of displacement. For displacements smaller than 5 mm, the capacity was shown to range approximately from 12 kN to 18 kN, with a mean of about 15 kN. The fork of the response curves narrows as the displacement increases, considering that a fairly constant resistance of about 14 kN was observed for displacements in the range 20-25 mm. The fork widens for larger displacements ranging from 25 mm to 35 mm, since softening was found in some cases and hardening in other ones. Failure and the subsequent strength drop started being observed for displacements slightly larger than 35 mm, though perhaps a 25 mm value constitutes a more sensible proposal as threshold for conventional failure of this type of connections/connectors.

As a general comment regarding damage/failure mechanism, it should be noted that, in some cases, the hook of the vertical connector opened up and the two portions of the specimen got disconnected, as shown by Figure 80.
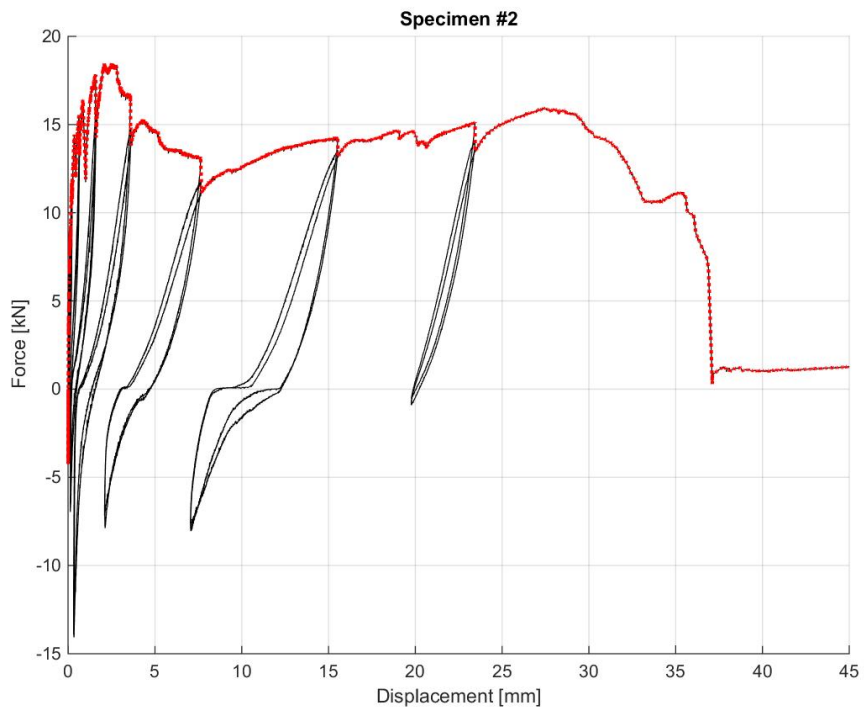
Figure 85. Force-displacement response of specimen #2 – Envelope and hysteretic curves.
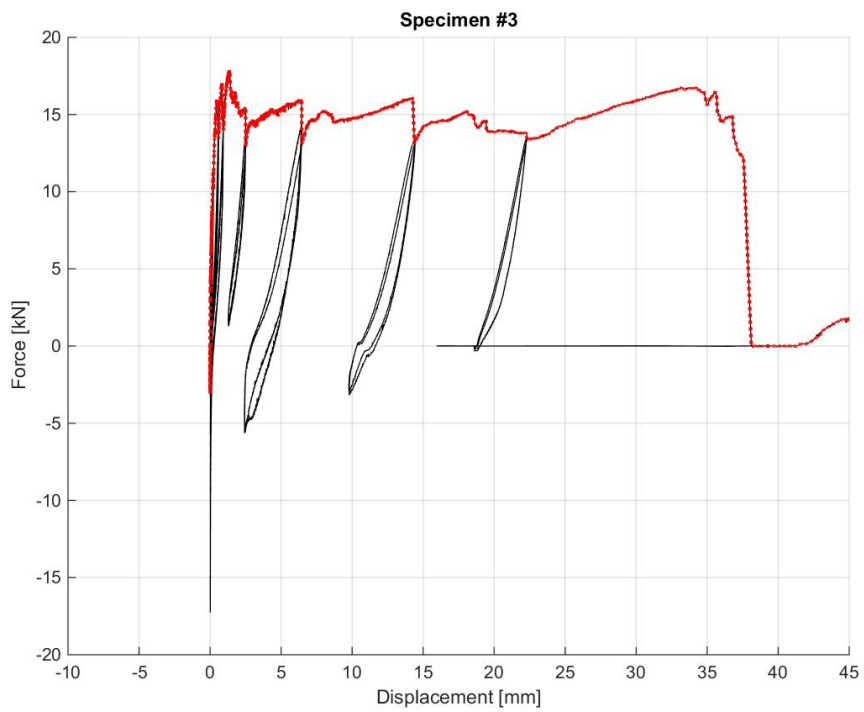
Figure 86. Force-displacement response of specimen #3 – Envelope and hysteretic curves.
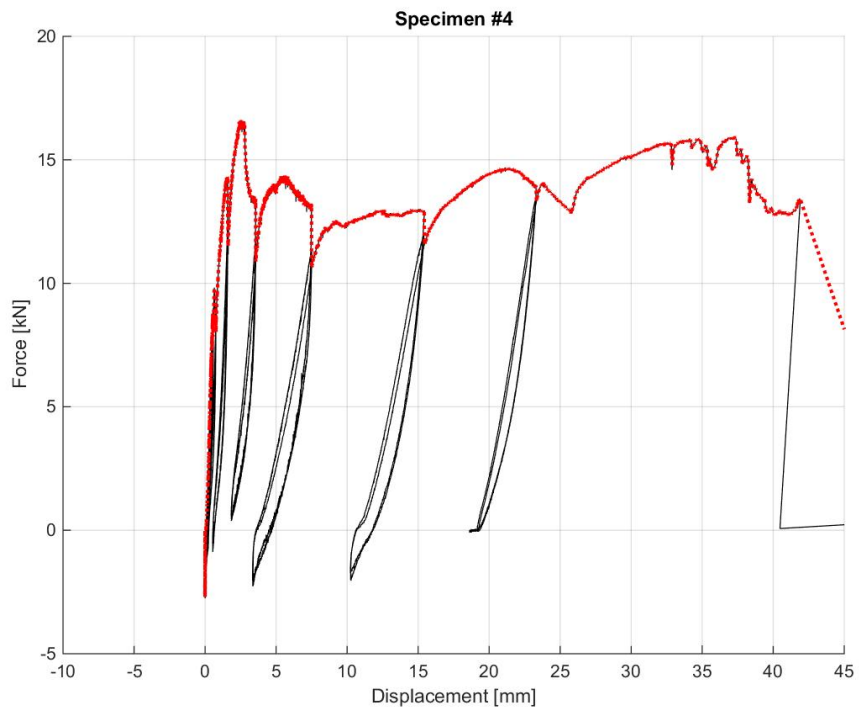
Figure 87. Force-displacement response of specimen #4 – Envelope and hysteretic curves.
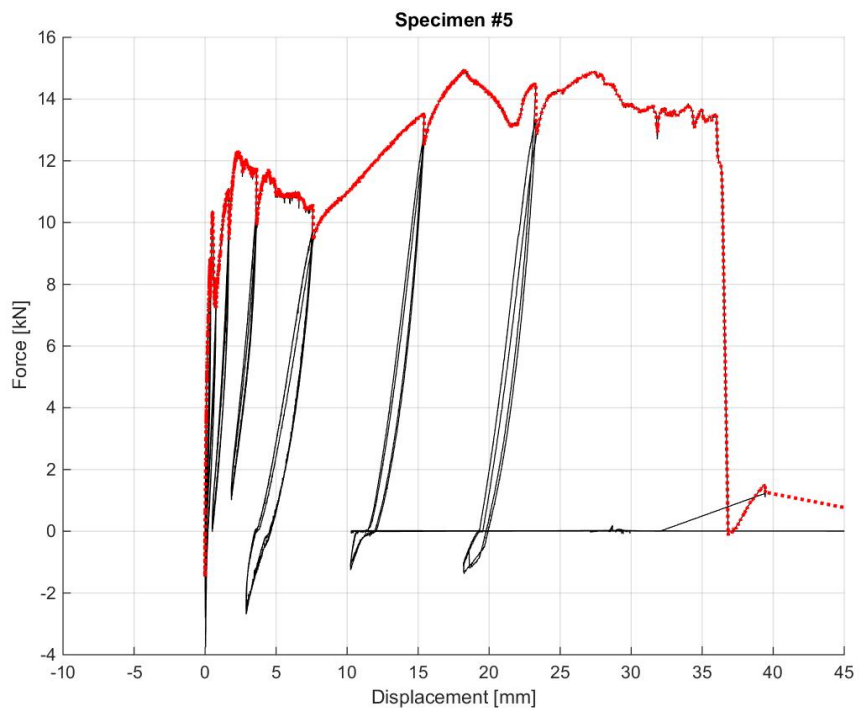
Figure 88. Force-displacement response of specimen #5 – Envelope and hysteretic curves.
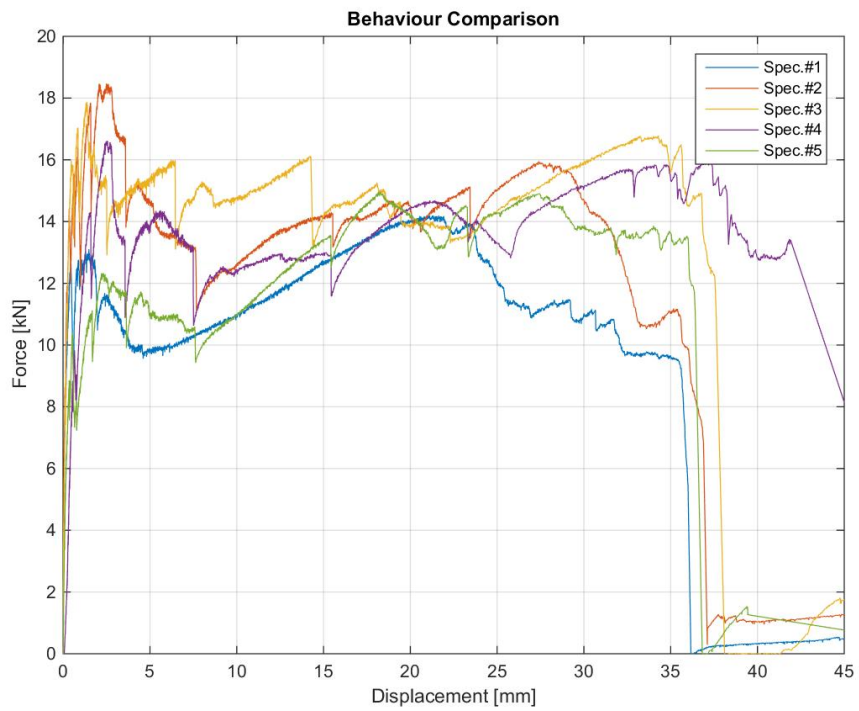
Figure 89. Comparison between the axial force-displacement response curves of the five specimens.
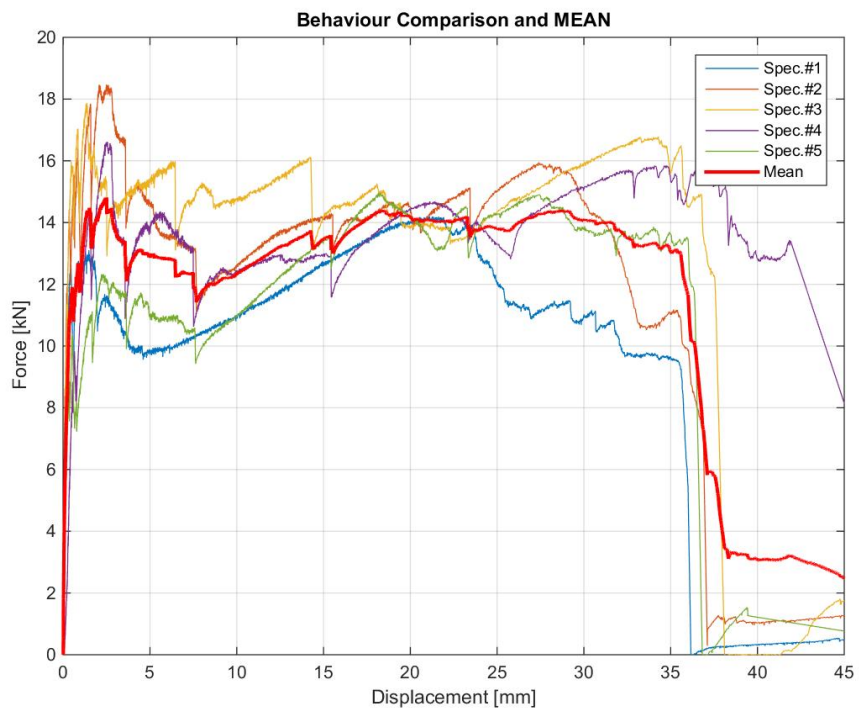
Figure 90. Mean and individual force-displacement response curves.

5 Full-scale test specimen, test setup and instrumentation

The full-scale test specimen, namely EUC-BUILD5, was meant to be nominally identical to another prefabricated building mock-up, namely EUC-BUILD4, which was tested cyclically in pseudostatic fashion (please refer to Eucentre test campaign report EUC173/2017U). Figure 91 and Figure 92 show photographs of the two structures before testing.

Figure 91. Photographs of EUC-BUILD4 specimen before cyclic testing.

Figure 92. Photograph of EUC-BUILD5 specimen before dynamic testing.

In what follows, an overview of the selected test specimen and its main characteristics is given, for completeness. In addition to the information contained hereafter, one should also consider Eucentre report *Cyclic testing of a full-scale two-storey RC precast wall-slab-wall structure representative of the Groningen building stock*, as a companion document for the key steps toward the identification and definition of the building mock-up. Exahustive details regarding the refinement process of the candidate structure in order to comply with laboratory-related issues/needs for dynamic testing are reported as well.

It is worthwhile to recall that although EUC-BUILD4 and EUC-BUILD5 specimens were conceived to be identical, the latter building featured after its erection a conspicuous gap between the stability walls and the floor slabs (and between the slab panels themselves), which instead was not at all evident in EUC-BUILD4. Construction process and details are thus of particular relevance and will be described extensively in a separate Section; detailed measurements of such gap, which was present at both first and second storeys, were taken and seemed to indicate the existence of a construction counter-flexure in the slab panels. Figure 93 presents a photograph of such gap.

Figure 93. Gap between the stability walls and the slabs.

After consultations with Groningen engineers and the Dutch contractor in charge of the construction process (i.e. Bouwborg), it was confirmed that during the erection of a building, when a gap is present, this is filled by means of the same non-shrink mortar employed for the other structural interfaces. Such a customary practice is usually operated in conjunction with the removal of the fabric felt layer so as to more effectively fill-in the gap.

In light of these considerations, the precast slab panels were propped-up to allow lab technicians to implement this intervention (see Figure 94). Further and more comprehensive details about these operations can be found in Section 5.3.

Figure 94. Propping-up of slab, to allow removal of felt layer and gap filling by means of non-shrink mortar.

In what follows, once construction-related issues are addressed, separate sections are presented to collect the main observations concerning the test setup and dynamic testing sequence, as well as instrumentation and acquisition system.

5.1 Preamble and selection of test specimen

EUC-BUILD5 was defined to feature the main characteristics of the existing buildings under study and standard details of reinforced precast concrete technology employed in the Dutch construction practice. The index building is a full-scale two-storey reinforced precast concrete wall-slab-wall structure representative of the Groningen building stock and was selected/designed based on an iterative process that consisted of:

- "ad hoc" selection of the candidate specimen among three possible solutions representative of different design criteria/concepts;
- refinement of the selected candidate in order to comply with laboratory-related issues/needs for what concerns test execution (i.e. experimental setup and procedure).

Key aspects concerning the latter part of this process are presented and discussed in the following sections, as background information for interested readers. In addition to the information contained herein, one may and should also consider Arup's *229746_031_NOT2008_Rev0.05_Issue EUC-*

BUILD-4 Prototype building description, as a valuable companion and complementary document. It is equally worth mentioning that construction details regarding the selected prototype structure can also be found in *229746_031.0_DRW2007_Rev0.05_Issue_EUC-BUILD-4_5 SWb Specimen drawings*.

5.2 Description of selected case-study structure

This section is concerned with the iterative refinement process towards the identification/definition of a candidate specimen in terms of geometrical characteristics, mechanical properties of materials and design assumptions compliant with Dutch building practice for this type of houses.

As mentioned in Section 1, reinforced concrete buildings in the Groningen region largely consist of wall-slab-wall structures, featuring no columns or beams, but only slabs and walls. These structures are a common form of housing and can be found in both cast-in-place (tunnel construction or not) as well as precast configurations. A brief overview of the main characteristics of the latter is given so as to motivate the selection of the candidate specimen, bearing also in mind that the construction process and details of these houses are very specific to the Netherlands as for instance confirmed by the photographic sequence presented in the following section.

This type of low-rise residential terraced buildings is usually constructed with precast floors, precast party/gable walls and precast walls in the longitudinal direction. The precast walls are erected first and shored up by steel diagonal props; the floor is then settled on the walls and supported by steel rebars that connect the first with the second-storey wall, through the floor. Noteworthy is that, however, these dowels are not always present in this type of construction scheme/technology. The most common precast slabs for this structural typology are hollow core sections presenting circular voids in accordance with their moderate thickness (i.e. 200-250 mm). A thickness in the range 200-250 mm and 120-150 mm is typically assumed for the party walls and the inner leaf gable walls, respectively.

Front and back façades of these multiple-unit buildings are generally cavity walls. The most common concrete grade used for these structures is C35/45 and the reinforcing steel is usually formed by a wiremesh. One layer of reinforcement in the precast walls is most likely used for small residential houses and two layers for the apartments. During the construction phase, use is made of cranes to erect and set in place the precast walls that rest directly on the foundations or on the ground floor slab, which in turn rests on the foundations. The latter option is anyway either less frequent or in non-standard configurations. Once the connections between the elements are realised, the temporary props used to ensure the stability of the structure against the horizontal wind actions are removed.

Starter rebars are usually not present in this construction system, and the wall-to-foundation connections merely consist of mortar joints. Mechanical anchors and felts are used as well, the latter being placed at the bottom of the hollow core slabs, which are not necessarily connected together through concrete topping. Discrete L-shaped metal restraints can sometimes be found in existing buildings to prevent the unseating of prefabricated wall-elements. Wall-to-wall joints are standardised solutions and are mainly constituted by mechanical connections that can be either two-way or three-way anchorages, depending on if two contiguous panels are linked or not with a perpendicular stability wall.

EUC-BUILD5 specimen, designed to combine several common features of this type of structures, was meant to feature stability walls, perpendicular to the lateral loadbearing walls, since these lightly reinforced wall-panels tend to be crucial elements for this structural scheme. The geometry of the tentative specimen was re-designed by varying the length of the stability walls according to three different criteria, which resulted in the corresponding three candidates:

- 229746_031.0_DRW2006_Rev0.05_Issue_EUC-BUILD-4_5 SWa Specimen drawings;
- 229746_031.0_DRW2007_Rev0.05_Issue_EUC-BUILD-4_5 SWb Specimen drawings;
- 229746_031.0_DRW2008_Rev0.05_Issue_EUC-BUILD-4_5 SWc Specimen drawings.

The second candidate (i.e. option b), which features half-span long stability walls, was selected and the corresopnding structural drawings were then further refined. Such a selection was due to on one hand the excessive slenderness of option a, in which these walls are assumed to be 2 m long, and on the other the fact that having squat stability walls such as the ones assumed for the third candidate (i.e. 3.75 m long) is not representative of the typical properties of the building stock of interest. In fact, the third option was designed by taking the length of the stability walls as two-thirds of the slab spans, which is a rare upper bound that can be referred to as the maximum length possible. Option b, in which the length of the stability walls is equal to the inter-storey height and approximately one half of the slab span as per existing buildings, is the most "reliable" and suitable structural prototype for the purposes of this experimental study. The choice was also consistent with the original design of the reference building and confirmed by preliminary computations of overturning moment (please refer to Arup's *229746_031_NOT2008_Rev0.05_Issue EUC-BUILD-4 Prototype building description* for other and more specific details).

The initial design concept was refined and a few adjustments were made with respect to the existing configurations and the assumptions based on which the index building was derived. This process is needed to fully comply with testing requirements in terms of both design of the setup and prevention of collapses during the execution of dynamic testing. In particular, it is noteworthy that:

- EUC-BUILD5 prototype, formerly designed as a two-bay (two-unit), two-storey RC precast building with dimensions in plane of 4.0 x 11.2 m and an inter-storey net height of 2.66 m, was modified to be a single-bay, two-storey structure with plane dimensions equal to 4.0 x 5.5 m, the latter being intended as the centre-to-centre wall spacing. This was due to the fact that the two contiguous units, separated by a cavity, are connected to each other by means of steel rods at the level of the floors and embedded in the hollow core slabs. According to that, no continuity can be ensured between the two units in terms of lateral force transfer. Hence, it was decided to split the original prototype into two nominally identical prefabricated one-bay, two-floor specimens. Dynamic shake-table test of EUC-BUILD5 is the major activity described in this report, whilst the main findings regarding cyclic pseudostatic testing of the twin specimen (i.e. EUC-BUILD4) can be found in a separate report (please refer to EUC-BUILD4 test campaign report EUC173/2017U).
- taking the decision of testing a one-unit mock-up allowed to increase the slabs span to 5.5 m (centre-to-centre) in order to better resemble the existing building sizes, anyway complying with the dimensions of Eucentre shake table. It is worth recalling that the chosen span bay fitted well with the assembly of the set of actuators on the strong wall of the laboratory so that it was possible to assume the same geometry for the two twin specimens. Although for cyclic testing on EUC-BUILD4 prototype an intermediate configuration was studied, in

which the span bay was adjusted to a value of 4.2 m, that configuration was abandoned, since it was decided not to shorten the span bay to take advantage of the same anchorage points to mount the actuators on the strong wall of the laboratory. As discussed and shown in Eucentre report *Cyclic testing of a full-scale two-storey RC precast wall-slab-wall structure representative of the Groningen building stock*, this was achieved by simply attaching the four actuators controlling the specimen in the transverse direction to the slabs.

- the hollow core slabs of each floor were selected to protrude in order to execute the tests in a safe manner with regards to the potential unseating of slabs in correspondence to the wall-slab joints. In more detail, the slabs are designed to overhang the wall-slab joints (i.e. 250 mm on each side of the specimen) so as (i) to prevent their unseating and (ii) to host L-shaped restrainers that inhibit out-of-plane collapses of wall-elements and sliding after an a priori-fixed gap is taken up (a 35 mm gap was assumed to carry out the testing of EUC-BUILD5 mock-up building).

A three-dimensional drawing of EUC-BUILD5 full-scale specimen is shown in Figure 95, and other key assumptions regarding the selected building are discussed hereafter. As mentioned above, the reference prototype is a single-bay, two-floor precast RC mock-up building with dimensions in plane of 4.0 x 5.5 m, and an inter-storey net height of 2.66 m. The flooring system consists of 200 mm thick hollow core slab elements; hollowcore K200-6D, spanning 5.5 m to the transversal walls (centre-to-centre distance), were selected. This configuration of precast slab panels is compliant with that shown in the design drawings. Although concrete topping is not always present in this structural typology, a 50 mm thick concrete screed was considered, so as to ensure more stiffness in the transversal direction (with respect to the direction of the slab span) and also to prevent any possible slab disassembly during large deformation testing stages; the floor steel mesh used for the screed consisted of 10 mm rebars spaced 150 mm (as opposed to the 5 mm rebars spaced 250 mm indicated in the drawings).

The prototype features two stability walls (one per each floor), perpendicular to the lateral load-bearing walls, placed in the central line of the specimen and half-span long. The lateral walls consist of 2.00 x 2.66 m contiguous precast panels connected together by means of two-way anchorages. By contrast, three-way anchorages are provided to connect the lateral wall panels with the stability wall, as shown in Figure 96. According to common Dutch practice, each panel wall accommodates four anchorages. The transversal walls and the stability walls were assumed to be 120 mm thick and to have the same reinforcement layout, which is composed of a steel grid Ø5/250 of ribbed rebars. However, following the operations of dismantling of EUC-BUILD4 specimen (see Eucentre report EUC173/2017U), it was realised that the steel mesh installed on the wall panels features a spacing of 180 mm in the vertical direction and 250 mm in the horizontal direction. Furthermore, it is worth noting that the steel net was not placed in the middle of the panel's cross-section, as indicated by the fact that the embedment depth of the steel connectors was 40 mm.

According to conventional practice for such structures, design loads were defined as follows:

- First floor: 1 kN/m^2 and 2 kN/m^2 for dead and live loads, respectively;
- Second floor: 1 kN/m^2 and 1.5 kN/m^2 for dead and live loads, respectively;
- Wind load: 0.85 kN/m^2 according to Dutch National Annex of Eurocode.

In this type of laboratory testing, gravity loading can be typically simulated through either additional concrete blocks or a further layer of non-collaborating concrete topping, the former being the solution adopted for this test, for the sake of simplicity. Details regarding the assumed configuration of concrete masses will be given in Section 5.4.
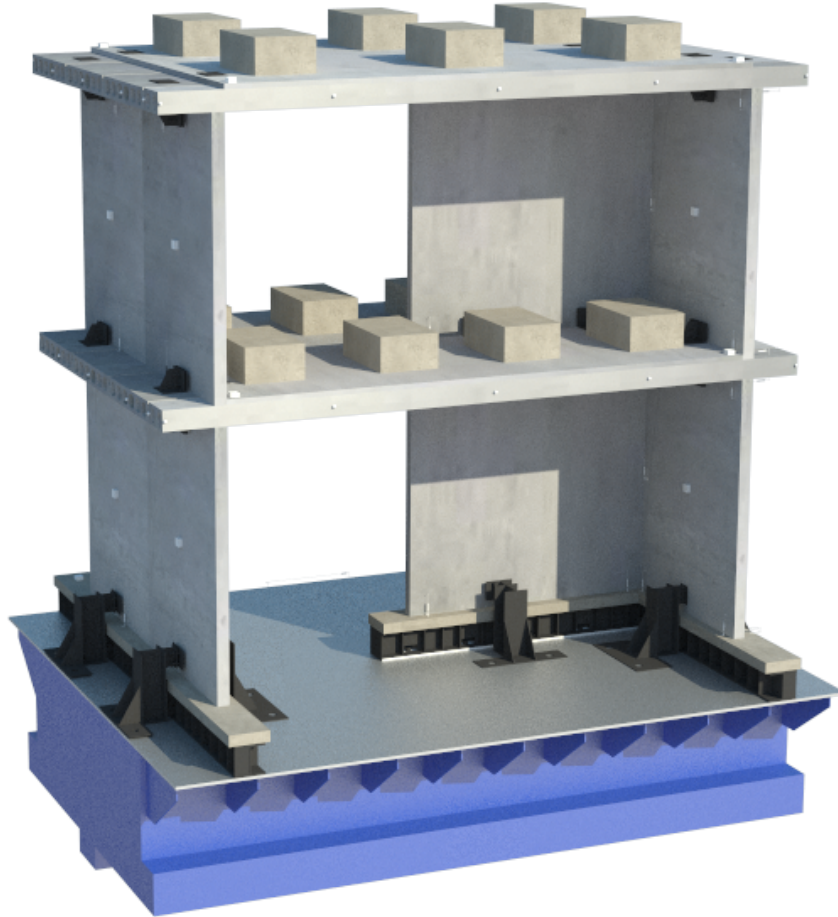
Figure 95. Isometric view of EUC-BUILD4 specimen.
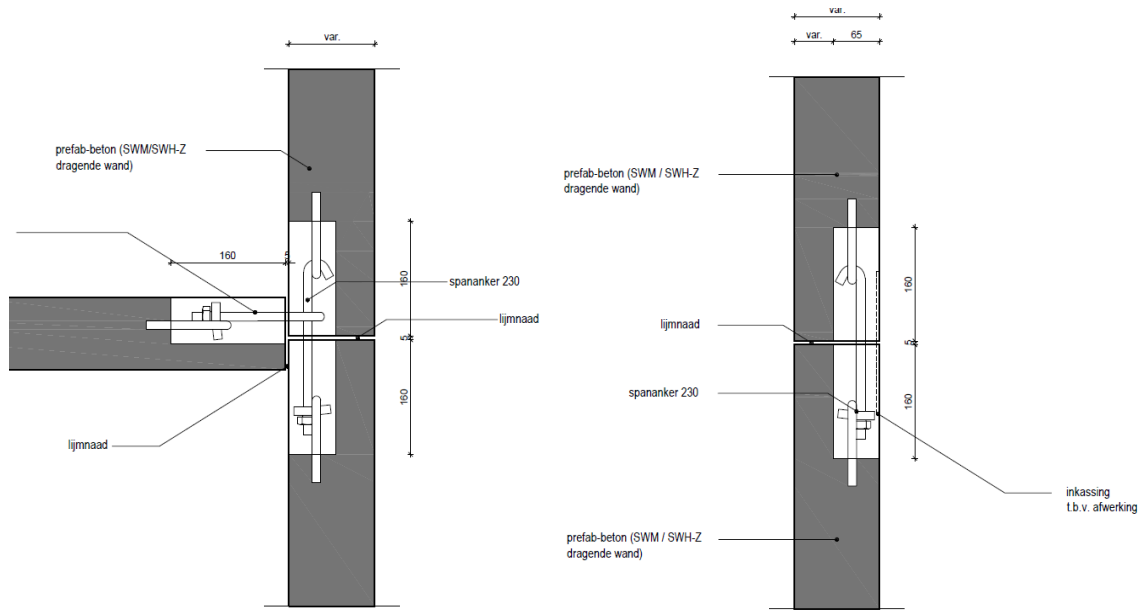
Figure 96. Examples of three-way and two-way anchorages for panel-to-panel connection. Courtesy of Arup (please refer to *229746_031_NOT2008_Rev0.05_Issue EUC-BUILD-4 Prototype building description*)

As previously mentioned, no starter rebars protruding from the concrete foundations are used in this building typology, and hence the walls rest on the underneath foundations by means of mortar joints without any mechanical connections. A similar construction scheme is assumed for the first floor as well, since common Dutch building practice foresees the slabs simply supported onto the walls underneath them through fabric felts like those studied via cyclic testing in this report and triplet testing in the companion report *Cyclic testing of a full-scale two-storey RC precast wall-slab-wall structure representative of the Groningen building stock*.

In addition, instead of L-shaped metal restraints/strips often seen in practice, use was made of concrete topping to ensure a minimum stiffness in the transversal direction of the floor slabs, as for EUC-BUILD4.

Needless to say that gable walls and front/back façades (i.e. longitudinal non-loadbearing walls) are not included in the prototype, as the testing was chiefly concerned with the assessment of the main load-bearing structure, for subsequent validation and calibration of numerical models.

5.3   Construction process and details

As previously discussed, EUC-BUILD5 prototype was meant and designed to be representative of a particular typology of Dutch buildings. It was thus decided that a Dutch contractor (i.e. Bouwborg) would be in charge of the construction process, which lasted for three days. Construction material arrived at Eucentre on 7th June 2017 and the building mock-up was erected from 19th June 2017 to 21st June 2017. Under controlled laboratory conditions, the specimen was built in accordance with common Dutch practice. EUC-BUILD5 prototype was assembled/built directly on the foundations mounted onto the shake table of Eucentre Laboratory, to avoid any eventual unintended damage due to transportation (if the specimen had been built outside of the lab).

As far as the construction material is concerned, it can be noted that one of the slab panels featured a very minor "scratch" (see Figure 97), which clearly had no impact on its performance. One of the stability wall panels exhibited some damage in one of the lifting hook areas (see Figure 98), which again had no impact in the resistance of the panel.

Figure 97. Example of precast hollow core slab panel and detail of minor scratch at one of its ends.

Figure 98. Detail of a stability wall panels featuring some damage in one of the lifting hook areas.

At close of the first day of construction, the first storey had already been erected without difficulties. The day after (i.e. June 20th), the second floor of EUC-BUILD5 was erected, thus allowing for the casting of the slabs topping to take place on the third day of construction, as initially planned. It can be reported that the damage observed in one of the stability walls (see Figure 98) did not affect the anchorage of the lifting hook.

In the following, the details of the construction of the test specimen are further illustrated. These details concern both the unloading of precast panels and construction material more in general and the assemblage of precast elements, as well as the arrangement of connections and the casting of concrete topping. A photographic sequence addressing these crucial aspects is shown and some considerations are given as needed to highlight key points.

In Figure 99 to Figure 112, one may find details regarding the precast elements delivered by the local Dutch contractor and the crane-driven uplifting system used in the laboratory. Photographs showing the process adopted by Dutch workers to assemble the specimen are collected in Figure 113 to Figure 120, in which it is described how precast wall panels and hollow core slabs were set in place. Further details regarding the entire construction sequence can be found from Figure 121 to Figure 152. The key steps concerning the erection of the first storey of EUC-BUILD5 specimen can be gathered from Figure 121 to Figure 127, whereas those related to the erection of the second storey are reported from Figure 128 to Figure 144. Further photos showing the casting of concrete topping, as well as the process of levelling and finishing, are collected in Figure 145 to Figure 152.

Figure 99. Delivery of precast wall panels.

Figure 100. Uplift of a precast wall-element by means of cranes and lifting hooks.

Figure 101. Crane-induced uplift of precast wall panels – Detail of the adopted two-points lifting scheme.

Figure 102. Detail of the static scheme adopted to store stability wall panels on truck for transportation.

Figure 103. Detail of the static scheme adopted to store lateral wall panels on truck for transportation.

Figure 104. Uplift and transportation of a precast panel – Detail 1.

Figure 105. Uplift and transportation of a precast panel – Detail 2.

Figure 106. Storage of precast panels in Eucentre laboratory.

Figure 107. Crane-induced uplift of precast slab panels – Detail of the adopted four-points lifting scheme.

Figure 108. Four-points lifting scheme for precast hollow core slab panels – Detail 1.

Figure 109. Four-points lifting scheme for precast hollow core slab panels – Detail 2.

Figure 110. Uplift and transportation of precast slab panels – Detail of a 1200 mm wide panel.

Figure 111. Uplift and transportation of precast slab panels – Detail of a 400 mm wide panel.

Figure 112. Delivered construction material – Mortar for finishings and structural interfaces.

Figure 113. Key details for construction of precast structures of this type – Three-way panel connections.

Figure 114. Key details – Crane-induced installation of precast panels and grout filling.

Figure 115. Key details – Two-way connections and temporary props for lateral stability during erection.

Figure 116. Key details – Arrangement of two-way connections and anchoring system for hook connectors.

Figure 117. Key details – L-shaped panel-to-slab steel connector, anchoring of long side to slab, first storey.

Figure 118. Key details – L-shaped panel-to-slab steel connector, anchoring of short side to wall, first storey.

Figure 119. Key details – Installation of temporary diagonal steel members on the shake-table of the laboratory.

Figure 120. Key details – Installation of spacers underneath precast wall panels for grouting of mortar layer.

Figure 121. Erection of the first-storey South-East-sided lateral wall on the steel foundation.

Figure 122. Erection of the first-storey North-sided lateral walls on the steel foundation.

Figure 123. Erection of the first-storey stability wall on the steel foundation and fastening of steel connectors.

Figure 124. Detail of the first-storey stability and lateral walls installed on the steel foundation.

Figure 125. Detail of placing fabric felt layers on top of precast wall panels – South-East-sided lateral wall.

Figure 126. Crane-induced uplift of a precast slab panel for flooring the first-storey of EUC-BUILD5 specimen.

Figure 127. Overall view of the erected first-storey of EUC-BUILD5 specimen.

Figure 128. Detail of the installed temporary props – Anchorage to shake-table.

Figure 129. Detail of the installed temporary props – Anchorage to precast wall panels.

Figure 130. Detail of the installed temporary props – Anchorage to precast wall panels of the second storey.

Figure 131. View of a two-way connection between the transversal walls of the specimen – Second storey.

Figure 132. Temporary props for the second-storey walls – Anchorage to precast wall panels.

Figure 133. Temporary props for the second-storey walls – Anchorage to precast slab panels.

Figure 134. Detail of a spacer underneath the second-storey transversal walls for mortar grout.

Figure 135. Erection of second-storey transversal walls – Opposite sides of EUC-BUILD5 specimen.

Figure 136. Detail of steel plates for panel-to-slab connection – Second storey, North side.

Figure 137. Uplift and transportation of the second-storey stability wall.

Figure 138. Installation of temporary props on the second-storey stability wall and arrangement of connectors.

Figure 139. Enlarged view of a three-way connection between stability and lateral walls – Second storey.

Figure 140. Detail of spacers beneath second-storey precast wall panels.

Figure 141. Crane-induced uplift and installation of precast slab panels – Second-storey floor.

Figure 142. Panel-to-slab steel plate connectors after mortar filling grouting underneath panels – South side.

Figure 143. Panel-to-slab steel plate connectors after mortar filling grouting underneath panels – North side.

Figure 144. Panel-to-slab steel plate connectors after mortar filling grouting – North side, opposite wall face.

Figure 145. Arrangement of steel mesh before casting of concrete topping – Second floor.

Figure 146. Arrangement of steel mesh before casting of concrete topping – First floor.

Figure 147. Detail of three-way panel connections after grouting of mortar – First storey.

Figure 148. Casting of concrete slab topping – Second storey.

Figure 149. Casting of concrete slab topping – Second storey, levelling.

Figure 150. Casting of concrete slab topping – Second storey, levelling and finishing.

Figure 151. Casting of concrete slab topping – First storey, levelling.

Figure 152. Casting of concrete slab topping – First storey after levelling and finishing.

Once the construction of EUC-BUILD5 specimen had been completed, the structure was surveyed, and it was possible to notice the presence of a conspicuous gap between the stability walls and the slabs, which instead was not at all that evident in EUC-BUILD4. Different views of such gap can be observed from Figure 153 to Figure 155. Furthermore, Figure 156 and Figure 157 present photographs of the gap between the slab panels themselves. Detailed measurements of such a prominent gap, which seem to point out the existence of a construction counter-flexure in the slab panels, are presented in Figure 158.

Needless to say that the presence of such an important gap between the stability walls and the slab was expected to have a non-negligible impact on the response of the specimen. Furthermore, EUC-BUILD4 specimen did not feature such a conspicuous gap (i.e. throughout the majority of its width the stability wall was indeed in contact with the wall), as one can clearly see from photos collected in Eucentre report EUC173/2017U.

Groningen engineers and the Dutch contractor in charge of the construction process (i.e. Bouwborg) were consulted on this matter, and although no unanimous consensus could be achieved on if it is customary for such a gap to be present in structures featuring this precast solution/scheme, it was certainly confirmed that when a gap is present and is identified during the erection of a building, it is then filled by means of the same non-shrink mortar employed for the other structural interfaces. Such a customary practice is usually operated in conjunction with the removal of the fabric felt layer so as to allow for more effectively filling of the gap.

Figure 153. EUC-BUILD5 specimen after construction – Gap between stability wall and slab panel (North edge).

Figure 154. EUC-BUILD5 specimen after construction – Gap between stability wall and slab panel (South edge).

Figure 155. Gap between the stability wall and slab panel of EUC-BUILD5 specimen – Opposite wall face.

Figure 156. EUC-BUILD5 specimen after construction – Gap between slab panels.

Figure 157. Enlarged view of the gap between the slab panels of EUC-BUILD5 specimen.
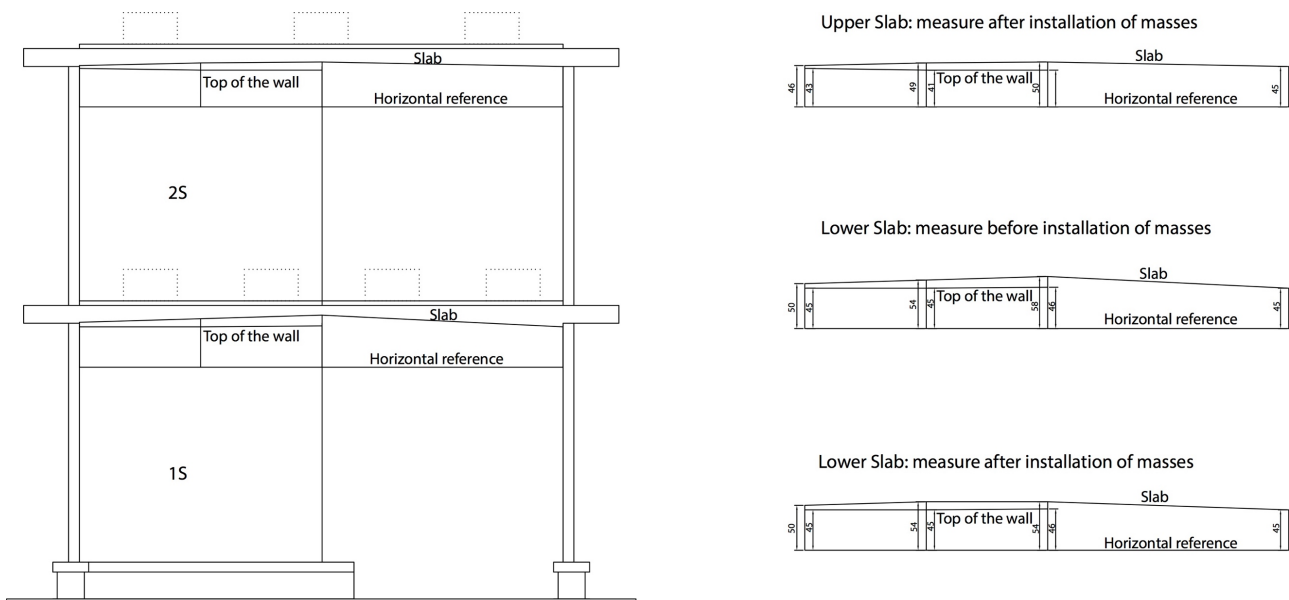
Figure 158. Measurements of the gap between the stability walls and the slabs – First and second storey.

As previously mentioned, laboratory technicians then implemented the "repair" intervention at the first and second storey of EUC-BUILD5 specimen, as documented by the following photographic sequence (Figure 159 to Figure 170). In particular, views of the mortar joint between the first-storey stability wall and the slabs are collected in Figure 159 to Figure 165, whilst details of the one between the second-storey stability wall and the slabs are documented in Figure 166 to Figure 170.

When present, additional mass blocks were removed and some of the precast slab panels were propped-up in such way that it was possible to remove the layer of fabric felt material and to fill the gap by means of the same non-shrink mortar employed for the other structural interfaces.

Mortar specimens were prepared and tested for characterisation of the mortar itself. As reported in Table 1, these characterisation tests were executed on 1st August 2017 (the second day of testing of EUC-BUILD5 specimen). Further information regarding compressive and tensile resistance can be found in Section 4.

It is important to note that this "repairing" operation hampered significantly the numerical analyses required for the definition of a tentative test loading protocol, given that:

- the configuration of the reference structure changed, in comparison with the structure that had been previously tested cyclically (and for which numerical models had been developed and verified);
- material characterisation tests, for the gap-filling mortar, were not available before the testing of the full-scale specimen.

Figure 159. Mortar filling intervention at the first-floor gap – Temporary steel elements for slab panel uplift.

Figure 160. Mortar filling intervention at the first-floor gap – Overall view of the mortar layer.

Figure 161. Mortar filling intervention at the first-floor gap – Detailed view of the mortar layer.

Figure 162. Mortar filling intervention at the first-floor gap – Overall view of the West-sided wall face.

Figure 163. Mortar filling intervention at the first-floor gap – Overall view of the East-sided wall face.

Figure 164. Mortar filling intervention at the first-floor gap – East-sided wall face, South-sided wall edge.

Figure 165. Mortar filling intervention at the first-floor gap – Detail of the South-sided wall edge.

Figure 166. Mortar filling at the second-floor gap – Temporary steel elements for slab panel uplift.

Figure 167. Mortar filling at the second-floor gap – Overall view of the mortar layer.

Figure 168. Mortar filling at the second-floor gap – Detailed view of the mortar layer.

Figure 169. Mortar filling at the second-floor gap – Overall view of the West-sided wall face.

Figure 170. Mortar filling at the second-floor gap – Detailed view of the West-sided wall face.

5.4 Test setup and dynamic loading sequence

In this Section, the main aspects regarding the test procedure are presented in detail. First of all, a brief overview concerning the rationale behind the design of the test setup and the definition of the tentative loading protocol is provided to highlight the primary assumptions that were considered for the execution of the test. Moreover, photographs showing the actual setup and tables summarising the load steps of the dynamic testing sequence are proposed and collected in separate sub-sections, one per each item.

5.4.1 Rationale

Figure 171 and Figure 172 show two isometric views of EUC-BUILD5 specimen together with the key components of the experimental setup conceived for dynamic shake-table testing of the mock-up building: (i) steel foundations; (ii) sliding restrainers, and (iii) additional concrete mass blocks. A set of CAD drawings presenting the top views of the two floors and the foundation system is provided in Figure 173, Figure 174 and Figure 175.

As usually foreseen during this type of tests, the foundations, which consist of a series of stiffened steel beams, were designed to remain elastic and were fixed to the shake-table of the laboratory so as to completely inhibit any relative motion during the dynamic testing of EUC-BUILD5 specimen. Given that the latter specimen and EUC-BUILD4 specimen were identical (stability wall-slab panel gaps apart), details regarding the configuration of both sliding restrainers and concrete masses were naturally very similar to those employed for specimen EUC-BUILD4 (refer to *Cyclic testing of a full-scale two-storey RC precast wall-slab-wall structure representative of the Groningen building stock*). In what follows, some considerations and minor differences are in any case reported.
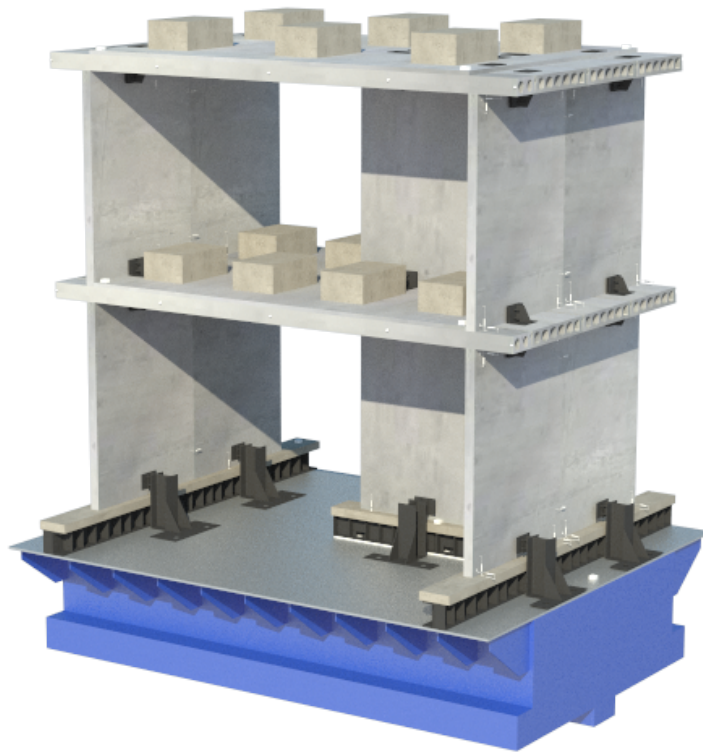
Figure 171. Isometric front view of EUC-BUILD5 specimen and installation of experimental setup.
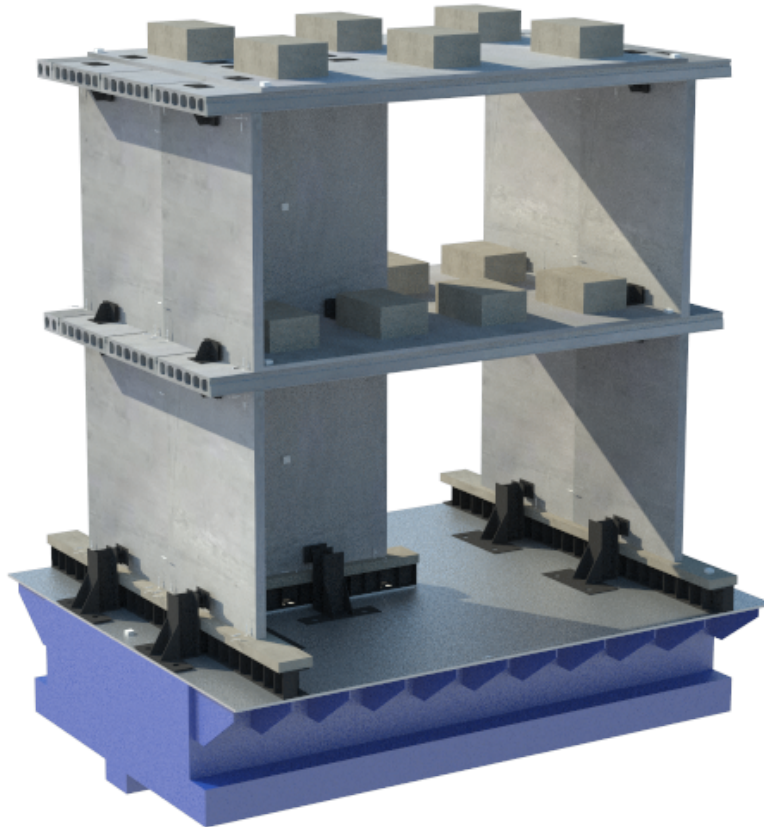
Figure 172. Isometric back view of EUC-BUILD5 specimen and installation of experimental setup.
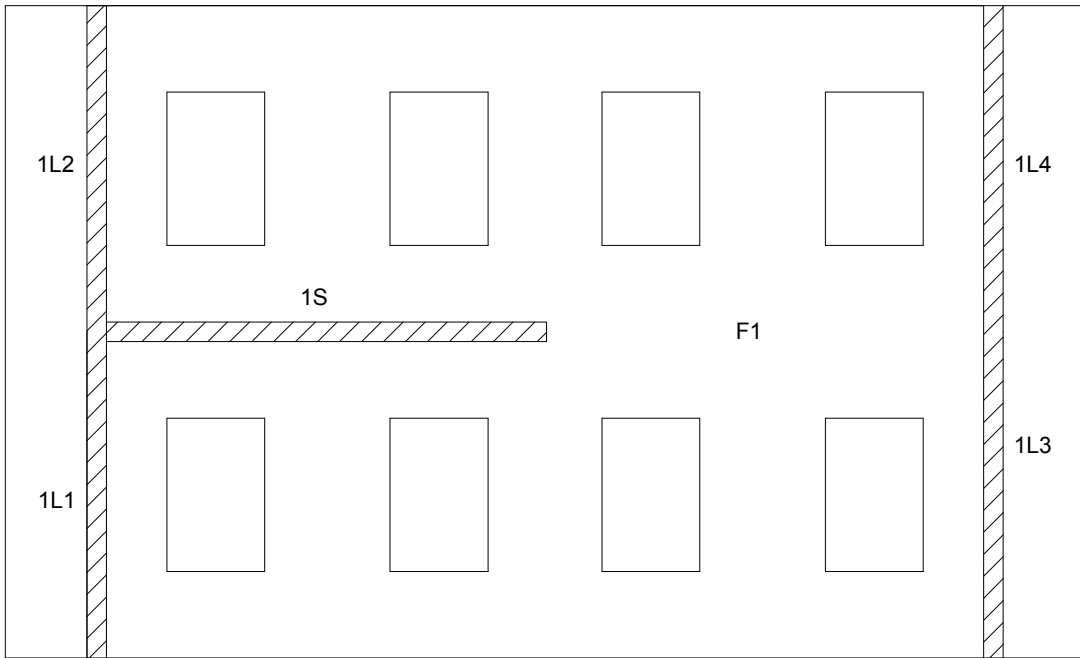
Figure 173. Schematic of EUC-BUILD5 specimen – Top view of the first floor slab.
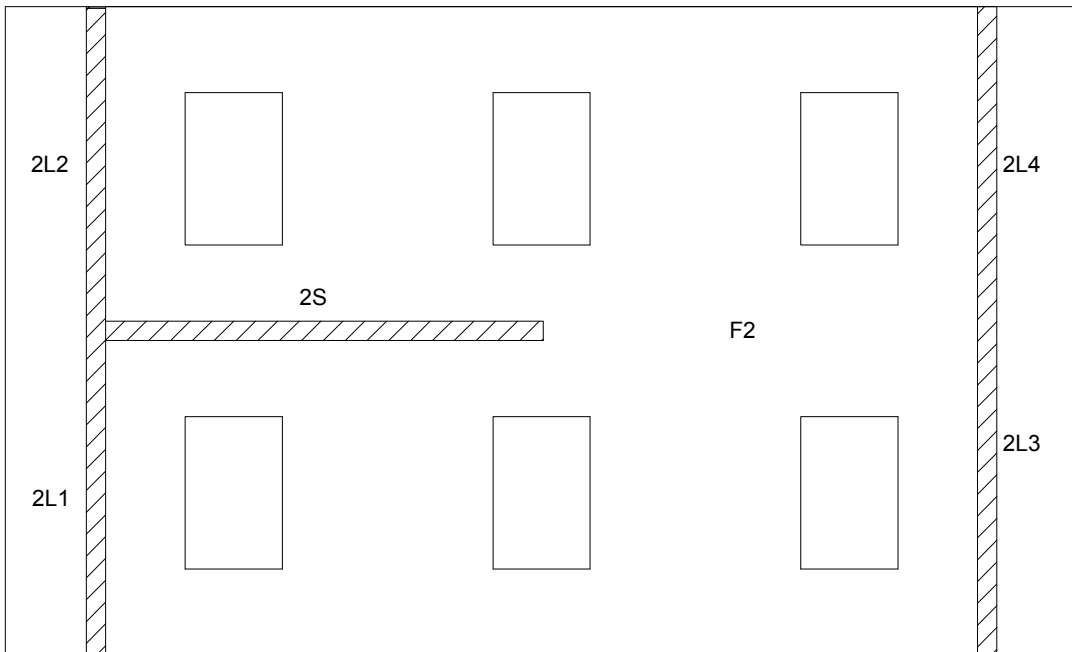
Figure 174. Schematic of EUC-BUILD5 specimen – Top view of the second floor slab.
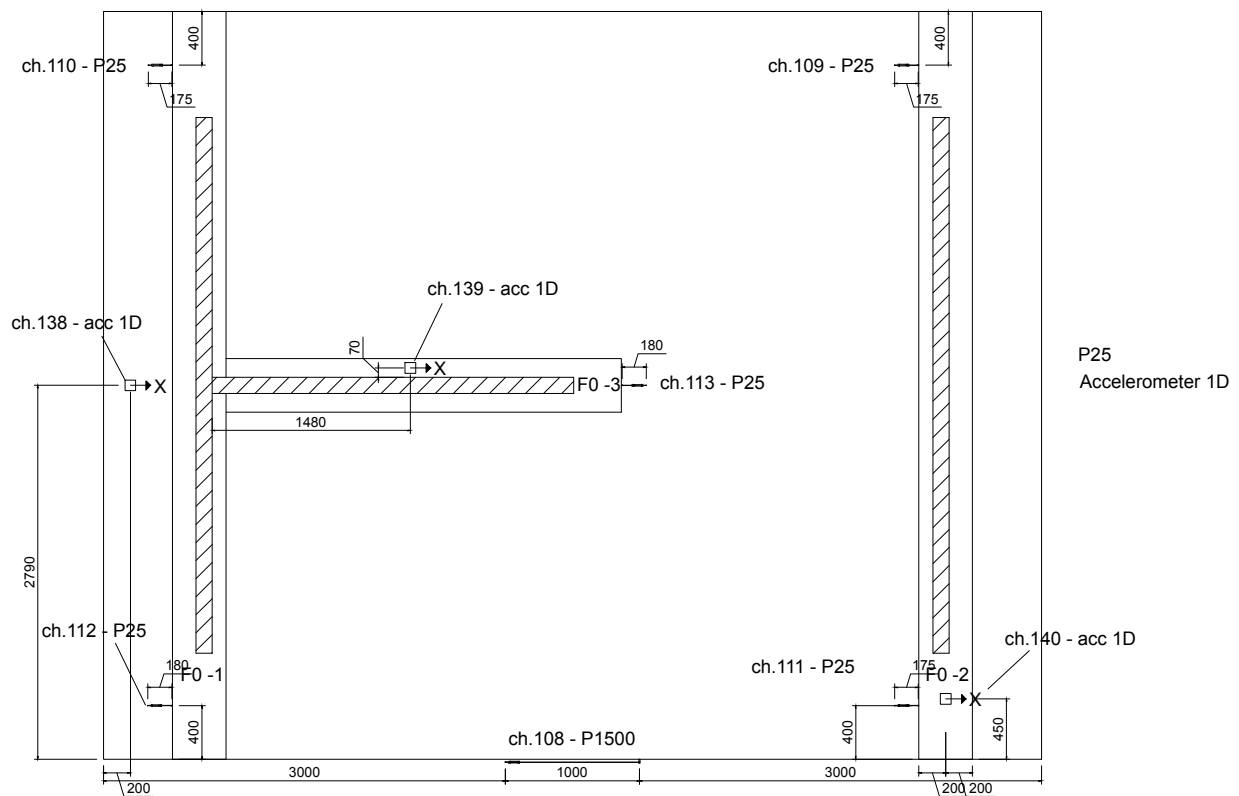
Figure 175. Schematic of foundation system – Top view and nomenclature.

It is worth recalling that, in the framework of a dynamic test, the additional vertical gravity load can be simulated through either concrete masses/blocks or a further layer of non-collaborating concrete topping. As can be gathered from Figure 173 and Figure 174, use was made of the former approach for simplicity and consistency with the cyclic tests of EUC-BUILD4 specimen. Figure 176 and Figure 177 show the number and the exact position of the concrete masses installed on the first and second floor slabs, respectively. Eight and six concrete blocks, whose dimensions are 35 x 60 x 94 cm, were placed on the first and second floors before testing. The adopted configuration is the one used for EUC-BUILD4 specimen (i.e. same concrete masses, number and position).

A similar consideration can be drawn for what concerns the configuration of sliding restrainers, as they were identical to those adopted for cyclic testing of EUC-BUILD4 specimen, except for those at the base of the first-storey precast walls. Although the latter ones were designed to eventually act in a very similar fashion, it is worth noticing that use was made of short steel columns bolted to the shake-table in order to set them in place. The scope of such a solution is twofold, since it allows the reduction of the foundation width and it ensures higher out-of-plane resistance whether restrainers would be activated. It is reiterated that the testing of EUC-BUILD5 specimen was executed without activation of the sliding restrainers, which are only a safety measure for prevention of collapse mechanisms and damages to the instrumentation and laboratory equipment. As noticed in Section 5.2, a gap of about 35 mm was assumed between the steel plates of the stoppers and the counterpart wall panel to carry out the test. Figure 178 shows the configuration of sliding restrainers.
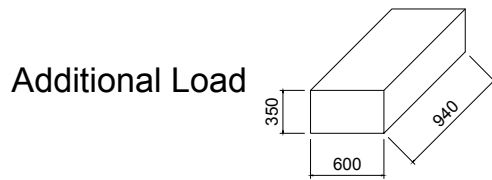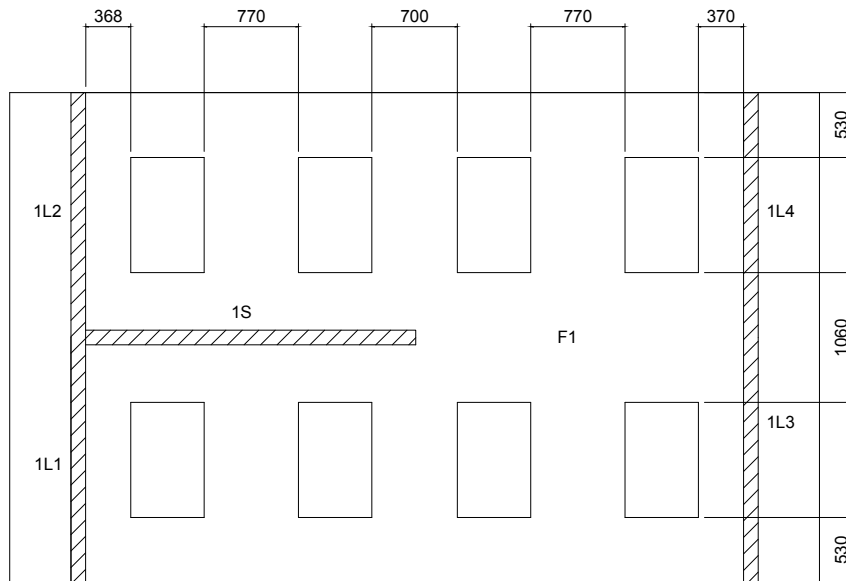
Figure 176. Number and position of concrete masses for additional gravity load – First floor slab.
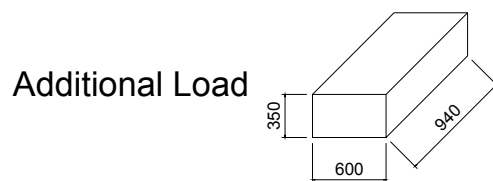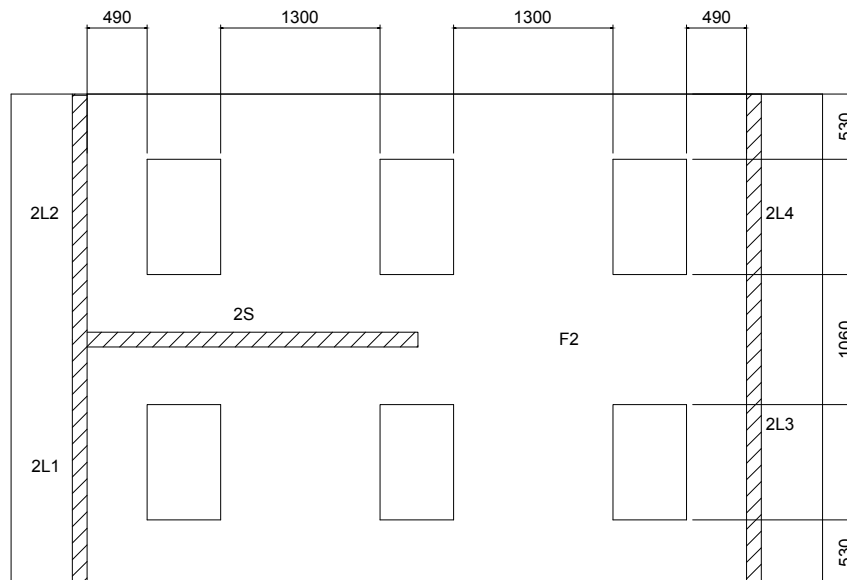
Figure 177. Number and position of concrete masses for additional gravity load – Second floor slab.
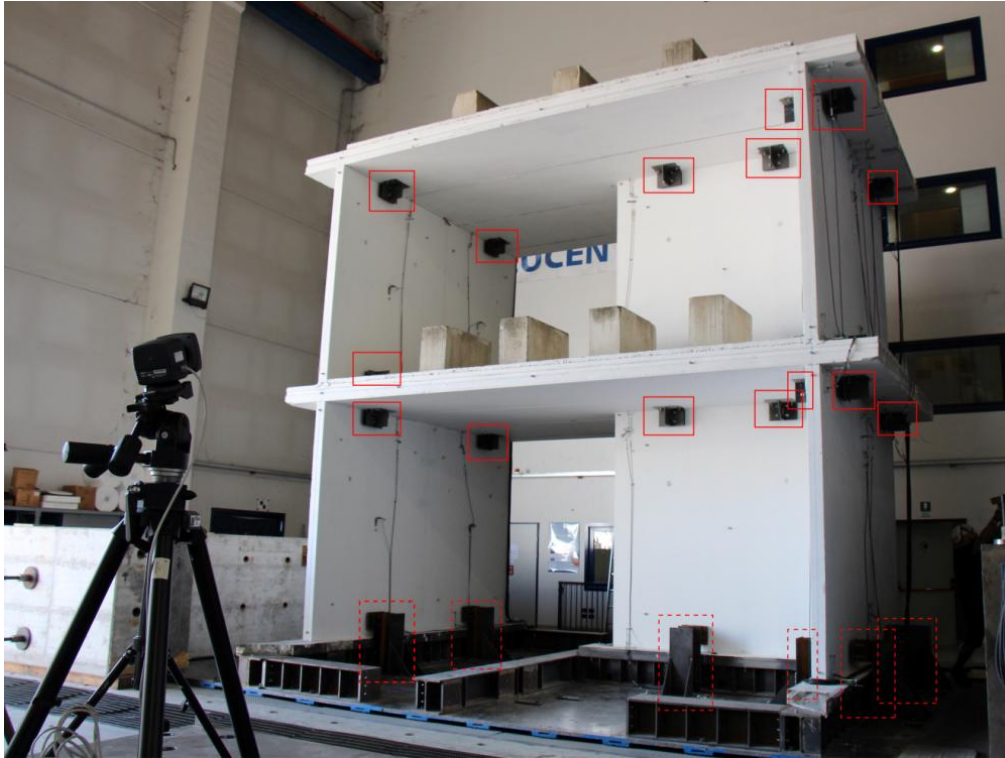
Figure 178. Type and configuration of stoppers/restrainers for collapse prevention.

Despite the fact that EUC-BUILD5 specimen accumulated a significant permanent displacement of about 14 cm (i.e. first storey-to-base displacement), restrainers were not activated during the testing sequence, in the sense that the precast wall panels and the counterpart stoppers did never touch.

Based on a set of preliminary/preparatory numerical analyses carried out before the execution of the test, a tentative loading protocol (that could be adapted during the test as a function of the observed structural response) was defined for shake-table testing of EUC-BUILD5 specimen. The main steps of the process can be summarised as follows:

- a hazard-compatible accelerogram was identified (please refer to the short explanatory note *Selection of accelerogram for shake-table test of EUC-BUILD5 specimen*, included in Appendix B);
- the selected acceleration record, reported in Figure 179, was used for numerical analyses of EUC-BUILD5 specimen by using the finite element model calibrated on the results of EUC-BUILD-4 specimen;
- differences had emerged between the two mock-up buildings, since EUC-BUILD5 specimen featured a conspicuous gap between the stability walls and the slabs, as extensively reported in Section 5.3;
- an additional series of analyses was run to study the response of EUC-BUILD5 specimen in the as-built configuration confirming that the presence of such an important gap between the stability walls and the slab will naturally have a non-negligible impact;
- a further set of analyses was carried out to simulate the response of EUC-BUILD5 specimen after gap-filling operations (please refer to Section 5.3), albeit without having results on the material characterisation tests of the mortar used for the intervention;

- calibration of compressive and tensile resistance of mortar was carried out empirically, and the analysis results seemed to indicate failure of the specimen for an amplification factor (of the selected accelerogram) of 1.5.

Preparatory numerical analyses were therefore hampered (i) by the fact that the configuration of the reference structure had changed and (ii) by the lack of material characterisation tests on the mechanical properties of mortar, which were found to play a key role in the response of the final structural configuration. It was anyway decided to favour (i) consistency with common construction practice for what concerns the choice of filling the wall-slab gaps and (ii) a readily interpretation of test results, which can be based on the availability of results representative of the actual mechanical properties of mortar during the days of testing.

By following this non-trivial process, it was concluded that a suitable loading protocol was to subject the structure to an input motion obtained by sequencing two copies of the chosen accelerogram, the first multiplied by a factor of 0.5 and the second by a factor of 1.0. It was also felt that, as a function of how the structure would then behave, a last run with an amplification factor of 1.5 could be feasible. It can be noted that exhaustive details regarding the dynamic loading sequence that was in the end applied to the specimen are reported in Section 5.4.3.
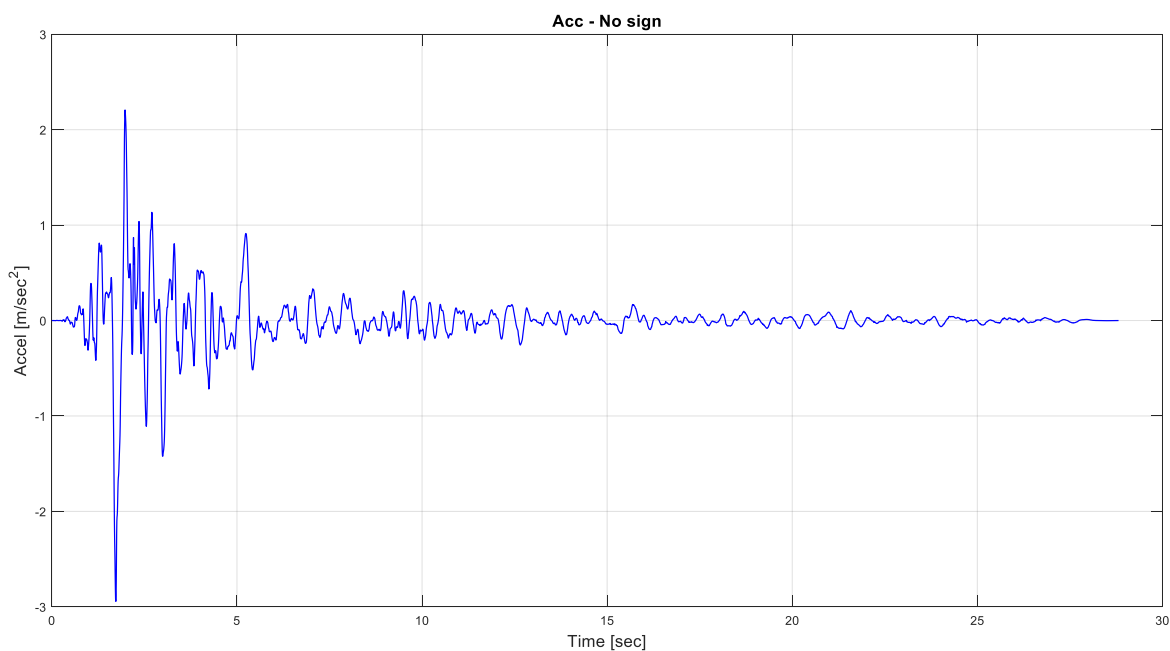
Figure 179. Accelerogram for shake-table testing of EUC-BUILD-5 specimen.

5.4.2   Actual setup

Photographs of the actual setup employed for the testing of EUC-BUILD5 specimen are provided in Figure 180, Figure 181 and Figure 182. More in detail, Figure 180 and Figure 181 present views of the specimen and details/components of the experimental setup. As shown therein and also pointed out by the set of CAD drawings collected in Section 5.4.1 (i.e. Figure 173 and Figure 174), use was made of the same concrete masses adopted for EUC-BUILD4 building mock-up in order to simulate the presence of the additional vertical loads. Furthermore, Figure 180 and Figure 181 also

show the number and position of steel restrainers, in their inactive configuration. Worthwhile to note is that, before the testing of EUC-BUILD5 specimen, all the restrainers were set to have a 35 cm clearance with respect to the counterpart structural elements, which made it easier for the structure to undergo the entire sequence of testing without activation of these safety measures.

Even though the restrainers at the base of the ground-floor precast walls of EUC-BUILD4 specimen were installed on the foundation beams, it was decided to bolt 50 cm tall steel columns to the shake-table and arrange them at approximately 20 cm from the base of the wall panels, which would have ensured a sturdier retaining system against any eventual out-of-plane collapse of the panels. Such an approach also permitted the adoption of foundation beams featuring a less wide flange for the same out-of-plane resistance.

Details of the foundation system are finally presented in Figure 182, where one may notice the type of stiffeners adopted and the anchoring system employed to fix the steel beams to the shake-table of the Eucentre laboratory.

Figure 180. Isometric view of EUC-BUILD5 specimen – Detail of restrainers and concrete masses.

Figure 181. Isometric top view of EUC-BUILD5 specimen – Detail of restrainers and concrete masses.

Figure 182. Details of the foundation system consisting of stiffened steel beams.

5.4.3   Execution of the test and dynamic loading sequence

As summarised in Table 1, dynamic shake-table testing of EUC-BUILD5 specimen was carried out on 31st July 2017, 1st August 2017 and 2nd August 2017. The building was subjected to incremental dynamic test runs, which consist of a series of table motions of increasing intensity, through the scaling of the hazard-compatible accelerogram discussed in Appendix B. Table 13 shows the dynamic input sequence that was effectively followed during the tests.

Table 13. Dynamic testing of EUC-BUILD5 specimen: summary of the applied testing sequence.

Test run #	Test Name	Test Input	Test type	Scale factor	Day of test
01	RNDM_1	RNDM	Calibration	-	
02	RNDM_2	RNDM	Calibration	-	
03	025NEG_COMP_A-D	EQ	Calibration	0.25	
04	050NEG	EQ	Test 50%	0.50	Jul 31, 2017
05	RNDM_3	RNDM	Calibration	-	
06	034NEG_COMP_A-C	EQ	Calibration	0.34	
07	100NEG	EQ	Test 100%	1.00	
08	RNDM_4	RNDM	Calibration	-	
09	RNDM_5	RNDM	Calibration	-	
10	034NEG_COMP_A-F	EQ	Calibration	0.34	
11	150NEG	EQ	Test 150%	1.50	Aug 01, 2017
12	RNDM_6	RNDM	Calibration	-	
13	050NEG_COMP_A-E	EQ	Calibration	0.50	
14	200NEG	EQ	Test 200%	2.00	
15	RNDM_7	RNDM	Calibration	-	
16	050NEG_COMP_A-D	EQ	Calibration	0.50	Aug 02, 2017
17	200NEG	EQ	Test 200%_bis	2.00	

As can be gathered from Table 13, the specimen was subjected to two different typologies of input motion, namely RNDM and EQ, the former signal being a random white noise for table calibration and structural identification purposes and the earthquake signal selected for testing and presented in Figure 179. Test runs for controller compensation were also executed scaling the earthquake signal used for testing to an amplification factor that was at least one half of the scale factor considered for the counterpart test run.

Table 14 summarises the main steps of the applied loading sequence, focusing on the application of seismic loading alone. Test runs identified with an odd label correspond to those executed before the main stages of the testing sequence for controller compensation purposes. As such, the results obtained for these runs are presented in a separate section of Chapter 6 (i.e. Section 6.6), which addressed the evolution of the response of EUC-BUILD5 specimen, demonstrating that those test runs had a negligible impact on the experimental response observed.

Table 14. EUC-BUILD5 specimen: dynamic testing sequence – Steps of interest.

Test run #	Test Name	Test Input	Test type	Scale factor	Day of test
01	025NEG_COMP_A-D	EQ	Calibration	0.25	
02	050NEG	EQ	Test 50%	0.50	Jul 31, 2017
03	034NEG_COMP_A-C	EQ	Calibration	0.34	
04	100NEG	EQ	Test 100%	1.00	
05	034NEG_COMP_A-F	EQ	Calibration	0.34	
06	150NEG	EQ	Test 150%	1.50	Aug 01, 2017
07	050NEG_COMP_A-E	EQ	Calibration	0.50	
08	200NEG	EQ	Test 200%	2.00	
09	050NEG_COMP_A-D	EQ	Calibration	0.50	Aug 02, 2017
10	200NEG	EQ	Test 200%_bis	2.00	

Finally, it can be anticipated that Sections 6.6.1 to 6.6.10 provide plots addressing the discrepancy between the planned/nominal signal and the imposed/recorded one in terms of spectral acceleration records. In particular, a specific comparison was provided for each test run.

5.5 Instrumentation of tested specimen

The sequence of dynamic test runs consisted in subjecting the base of the specimen to incrementally increased seismic excitations in the longitudinal direction of the building mock-up (i.e. North-South one). Several instruments were installed on the prototype building in order to monitor the structural response under different levels of input motion. Clearly, their location and typology was established following the identification of both critical portions of the structure and physical parameters that are supposed to be recorded.

A large number of instruments, 139 in total, were adopted to monitor the response of EUC-BUILD5 specimen. In what follows, interested readers can find detailed information on the instrumentation, whilst, as a general observation, it can be stated that the instrumentation planned naturally was very similar to that employed for cyclic tests of EUC-BUILD4 specimen, but now featuring the (equally obvious) addition of a number of 2g accelerometers:

- one at the centre of each panel (direction of motion);
- four on each slab, close to the four corners (measuring X-Y-Z);
- two on the foundations;
- one on the shake-table itself.

Key aspects regarding the rationale behind the instrumentation are briefly reported in the following section, whereas detailed drawings for the identification of the position of instruments and channels are provided in Section 5.5.2.

5.5.1 Rationale

Monitoring of displacements and forces applied to the test-specimen is of paramount importance to shed light into the observed structural behaviour. To summarise the number and type of instruments used to monitor the testing of EUC-BUILD5 specimen, tables are reported hereafter, along with the

nomenclature assumed for the panel-elements. Moreover, schematics are also presented in Section 5.5.2 so as to provide a clear picture of the position of these instruments. Reference front views (i.e. South and North ones) are shown in Figure 183. A side (i.e. East) view is presented in Figure 184, whereas three plan views corresponding to each floor level of interest are collected in Figure 185.
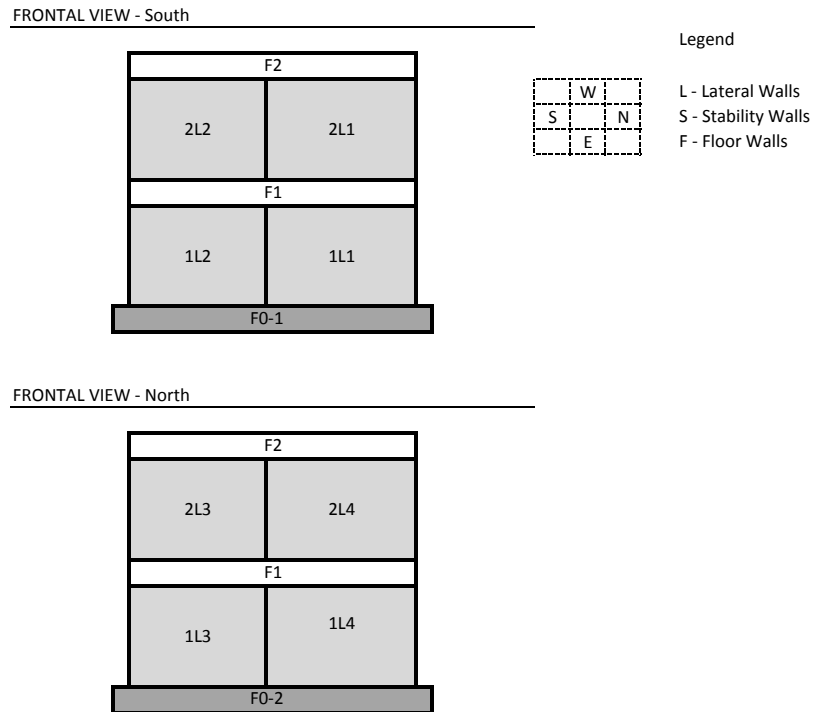
Figure 183. EUC-BUILD5 specimen: reference front (South–North) views for instrumentation.
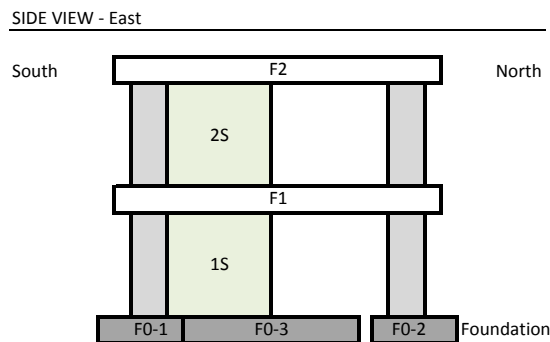
Figure 184. EUC-BUILD5 specimen: reference side (East) views for instrumentation.
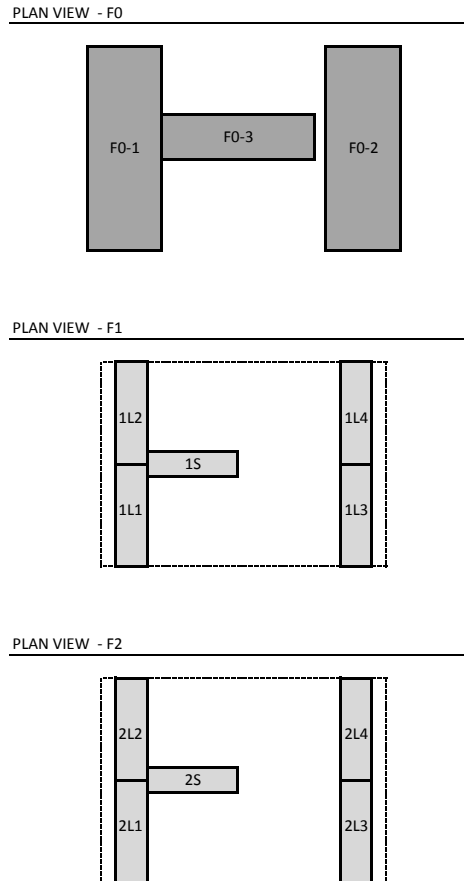
Figure 185. EUC-BUILD5 specimen: reference plan views for instrumentation (ground, first and second floors).

As highlighted by Table 15, the out-of-plane displacement of lateral walls is monitored at both base and top, and the same applies to the monitoring of the in-plane rocking and the transversal rocking of those elements (see Table 16 to Table 21). Furthermore, Table 22 collects the set of instruments that are positioned to measure the sliding of the lateral walls at their top and bottom. Particular care was also paid to the two stability walls, in terms of relative sliding with respect to the corresponding lateral walls (see Table 23), as well as for what concerns in-plane deformation, transversal rocking and out-of-plane displacement (see Table 24 to Table 27). As can be gathered from Table 28, it was also decided to keep track of the eventual sliding of steel foundations, though this is naturally a very unlikely deformation mechanism. Lastly, a set of 1D and 3D accelerometers was adopted to monitor the accelerations experienced by the precast wall panels as well as those exerted on key positions of the two slabs.

Track was also kept of the acceleration applied by the shake-table as well as of that imposed at the base of the structure at the foundation level (see Table 29 to Table 33). As reported in those tables and already mentioned in Section 5.5, ten mono-directional 2g accelerometers were installed on the precast wall panels and other three accelerometers of this type were mounted at the base level, one of them to monitor the shake-table and the other two so as to obtained the input that was effectively applied to the structure. On the other hand, four 3D accelerometers were positioned at the corner of the first-storey and second-storey slabs.

Table 15. Instrumentation: out-of-plane displacement of lateral walls.

General note	Instrument #	Type	Stroke [mm]	Description
Lateral Wall - 1L1	1	Pot.	50	W1L1 - SE - Out-of-Plane Displ. @Top
Out-of-plane displacement	2	Pot.	50	W1L1 - SW - Out-of-Plane Displ. @Top
	3	Pot.	50	W1L1 - SE - Out-of-Plane Displ. @Base
	4	Pot.	50	W1L1 - SW - Out-of-Plane Displ. @Base
Lateral Wall - 1L2	5	Pot.	50	W1L2 - SE - Out-of-Plane Displ. @Top
Out-of-plane displacement	6	Pot.	50	W1L2 - SW - Out-of-Plane Displ. @Top
	7	Pot.	50	W1L2 - SE - Out-of-Plane Displ. @Base
	8	Pot.	50	W1L2 - SW - Out-of-Plane Displ. @Base
Lateral Wall - 2L1	9	Pot.	50	W2L1 - SE - Out-of-Plane Displ. @Top
Out-of-plane displacement	10	Pot.	50	W2L1 - SW - Out-of-Plane Displ. @Top
	11	Pot.	50	W2L1 - SE - Out-of-Plane Displ. @Base
	12	Pot.	50	W2L1 - SW - Out-of-Plane Displ. @Base
Lateral Wall - 2L2	13	Pot.	50	W2L2- SE - Out-of-Plane Displ. @Top
Out-of-plane displacement	14	Pot.	50	W2L2 - SW - Out-of-Plane Displ. @Top
	15	Pot.	50	W2L2 - SE - Out-of-Plane Displ. @Base
	16	Pot.	50	W2L2 - SW - Out-of-Plane Displ. @Base

Table 16. Instrumentation: in-plane and transversal rocking of lateral wall 1L1.

General note	Instrument #	Type	Stroke [mm]	Description
Lateral Wall - 1L1	17	Pot.	50	W1L1 - SE - Rocking @Top
In-plane rocking	18	Pot.	50	W1L1 - SW - Rocking @Top
	19	Pot.	50	W1L1 - SE - Rocking @Base
	20	Pot.	50	W1L1 - SW - Rocking @Base
Lateral Wall – 1L1	33	Pot.	50	W1L1 - NE - Rocking @Top
Transversal rocking	34	Pot.	50	W1L1 - NW - Rocking @Top
	35	Pot.	50	W1L1 - NE - Rocking @Base
	36	Pot.	50	W1L1 - NW - Rocking @Base

Table 17. Instrumentation: in-plane and transversal rocking of lateral wall 1L2.

General note	Instrument #	Type	Stroke [mm]	Description
Lateral Wall - 1L2	21	Pot.	50	W1L2 - SE - Rocking @Top
In-plane rocking	22	Pot.	50	W1L2 - SW - Rocking @Top
	23	Pot.	50	W1L2 - SE - Rocking @Base
	24	Pot.	50	W1L2 - SW - Rocking @Base
Lateral Wall – 1L2	37	Pot.	50	W1L2 - NE - Rocking @Top
Transversal rocking	38	Pot.	50	W1L2 - NW - Rocking @Top
	39	Pot.	50	W1L2 - NE - Rocking @Base
	40	Pot.	50	W1L2 - NW - Rocking @Base

Table 18. Instrumentation: transversal rocking of lateral walls 1L3 and 1L4.

General note	Instrument #	Type	Stroke [mm]	Description
Lateral Wall – 1L3	49	Pot.	50	W1L3 - S - Rocking @Top
Transversal rocking	50	Pot.	50	W1L3 - S - Rocking @Base
Lateral Wall – 1L3	57	Pot.	50	W1L3 - N - Rocking @Top
Transversal rocking	58	Pot.	50	W1L3 - N - Rocking @Base
Lateral Wall – 1L4	51	Pot.	50	W1L4 - S - Rocking @Top
Transversal rocking	52	Pot.	50	W1L4 - S - Rocking @Base
Lateral Wall – 1L4	59	Pot.	50	W1L4 - N - Rocking @Top
Transversal rocking	60	Pot.	50	W1L4 - N - Rocking @Base

Table 19. Instrumentation: in-plane and transversal rocking of lateral wall 2L1.

General note	Instrument #	Type	Stroke [mm]	Description
Lateral Wall - 2L1	25	Pot.	50	W2L1 - SE - Rocking @Top
In-plane rocking	26	Pot.	50	W2L1 - SW - Rocking @Top
	27	Pot.	50	W2L1 - SE - Rocking @Base
	28	Pot.	50	W2L1 - SW - Rocking @Base
Lateral Wall – 2L1	41	Pot.	50	W2L1 - NE - Rocking @Top
Transversal rocking	42	Pot.	50	W2L1 - NW - Rocking @Top
	43	Pot.	50	W2L1 - NE - Rocking @Base
	44	Pot.	50	W2L1 - NW - Rocking @Base

Table 20. Instrumentation: in-plane and transversal rocking of lateral wall 2L2.

General note	Instrument #	Type	Stroke [mm]	Description
Lateral Wall - 2L2	29	Pot.	50	W2L2 - SE - Rocking @Top
In-plane rocking	30	Pot.	50	W2L2 - SW - Rocking @Top
	31	Pot.	50	W2L2 - SE - Rocking @Base
	32	Pot.	50	W2L2 - SW - Rocking @Base
Lateral Wall – 2L2	35	Pot.	50	W2L2 - NE - Rocking @Top
Transversal rocking	46	Pot.	50	W2L2 - NW - Rocking @Top
	47	Pot.	50	W2L2 - NE - Rocking @Base
	48	Pot.	50	W2L2 - NW - Rocking @Base

Table 21. Instrumentation: transversal rocking of lateral walls 2L3 and 2L4.

General note	Instrument #	Type	Stroke [mm]	Description
Lateral Wall – 2L3	53	Pot.	50	W2L3 - S - Rocking @Top
Transversal rocking	54	Pot.	50	W2L3 - S - Rocking @Base
Lateral Wall – 2L3	61	Pot.	50	W2L3 - N - Rocking @Top
Transversal rocking	62	Pot.	50	W2L3 - N - Rocking @Base
Lateral Wall – 2L4	55	Pot.	50	W2L4 - S - Rocking @Top
Transversal rocking	56	Pot.	50	W2L4 - S - Rocking @Base
Lateral Wall – 2L4	63	Pot.	50	W2L4 - N - Rocking @Top
Transversal rocking	64	Pot.	50	W2L4 - N - Rocking @Base

Table 22. Instrumentation: sliding of lateral walls.

General note	Instrument #	Type	Stroke [mm]	Description
Lateral Wall – 1L1 / 1L2	65	Pot.	25	W1L1/1L2 - S - Sliding @Top
Wall sliding	66	Pot.	25	W1L1/1L2 - N - Sliding @Base
Lateral Wall – 1L3 / 1L4	69	Pot.	25	W1L3/1L4 - S - Sliding @Top
Wall sliding	70	Pot.	25	W1L3/1L4 - N - Sliding @Base
Lateral Wall – 2L1 / 2L2	67	Pot.	25	W2L1/2L2 - S - Sliding @Top
Wall sliding	68	Pot.	25	W2L1/2L2 - N - Sliding @Base
Lateral Wall – 2L3 / 2L4	71	Pot.	25	W2L3/2L4 - S - Sliding @Top
Wall sliding	72	Pot.	25	W2L3/2L4 - N - Sliding @Base

Table 23. Instrumentation: lateral wall-to-stability wall sliding.

General note	Instrument #	Type	Stroke [mm]	Description
Lateral Wall / Stability Wall_1L1 – 1S	73	Pot.	50	1S-SE – Relative Sliding @Center
Lateral Wall / Stability Wall_1L2 – 1S	74	Pot.	50	1S-SW – Relative Sliding @ Center
Lateral Wall / Stability Wall_2L1 – 2S	75	Pot.	50	2S-SE – Relative Sliding @ Center
Lateral Wall / Stability Wall_2L2 – 2S	76	Pot.	50	2S-SW – Relative Sliding @ Center

Table 24. Instrumentation: out-of-plane displacement of stability walls.

General note	Instrument #	Type	Stroke [mm]	Description
Stability Wall – 1S	77	Pot.	50	1S - SE - Out-of-plane Displ. @Top
Out-of-plane displacement	78	Pot.	50	1S - NE - Out-of-plane Displ. @Top
	79	Pot.	50	1S - SE - Out-of-plane Displ. @Base
	80	Pot.	50	1S - NE - Out-of-plane Displ. @Base
Stability Wall – 2S	81	Pot.	50	2S - SE - Out-of-plane Displ. @Top
Out-of-plane displacement	82	Pot.	50	2S - NE - Out-of-plane Displ. @Top
	83	Pot.	50	2S - SE - Out-of-plane Displ. @Base
	84	Pot.	50	2S - NE - Out-of-plane Displ. @Base

Table 25. Instrumentation: in-plane deformation and transversal rocking of stability wall 1S.

General note	Instrument #	Type	Stroke [mm]	Description
Stability Wall – 1S	85	Pot.	50	1S - SE - Rocking @Top
In-plane deformation	86	Pot.	50	1S - NE - Rocking @Top
	87	Pot.	50	1S - SE - Rocking @Base
	88	Pot.	50	1S - NE - Rocking @Base
	89	Pot.	100	1S - E - Sliding @Top
	90	Pot.	50	1S - E - Sliding @Base
Stability Wall – 1S	97	Pot.	50	1S - SW - Rocking @Top
Transversal rocking	98	Pot.	50	1S - NW - Rocking @Top
	99	Pot.	50	1S - SW - Rocking @Base
	100	Pot.	50	1S - NW - Rocking @Base

Table 26. Instrumentation: in-plane deformation and transversal rocking of stability wall 2S.

General note	Instrument #	Type	Stroke [mm]	Description
Stability Wall – 2S	91	Pot.	50	2S - SE - Rocking @Top
In-plane deformation	92	Pot.	50	2S - NE - Rocking @Top
	93	Pot.	50	2S - SE - Rocking @Base
	94	Pot.	50	2S - NE - Rocking @Base
	95	Pot.	100	2S - E - Sliding @Top
	96	Pot.	50	2S - E - Sliding @Base
Stability Wall – 2S	101	Pot.	50	2S - SW - Rocking @Top
Transversal rocking	102	Pot.	50	2S - NW - Rocking @Top
	103	Pot.	50	2S - SW - Rocking @Base
	104	Pot.	50	2S - NW - Rocking @Base

Table 27. Instrumentation: out-of-plane displacement (stability wall-to-lateral wall).

General note	Instrument #	Type	Stroke [mm]	Description
Lateral Wall / Stability Wall_1L1 – 1S	111	Tast.	25	W1L1/1S – SE – Out-of-plane Displ. @Top
Out-of-plane displacement	112	Tast.	25	W1L1/1S – SE – Out-of-plane Displ. @Base
Lateral Wall / Stability Wall_1L2 – 1S	115	Tast.	25	W1L2/1S – SW – Out-of-plane Displ. @Top
Out-of-plane displacement	116	Tast.	25	W1L2/1S – SW – Out-of-plane Displ. @Base
Lateral Wall / Stability Wall_2L1 – 2S	113	Tast.	25	W2L1/2S – SE – Out-of-plane Displ. @Top
Out-of-plane displacement	114	Tast.	25	W2L1/2S – SE – Out-of-plane Displ. @Base
Lateral Wall / Stability Wall_2L2 – 2S	117	Tast.	25	W2L2/2S – SW – Out-of-plane Displ. @Top
Out-of-plane displacement	118	Tast.	25	W2L2/2S – SW – Out-of-plane Displ. @Base

Table 28. Instrumentation: sliding of foundations and displacement of the shake-table.

General note	Instrument #	Type	Stroke [mm]	Description
Shake-table – Sliding	105	Pot.	1500	Table Displacement
F0 – Foundation	106	Pot.	25	F0-2 - NW - Sliding
	107	Pot.	25	F0-1 - SW - Sliding
	108	Pot.	25	F0-2 - NE - Sliding
	109	Pot.	25	F0-1 - SE - Sliding
	110	Pot.	25	F0-3 – Sliding @Center

Table 29. Instrumentation: acceleration – Lateral walls.

General note	Instrument #	Type	Full scale	Description
Lateral Wall - 1L1	119	Acc.1D	$\pm$ 2 g	W1L1 - Acceleration @Center
Lateral Wall - 1L2	120	Acc.1D	$\pm$ 2 g	W1L2 - Acceleration @Center
Lateral Wall - 1L3	123	Acc.1D	$\pm$ 2 g	W1L3 - Acceleration @Center
Lateral Wall - 1L4	124	Acc.1D	$\pm$ 2 g	W1L4 - Acceleration @Center
Lateral Wall - 2L1	121	Acc.1D	$\pm$ 2 g	W2L1 - Acceleration @Center
Lateral Wall - 2L2	122	Acc.1D	$\pm$ 2 g	W2L2 - Acceleration @Center
Lateral Wall - 2L3	125	Acc.1D	$\pm$ 2 g	W2L3 - Acceleration @Center
Lateral Wall - 2L4	126	Acc.1D	$\pm$ 2 g	W2L4 - Acceleration @Center

Table 30. Instrumentation: acceleration – Stability walls.

General note	Instrument #	Type	Full scale	Description
Stability Wall - 1S	127	Acc.1D	± 2 g	S1 - Acceleration @Center
Stability Wall - 2S	128	Acc.1D	± 2 g	S2 - Acceleration @Center

Table 31. Instrumentation: acceleration – Foundations.

General note	Instrument #	Type	Full scale	Description
F0 – Shake-table	129	Acc.1D	± 2 g	SE – Acceleration Table
F0 – Foundation	130	Acc.1D	± 2 g	F0-3 – Acceleration @Center
	131	Acc.1D	± 2 g	F0-2 - NE – Acceleration

Table 32. Instrumentation: acceleration – First floor slab.

General note	Instrument #	Type	Full scale	Description
F1 – Floor	132-x	Acc.3Dx	± 2 g	F1 – NW – Acceleration
	132-y	Acc.3Dy	± 2 g	F1 – NW – Acceleration
	132-z	Acc.3Dz	± 2 g	F1 – NW – Acceleration
	133-x	Acc.3Dx	± 2 g	F1 – SW – Acceleration
	133-y	Acc.3Dy	± 2 g	F1 – SW – Acceleration
	133-z	Acc.3Dz	± 2 g	F1 – SW – Acceleration
	134-x	Acc.3Dx	± 2 g	F1 – NE – Acceleration
	134-y	Acc.3Dy	± 2 g	F1 – NE – Acceleration
	134-z	Acc.3Dz	± 2 g	F1 – NE – Acceleration
	135-x	Acc.3Dx	± 2 g	F1 – SE – Acceleration
	135-y	Acc.3Dy	± 2 g	F1 – SE – Acceleration
	135-z	Acc.3Dz	± 2 g	F1 – SE – Acceleration

Table 33. Instrumentation: acceleration – Second floor slab.

General note	Instrument #	Type	Full scale	Description
F2 – Floor	136-x	Acc.3Dx	± 2 g	F2 – NW – Acceleration
	136-y	Acc.3Dy	± 2 g	F2 – NW – Acceleration
	136-z	Acc.3Dz	± 2 g	F2 – NW – Acceleration
	137-x	Acc.3Dx	± 2 g	F2 – SW – Acceleration
	137-y	Acc.3Dy	± 2 g	F2 – SW – Acceleration
	137-z	Acc.3Dz	± 2 g	F2 – SW – Acceleration
	138-x	Acc.3Dx	± 2 g	F2 – NE – Acceleration
	138-y	Acc.3Dy	± 2 g	F2 – NE – Acceleration
	138-z	Acc.3Dz	± 2 g	F2 – NE – Acceleration
	139-x	Acc.3Dx	± 2 g	F2 – SE – Acceleration
	139-y	Acc.3Dy	± 2 g	F2 – SE – Acceleration
	139-z	Acc.3Dz	± 2 g	F2 – SE – Acceleration

Given that the response/behaviour of the lateral walls is controlled by phenomena/mechanisms of rocking (both in-plane one and transversal one), the in-plane deformation of these precast walls was not monitored during the testing of EUC-BUILD5 specimen. On the contrary, both sliding and out-of-plane deformations were measured. Eight instruments per each storey were adopted for the latter mechanisms, whereas two potentiometers per each wall panel were used to measure sliding relative to the companion lateral wall (Table 22). It is also worth noting that sliding of the lateral walls with respect to the companion stability wall, if present, is monitored as summarised in Table 23. The out-of-plane displacements (i.e. lateral wall-to-stability wall) at the top and bottom of the two different wall-elements were monitored as well (see Table 27). The in-plane deformation of the two stability walls is monitored according to the rationale and scheme reported in Table 25 and Table 26, and the same applies to their transversal rocking and out-of-plane displacements.

In addition to the tables collected above, a series of CAD drawings of the instrumentation used for EUC-BUILD5 specimen is shown in the following Section.

5.5.2 Identification of the position of potentiometers and accelerometers

As planned and discussed in the previous section, a total of 139 instruments were considered to measure crucial structural response parameters at key locations throughout the structure. Figure 186 shows a few plan views of EUC-BUILD5 specimen that can be considered as a helpful reference for the identification of the position of the installed instrumentation. In particular, Figure 187 to Figure 190 show front views of the instrumented building, showing the number and position of each single instrument mounted onto the lateral walls at both South and North sides. Furthermore, in Figure 191 and Figure 192, East and West side views of the full-scale specimen are provided in order to clarify the position of the instrumentation installed onto the two stability walls. The information contained therein could then be merged also with the details pointed out by Figure 193 and Figure 194, which instead identify the series of accelerometers placed in correspondence to the first- and second-storey slabs, respectively.

Three-dimensional drawings of the instrumented building mock-up are finally given in Figure 195, and Figure 196 (presenting anyway the same information reported in the series of two-dimensional drawings), whilst photos of the instrumentation used are collected in Figure 197 to Figure 232.

As noticeable in the series of drawings collected below, the accelerations of both the two floor slabs are monitored by means of four 3D accelerometers per each floor. As presented in Figure 187 and Figure 190, the transversal walls of both the North and South sides of the structure were monitored in terms of out-of-plane displacement, as well as in respect to the in-plane and transversal rocking.

As far as the South-sided lateral walls are concerned, four 50 mm-stroke potentiometers were used for each panel to measure out-of-plane displacements at their corners, whilst two instruments were considered for the out-of-plane displacements of the North-side transversal walls. Eight instruments per each wall panel were utilised to monitor the in-plane and transversal rocking mechanism of the South-sided lateral walls. By contrast, two potentiometers were used to track these resisting mechanisms in lateral walls placed on the opposite side of the specimen. Obviously, it was decided to install them at the top of the wall and in correspondence to the wall base. Moreover, two 25 mm-stroke potentiometers were mounted on each lateral wall to monitor sliding of these wall-elements.

Figure 191 and Figure 192 provide a clear view of the instrumentation installed on the two sides of the first-storey and second-storey stability walls. In detail, four 50 mm-stroke potentiometers were

used to monitor the in-plane deformation of each panel. The same type and number of displacement transducers were considered for transversal rocking and out-of-plane displacements of this element typology, whilst use was made of only two 50 mm-stroke potentiometers for what concerns sliding. One of the two was placed at the top of the wall, whilst the other one was installed at the wall base. Other twelve linear variable displacement transducers (LVDTs) were used to monitor local relative mechanisms that might occur between the stability wall and the lateral walls (i.e. sliding and out-of-plane displacements).
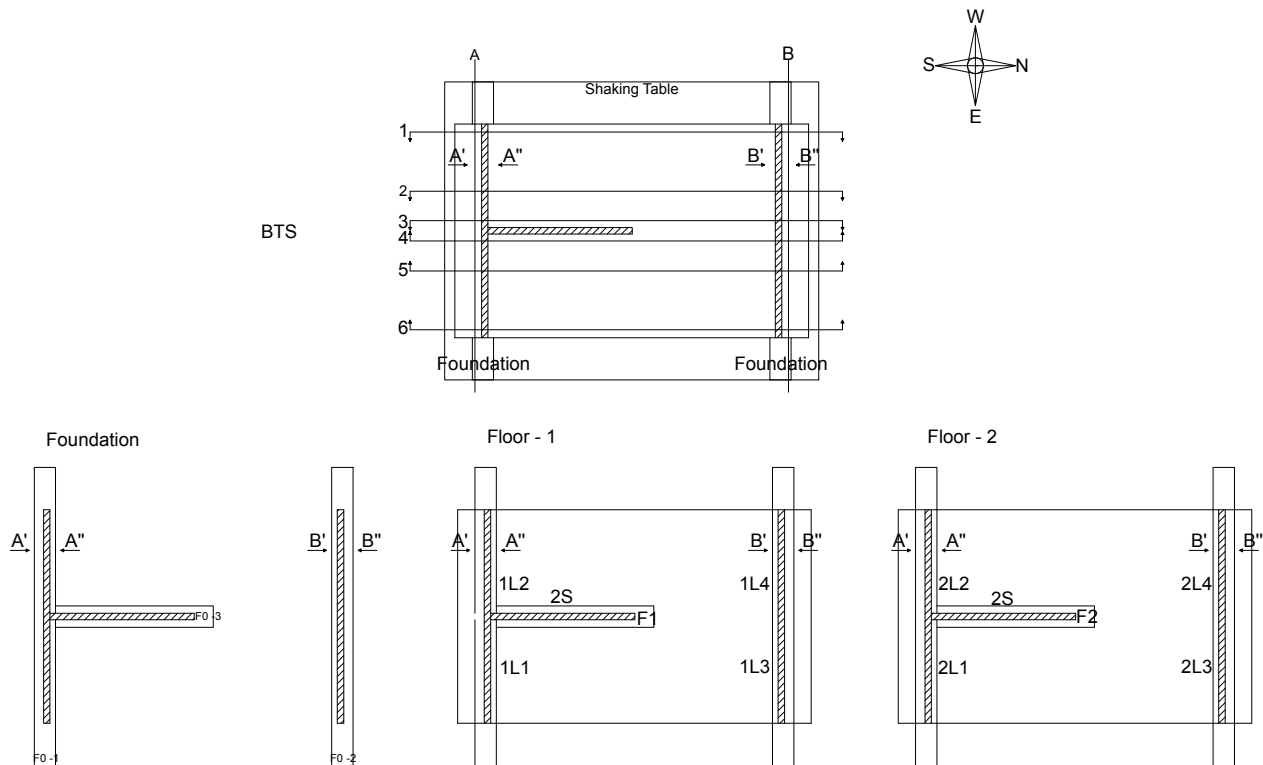
Figure 186. Plan views of EUC-BUILD5 specimen – Position of the installed instrumentation.
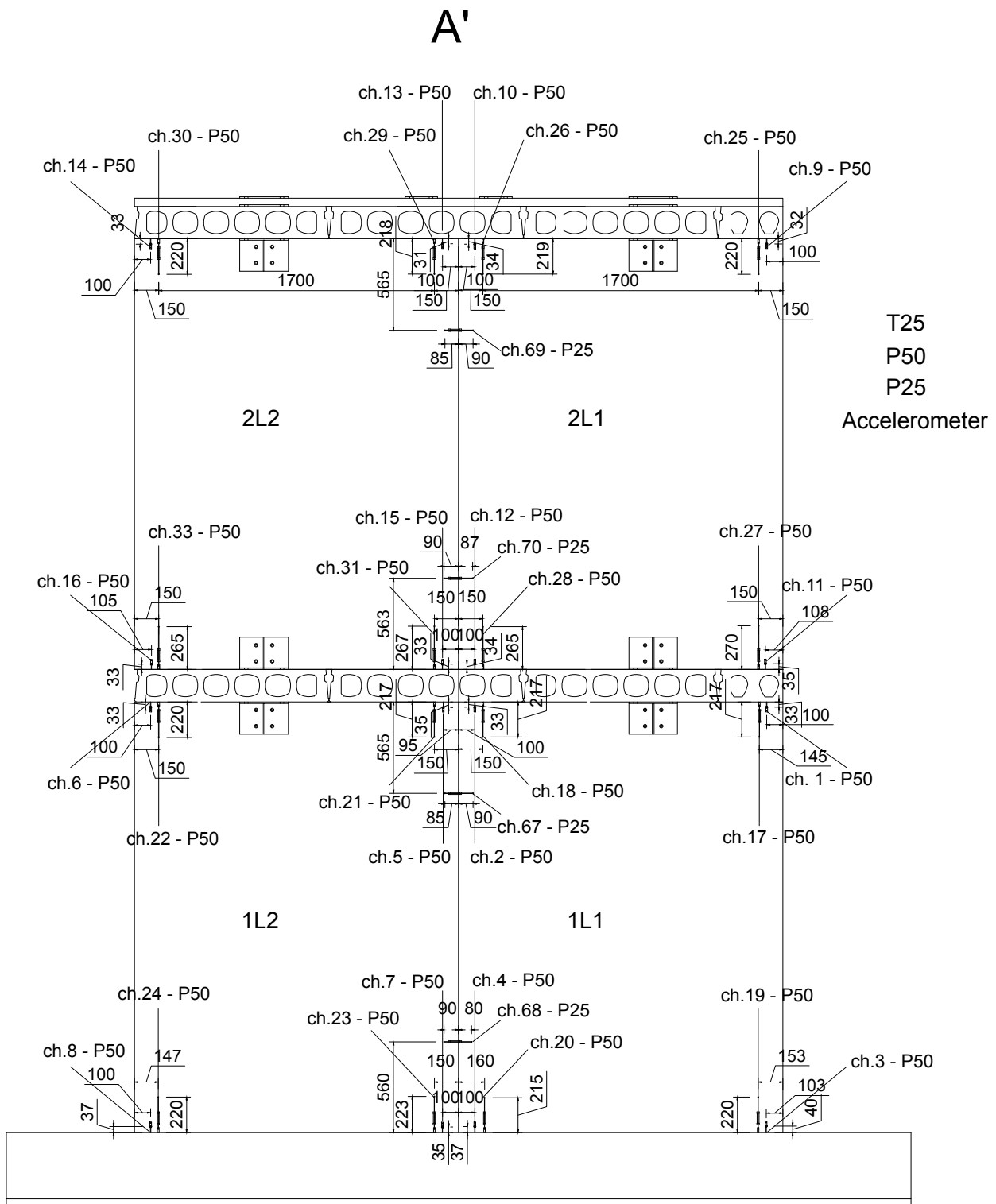
Figure 187. Schematic of the installed instrumentation: front views of the specimen – Lateral walls, A'.
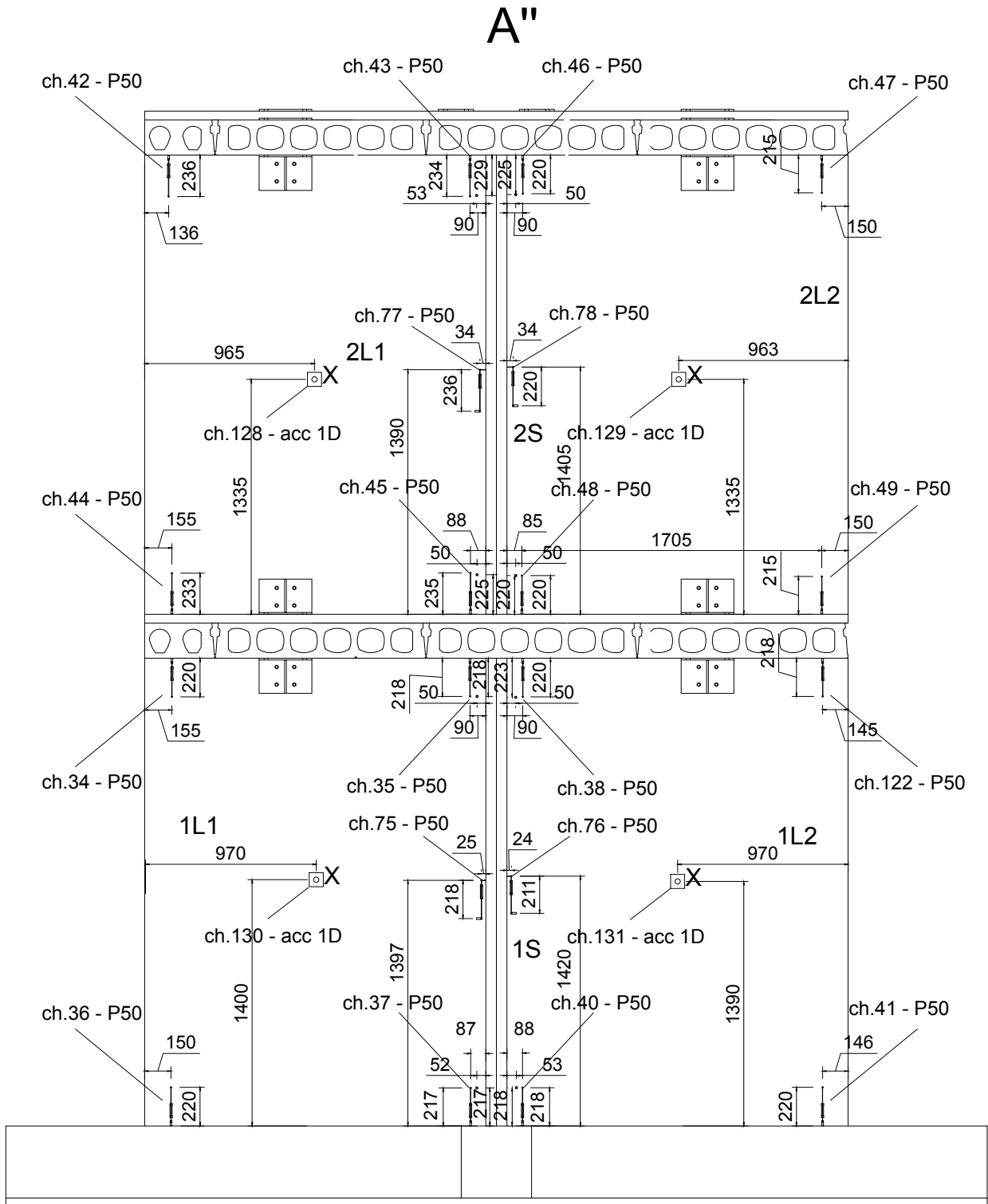
Figure 188. Schematic of the installed instrumentation: front views of the specimen – Lateral walls, A''.
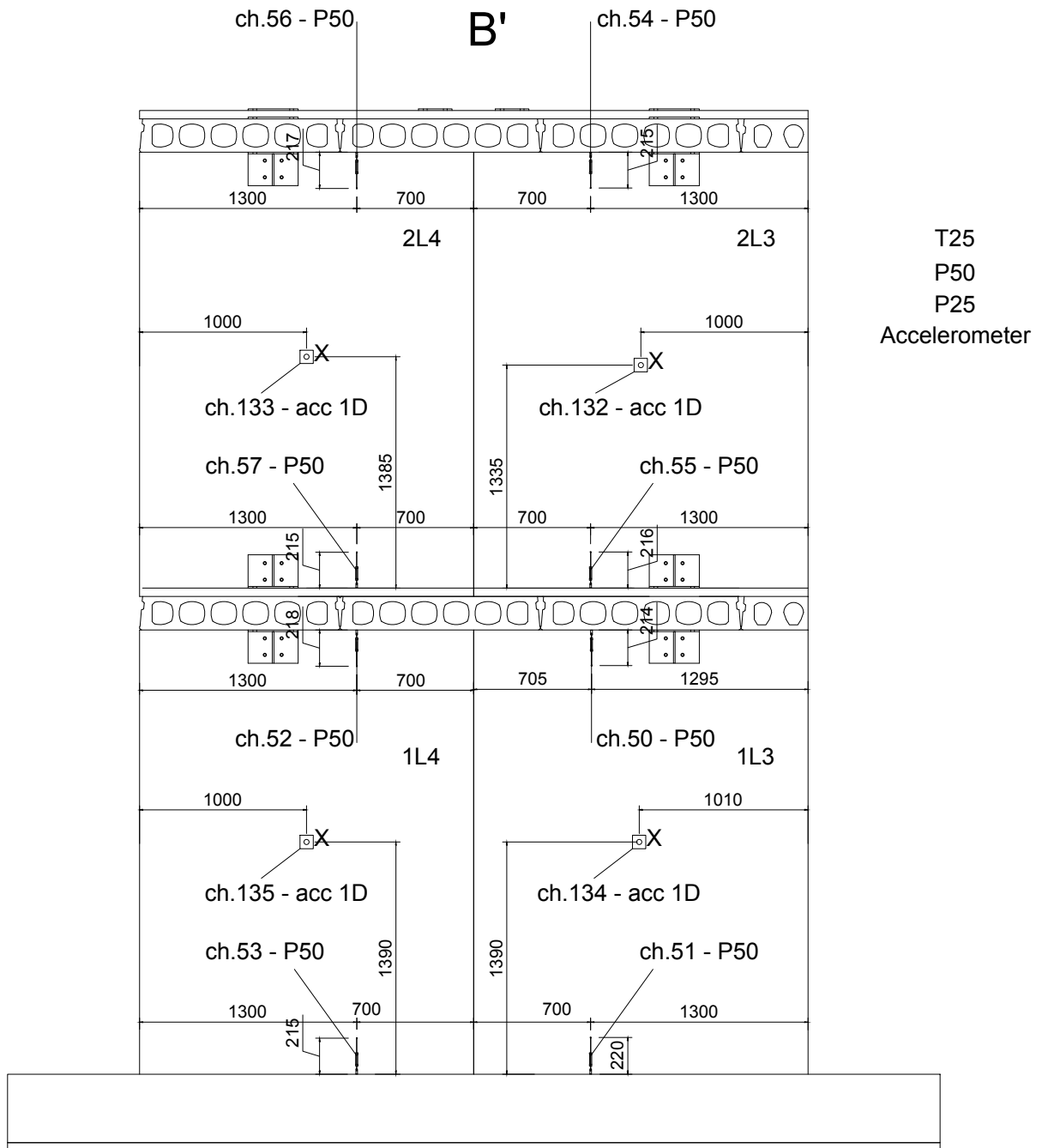
Figure 189. Schematic of the installed instrumentation: front views of the specimen – Lateral walls, B'.
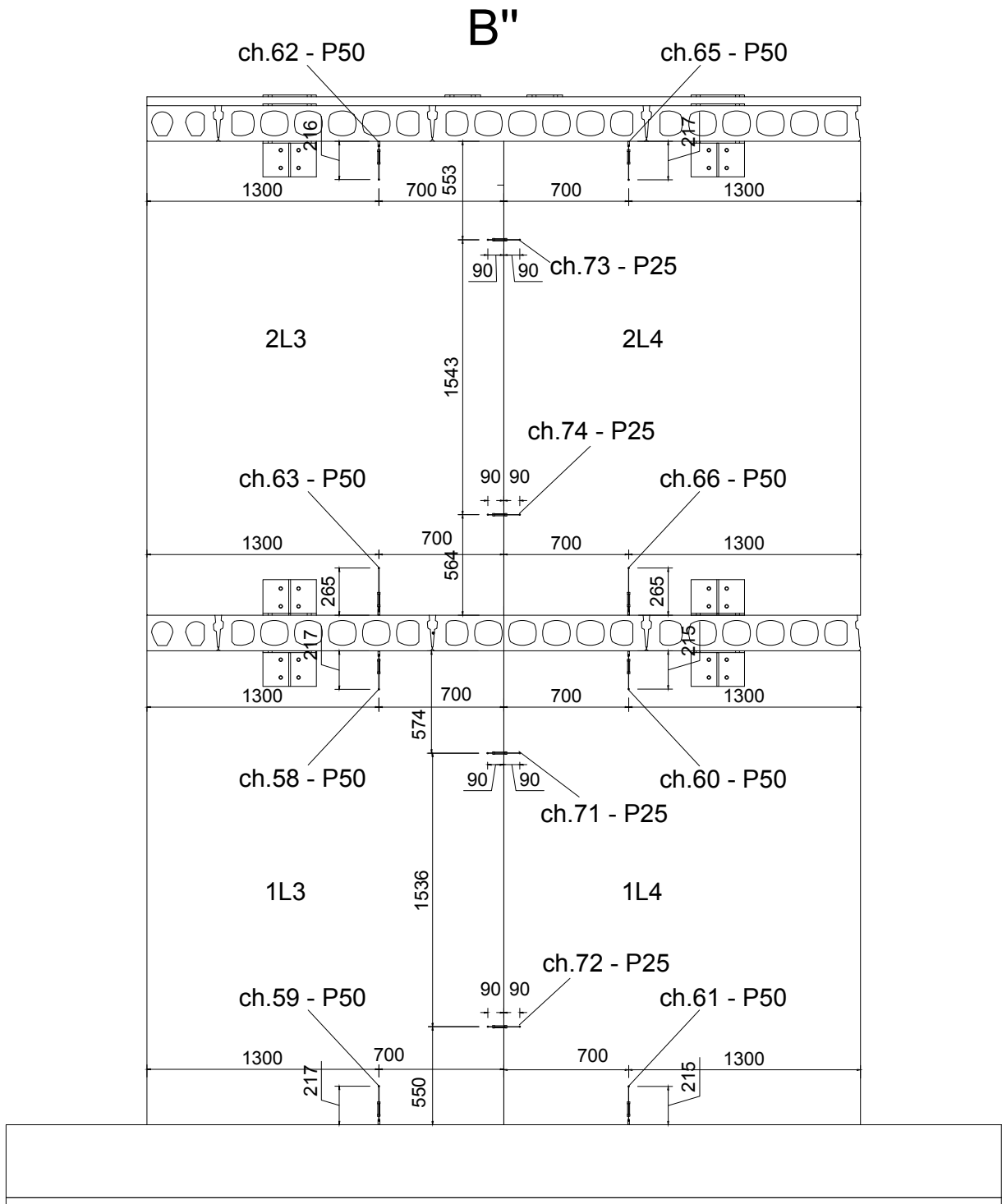
Figure 190. Schematic of the installed instrumentation: front views of the specimen – Lateral walls, B''.
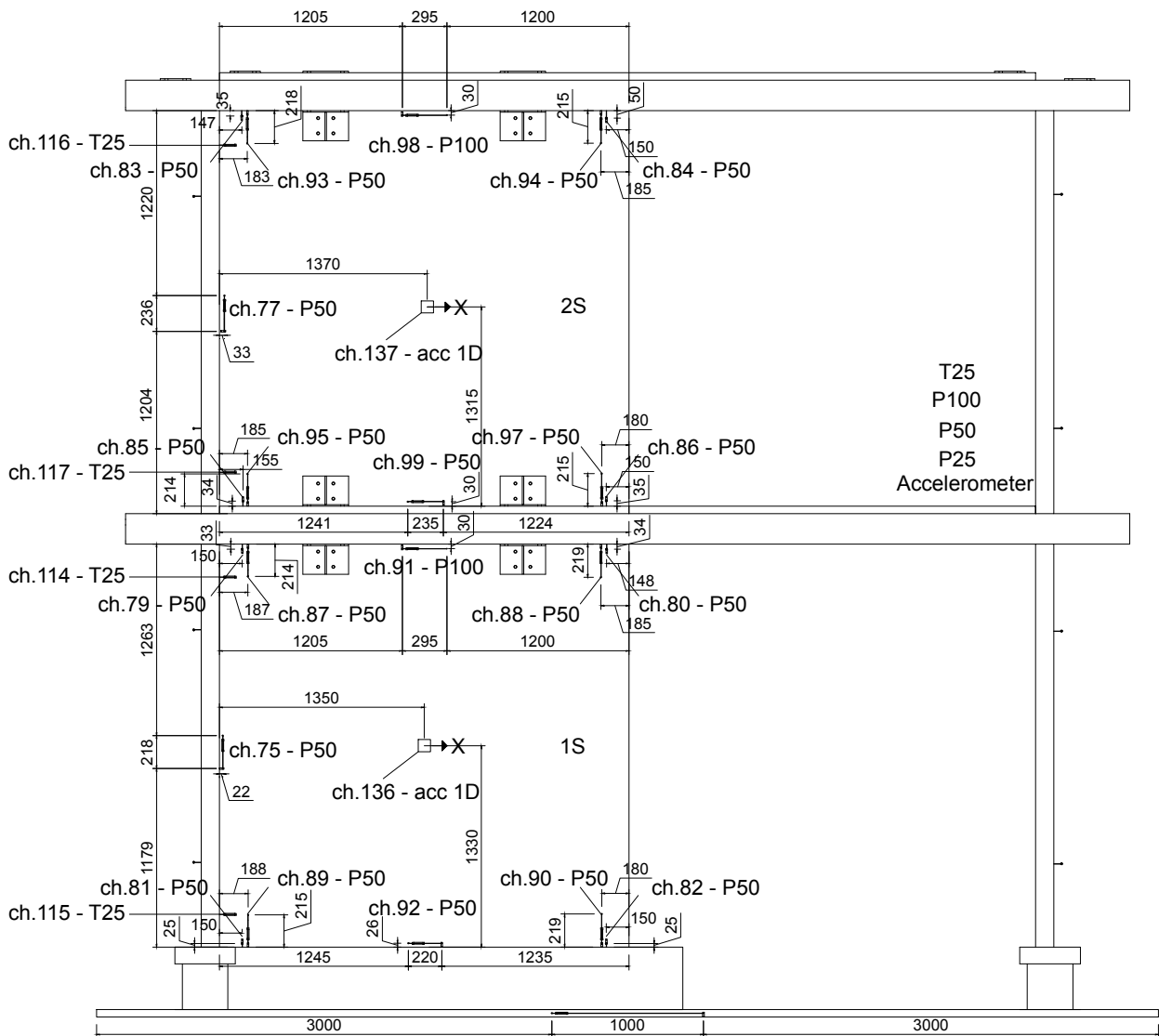
Figure 191. Installed instrumentation: side views of the specimen – Stability walls, East.
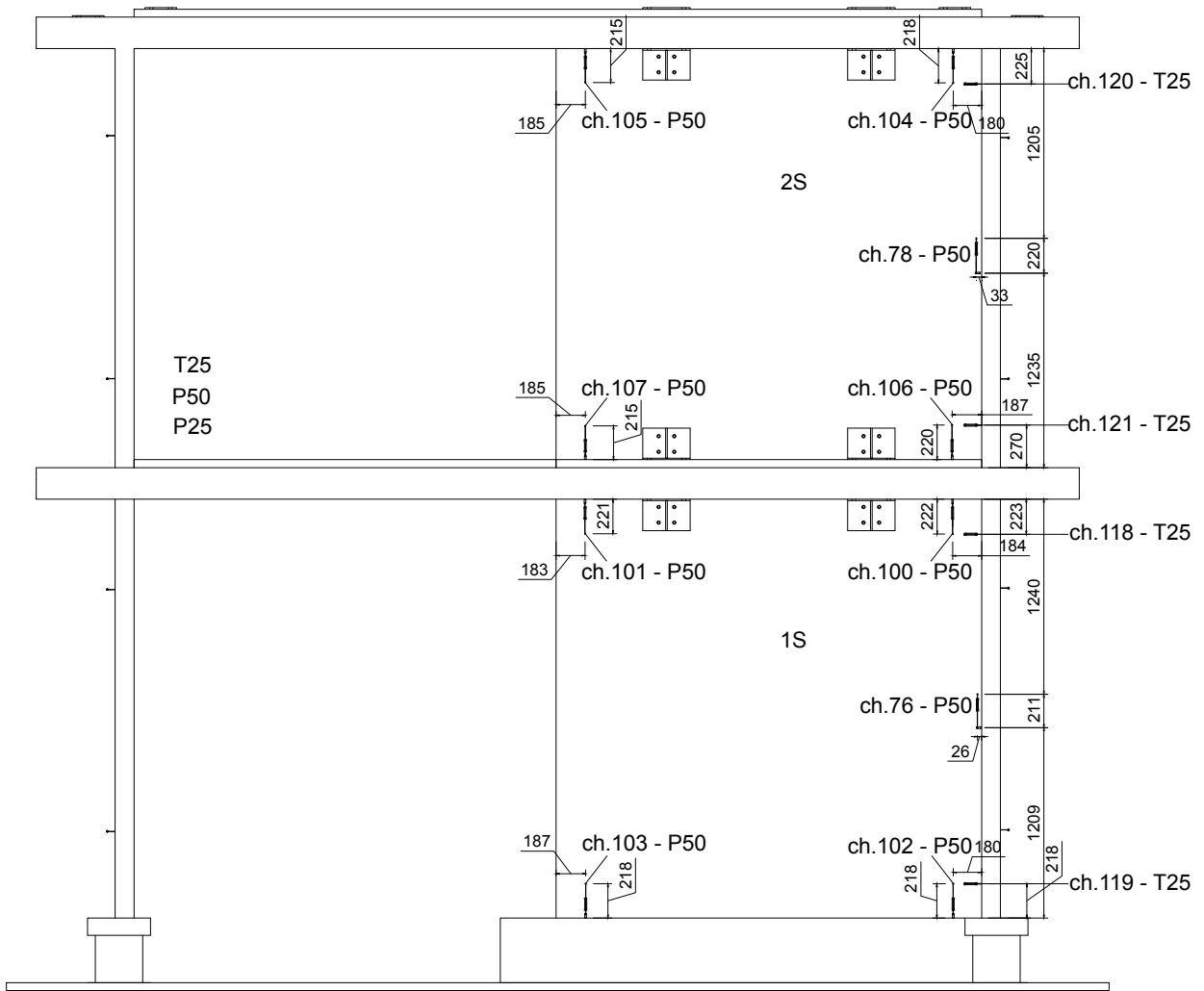
Figure 192. Installed instrumentation: side views of the specimen – Stability walls, West.
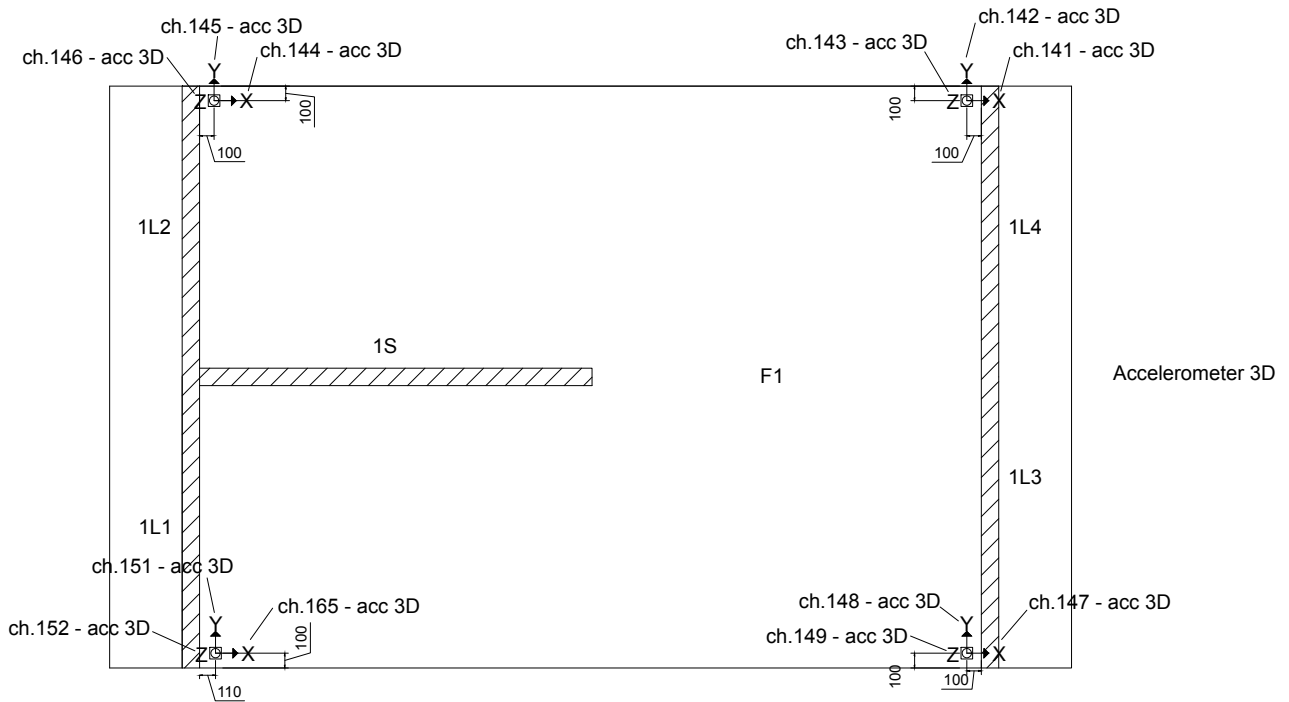
Figure 193. Schematic of the installed instrumentation: plan view of the specimen – Floor Slab, 1.
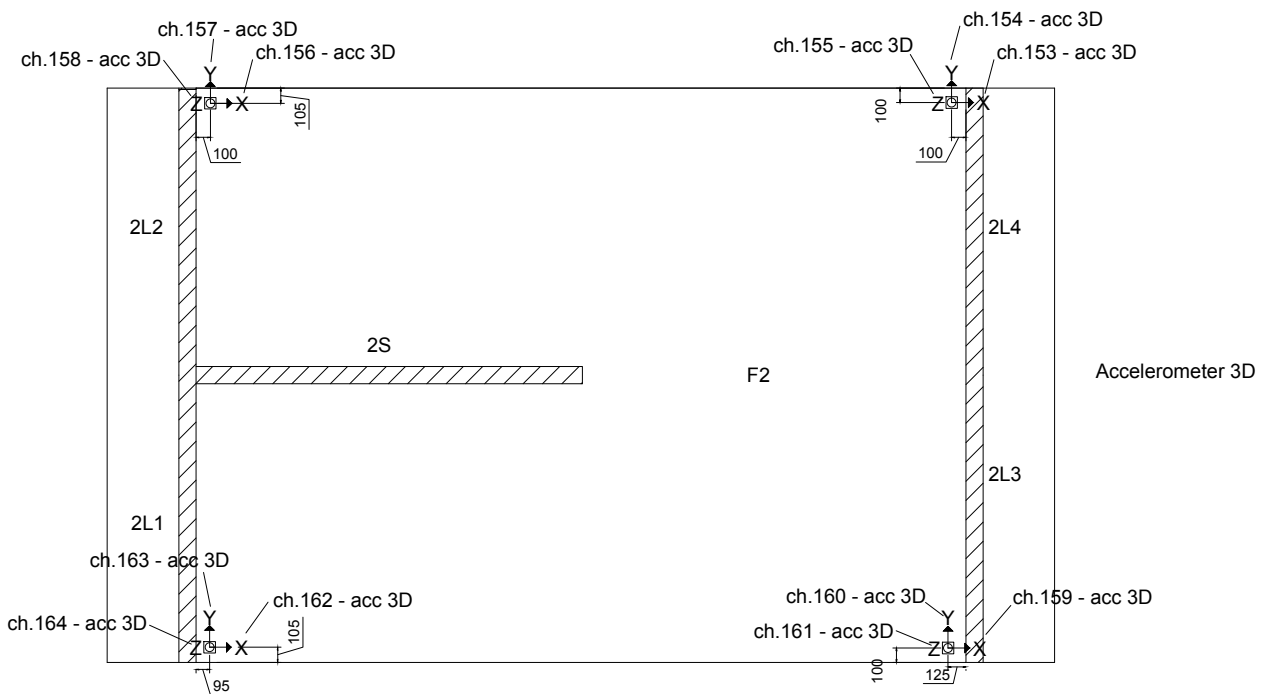
Figure 194. Schematic of the installed instrumentation: top view of the specimen – Floor Slab, 2.
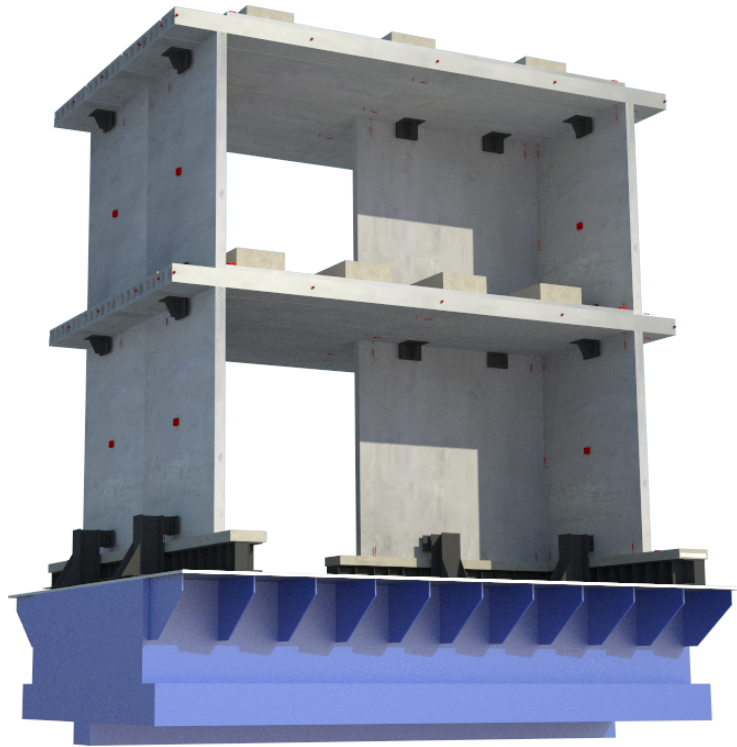
Figure 195. Isometric views of the installed instrumentation – Front view.

Figure 196. Isometric views of the installed instrumentation – Back view.

Figure 197. Instruments installed at the top of stability wall and counterpart lateral wall.

Figure 198. Instrumentation installed on the North-sided transversal walls – Second storey, South wall face.
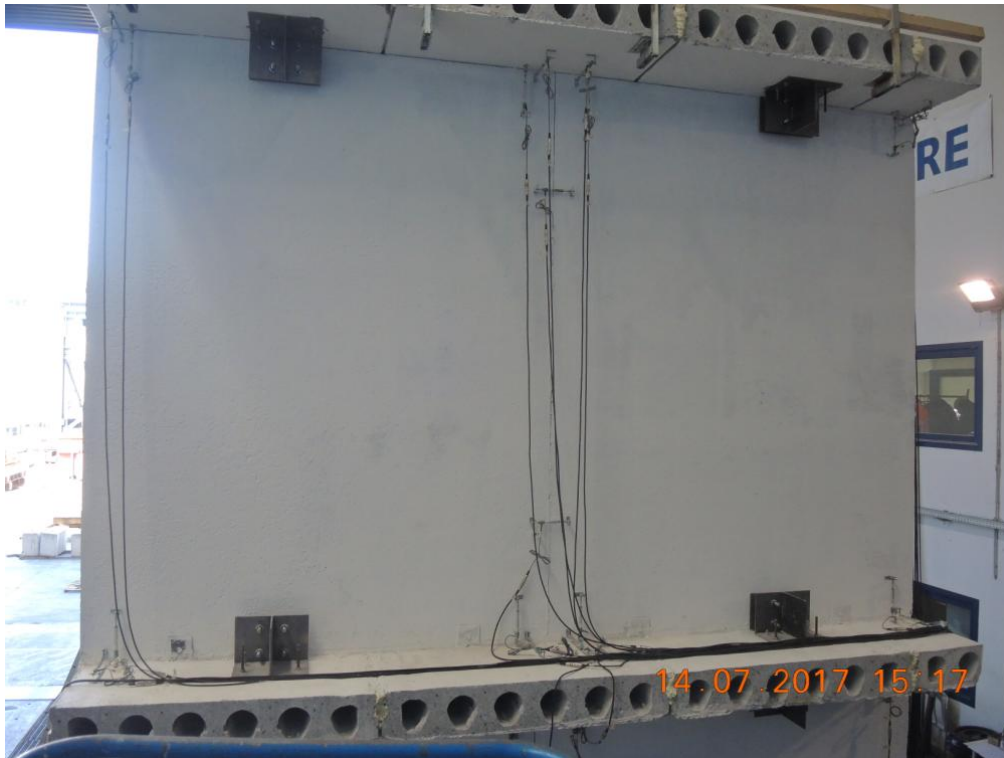
Figure 199. Instrumentation installed on the South-sided transversal walls – Second storey, South wall face.
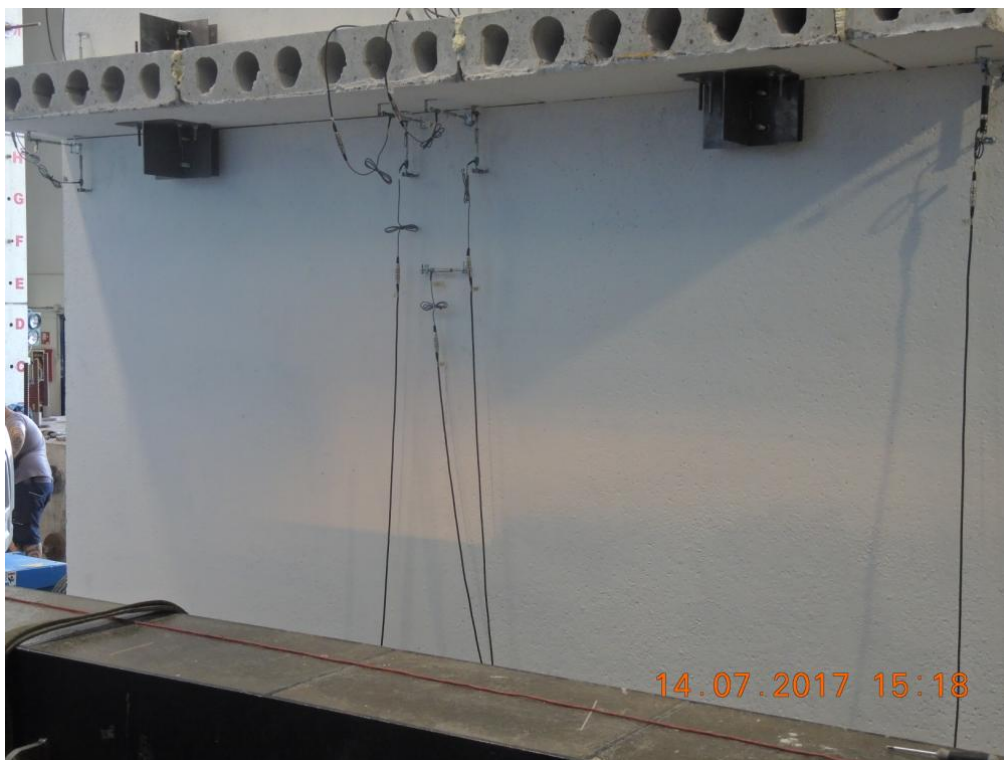
Figure 200. Instrumentation installed on the South-sided transversal walls – First storey, South wall face.

Figure 201. Instruments at the base of the South-sided transversal walls – First storey, South wall face.

Figure 202. Instruments installed on stability and lateral walls – Global view and detail of the base.

Figure 203. Potentiometer at the top of the South-East-sided lateral wall – South wall face, East corner.

Figure 204. Potentiometer at the top of the South-East-sided lateral wall – South wall face, West corner.
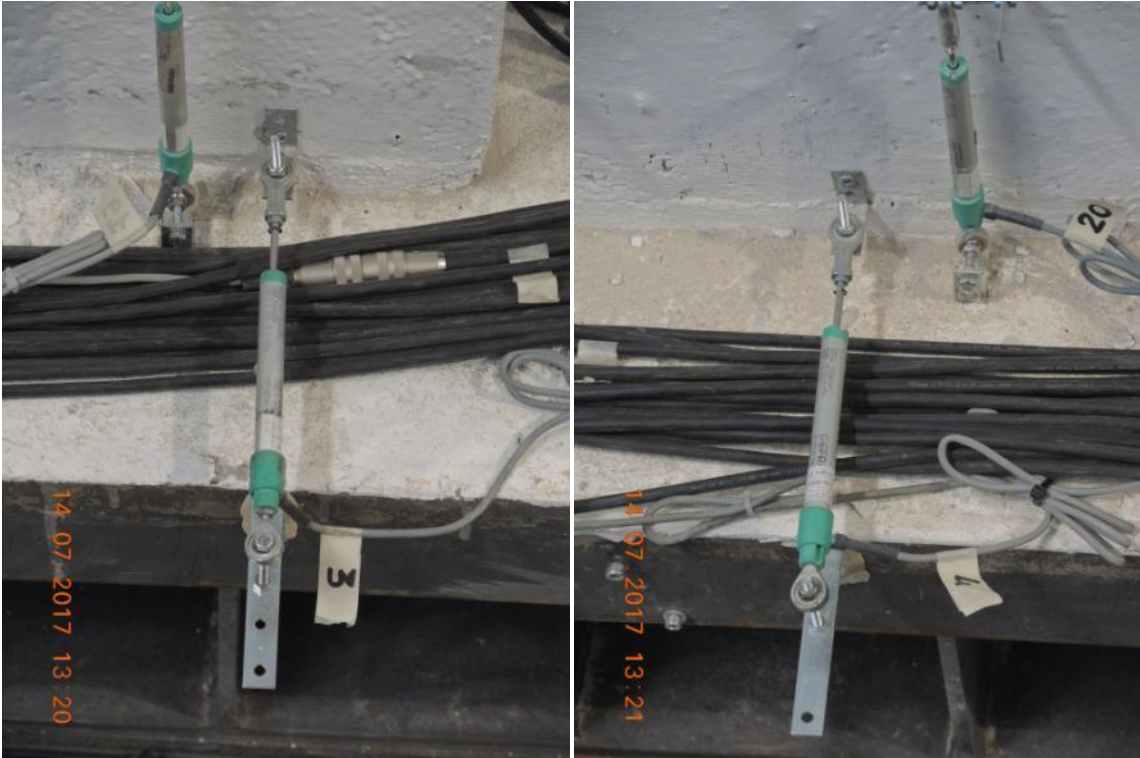
Figure 205. Potentiometers at the base of the South-East-sided lateral wall – East and West corners.

Figure 206. Potentiometer at the top of the South-West-sided lateral wall – South wall face, East corner.

Figure 207. Potentiometer at the top of the South-West-sided lateral wall – South wall face, West corner.
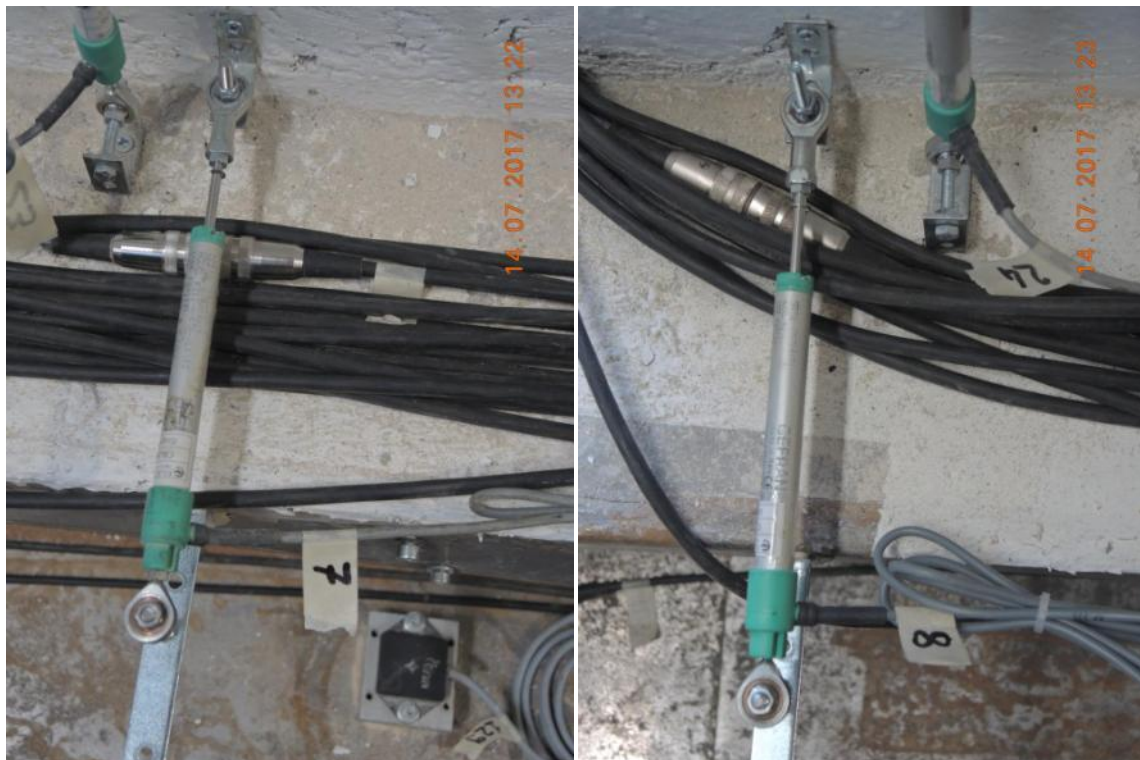
Figure 208. Potentiometers at the base of the South-West-sided lateral wall – East and West corners.

Figure 209. Instrument at the top of the second-storey South-East-sided lateral wall – East corner.

Figure 210. Instrument at the top of the second-storey South-East-sided lateral wall – West corner.

Figure 211. Instrument at the top of the second-storey South-West-sided lateral wall – East corner.

Figure 212. Instrument at the top of the second-storey South-West-sided lateral wall – West corner.

Figure 213. Potentiometers installed onto the top of the lateral walls – First storey.

Figure 214. Potentiometers installed onto the top of the lateral walls – First storey, opposite side.

Figure 215. Potentiometers at the base of the lateral walls – Corner.

Figure 216. Potentiometers at the base of the lateral walls – Centre.

Figure 217. Detail of a potentiometer installed at the top of lateral walls.

Figure 218. Detail of a potentiometer installed at the top of lateral walls – Opposite side.

Figure 219. Detail of potentiometers installed on stability wall and counterpart lateral wall.

Figure 220. Instrumentation at the base of the first-storey stability and lateral walls.

Figure 221. Instrumentation at the base of a first-storey transversal wall.

Figure 222. Instrumentation at the base of the second-storey stability wall.

Figure 223. Instrumentation at the top of the second-storey stability wall.

Figure 224. Potentiometer installed between precast wall and slab panels.

Figure 225. Potentiometer for sliding of steel foundation on the shake-table.

Figure 226. Instrumentation installed on a stability wall – Out-of-plane displacement monitoring.

Figure 227. Detail of a 1D accelerometer installed on one of the lateral wall panels.

Figure 228. Detail of a 1D accelerometer mounted on a stability wall panel.

Figure 229. Detail of the 1D accelerometer installed on the shake-table.

Figure 230. Detail of one of the two 1D accelerometers installed on the foundation of EUC-BUILD5 specimen.

Figure 231. Detail of a 3D accelerometer installed on the second floor slab – North-West side.

Figure 232. Detail of a 3D accelerometer installed on the second floor slab – South-West side.

6 Test results

The EUC-BUILD5 test started on 31 July 2017 and was completed on 2 August 2017. Out of all the seventeen test runs performed and reported in Table 13, twelve of them were necessarily undertaken for table calibration and structural identification purposes. As such, the seven runs that consisted in the application a random white noise are omitted here, whilst the five runs for controller compensation that consisted of sequencing the selected accelerogram at a lower intensity (than the one planned for the subsequent test) were considered, as can be gathered from Table 14, which summarises the test runs of interest and defines the nomenclature/labelling assumed for the discussion of test results. Out of the ten test runs presented in Table 14, the following main stages can be identified:

- Test run #02 and test run #04, by which specimen EUC-BUILD5 was subjected to 50% and 100% input motions, responding in a fairly elastic manner, since only minor cracks could be observed at the base of the first-storey and second-storey stability walls.
- Test run #06, by which specimen EUC-BUILD5 was subjected to a 150% input motion that caused the propagation of previous horizontal cracks at the base of the stability walls and the development of new cracks along the boundaries of the connectors sockets.
- Test run #08, by which specimen EUC-BUILD5 was subjected to a 200% input motion that caused cracking spreading all over the structure and also a permanent displacement of 1 cm in certain parts of the specimen (i.e. top three-way connection between precast walls).
- Test run #10, by which specimen EUC-BUILD5 was subjected to a second 200% input motion that caused near collapse of the structure, which was immediately propped-up in face of what appeared to be a very precarious stability of the specimen.

At the end of every test run of the dynamic testing sequence, detailed surveys of the crack patterns developed were carried out so as to detect every possible sign of damage having affected the mock-up building. As emerged from those surveys, the behaviour of the tested specimen was mainly governed (i) by the wet mortar joints between the stability walls and the slabs, (ii) by sliding of precast slabs on the precast walls underneath them and subsequent accumulation of permanent displacements after that damage started propagating in the wet mortar joints, and (iii) by the response of the steel connectors between the stability and transversal walls, which were severely damaged and outwardly/upwardly bent in a permanent fashion, causing the precast wall panels to be completely disconnected. Furthermore, it is worth noting that concrete cracking was observed also at the base of both first-storey and second-storey stability walls and at the base of all the transversal walls because of their out-of-plane rocking mechanism.

In what follows, once an overview of the experimental response/behaviour observed is provided, a more detailed account of the main findings obtained for each test run is given.

6.1 Overview of specimen's response

On Monday 31 July 2017, the shake-table test of EUC-BUILD5 specimen started and at close of the first day of test the building had already been subjected to the first two test runs of interest (i.e. Test run #02 and Test run #04), which are the 50% and 100% input motions. At this stage of testing, no cracking or damage of any sort was observed, apart from a partial crack at the base of the first-

storey stability wall and from even less significant ones in the concrete topping of the first floor slab. The specimen, responding in a fairly elastic manner for these two test runs, as confirmed by the hysteretic response curves presented in Sections 6.2, and was subjected to other two test runs on the day of Tuesday 1 August 2017.

At an intensity of 150% (i.e. Test run #06), the specimen started to show some damage, in the form of cracks along the boundaries of the connectors sockets (please refer to Section 6.5.2 of this report for illustrative photos), as well as along the base of the stability wall. The horizontal flexural cracks had already formed after Test run #04 propagated along the entire depth of the wall. The hysteresis plots presented in Sections 6.2 and 6.6.6 also lay evident the fact that at this test run the response of the structure started deviating from a linear elastic behaviour, albeit the levels of displacement were still very small (i.e. maximum displacement of 4.5 mm). On the same day, EUC-BUILD5 specimen was then subjected to the 200% input motion.

At this intensity level (200%, Test run #08), noticeable damage was finally observed, with cracking spreading all over the specimen, as triggered by the sliding of both transverse and stability walls. It is noteworthy that permanent displacements of 1 cm were reached in certain parts of the specimen, as clearly confirmed by some of the photos collected in Section 6.5.3. This is also reaffirmed by the hysteresis plots reported in Sections 6.2 and 6.6.8, where the nonlinear response of the specimen is conspicuous. It was finally planned to subject the specimen to one further test run, again at intensity of 200%, after which it was expected that the permanent damage would become excessive, and the testing would need to be brought to a halt.

As expected and noted above, the testing of EUC-BUILD5 specimen was completed on the day of Wednesday 2 August 2017, subjecting the structure to another test run (5th one if those for purposes of controller compensation are not included), at the same 200% intensity that had been used for Test run #08. As one will be able to quickly realise by looking at the hysteresis plots of Test run #10 (see Sections 6.2 and 6.6.10), the specimen started collapsing right after the first few cycles of loading, rapidly loosing shear capacity and accumulating a significant 14 cm of permanent displacement. A photographic sequence that illustrates well the (battered) state of EUC-BUILD5 specimen after the test is given in Section 6.5.4. It is worthwhile to mention that these photos were taken in the very first minutes after the test, in parallel with an equally immediate propping-up of the structure, which was deemed urgent in face of what appeared to be a very precarious stability of the building. The urgent dismantling of the collapsed specimen was then undertaken, as presented in a separate Chapter (see Chapter 7 for details concerning the operations of dismantling and survey of permanently-bent steel connectors of the test specimen).

The following sections of this chapter report the building damage evolution throughout the dynamic testing sequence in terms of the crack patterns that formed, together with response graphs showing the main behavioural characteristics of the specimen and of key portions of it. Separate sub-sections were drafted to present the global response of the specimen, the local response of walls in terms of base rocking and vertical sliding and the observation of damage caused by the most significant stages of testing. Deformed shapes of the building mock-up and response plots presenting the evolution of the structural response, in orderly way, are given as well.

To lead to a readily interpretation of the results discussed in this chapter, Table 34 summarises the maximum storey drift for each test run as well as the floor level at which it was recorded. Given

that floor displacements were used to compute the storey drifts collected there, these values result from a combination of (i) rocking of the precast wall-elements, and (ii) sliding of the floor slabs on them after that damage started accumulating in the wet mortar joints between stability walls and slabs.

Table 34. EUC-BUILD5: maximum and residual storey drift for each test run.

Test run #	Scale factor	Maximum Drift [%]		Residual Drift [%]	
		1st Floor	2nd Floor	1st Floor	2nd Floor
02	50%	0.018	**0.018**	0.002	**0.002**
04	100%	**0.052**	0.038	**0.008**	0.002
06	150%	**0.164**	0.087	**0.037**	0.003
08	200%	**0.534**	0.432	0.275	**0.355**
10	200%	**5.168**	0.581	**5.130**	0.497

6.2 Global response of the specimen

In Figure 233, the base shear-top displacement response curve of EUC-BUILD5 specimen is shown with a view to clarify the response for each single test run, whilst the backbone curve is a bit more clearly reported and compared to hysteresis loops in Figure 234. It is worth mentioning that the top-to-base displacement is used to derive these plots. Care was also paid to the response of each single storey, so as to decouple the behaviour observed for each one of them. As one may notice in Figure 235 to Figure 238, the same approach was used to present results with respect to the cyclic curve and the envelope of cyclic response.
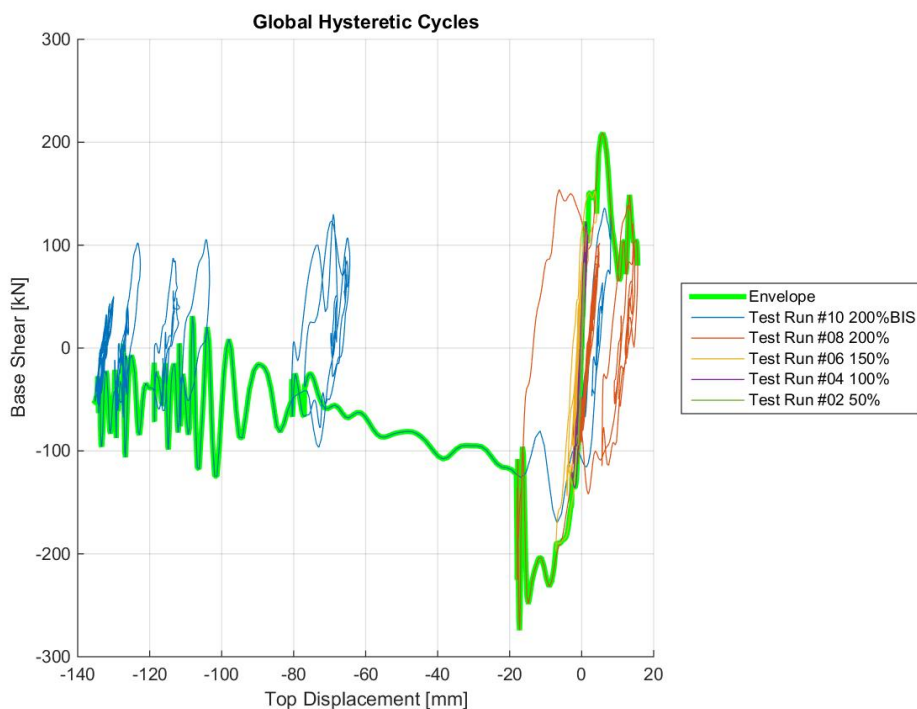
Figure 233. Total base shear-top displacement response of EUC-BUILD5 specimen.
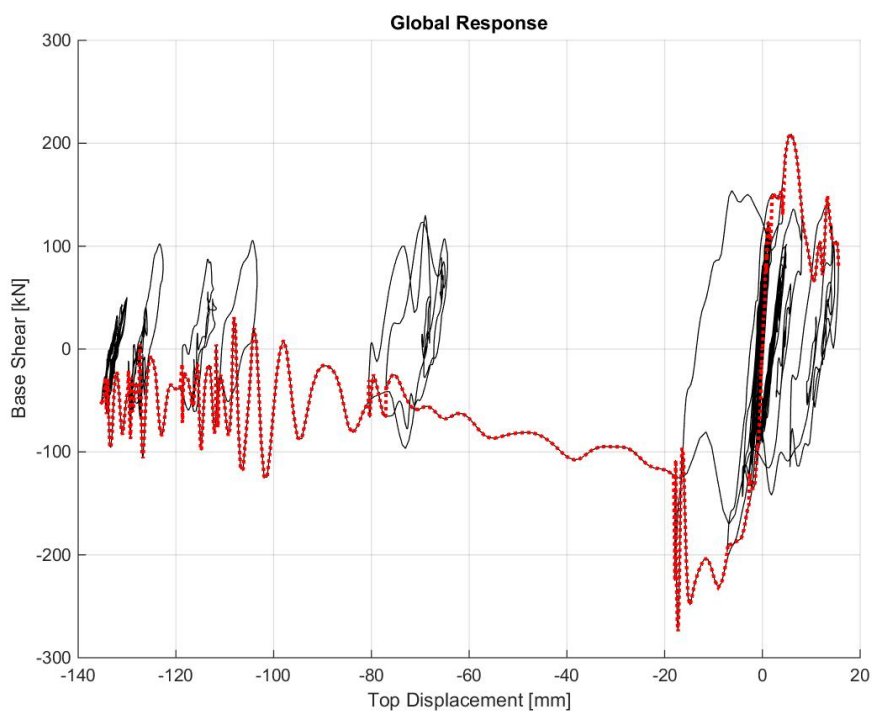
Figure 234. Base shear-top displacement response of EUC-BUILD5 specimen – Envelope and hysteretic curves.

First of all, it is noteworthy that the behaviour of the building mock-up is not symmetric in positive (i.e. Northward) and negative directions, since EUC-BUILD5 specimen accumulated a significantly large permanent top-to-base displacement of about 14 cm. As can be gathered from Figure 235 and Figure 237, slightly larger values of up to approximately 15 cm are obtained if reference is made to the inter-storey displacements (first storey-to-base one), owing to the counter permanent displacement that the second floor accumulated in the opposite (positive) direction (Figure 236 and Figure 238).

During the last test run (i.e. Test run #10), the specimen resisted a peak base shear of about 170 kN and 136 kN in the negative and positive directions, respectively. Both positive and negative values of maximum base shear were reached for a fairly similar level of top-to-base displacement (7 mm). The two values of base shear reported above are anyway lower than the maxima experienced by the specimen during the entire testing sequence, since a maximum base shear of up to 274 kN and 209 kN was recorded during Test run #08 for negative and positive directions, respectively. For this test run, however, the maximum negative base shear was observed for a top-to-base displacement of 17 mm, whilst the peak lateral load-carrying capacity in the opposite direction of testing occurred for a top-to-base displacement that equalled 6 mm.

Moreover, during Test run #08, the maximum top-to-base displacement for the positive and negative directions started differentiating significantly, thus implying a more asymmetric response in comparison with what had been observed for previous test runs. The asymmetry is even more clearly pointed out by referring to the inter-storey displacements (instead of the top-to-base ones). As illustrated by Figure 235, the storey shear peaks in the negative and positive directions of the

specimen were achieved for inter-storey displacements of 15 mm and 1 mm, respectively. Figure 236 shows an asymmetry that is similar in type, but weaker in character and opposed in sign, since the second storey accumulated residual displacements/drifts that pointed toward the North side of the specimen.

The hysteretic curves shown in Figure 235 and Figure 236, along with the global response curve of the structure (Figure 233) confirmed that the collapse mechanism observed during Test run #10 had been already mobilised by Test run #08. Once damage propagated in the mortar joints between the stability walls and the slabs, the response of the specimen was dominated by issues of sliding and connection behaviour. These two mechanisms far outstripped any of the other ones experienced by the specimen, as clearly highlighted by the series of damage patterns collected after each single test run (see Sections 6.5.3 and 6.5.4).

Residual displacements started accumulating because of sliding of the floor slabs on the precast walls, and the steel connectors between the transversal and stability ground-floor walls failed at relatively low levels of storey drift (i.e. 0.5-1.0%), given that they were not able to sustain much load. It is noteworthy that the failure mode of the steel connectors and the drift thresholds corresponding to the attainment of this mechanism are consistent with the outcomes of EUC-BUILD4 test. The only difference is the fact that, in the latter case, the connector rebars in the sockets of the stability wall were intact after cyclic testing.

Permanent bending of the connector bar embedded in the transverse and stability ground-floor walls is the failure mode of EUC-BUILD5, as confirmed by a detailed inspection of the failed connectors that was undertaken during dismantling of the specimen. This mechanism was evident from visual observations of the full-scale building prototype and appears to be portreited, even more clearly, by the shape and type of the obtained hysteretic loops, as clarified in what follows.

The non-negligible difference in the base shear resisted by the building during test runs #08 and #10 (i.e. 274 kN vs. 170 kN) is attributable to the extensive damage undergone by all the four three-way connections between the ground-floor stability walls and the corresponding South-sided transversal walls. The connectors embedded in the niche of the lateral walls were pulled and bent permanently (towards the North side of the building) by the counterpart anchors installed into the sockets of the stability wall, owing to shear transfer mechanisms in the precast wall-elements of this portion of the structure. Noteworthy is that also the latter connectors (i.e. the ones embedded in the sockets of the stability wall) were abruptly bent upwards, which causes the hook at their ends to become straight and the three wall panels to get completely disconnected. In light of this, a 38% strength reduction was observed (Figure 233 and Figure 235), which implies that the specimen is unable to withstand any further load of relevance, as confirmed by the gap opening between the transversal and stability wall and the subsequent accumulation of displacements shown by the response curves.

With respect to the accumulation of residual displacements in the two storeys of the building mock-up and with regards to the asymmetry of the observed response, several considerations can be drawn whether the response curves of the two floors are examined even further. As mentioned earlier, the storey shear versus inter-storey displacement response of the two floor levels are separately shown in Figure 235 and Figure 236. The information contained there can be merged also with the series of response time-history plots collected in Figure 239 to Figure 243, in which displacement and storey force time-histories for each run are provided.
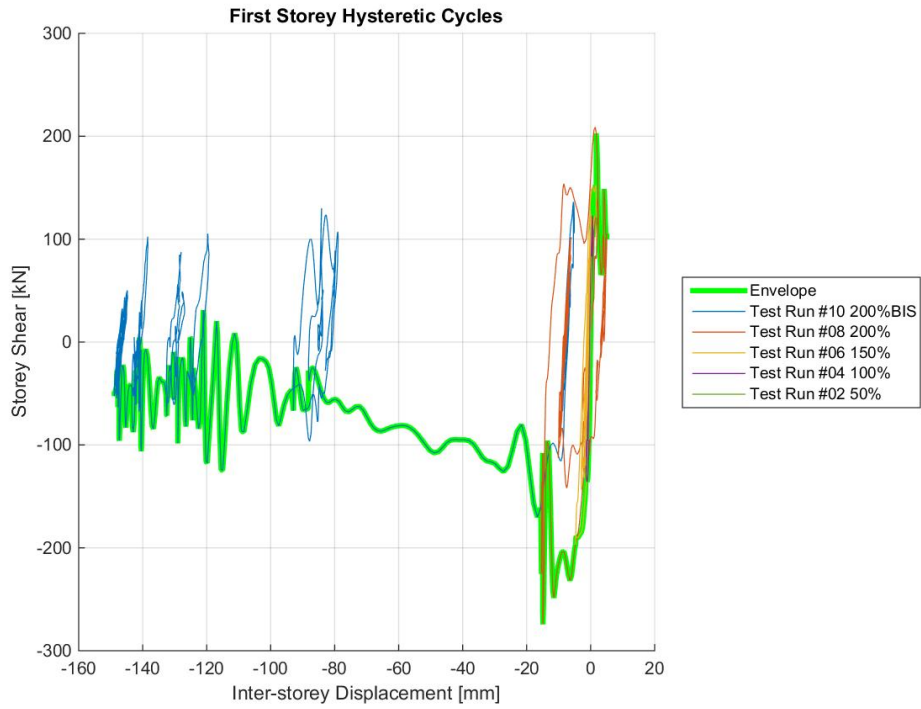
Figure 235. Storey shear vs. inter-storey displacement response – First storey.
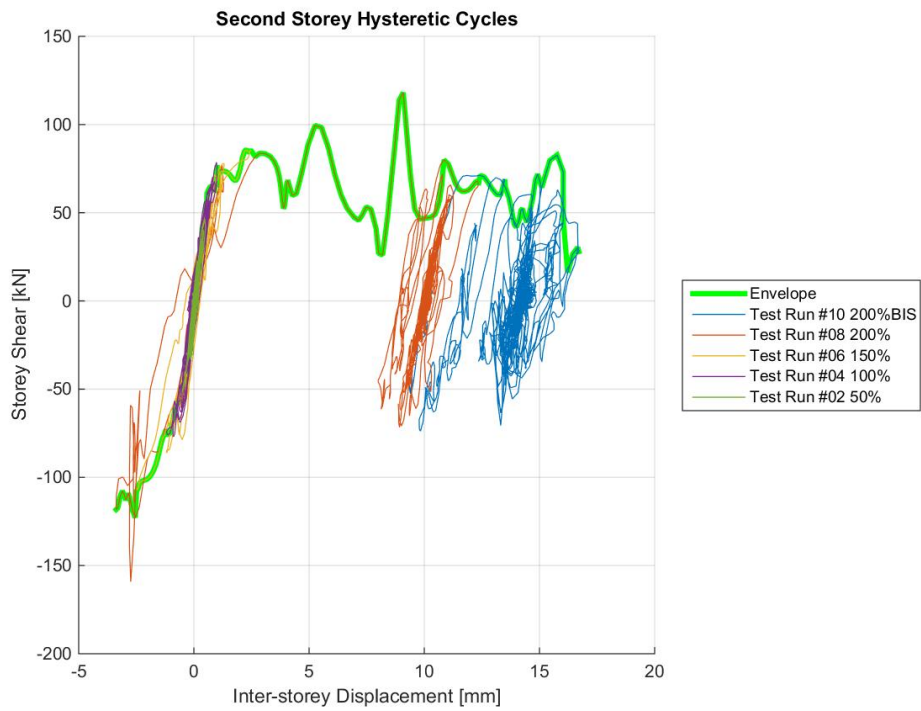
Figure 236. Storey shear vs. inter-storey displacement response – Second storey.
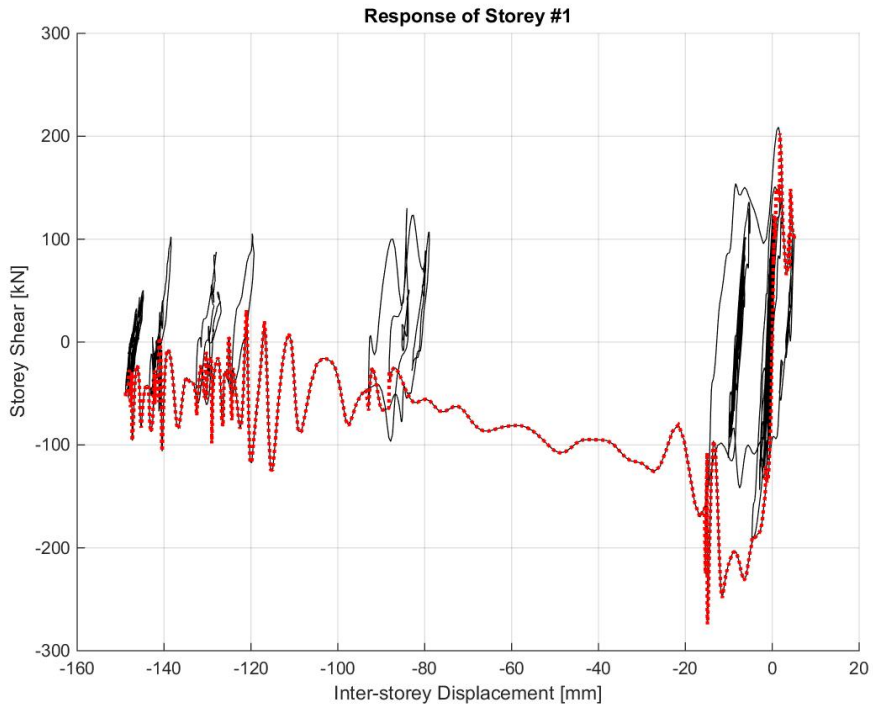
Figure 237. Storey shear vs. inter-storey displacement response – First storey, envelope and hysteretic curves.
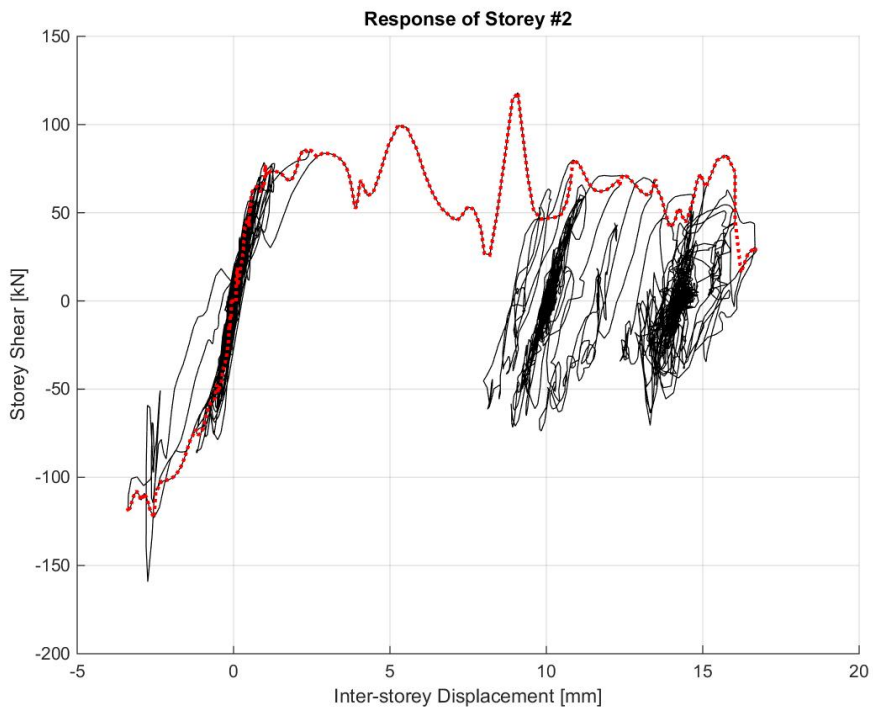
Figure 238. Storey shear vs. inter-storey displacement response – Second storey, envelope and hysteretic curves.

By taking a look at the respose curves reported in Figure 235 and Figure 236, it becomes clear that the first floor experienced maximum negative inter-storey displacement of up to 149 mm, whilst the

second storey was found to undergo peak negative inter-storey displacements slightly lower than 17 mm for a nearly 30% lower storey force. Sliding and accumulation of residual displacements can be clearly observed, especially in correspondence to the first storey (Figure 235). The response curves of the two storeys are thus heavily unsymmetric and are also opposed in phase, if they are compared together. As shown in Figure 238, the backbone curve computed from the storey shear versus inter-storey displacement response of the second floor is characterised a relatively moderate displacement residual, which agrees with the fact that the sockets and steel connectors of the second-storey three-way connections were intact. On the other hand, the permanent top-to-base displacement shown by the global response curve of EUC-BUILD5 specimen is a direct consequence of damage at the first-storey elements and connections. Accumulation of residuals and the corresponding non-re-centering response are evident after the achievement of the maximum base shear experienced during Test run #08. Before that step of the testing sequence, no damage of any sort was observed in the wet joints between the stability walls and the slabs, which implies that sliding of the slabs on the precast walls was prevented from occurring because of shear force transfer mechanisms across the mortar joints.

Response time-histories obtained for each test run of interest are shown in Figure 239 to Figure 243. The horizontal forces exerted at the two floor levels and the corresponding horizontal displacements recorded during the stages of testing are collected therein, together with the hysteretic curves. More in detail, care was paid to storey force-storey displacement response curves and storey shear versus inter-storey displacement curves.
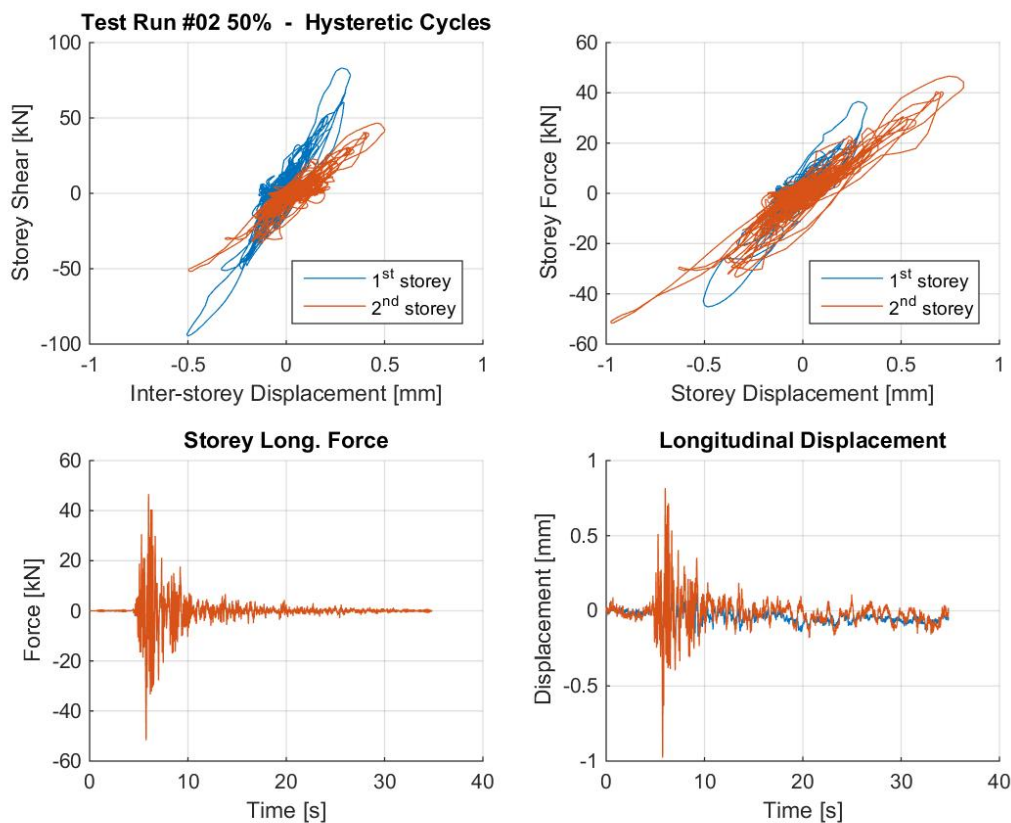
Figure 239. Response time-histories: displacement, storey force and storey shear – Test run #2.
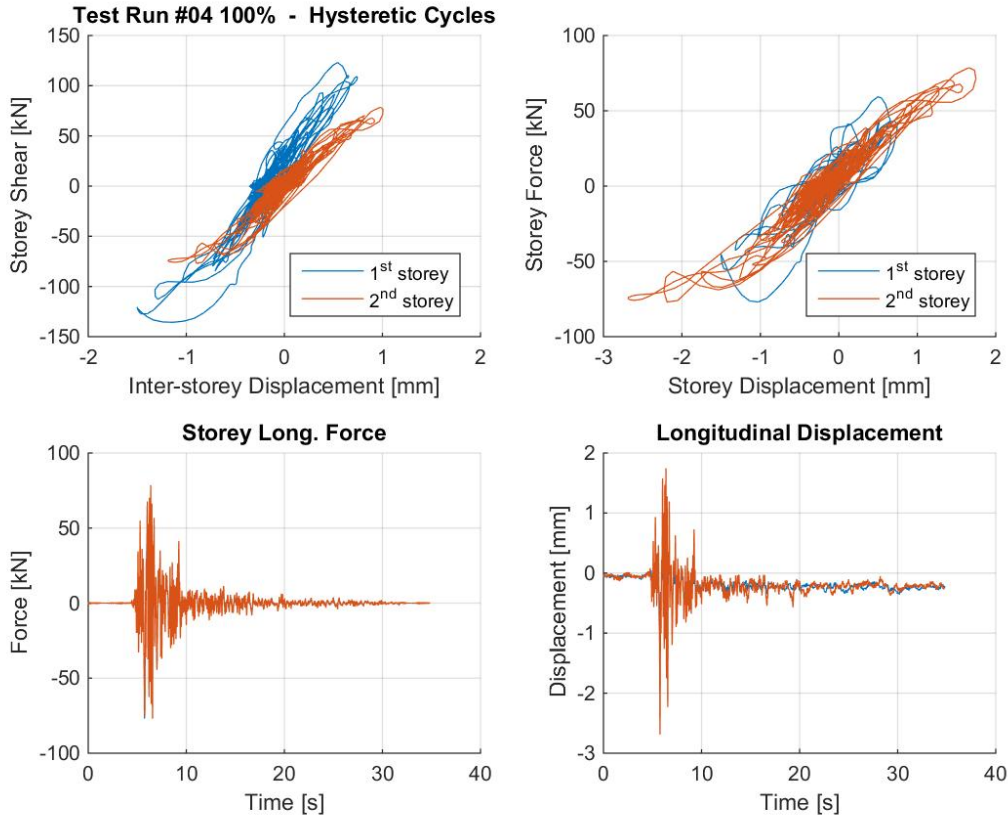
Figure 240. Response time-histories: displacement, storey force and storey shear – Test run #4.
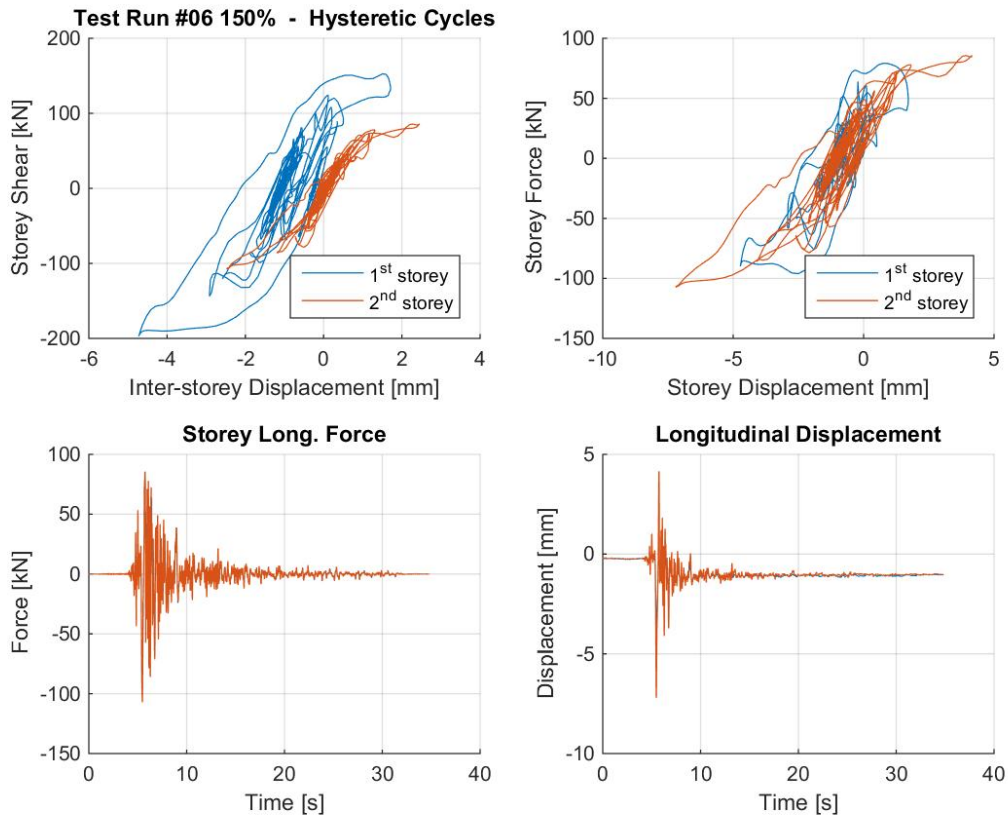
Figure 241. Response time-histories: displacement, storey force and storey shear – Test run #6.
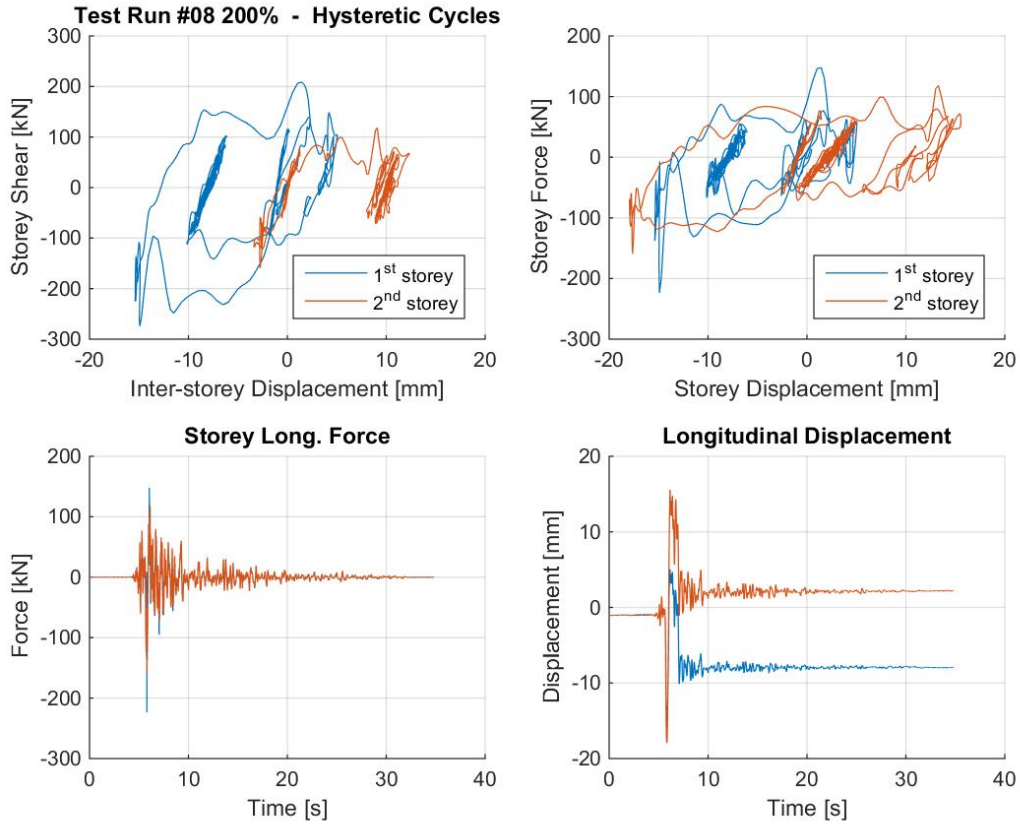
Figure 242. Response time-histories: displacement, storey force and storey shear – Test run #8.
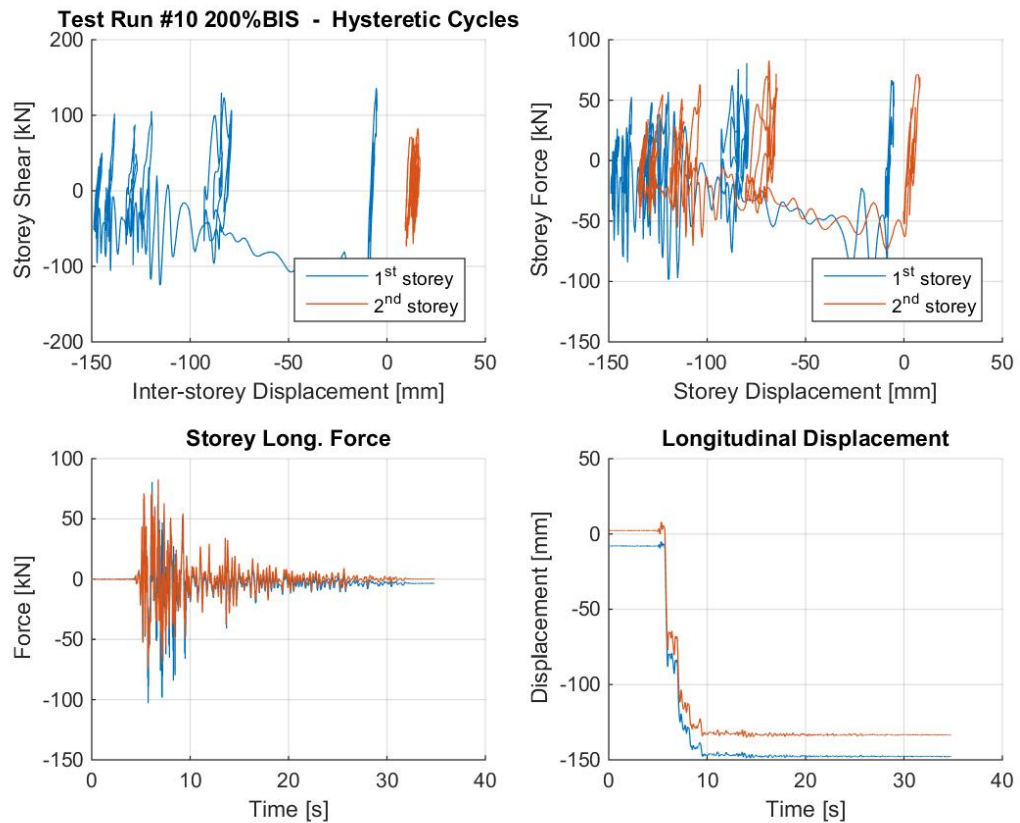
Figure 243. Response time-histories: displacement, storey force and storey shear – Test run #10.

The above response graphs, showing the hysteretic response of each test run of interest in terms of both storey shear versus inter-storey displacement and storey force versus storey displacement with reference to each one of the two floor levels, are presented for interested readers with the main aim of clarifying even further some aspects of the experimental response. In addition to the response curves shown in this section and the set of deformed shapes discussed in the next one, they provide the reader with insights into specific behavioural characteristics of the specimen like accumulation of residual displacements during the testing sequence.

As can be gathered from Figure 239 and Figure 240, the first two test runs revealed a fairly elastic response, with the accumulation of almost negligible permanent displacements. As far as the storey force is concerned, it can be noted that the second storey of the specimen experienced higher values of maximum positive and negative force in comparison with those exerted at the first storey, and the same applies also to the third test run. At the 150% intensity, the hysteresis loops reported in Figure 241 lay evident the fact that the response of EUC-BUILD5 specimen started deviating from a linear elastic behaviour, although the levels of displacement were still very small. The displacement time-histories also revealed that permanent displacement started accumulating towards the South side of the building, albeit small values of approximately 1 mm can be appreciated in the bottom-rigth plot of Figure 241. Such values are clearly well-aligned with the type of damage observed (see Section 6.5.2), which is relatively modest and appeared in the form of cracks along the base of the stability wall at the base of the specimen as well as along the boundaries of the connectors sockets.

Previous considerations concerning the structural behaviour observed for Test runs #08 and #10 are corroborated by the set of response curves presented in Figure 242 and Figure 243. Both hysteresis loops and response time-histories allows one to argue that the specimen was severely damaged after Test run #08 and close to a global collapse after Test run #10. As was discussed before and will be shown later on when addressing damage patterns, cracking was observed spreading throughout the mortar joints between the stability walls and the slabs, which made them slide on the precast walls, accumulating large permanent displacements and causing the steel connectors to prematurely fail by an abrupt flexural mechanism.

It becomes also evident, from hysteresis loops and displacement time-histories, that such a behaviour/resisting mechanism was initially mobilised during Test run #08, for which the first and second storeys accumulated permanent inter-storey displacements that are fairly equal in magnitude (i.e. 1 cm) but opposed in phase and sign. As reported in Figure 243, the above-mentioned resisting mechanism developed noticeably during Test run #10, pushing the specimen in a very battered state, deemed representative of a condition of incipient collapse. Significant strength degradation was observed in the hysteretic response of the structure in accordance with the fact that huge damage was found to develp in the three-way connections. Residuals were getting higher and higher, as clearly highlighted by the hysteretic curves and displacement time-histories presented in Figure 243 and pertaining to Test run #10.

6.3 Deformed shapes

This section is chiefly concerned with the analysis and discussion of the observed deformed shapes at positive and negative displacement peaks reached during each run of the testing. A series of plots, shown in Figure 244 to Figure 247, are thus presented to shed light on this aspect in a synthetic and systematic manner. An example of these plots is given below, with reference to the

first run of the testing sequence (i.e. Test run #2 – Figure 244), whilst a few considerations regarding the approach used to create and present them can be given as listed below.

The dataset obtained from the instrumentation was examined in such way that absolute and relative displacements of the specimen and key portions of it can be identified. Sliding of the two floor slabs can thus be determined and taken as reference for the development of qualitative deformed shapes, which are, of course, amplified with respect to actual displacements red by potentiometers installed onto the specimen. To lead to a readily interpretation of these deformed shapes, they are all graphed together with the undeformed configuration of EUC-BUILD5 specimen.

The plots collected below confirm the resisting mechanisms commented in the previous sections, in terms of asymmetric response of the specimen and sliding of the floor slabs on the precast walls underneath, once damage had developed in the wet joints; the same applies to the detachment of the ground-floor stability wall from the corresponding transversal wall panels because of damage in the connections between them (Figure 247). The out-of-plane rocking of the opposite transversal walls is confirmed as well.

It is worthwhile to mention that the deformed shapes at maximum displacement are missing for Test run #10 because the exaggerated levels of deformation attained in such final run were such that the instruments were either dislodged or saturated.

Figure 244. Deformed shape of EUC-BUILD5 specimen (max and min) – Test run #2.

Deformed shape @ Test Run #04 100%
Minimum and Maximum Displacement
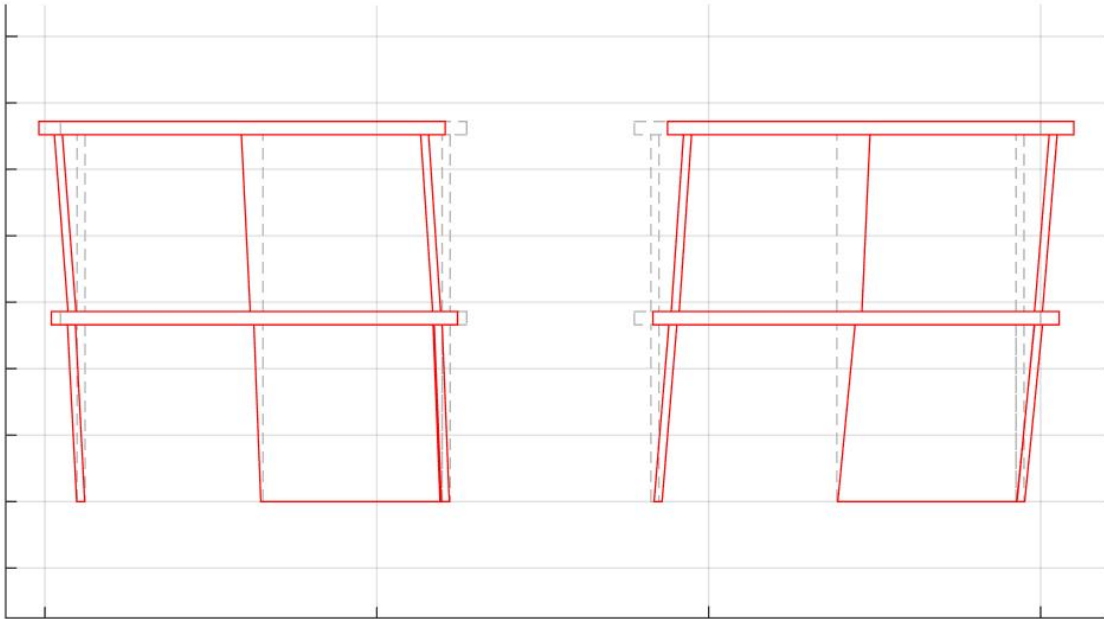
Figure 245. Deformed shape of EUC-BUILD5 specimen (max and min) – Test run #4.

Deformed shape @ Test Run #06 150%
Minimum and Maximum Displacement
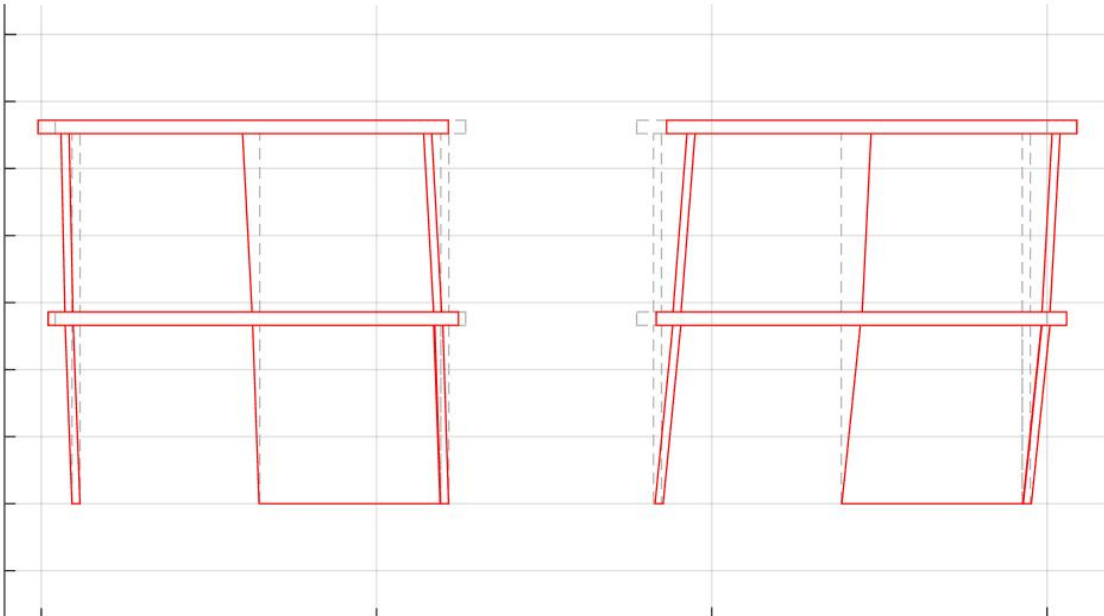
Figure 246. Deformed shape of EUC-BUILD5 specimen (max and min) – Test run #6.
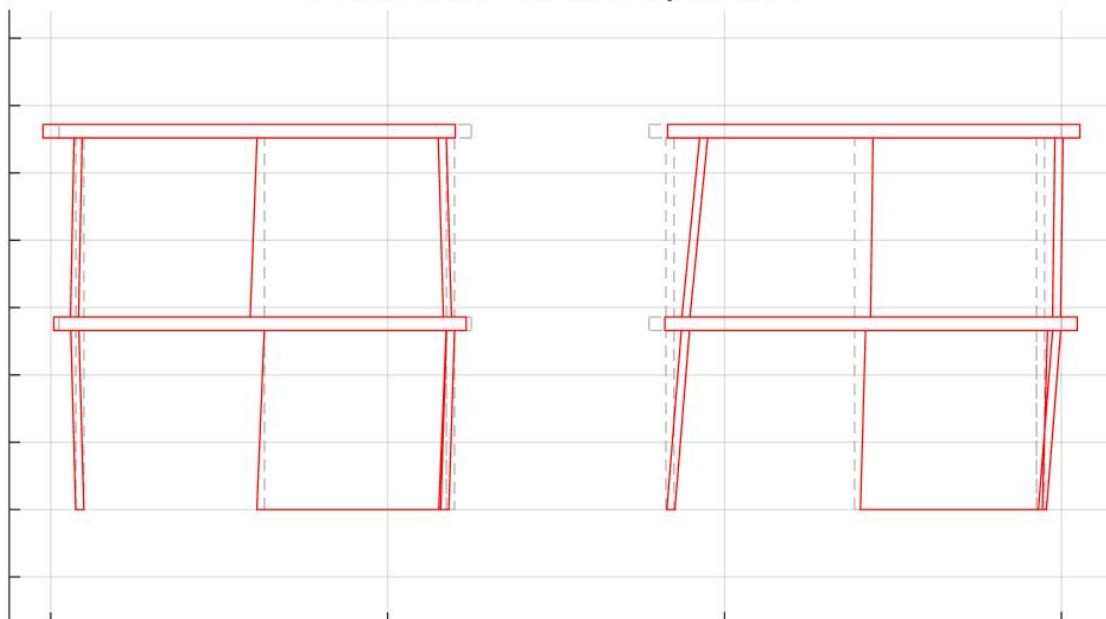
Figure 247. Deformed shape of EUC-BUILD5 specimen (max and min) – Test run #8.

6.4 Local response of key structural portions

Rotation response data were studied in detail, placing particular emphasis on the base rotation due to rocking of the first-storey and second-storey stability walls. In both cases, that parameter was of course evaluated using the in-plane displacement transducers installed according to what was shown and discussed in Section 5.5.2. Accordingly, the plots given below were created by means of the set of instruments placed on the West and East sides separately. The average of them was presented as well, thus resulting in a total of three response graphs per each wall. The same approach was used to assess the vertical sliding of the first-storey and second-storey stability walls, which was determined by taking as reference the corresponding transversal walls. Therefore, three plots per each storey are presented.

The rocking response of the ground-floor stability wall is provided in Figure 248 and Figure 249, in which it is graphed against the storey shear force. Furthermore, Figure 250 and Figure 251 highlight the experimental behaviour of this panel wall in terms of observed vertical sliding. Finally, response plots of the second-storey stability wall are collected in Figure 252 to Figure 255. None of the two mechanisms was found to be particularly pronounced before the last test run (i.e. Test run #10), and this applies to the first-floor and the second-floor walls. Rocking was clearly more significant in the ground-floor stability wall, and the observed mechanism/response was almost symmetric in positive and negative directions (see Figure 248 and Figure 249). A similar conclusion can be drawn for the second-storey stability wall (Figure 252 and Figure 253). The response curves of both walls present fairly regular trends, despite the fact that they are not necessarily smooth. Rotation maxima of about $2 \cdot 10^{-3}$ rad were obtained in the ground-floor stability wall, whilst peaks much lower (i.e. almost one order of magnitude) can be observed at the second storey.
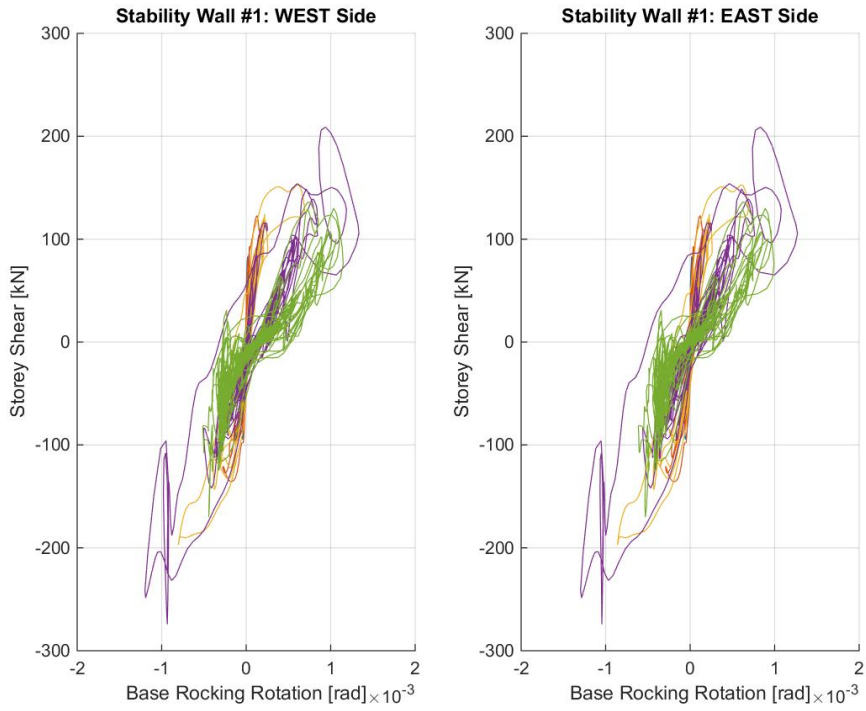
Figure 248. First-storey stability wall: base rotation due to rocking – West and East sides.
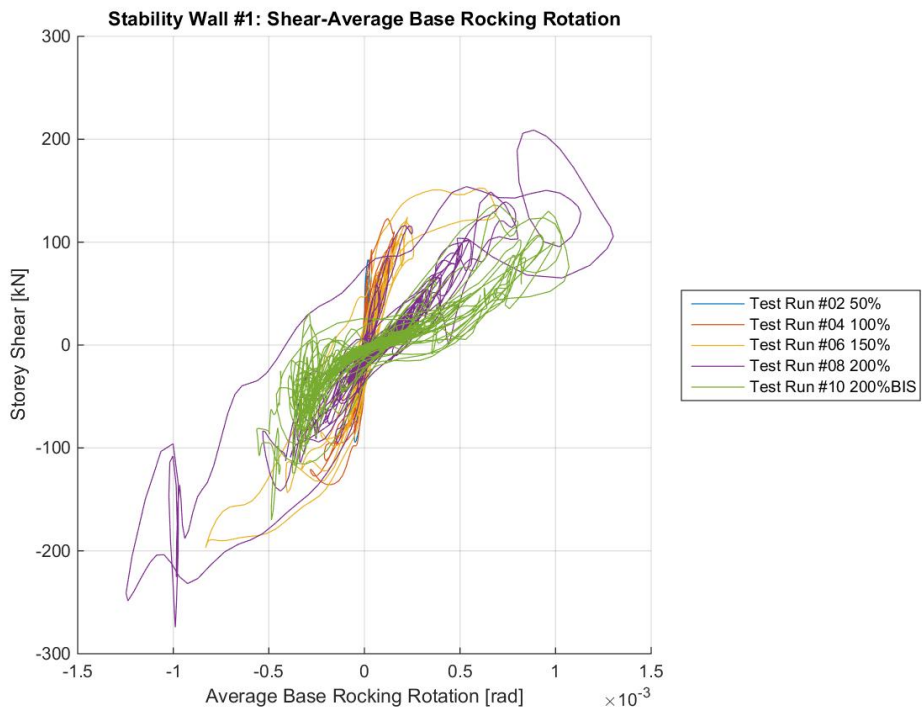
Figure 249. First-storey stability wall: base rotation due to rocking – Average of West and East sides.
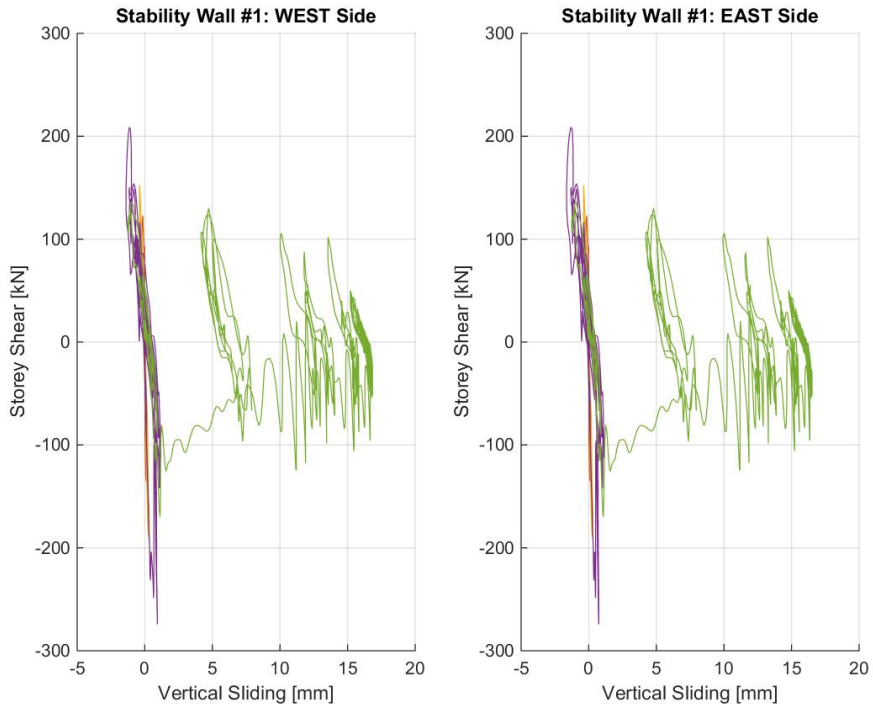
Figure 250. Vertical sliding of first-storey stability wall – West and East sides.
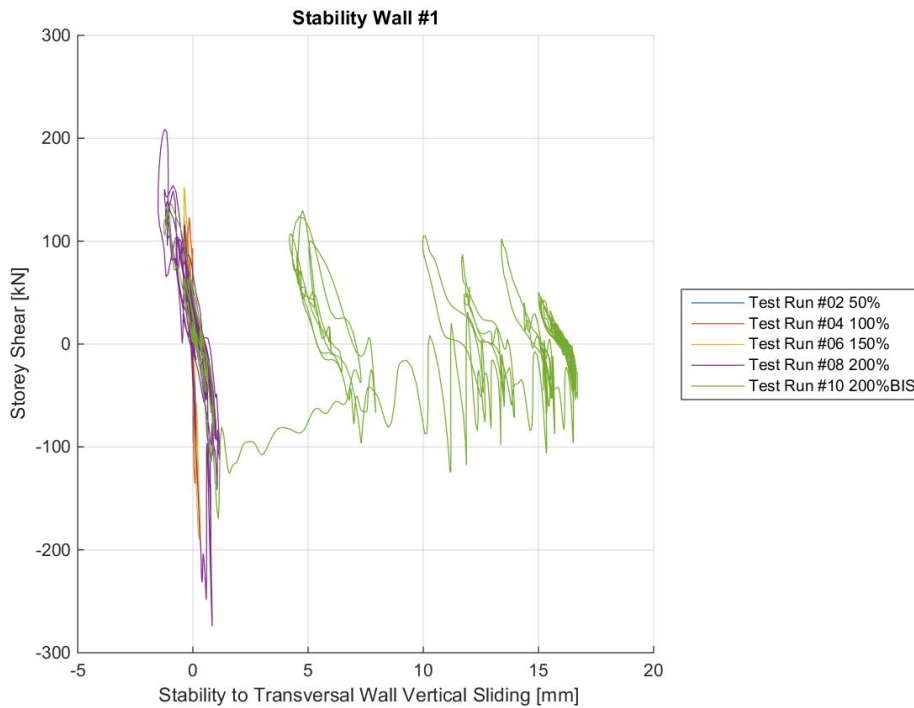
Figure 251. Vertical sliding of first-storey stability wall – Average of West and East sides.
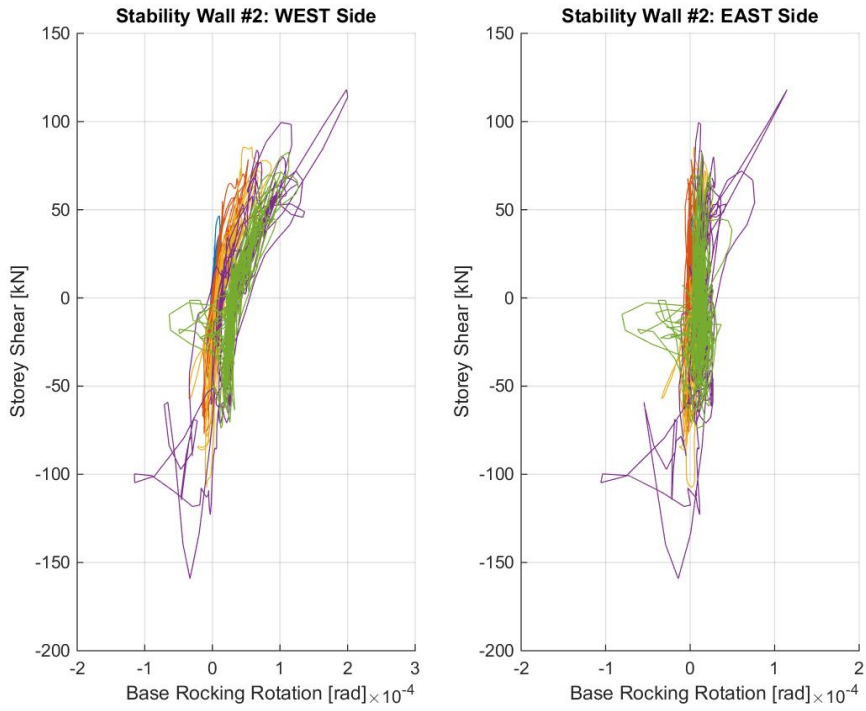
Figure 252. Second-storey stability wall: base rotation due to rocking – West and East sides.
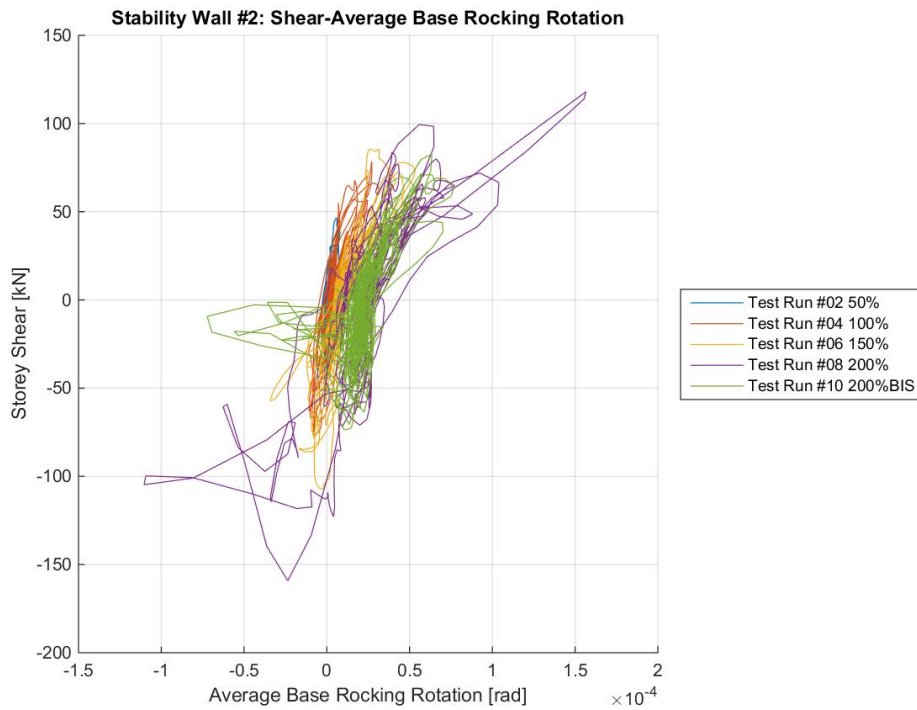
Figure 253. Second-storey stability wall: base rotation due to rocking – Average of West and East sides.
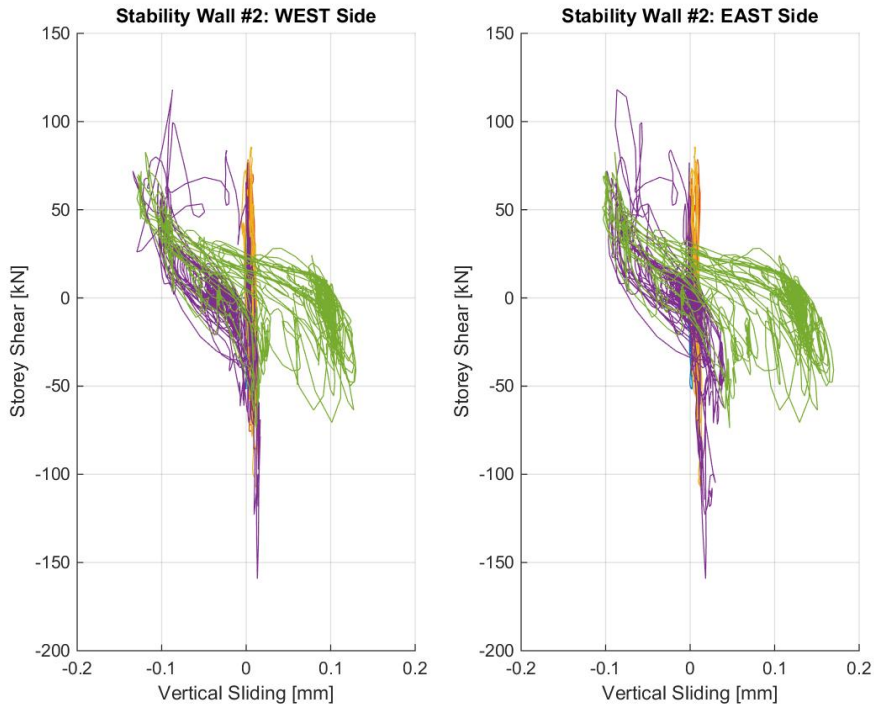
Figure 254. Vertical sliding of second-storey stability wall – West and East sides.
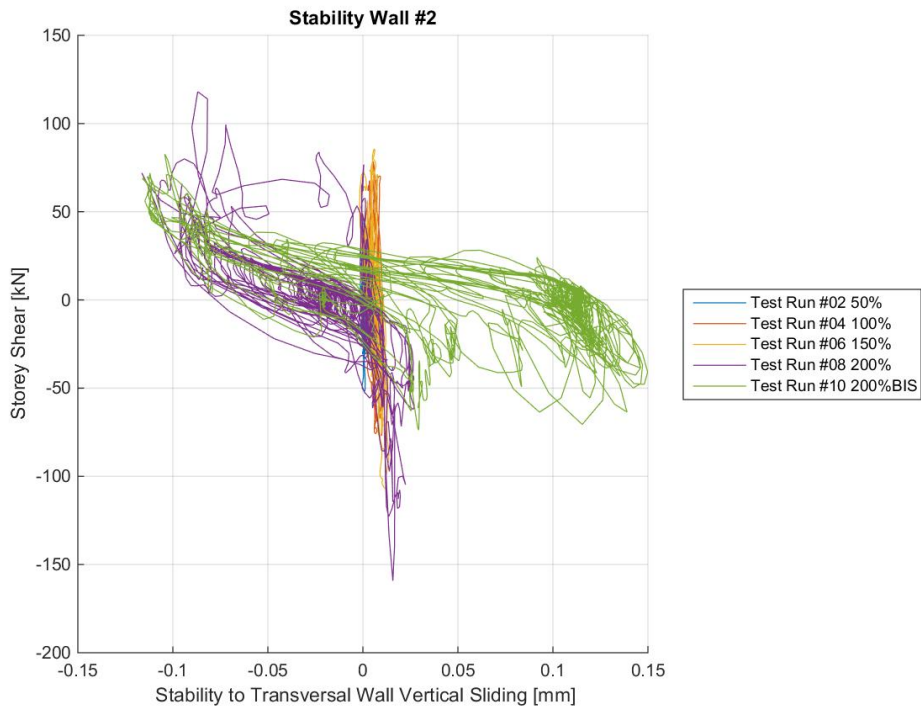
Figure 255. Vertical sliding of second-storey stability wall – Average of West and East sides.

For what concerns vertical sliding, it can be seen from both Figure 250 and Figure 251 that peaks of up to 2 mm were obtained between the stability and transversal walls at the first storey, before Test run #10, confirming that sliding was almost negligible, before any type/sort of damage took place in the three-way panel-to-panel joints. By contrast, values slightly lower than 2 cm were found during the last test run because the stability and transversal walls got completely disconnected after failure of their steel connectors. As far as the second-storey stability wall is concerned, it can be noted that sliding was clearly negligible because no damage occurred in the steel connectors. As evidenced by Figure 254 and Figure 255, sliding was less than 0.2 mm on average, and very similar values can be found whether displacement transducers on the East and West sides are considered separately.

6.5 Damage pattern evolution

In what follows, the primary observations collected during the detailed surveys undertaken at the end of each test run of interest are presented and discussed. A separate sub-section per each run was prepared to show a photographic sequence of damage patterns/mechanisms and to comment on them in a synthetic and systematic manner.

Note that no observations are reported for test runs carried out before Test run #04, given that EUC-BUILD5 specimen did not exhibit cracking or damage of any sort. Moreover, it is worth specifying also that the structure was obviously not inspected after test runs for controller compensations.. Interested readers should refer to Section 6.6 for a general overview of the building response evolution and/or Appendix A for details regarding test runs for compensation of controllers as well as information on their influence.

6.5.1 Observed damage after Test run #4 – SF = 100% (max storey drift of 0.05% measured)

The first sign of damage that affected EUC-BUILD5 specimen was observed at the end of Test run #4, for which intensity (i.e. 100% input motion) partial cracks of minor importance formed close to the first-storey and second-storey walls. A few photos are collected hereafter (Figure 256 to Figure 265) to show detailed views of a partial flexural crack that developed horizontally at the base of the ground-floor stability wall. This crack, running from the edge to the centre of the first-storey stability wall, was found to form on the East and West faces of the precast-wall panel, as can be observed in Figure 256 to Figure 261.

In addition, a few cracks developed in the concrete topping close to the North corner of the second-storey stability wall. As shown for the ground-floor stability wall, the cracks formed on the two wall faces, albeit it becomes clear, from Figure 262 to Figure 265, that cracks of this type are reported in this section only for the sake of completeness.

As expected, the first-storey stability wall resulted to be more damaged than the second-storey one, but it can be concluded that the crack patterns shown in Figure 256 to Figure 265 agree with the fairly elastic response curves presented in Figure 240.

A maximum storey drift of about 0.05% was measured during this test run, which lays evident the fact that the specimen is still responding elastically.

Figure 256. Development of cracks at the base of the ground-floor stability wall.

Figure 257. Crack pattern at the base of the first-floor stability wall – Edge of the wall.

Figure 258. Detail of crack at the base of the first-storey stability wall – Centre of the wall panel.

Figure 259. Crack running from the edge to the centre of the first-storey stability wall – Wall base.

Figure 260. Crack running from the edge to the centre of the first-storey stability wall – East wall face.

Figure 261. Detail of the crack at the base of the East face of the first-storey stability wall – South side.

Figure 262. Minor cracks in the concrete topping close to the North edge of the second-storey stability wall.

Figure 263. Crack running from the centre of the second-storey stability wall – West wall face.

Figure 264. Crack running from the North edge of the second-storey stability wall – West wall face.

Figure 265. Cracks developed at the base of the second-storey stability wall – West wall face, North edge.

6.5.2 Observed damage after Test run #6 – SF = 150% (max storey drift of 0.16% measured)

At an intensity of 150% (i.e. Test run #06), the specimen started to show some damage of relevance at the base of first-storey stability wall and in the three-way connections between the latter element and the counterpart transversal walls. As far as this latter occurrence is concerned, damage appeared in the form of cracks along the boundaries of the connectors sockets. It is worth noting that all four three-way panel joints of the first storey presented crack patterns of a very similar type. Moreover, a vertical crack opened up in the three-way connection between the stability and transversal walls and ran along the height of the first-storey stability wall, from its base to the top.

As expected and also mentioned earlier, the partial horizontal cracks that had developed during Test run #04 were found to propagate, now running along the entire depth of the ground-floor stability wall.

Other horizontal flexural cracks formed partially at the base of the first-storey and second-storey transversal walls on the North and South sides of the building because of their out-of-plane rocking mechanism.

The last form of damage that was surveyed at the end of Test run #06 consists of widespread multiple cracks in the top two two-way connections between the ground-floor transversal walls on the North side of EUC-BUILD5 specimen.

Below (Figure 266 to Figure 293), a series of photos presenting the forms/types of damage patterns described above is provided, with a view to detail the building damage evolution at this stage of the testing sequence.

The two photos shown in Figure 266 and Figure 267 illustrate the development of flexural cracks at the base of the North-sided second-storey transversal walls, whereas Figure 268 presents an overall view of crack pattern of the ground-floor stability wall, showing damage at the wall base and in the connectors sockets.

As can be gathered from Figure 269 to Figure 275, the horizontal crack formed at the base of the wall runs along the entire depth and joins another vertical one at the South corner of the panel. Details of such a full-height crack are reported in Figure 270 to Figure 275, which also feature the nature and type of cracks that formed along the boundaries of the connectors sockets. In Figure 276 to Figure 282, interested readers may find similar damage patterns that developed on the opposite wall face (i.e. East wall face).

Finally, Figure 283 to Figure 293 depict the observations of damage that propagated in the transversal walls at the first and second storeys of the test specimen. Of relevance amongst them are the ones showing the above-mentioned widespread cracking in the mortar of the two-way panel joints (i.e. Figure 288 to Figure 292).

Figure 266. Development of flexural cracks at the base of the North-sided second-storey transversal walls.

Figure 267. Crack running from the centre of the second-storey stability wall – East wall face.

Figure 268. Crack pattern of the ground-floor stability wall – Wall base and connectors sockets.

Figure 269. Propagation of horizontal crack along the depth of the ground-floor stability wall – Wall base.

Figure 270. Crack running along the entire depth of the ground-floor stability wall – Wall base.

Figure 271. Vertical crack along the height of the first-storey stability wall – South edge.
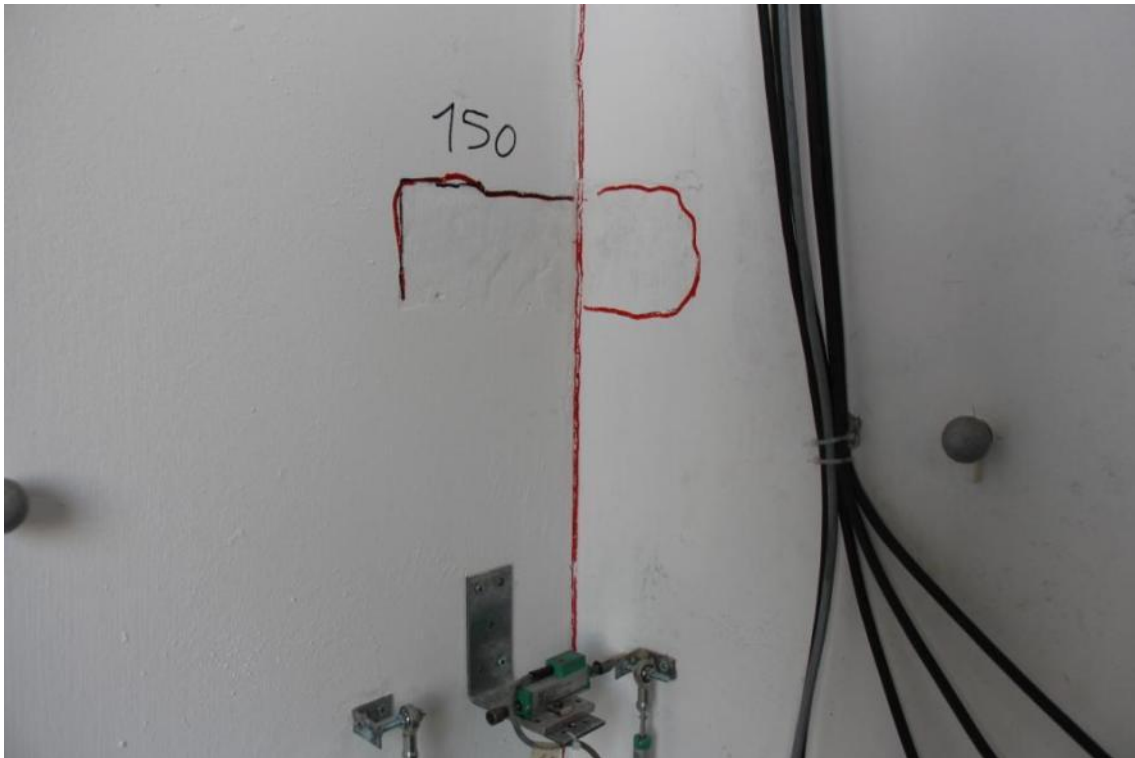
Figure 272. Cracks along the boundaries of the connectors sockets – Detail of the bottom three-way joint.

Figure 273. Development of cracks along the boundaries of the connectors sockets.
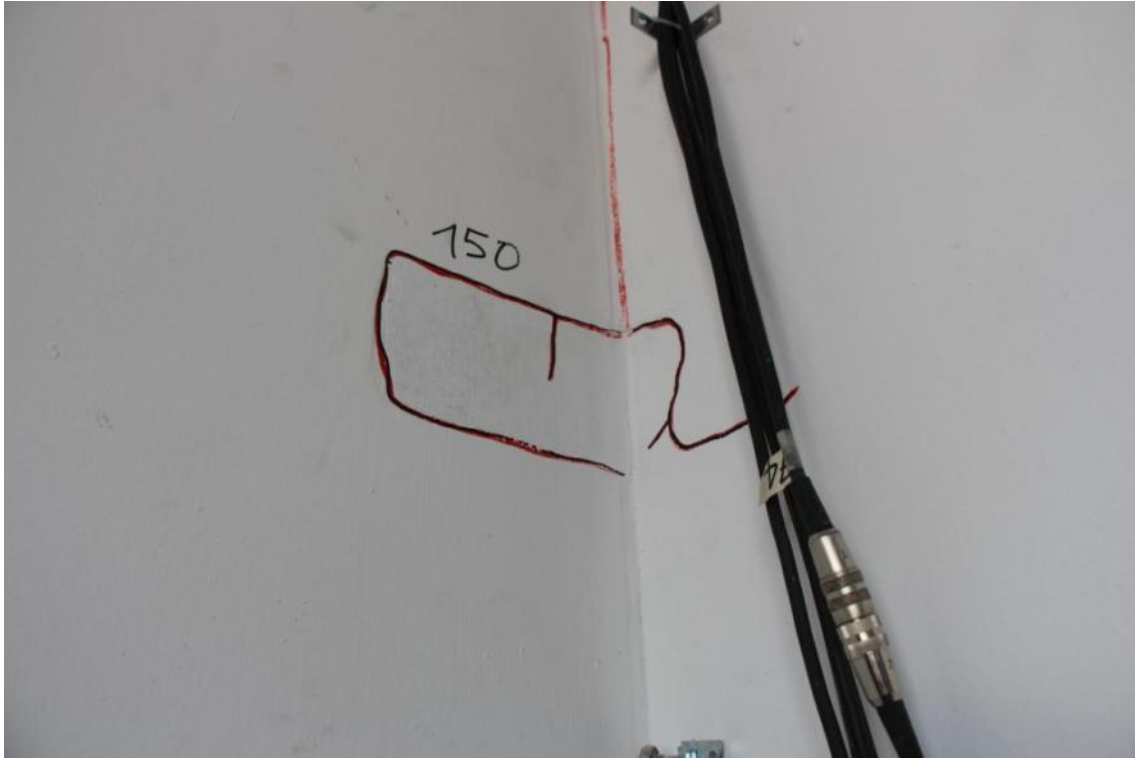
Figure 274. Cracks along the boundaries of the connectors sockets – Stability wall, West face, first storey.
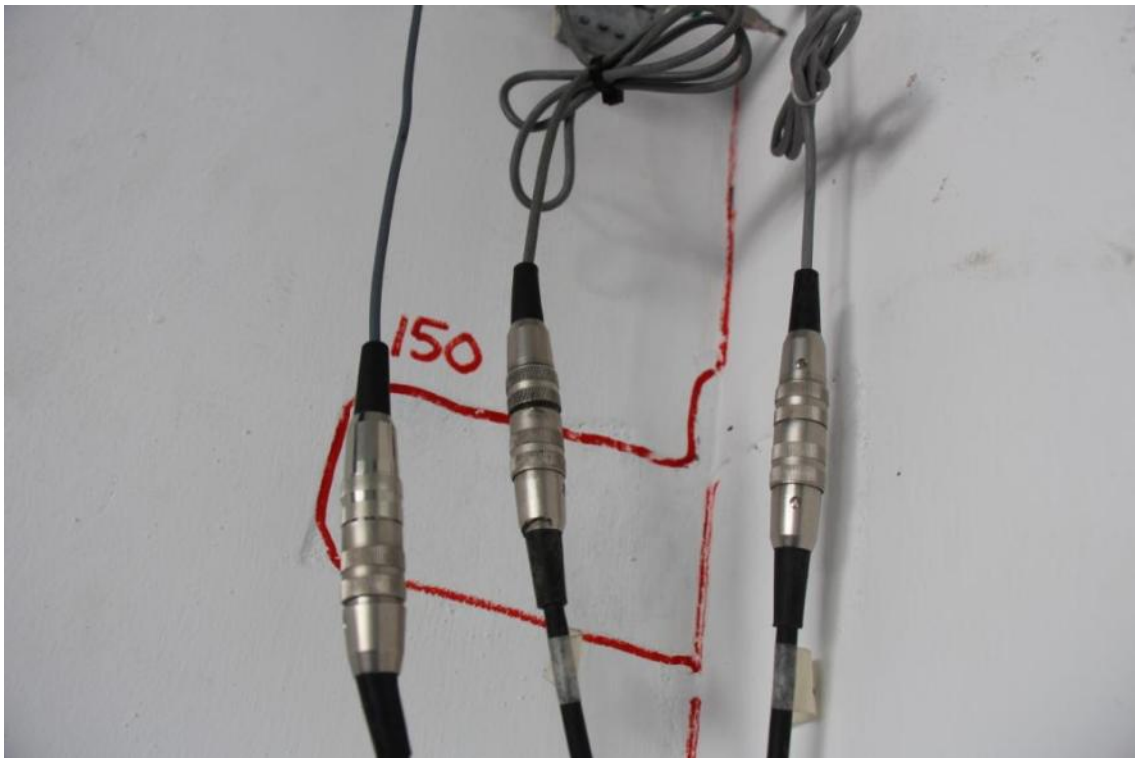
Figure 275. Cracks along the boundaries of the connectors sockets – Detail of the top three-way joint.

Figure 276. Crack pattern of the ground-floor stability wall – East wall face, base and connectors sockets.

Figure 277. Crack running along the entire depth of the ground-floor stability wall – East wall face, base.

Figure 278. Vertical crack and detachment between stability and transversal walls – East wall face.
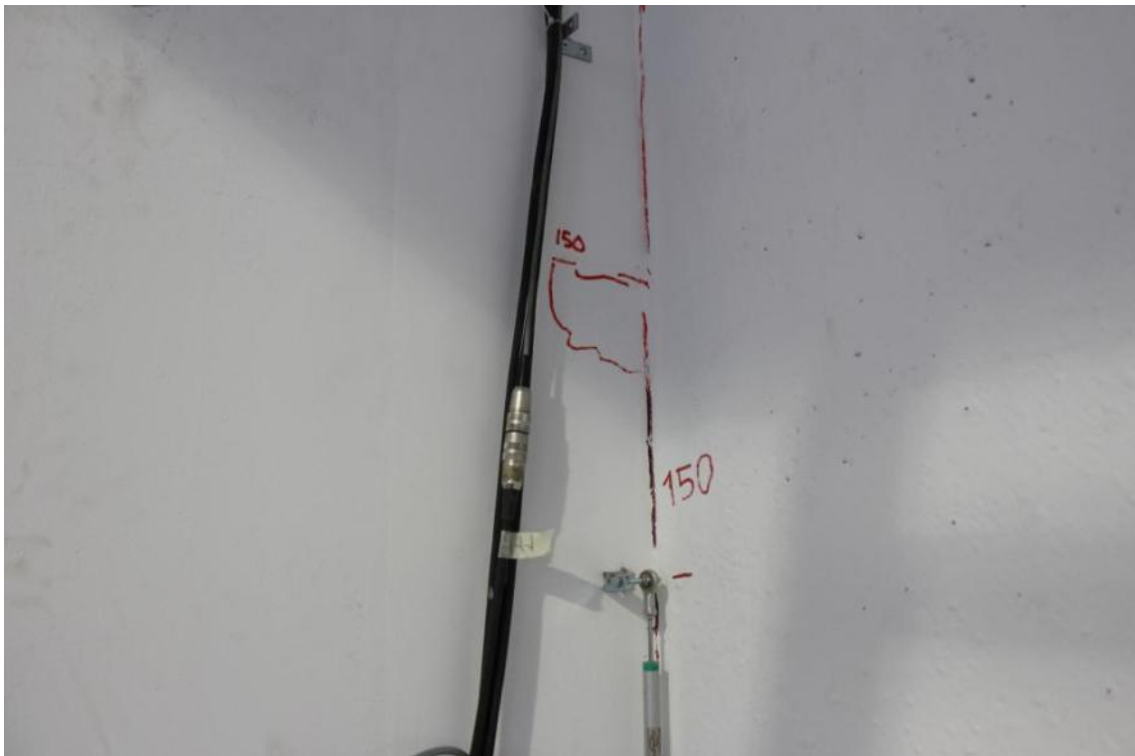
Figure 279. Propagation of a wide crack along the height of the first-storey stability wall – East wall face.
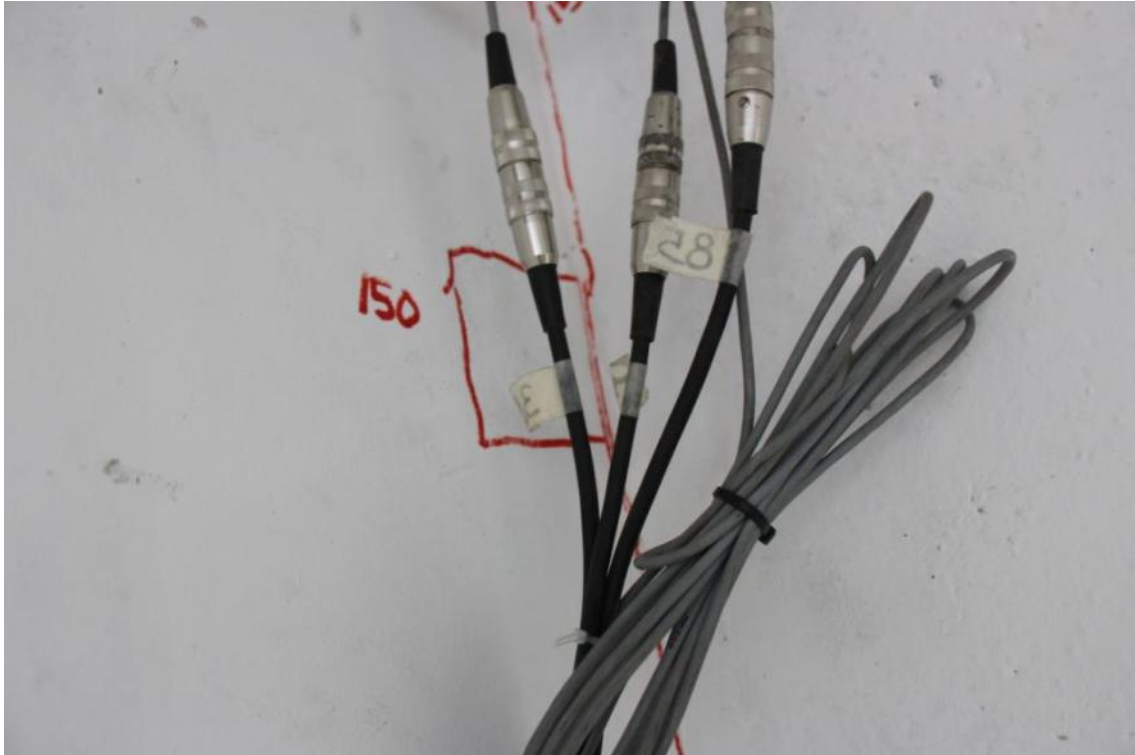
Figure 280. Cracks along the boundaries of the connectors sockets – Top three-way joint, panel.
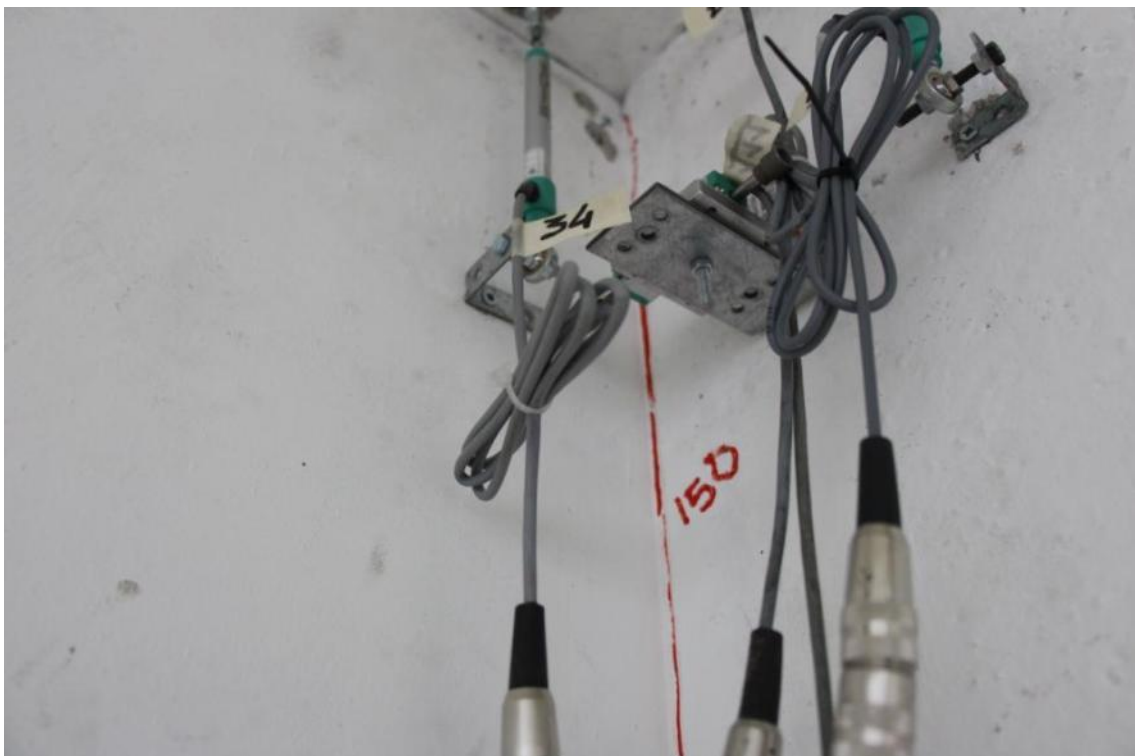
Figure 281. Vertical crack along the entire height of the ground-floor stability wall – East wall face.

Figure 282. Crack pattern of three-way joints – East and West faces of the ground-floor stability wall.

Figure 283. Formation of a new crack at the base of transversal walls – Panel 1L1, South-East side.
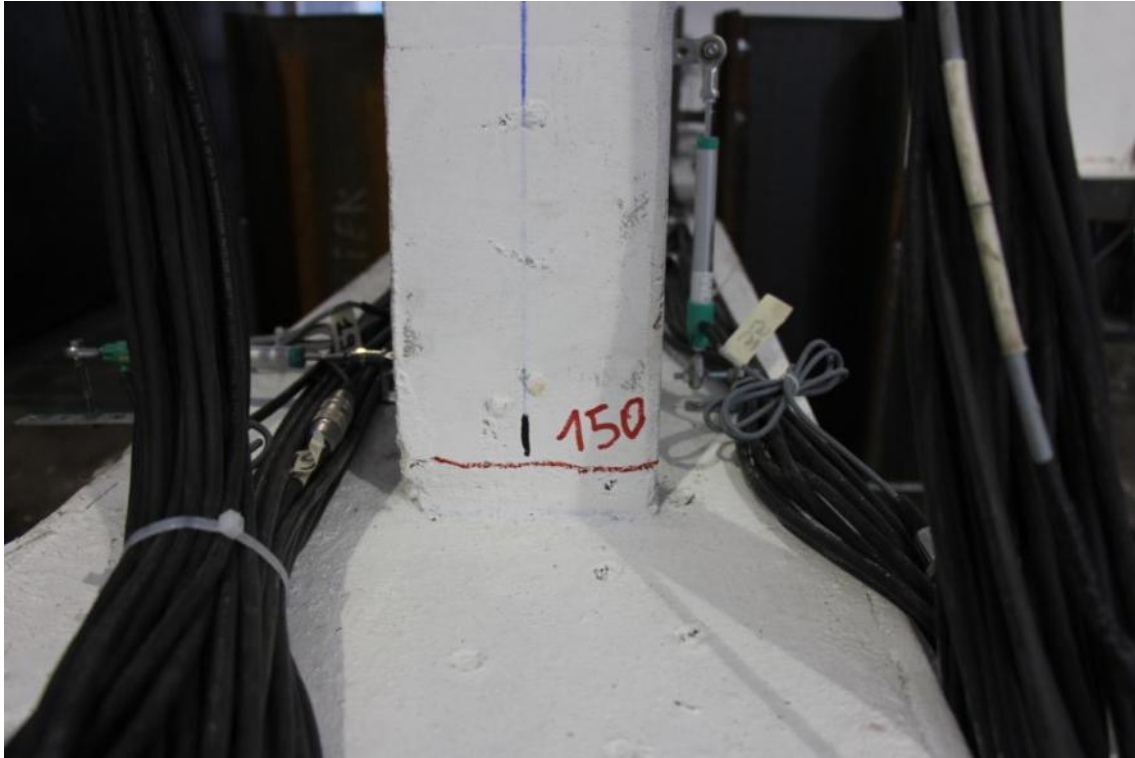
Figure 284. Detail of horizontal crack running through the entire width of transversal wall 1L1.

Figure 285. Development of horizontal flexural cracks at the base of panel 2L1 – Second-storey lateral wall.
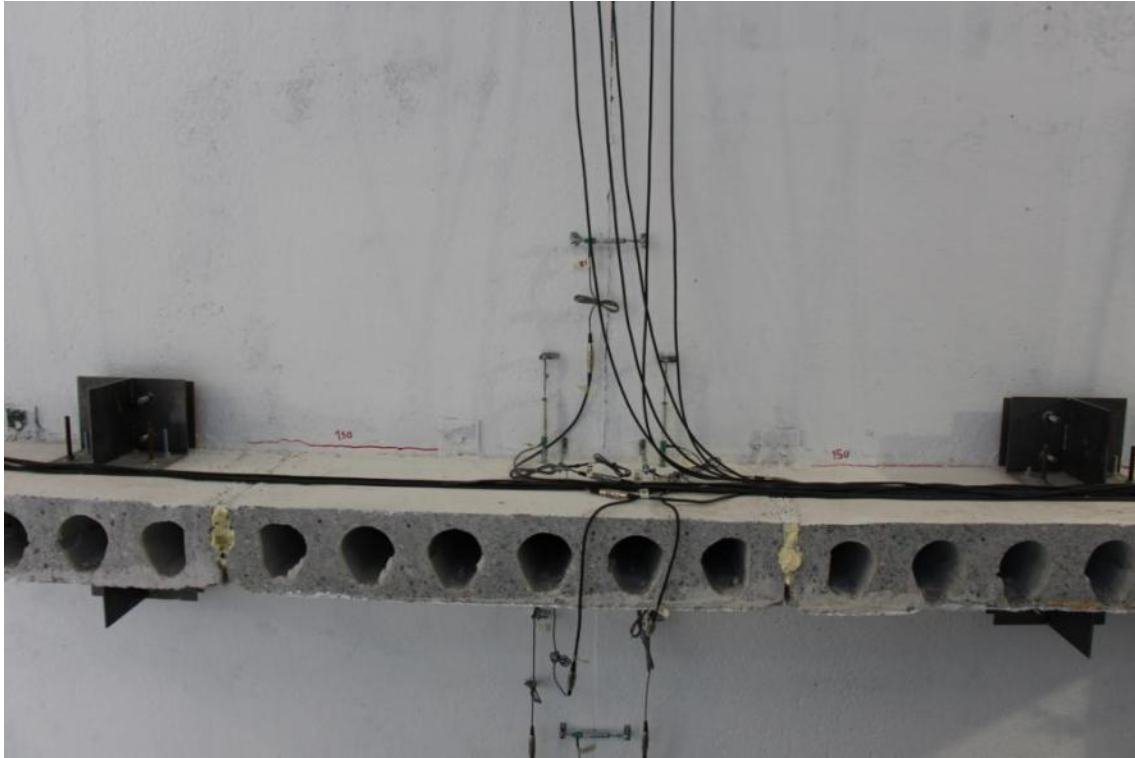
Figure 286. Horizontal flexural cracks at the base of the South-sided second-storey transversal walls.

Figure 287. Development of horizontal flexural cracks at the base of panel 2L2 – Second-storey lateral wall.

Figure 288. Cracks along the boundaries of the connectors sockets – North-sided ground-floor lateral walls.
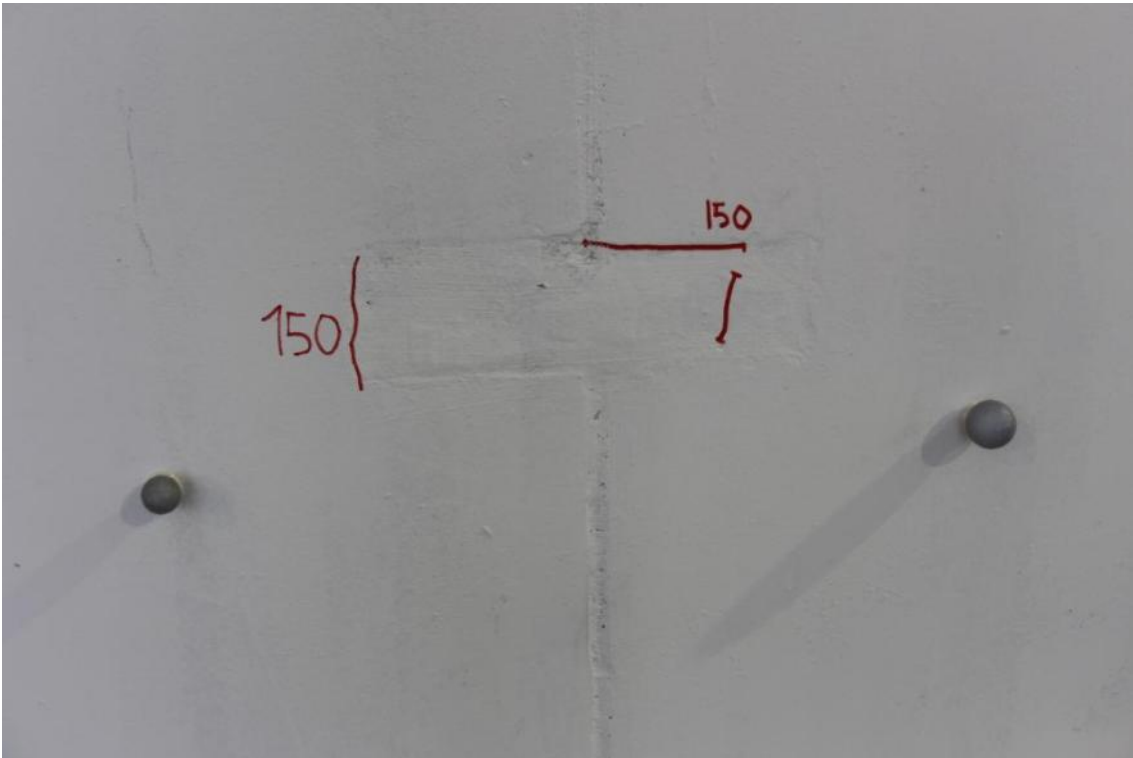
Figure 289. Cracks along the boundaries of the connectors sockets – Bottom two-way connection.
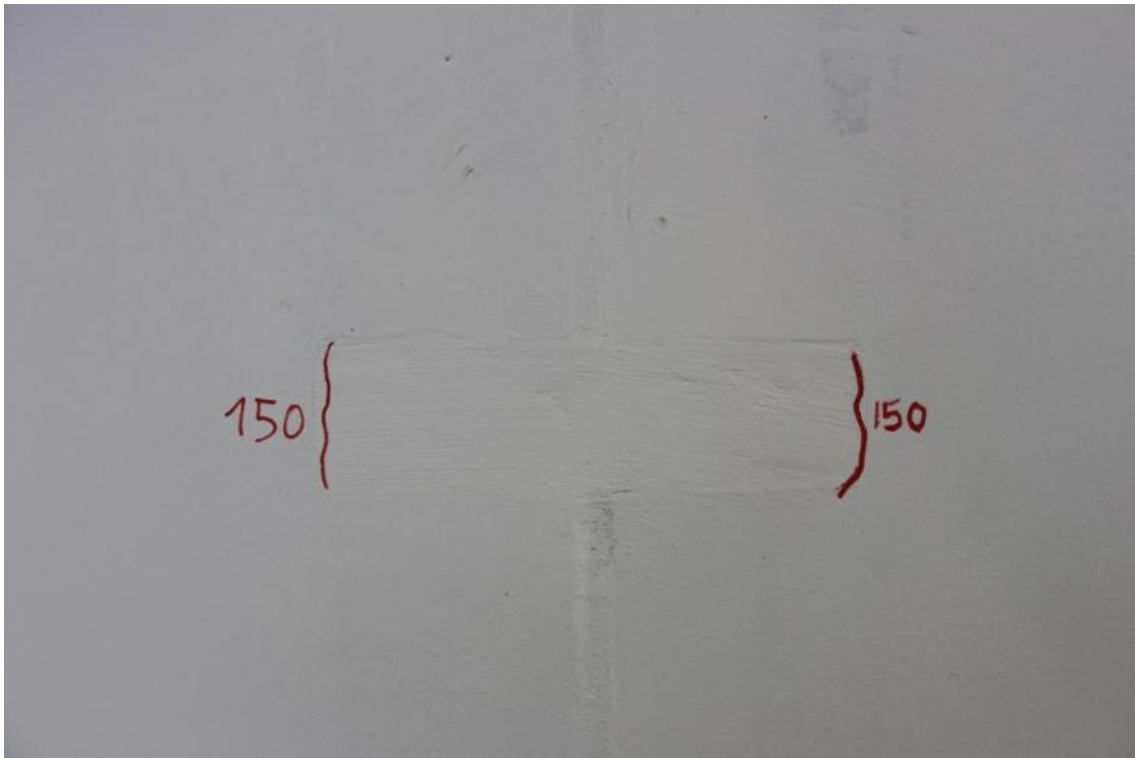
Figure 290. Cracks along the boundaries of the two-way connection – Second joint from the base.
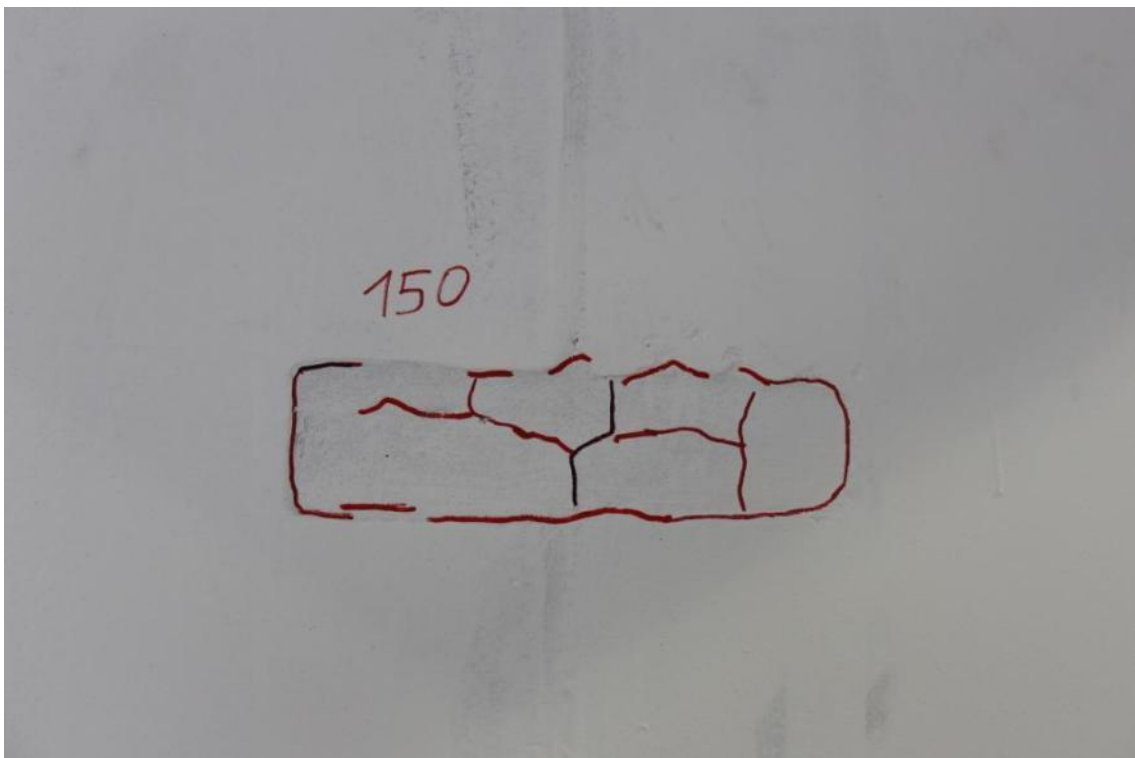
Figure 291. Cracks along the boundaries of the two-way connection – Third joint from the base.
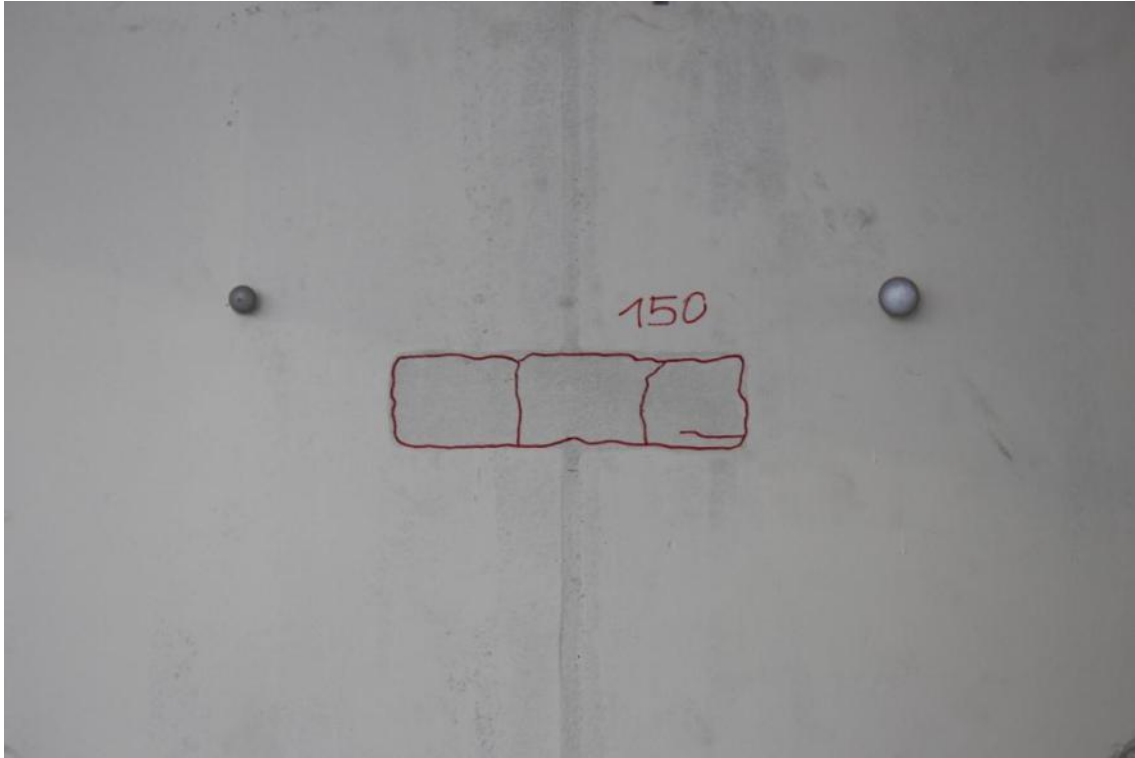
Figure 292. Detail of cracks along the boundaries of the connectors sockets – Top two-way connection.
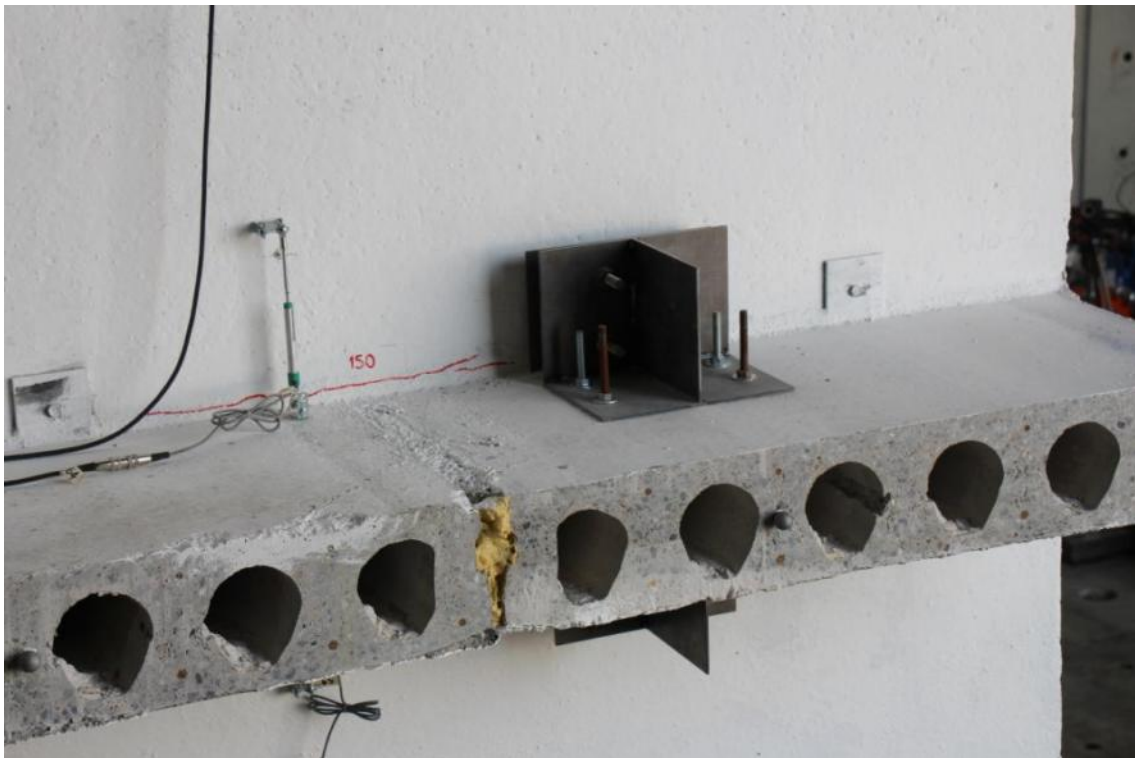
Figure 293. Horizontal flexural cracks at the base of the North-sided second-storey transversal walls.

6.5.3 Observed damage after Test run #8 – SF = 200% (max storey drift of 0.53% measured)

The first 200% input motion was observed to cause more severe damage than what had been shown and analysed in Sections 6.5.1 and 6.5.2. At this intensity level (i.e. 200%, Test run #08) noticeable damage was observed, with cracking spreading all over the specimen, as triggered by the sliding of both transversal and stability walls. Permanent displacements of 1 cm were reached in key parts of the specimen, as more comprehensively discussed in what follows.

Figure 294 to Figure 316 present a photographic sequence that provides the reader with a clear view of the main damage patterns surveyed at the end of Test run #08. In particular, Figure 294 to Figure 297 show the details of the damage patterns of the ground-floor stability wall at the base and top of it, as well as in correspondence to the four three-way connections between this and the South-sided lateral walls. A full-depth/full-width horizontal crack was seen spreading at the base of the stability wall and also at the base of the transverse walls. One of the two ground-floor ones presents also an inclined crack running from the base of the panel to one of the four connectors socket.

As reaffirmed by Figure 298 to Figure 301, the South-sided ground-floor lateral walls were heavily damaged and presented a full-height vertical crack on their South face, at the wall-to-wall interface. Furthermore, Figure 302 to Figure 305 show different views of the full-depth/full-width crack at the base of the first-storey stability wall, and also point out how the damage patterns of the panel joints propagated on both wall sides.

Test run #08 has also highlighted that the accumulation of damage in the wet joints implies sliding of the slabs on the precast walls underneath them (see Figure 306 to Figure 314). As a result of this, non-negligible permanent displacement were reached in key parts of the specimen at both first and second floor levels.

Finally, Figure 315 and Figure 316 provide enlarged and very detailed views of the damage pattern of the top and bottom three-way joints at the end of Test run #08. More in detail, Figure 316 shows the gap opening between the stability and transverse ground-floor walls and may thus provide a very clear picture of the state of EUC-BUILD5 specimen at the end of Test run #08.

For the sake of completeness, it is recalled here that, during this test run, the building experienced a maximum storey drift slightly larger than 0.5%, accumulating a residual (storey drift) slightly lower than 0.4%.

Figure 294. Crack pattern of the ground-floor stability wall – Enlarged view and detail of three-way joints.
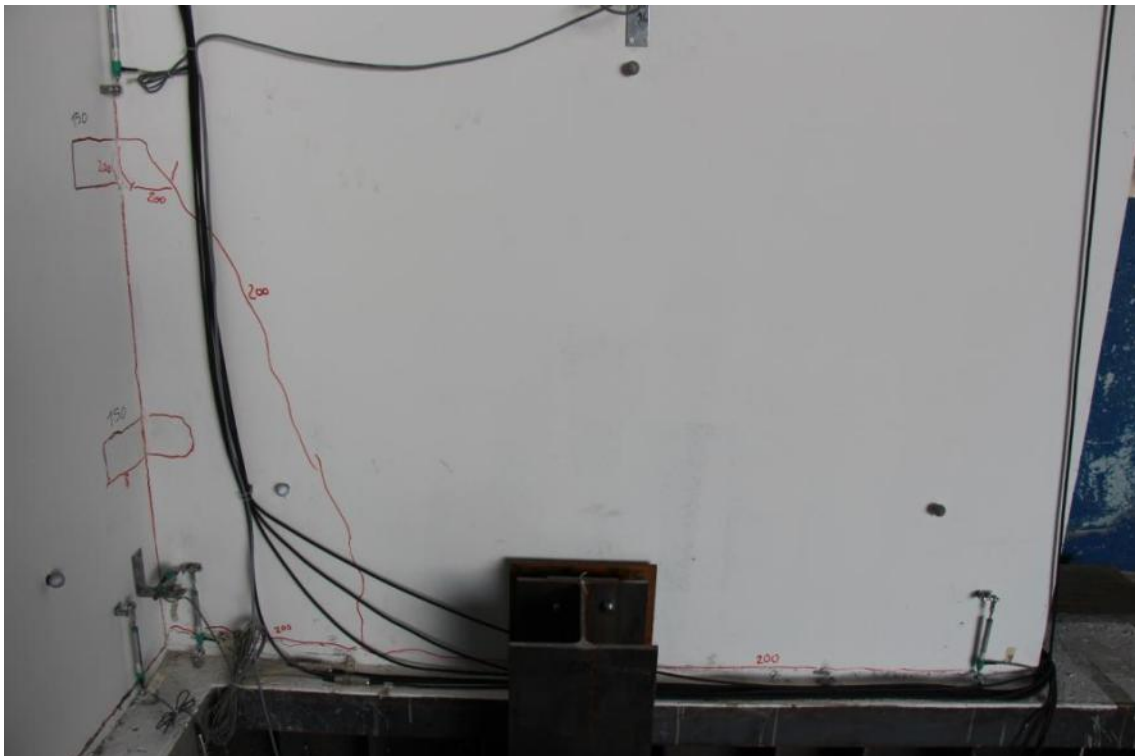
Figure 295. Inclined and full-depth/full-width/base horizontal crack in the lateral wall 1L2.

Figure 296. Damage pattern of the mortar joint between the ground-floor stability wall and the slab panel.

Figure 297. Full-depth/full-width horizontal crack at the base of the first-storey stability wall.

Figure 298. Full-depth/full-width horizontal crack at the base of the first-storey lateral wall 1L2.
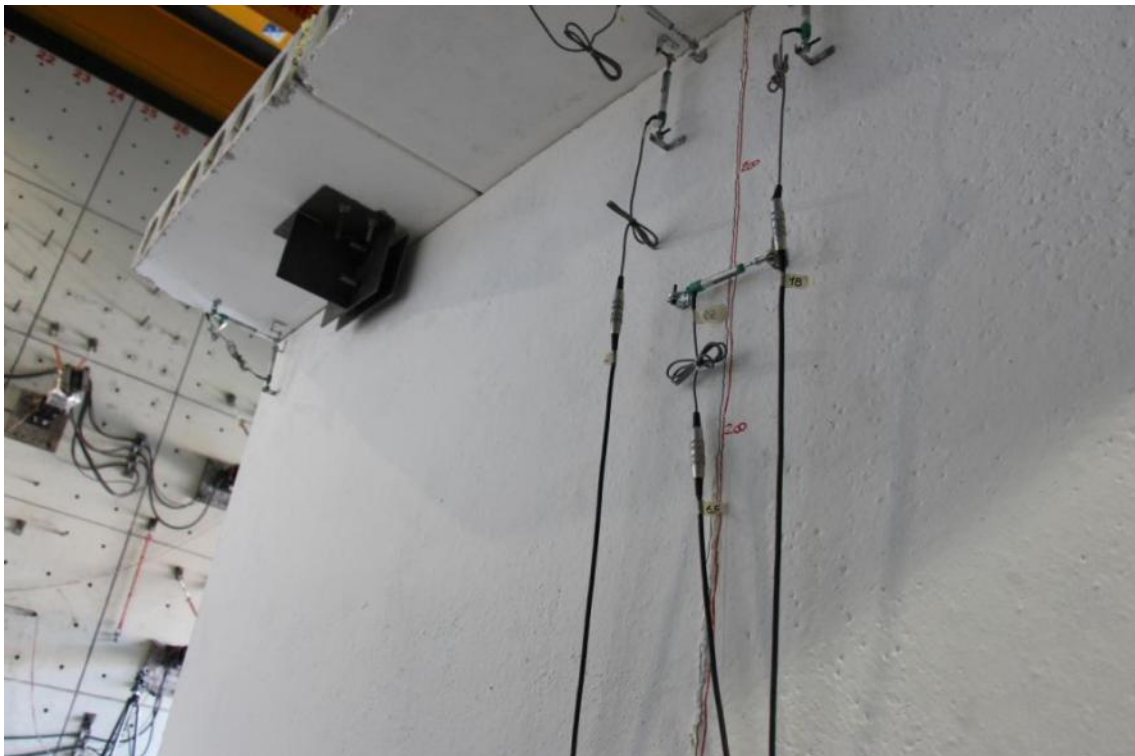
Figure 299. Development of a full-height vertical crack between adjacent lateral walls – South side, South face.

Figure 300. Damage pattern at the base of the South-sided ground-floor lateral walls.

Figure 301. Full-depth/full-width horizontal crack at the base of the first-storey lateral wall 1L1.

Figure 302. Extensive damage of the top three-way joint – East face of the first-storey stability wall.
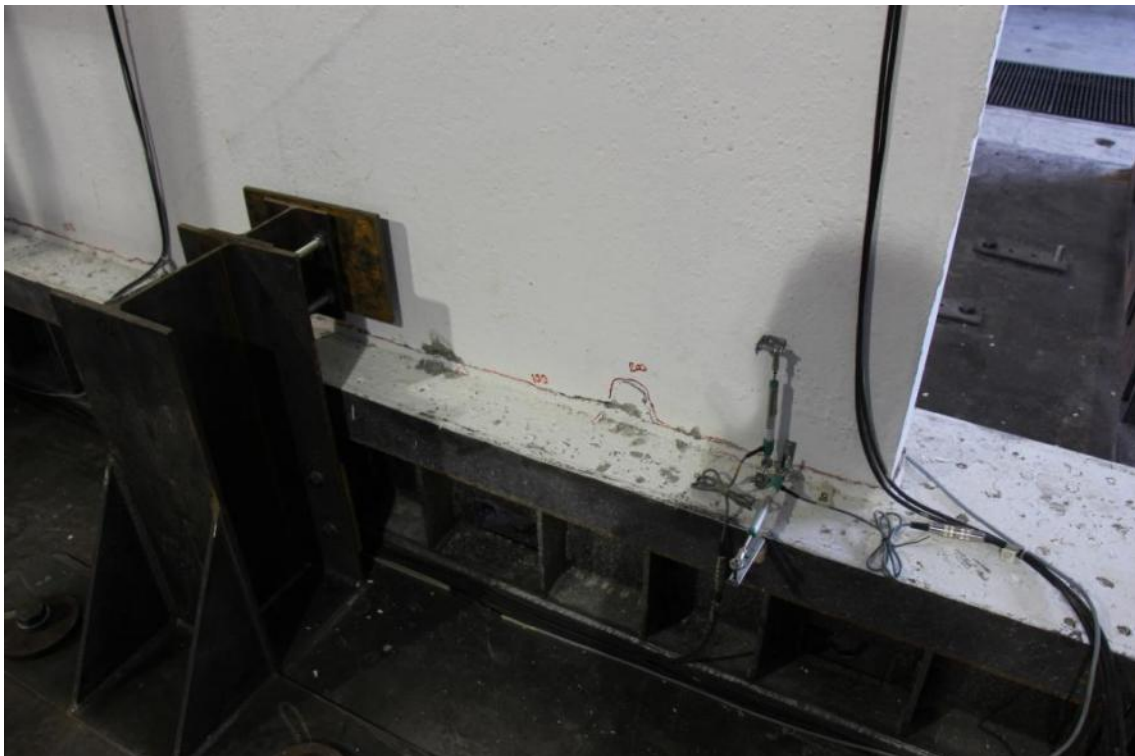
Figure 303. Full-depth/full-width crack at the base of the first-storey stability wall – East wall face.

Figure 304. Crack running through the entire width of the first-storey stability wall – Corner, front view.

Figure 305. Crack running through the entire width of the first-storey stability wall – Corner, side view.

Figure 306. Concrete damage/chipping at the top of the first-storey lateral wall 1L2.

Figure 307. Sliding and accumulation of displacement residuals – Second-storey floor slab, North side.

Figure 308. Sliding and accumulation of displacement residuals – Second-storey floor slab, South side.

Figure 309. Damage pattern of the mortar joint between the second-storey stability wall and slab.
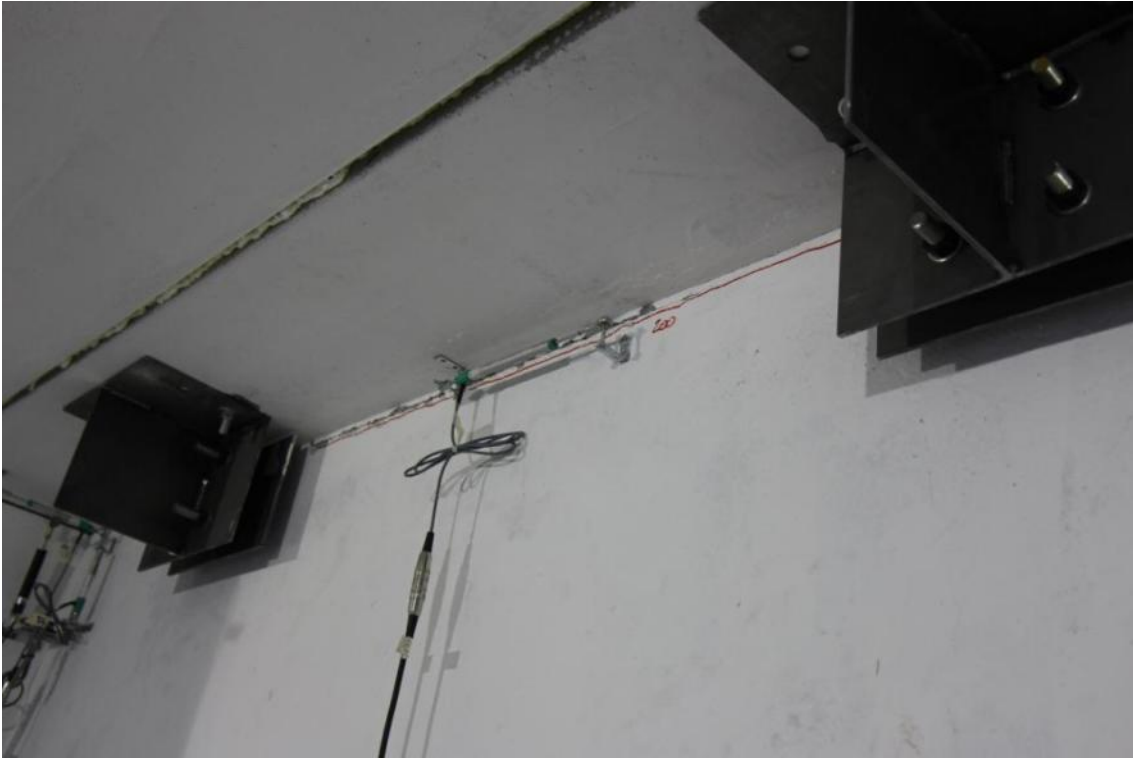
Figure 310. Full-depth crack of mortar joint between the second-storey stability wall and slab.

Figure 311. Full-depth/full-width crack of mortar joint between the second-storey stability wall and slab.

Figure 312. Damage of the mortar joint beneath the second-storey slab and accumulation of displacements.
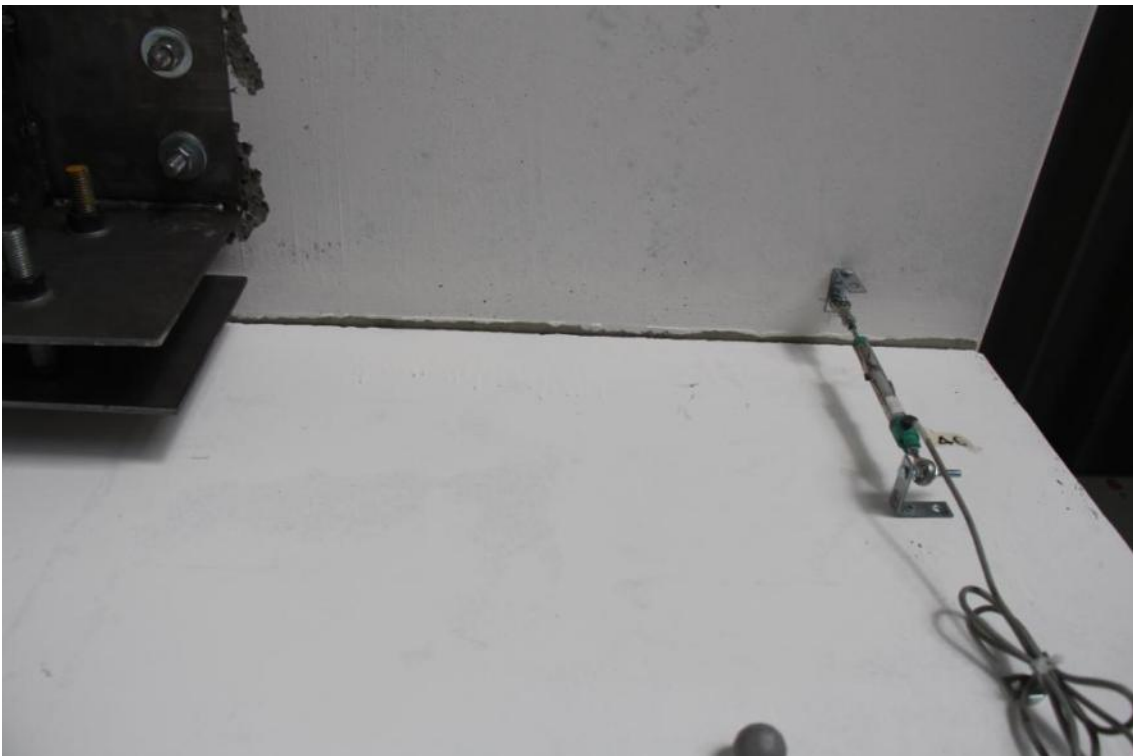
Figure 313. Sliding of second-storey slab and accumulation of displacements – Detail of a lateral wall.

Figure 314. Development of a full-height vertical crack between adjacent lateral walls – North side.

Figure 315. Damage pattern of top and bottom three-way joints at the end of Test run #8.

Figure 316. Damage in the top panel joint and gap opening between stability and lateral walls – West face.

6.5.4 Observed damage after Test run #10 – SF = 200% (max storey drift of 5.17% measured)

After careful visual inspections of the structure and analysis of the full dataset of previous test runs, a decision was taken to subject specimen EUC-BUILD5 to a last test run, at the same intensity that had been used for Test run #08 (200%).

As previously discussed when inspecting the response curves, the structure started collapsing right after the first few cycles of loading, rapidly loosing shear capacity and accumulating a significant 14 cm of permanent displacement.

Photos of the building were taken in the first minutes after the test, in parallel with its equally immediate propping-up, deemed urgent in face of what appeared to be a very precarious stability of the structure. The outcome of the visual inspections is illustrated through Figure 317 to Figure 339, which depict well the (battered) state of the specimen after the test.

Firstly, Figure 317 shows the deformed shape of the specimen at the end of dynamic testing and gives account of the exaggerated levels of deformation that were reached during the last test run. In Figure 318, an enlarged view of the accumulated permanent displacements is also provided so as to portray even more clearly how close to collapse the building appeared at the end of the second input motion at 200% intensity.

As can be observed e.g. in Figure 337 to Figure 339, the three-way panel joints failed abruptly because of a severe and sudden permanent bending of the steel connectors embedded in the niches of both stability and transversal walls. The gap that had already developed during Test run #08 was shown to widen conspicuously, which implies that the lateral walls lost uprightness rapidly and that displacement residuals accumulated accordingly.

Details regarding the latter occurrence can be found in Figure 319 to Figure 323, which also present the full-depth/full-width crack at the base of the ground-floor stability wall and the damage patterns of the mortar joints between the stability walls and the slabs. Furthermore, Figure 325 to Figure 336 provide photos of both North-sided and South-sided transverse walls, showing the loss of verticality of the first-storey lateral walls and the sliding mechanism of the precast slabs on the second-storey wall-elements. Details concerning the propping-up operations are presented as well.

It is finally recalled that Figure 337 to Figure 339 shed light into the behaviour of permanently-bent steel connectors and completely-crushed connectors sockets. Although detailed views of all the four three-way panel connections are herein presented, interested readers may and should also consider the set of photos taken during the dismantling of EUC-BUILD5 specimen (see Chapter 7).

Figure 317. Deformed shape of EUC-BUILD5 specimen at the end of dynamic testing.

Figure 318. Loss of verticality and accumulation of residuals due to failure of bent three-way panel joints.

Figure 319. Accumulation of permanent displacements at the second storey of the test specimen.

Figure 320. Detail of damage pattern in the mortar joint beneath the second-storey slab – West-side view.

Figure 321. Sliding and concrete crushing at the base of the first-storey stability wall – West-side view.

Figure 322. Connection failure and damage pattern in the mortar joint beneath the first-storey slab.

Figure 323. Failure of bottom three-way joints damage pattern at the base of the stability wall.

Figure 324. Failure mechanism of three-way panel connections – Detail of permanently-bent steel connectors.

Figure 325. Damage at the base of lateral walls and rocking with loss of verticality – Detail of wall 1L2.

Figure 326. Damage at the base of lateral walls and rocking with loss of verticality – Detail of wall 1L4.

Figure 327. Overall and detailed views of the North-sided transversal walls at the end of testing.

Figure 328. Detailed views of the first-storey and second-storey slabs and North-sided lateral walls.

Figure 329. Overall and detailed views of the South-sided transversal walls at the end of testing.

Figure 330. North-sided ground-floor lateral walls at the end of testing – North and South wall faces.

Figure 331. Propping-up at the end of the last test run – North and South sides.
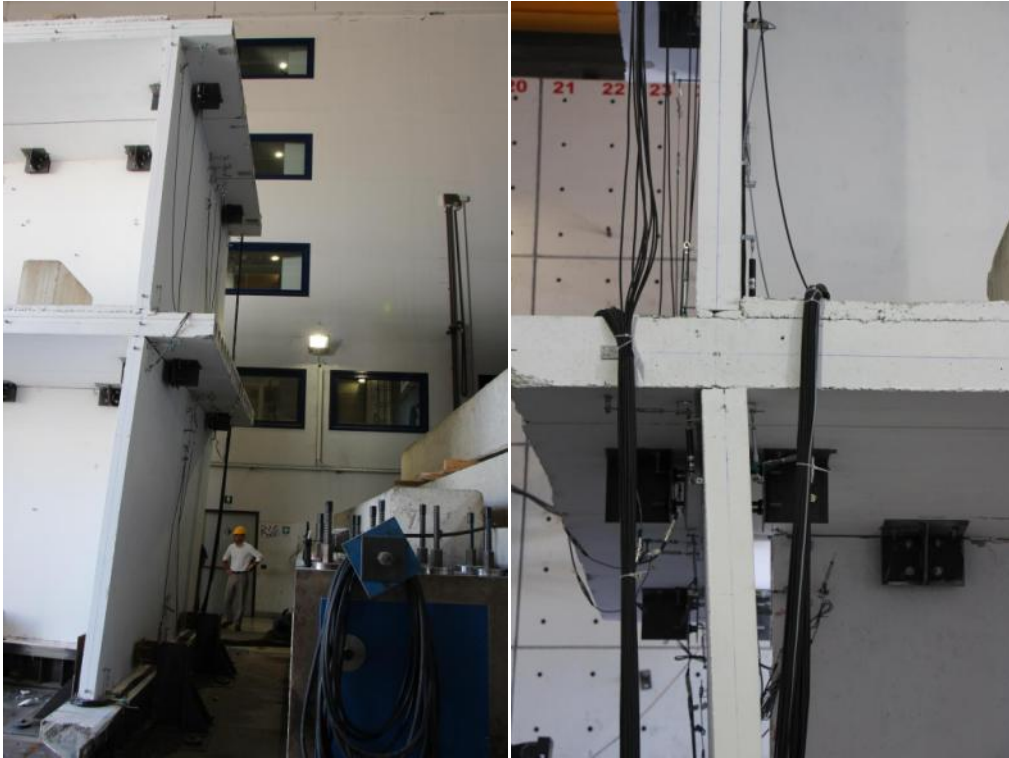
Figure 332. Loss of verticality and gap opening between stability and lateral walls – East and West sides.
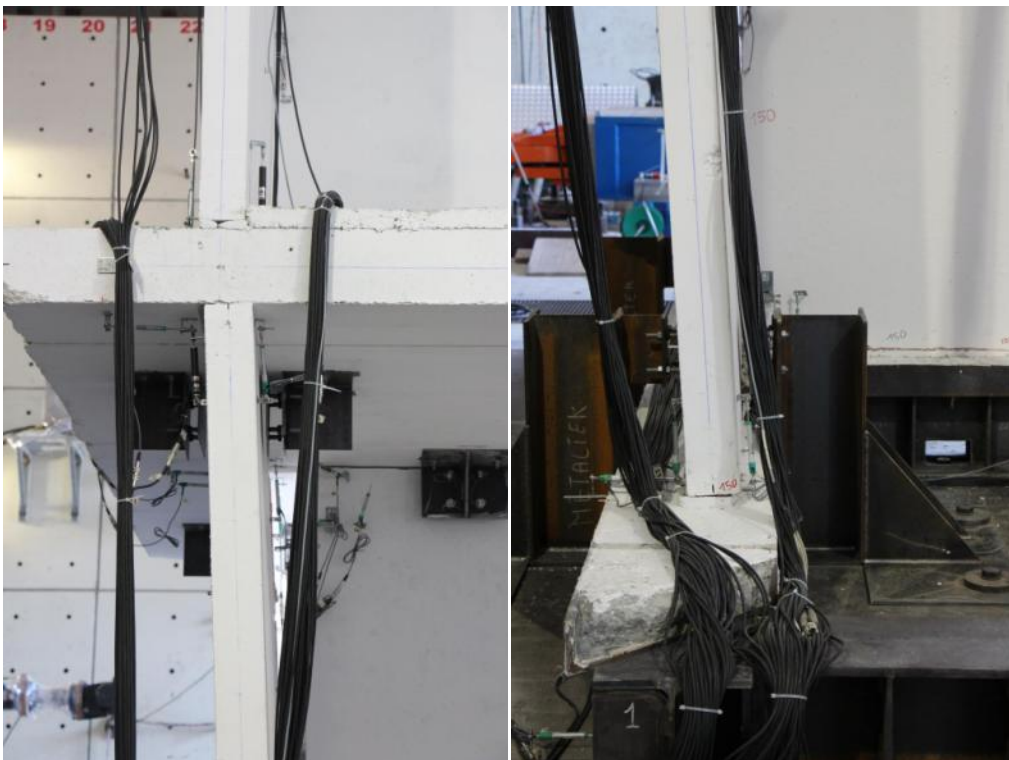
Figure 333. Transversal wall 1L1 at the end of testing – Detail of wall base and top of the wall.

Figure 334. Installation of props in face of the very precarious stability of the structure after the test.

Figure 335. Detail of concrete spalling/crushing at the top of lateral wall 1L2.

Figure 336. Sliding of second-storey slab on the precast wall – South side of the specimen.

Figure 337. Permanently-bent steel connectors in the top three-way panel joint.
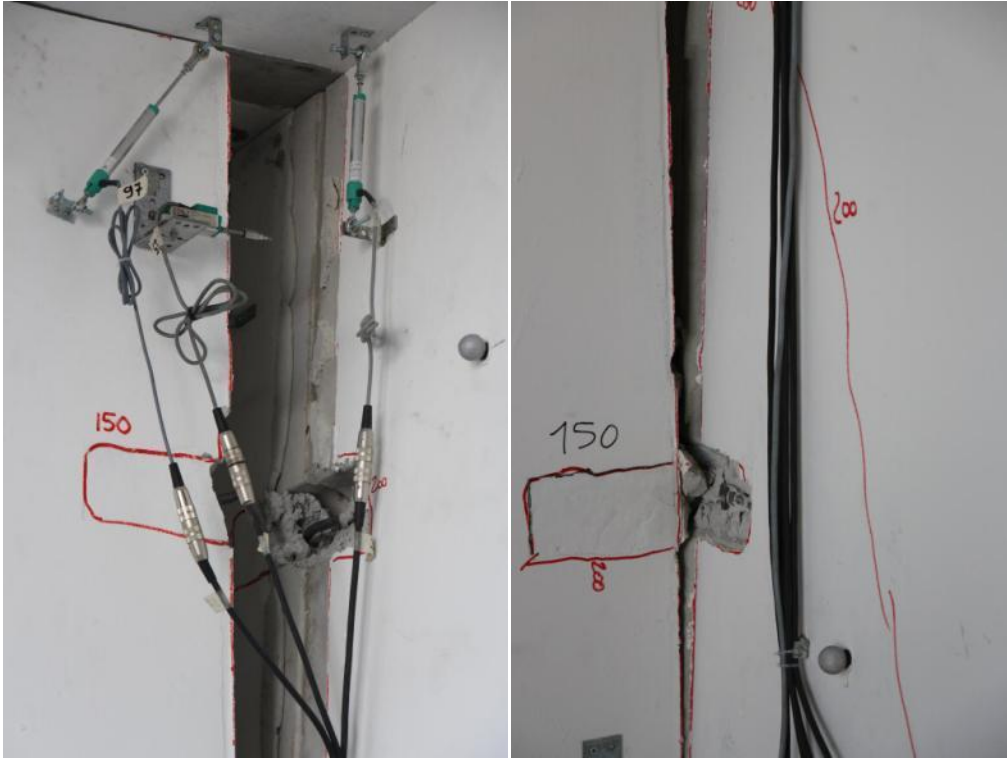
Figure 338. Damage/failure of the top and bottom three-way connections at the end of the last test run.
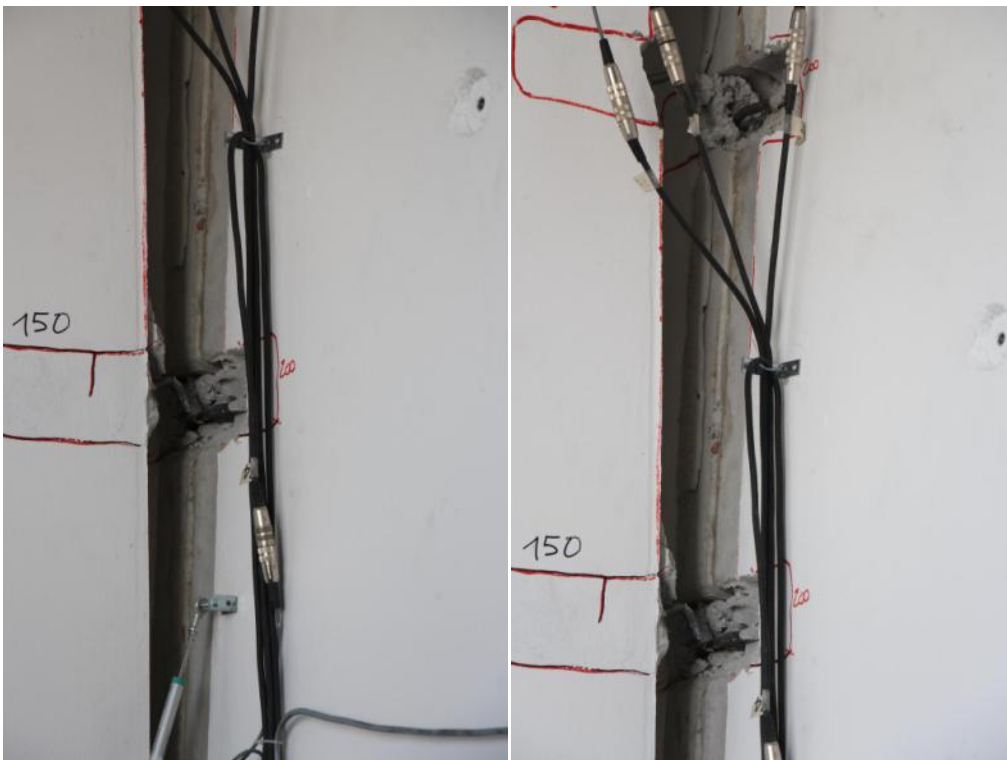
Figure 339. Damage/failure of the intermediate three-way connections at the end of the last test run.

6.6 Structural response evolution

In this section, incremental response plots of EUC-BUILD5 test are shown with a view to analyse the evolution of the structural response to the applied dynamic loading sequence (see Table 14). It is thus clear that, to this end, the testing sequence in its entirety has to be considered. In what follows, separate sub-sections, one per each test run of interest, were prepared to present the obtained results for all the ten test runs reported in Table 14, in a brief and systematic manner.

Contrary to the previously employed approach, test runs for controller compensation were explicitly included and treated here, as also conveyed by the outline of the section. The scope is twofold, since this approach permits one (i) to identify the response of the specimen throughout the actual dynamic sequence of loading undergone during the testing, and (ii) to evaluate the influence that runs carried out for purposes other than structural assessment-driven ones (i.e. more specifically, for compliancy with the experimental test framework adopted) had on the structural response itself.

The series of plots collected for each test run consists of (i) acceleration and displacement time-histories at key locations (i.e. the foundation and each one of the two storeys), (ii) acceleration floor spectra, (iii) hysteretic response curves of both the structure and its storeys separately, and (iv) incremental relationships concerning the evolution of dynamic properties. It is worth noting that, for the sake of completeness and transparency, information on the accuracy of the testing apparatus itself can also be found. The first plot of each section reports the acceleration feedback, as recorded by the shake-table controller, and the tenth plot of each section presents a comparison between the imposed and recorded base shear time-histories.

To lead to a readily interpretation of the results presented in what follows, it is worth recalling that odd-labelled test runs identify those for controller compensation, whilst the even-labelled ones are actually those of interest for structural response assessment purposes.

Lastly, it is also recalled that further information on test runs for controller compensation can be found in Appendix A. Deformed shapes and overall comparative plots such as those presented in Section 6.2 for the other runs can be observed there and can help understanding of the following test results.

6.6.1 Test run #1 – SF = 25% – Controller compensation

Figure 340 shows the comparison between the acceleration spectra from time-histories at reference and feedback (as recorded by the shake-table controller). The experimental acceleration time-history used for the spectrum comparison is the average of the recorded accelerations on the foundation of EUC-BUILD5 specimen (accelerometers #139 and #140). Furthermore, Figure 341 shows the discrepancy in percentage.
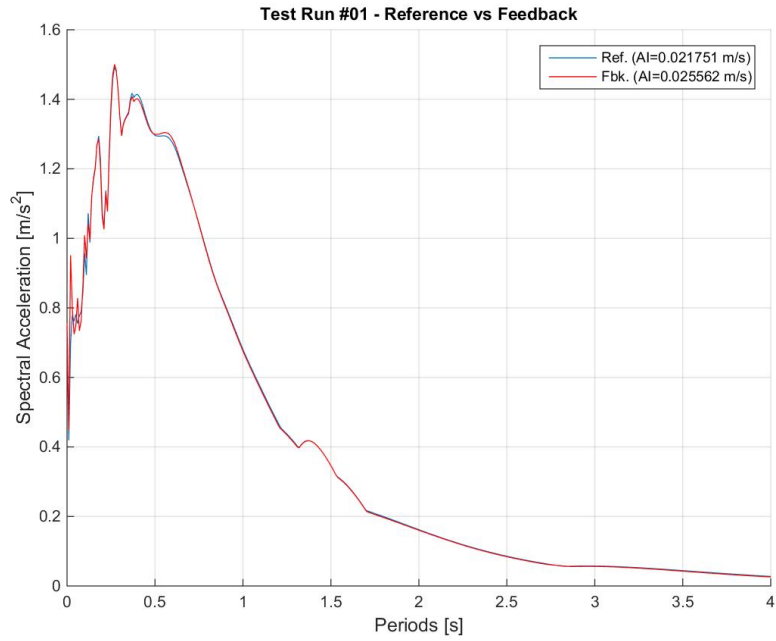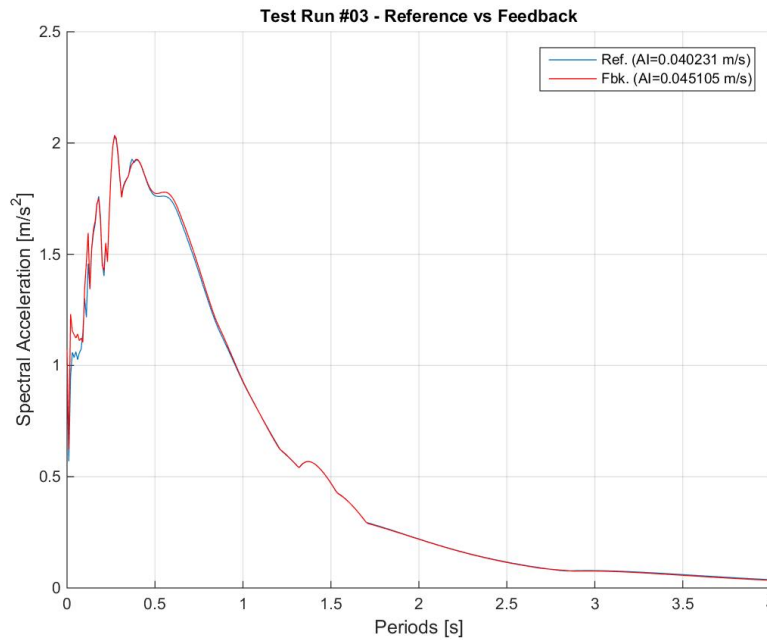
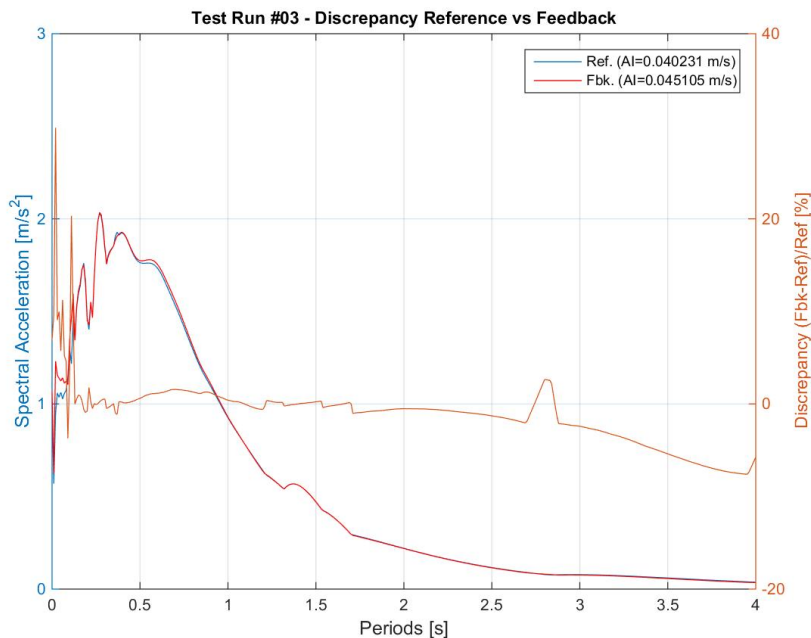**Figure 340. Comparison between acceleration spectra from time-histories at reference and feedback.**
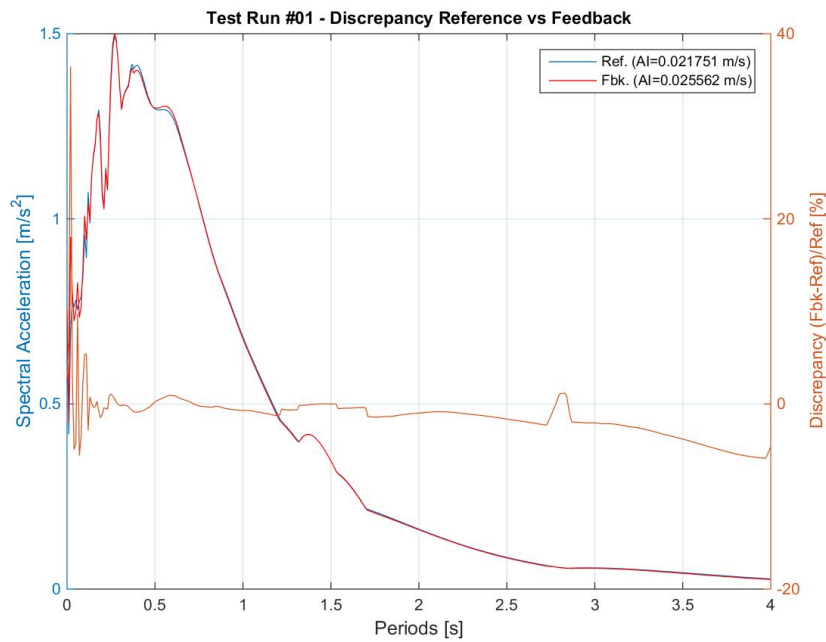
Figure 341. Discrepancy between acceleration spectra from time-histories at reference and feedback.

Figure 342 shows the acceleration time-histories recorded at the foundation level (accelerometers #139 and #140) and the average of the accelerations recorded by the two accelerometers.
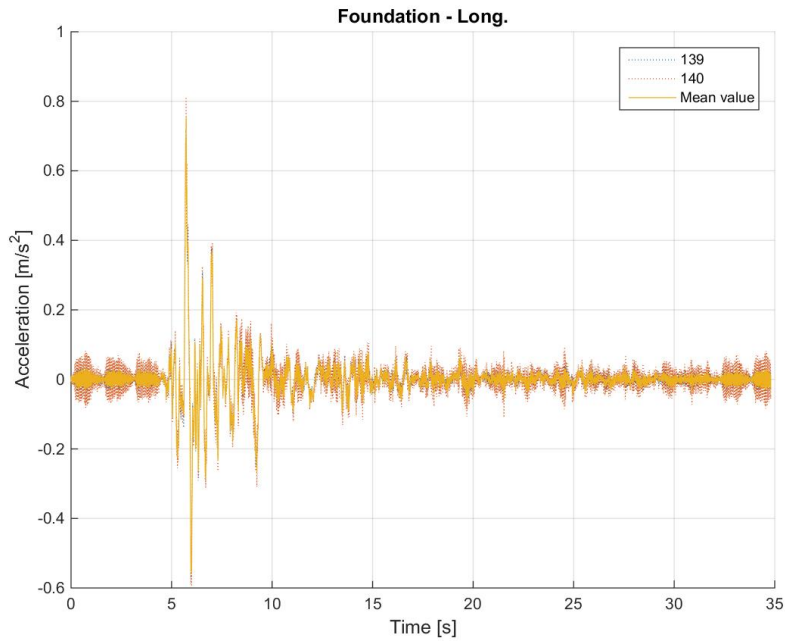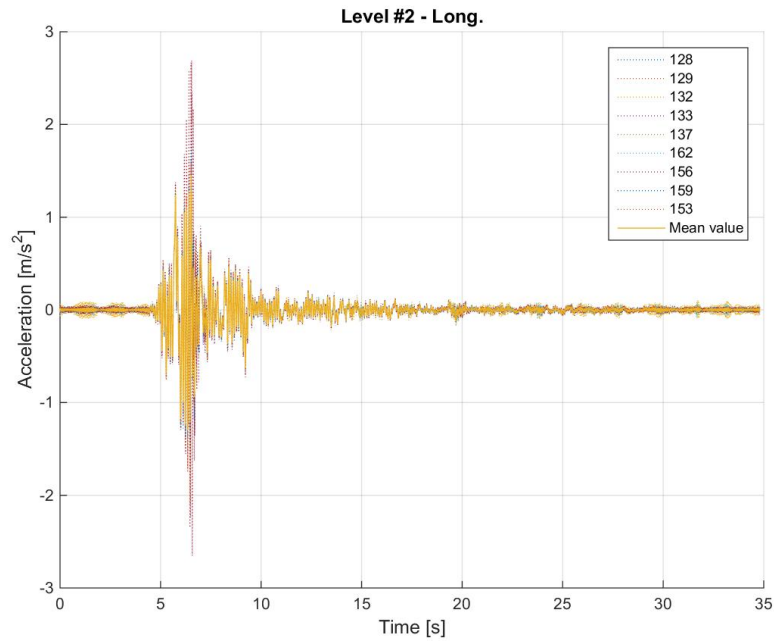
Figure 342. Acceleration time-histories at the foundation level – Individual and average of accelerometers.

Figure 343 shows the acceleration time-histories recorded at the first floor of the specimen and the average of the accelerations recorded by all the accelerometers installed at this level.
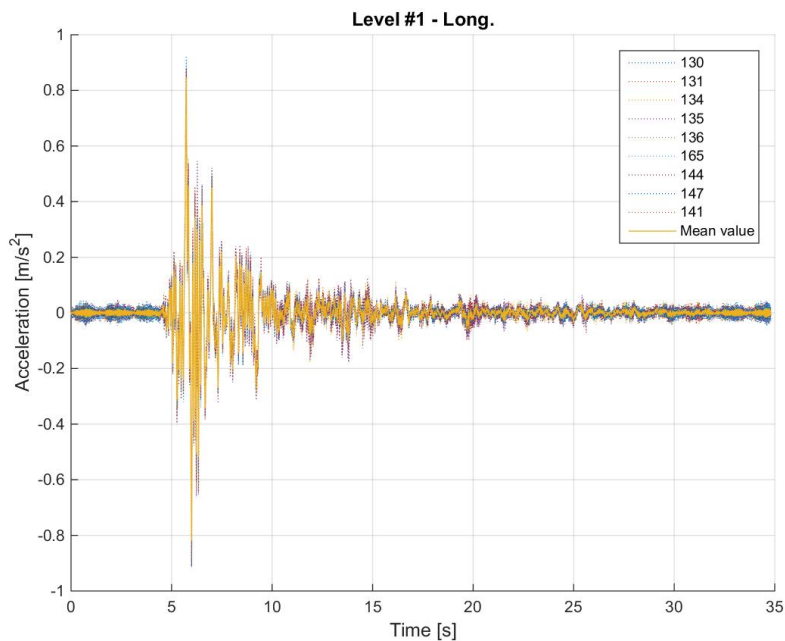
Figure 343. Acceleration time-histories at the first floor – Individual and average of accelerometers.

Figure 344 shows the acceleration time-histories recorded at the second floor and the average of the accelerations recorded by all the accelerometers installed at this level.
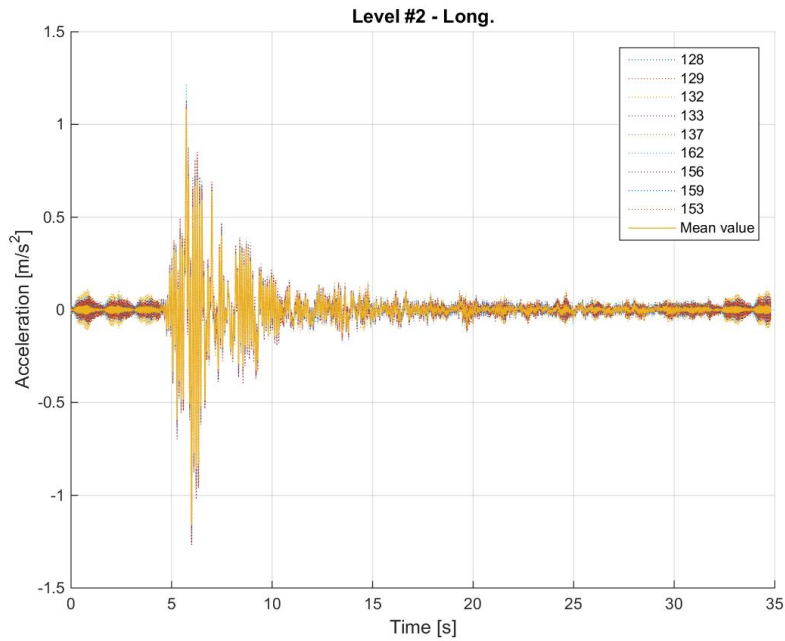
Figure 344. Acceleration time-histories at the second floor – Individual and average of accelerometers.

Figure 345 shows a comparison between the average acceleration time-history at the foundation, the first floor and the second floor of the specimen.
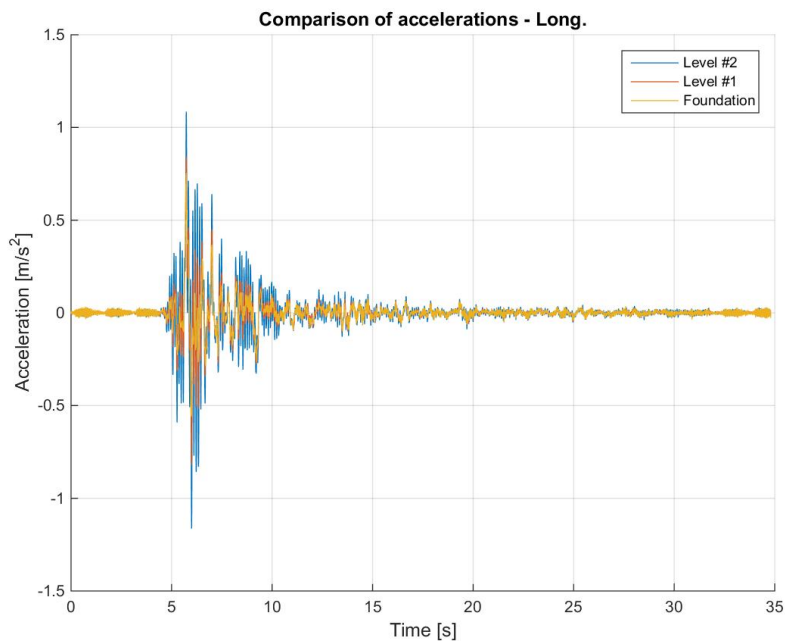
**Figure 345. Comparison between average acceleration time-histories – Foundation, first and second storeys.**

Figure 346 shows a comparison between the acceleration spectra at the base, the first storey and the second storey, which were computed using the average acceleration time-history at the foundation, the first floor and the second floor of the specimen. The spectral accelerations were also normalised with respect to the one at the base and the obtained spectral acceleration ratios are plotted together

in Figure 347. Obviously, the curve obtained for the base is the horizontal blue line, which is plotted since it serves as reference for the two floors (and their amplification).
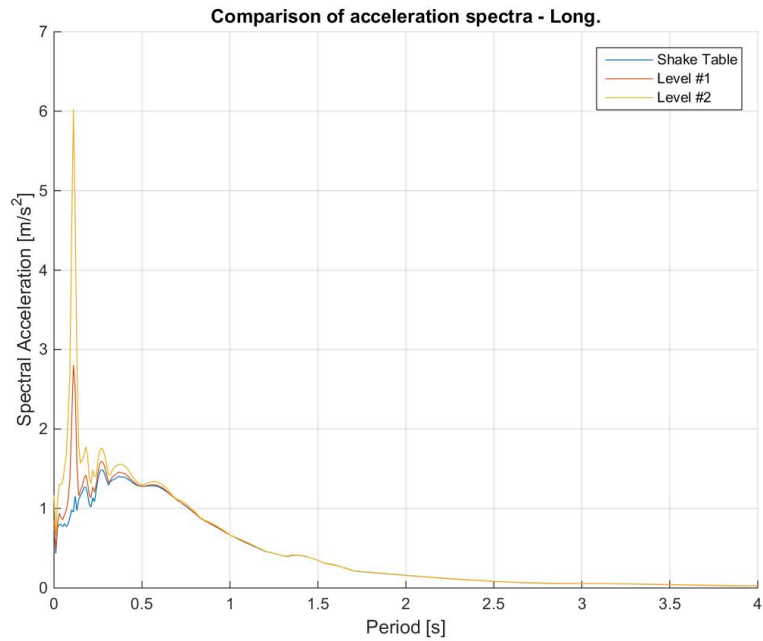
Figure 346. Acceleration spectra from average time-histories at the foundation, first and second floors.
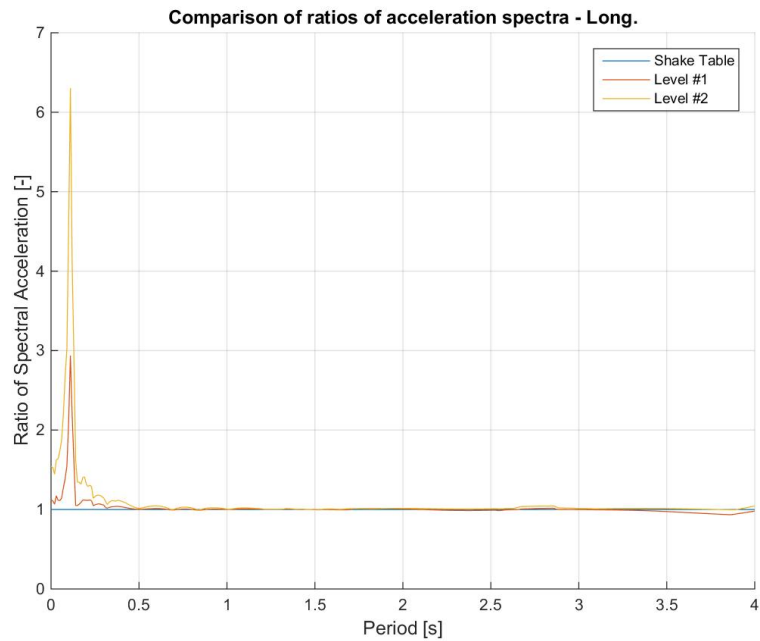
Figure 347. Spectral acceleration ratios: first floor-to-foundation and second floor-to-foundation.

Figure 348 shows a comparison between the displacement time-histories at the foundation, the first floor and the second floor of the specimen.
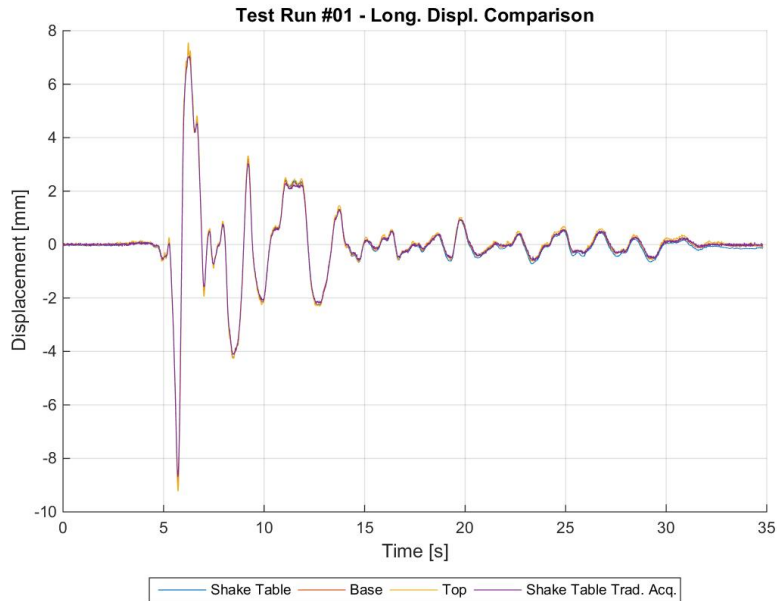
Figure 348. Comparison between average displacement time-histories – Foundation, first and second storeys.

Figure 349 shows a comparison between the imposed base shear time-history and the recorded base shear time-history, the former one being the force applied by the actuators of the shake-table.
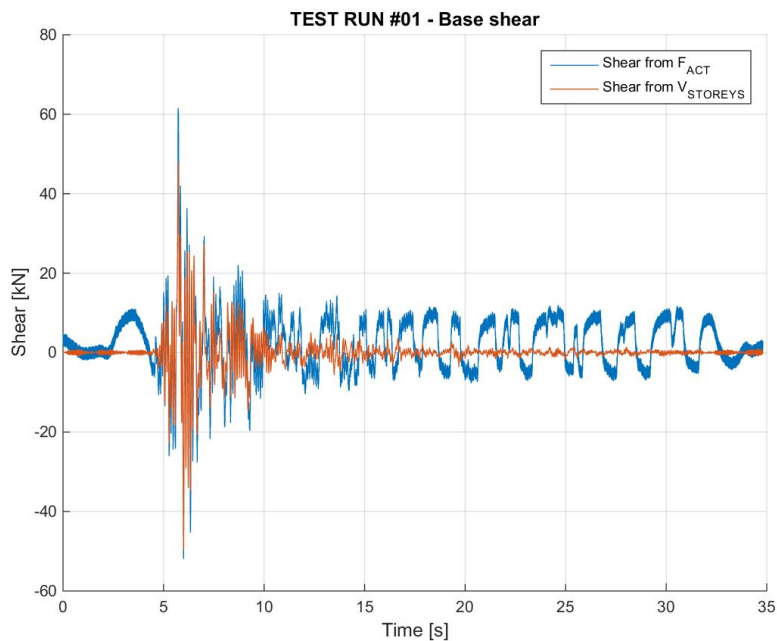
Figure 349. Imposed base shear vs. measured base shear – Comparison through time.

Figure 350 shows the hysteretic base shear-top displacement response of the specimen. For the sake of clarity, it is noted that the total base shear is plotted against the top-to-base displacement of EUC-BUILD5 specimen. Hysteresis loops were also processed to obtain a linear approximation that takes into account both Northward and Southward (i.e. positive and negative) motion and identifies,

in an equivalent manner, the corresponding base shear-displacement couples. The hysteretic response and the linear approximation are superimposed in Figure 351.
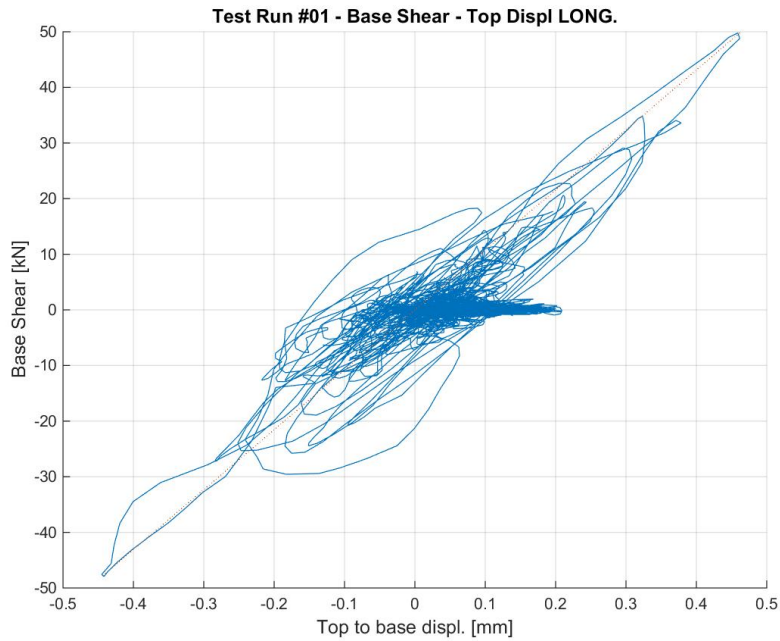
Figure 350. Base shear-top displacement response of EUC-BUILD5 – Test run #1, top-to-base displacement.
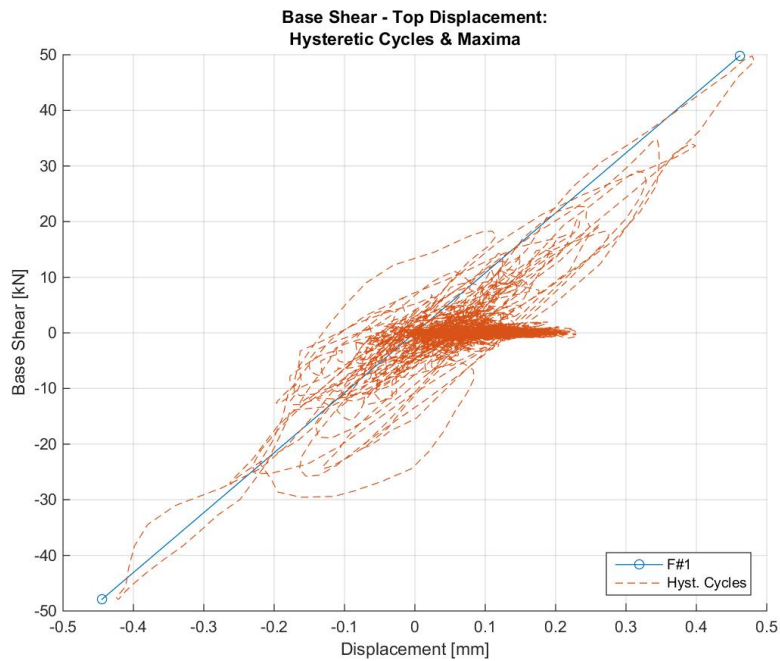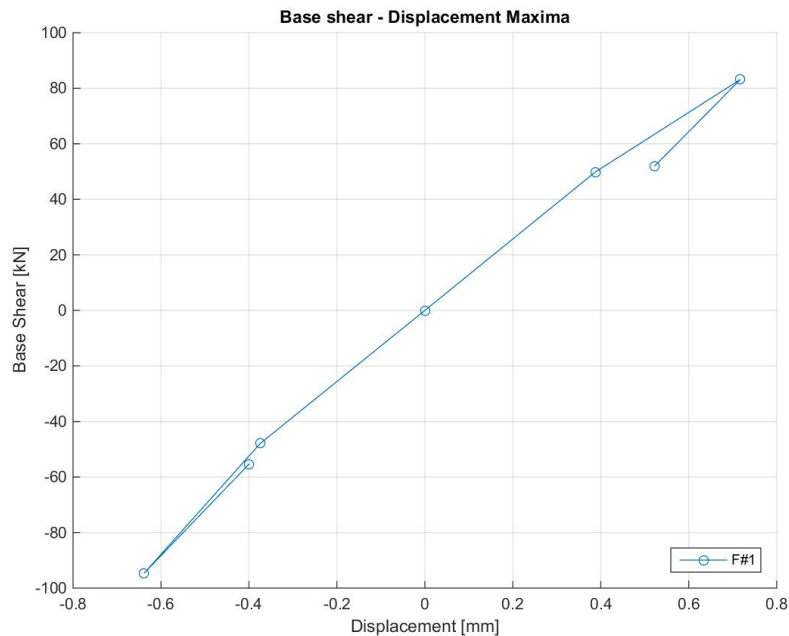

Figure 351. Base shear vs. top-to-base displacement – Hysteretic response and maxima (positive and negative).

Figure 352 shows the absolute maxima – positive or negative – top displacement-base shear couples that were obtained from the hysteresis loops of the specimen.
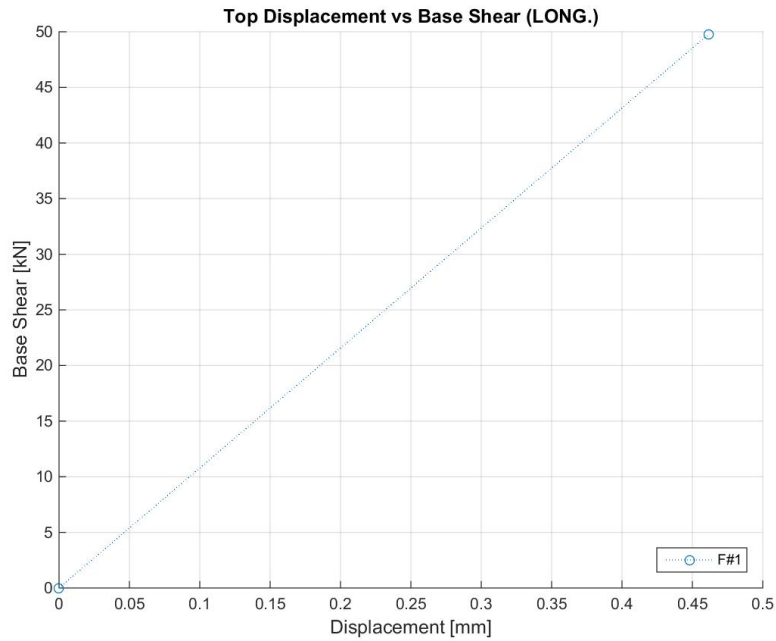
Figure 352. Base shear vs. top-to-base displacement maxima – Test run #1.

Figure 353 shows the maxima – positive and negative – top displacement-base shear couples that were obtained from the linear approximation of the specimen response (see Figure 351).
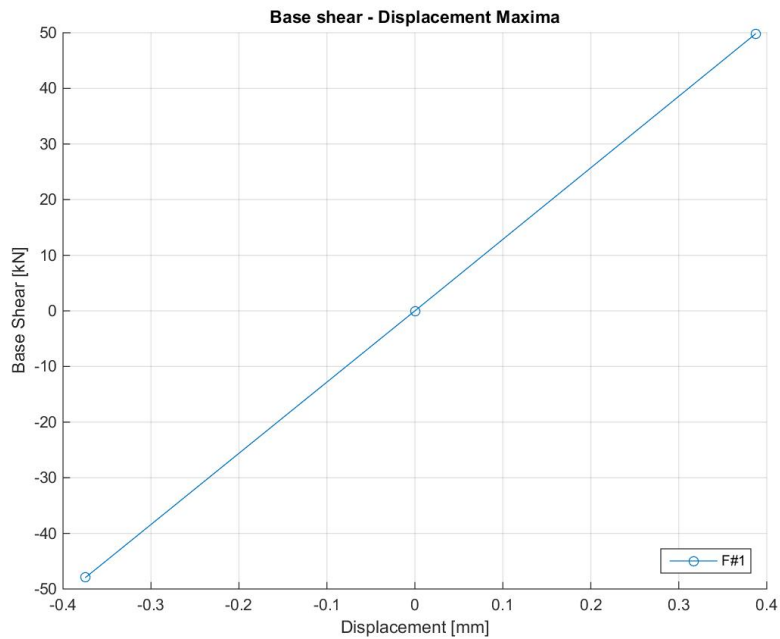

Figure 353. Base shear vs. top-to-base displacement maxima – Positive and negative, Test run #1.

Figure 354 shows the hysteretic response of the first storey of the specimen, which is illustrated in terms of storey shear versus inter-storey displacement relationship.
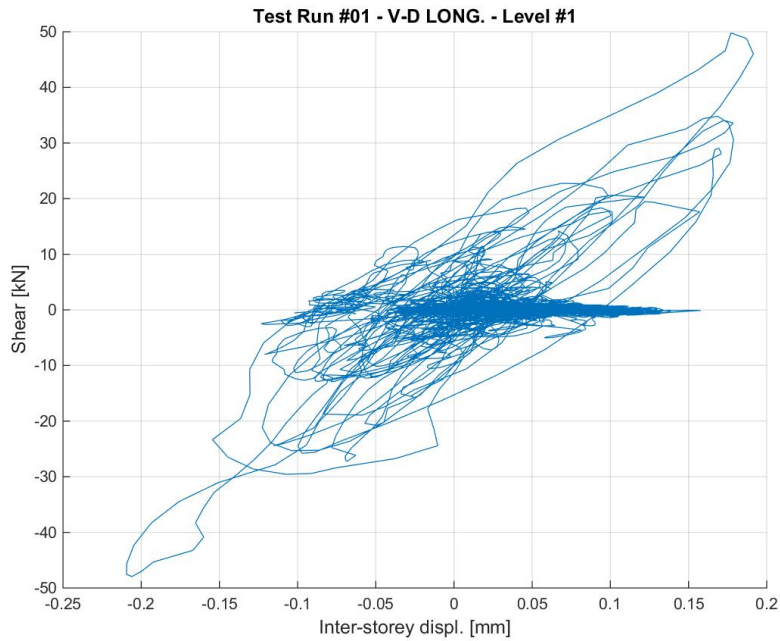
Figure 354. Storey shear vs. inter-storey displacement response – First storey, Test run #1.

Figure 355 shows the hysteretic response of the second storey of the specimen, which is illustrated in terms of storey shear versus inter-storey displacement relationship.
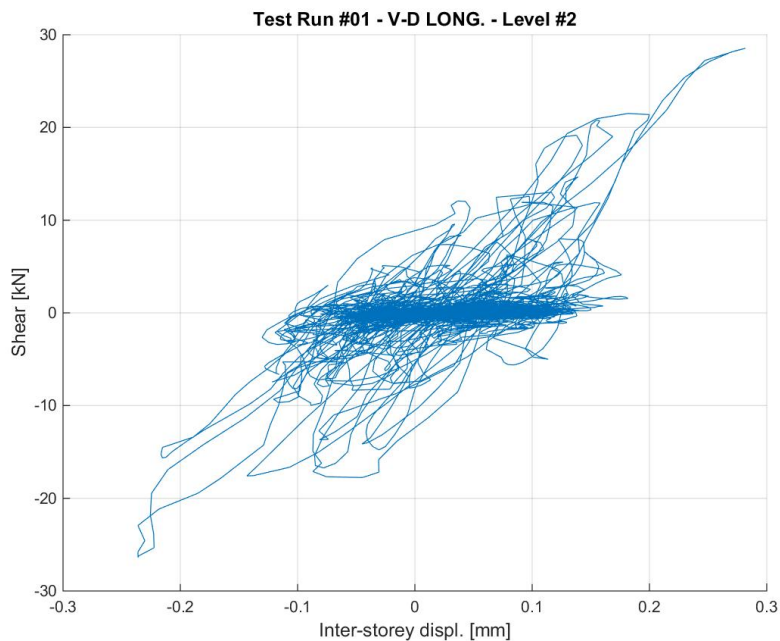
Figure 355. Storey shear vs. inter-storey displacement response – Second storey, Test run #1.

Figure 356 shows the PGA versus maxima – positive and negative – top displacement relationship, the latter parameter being identified according to the linear approximation reported in Figure 351.
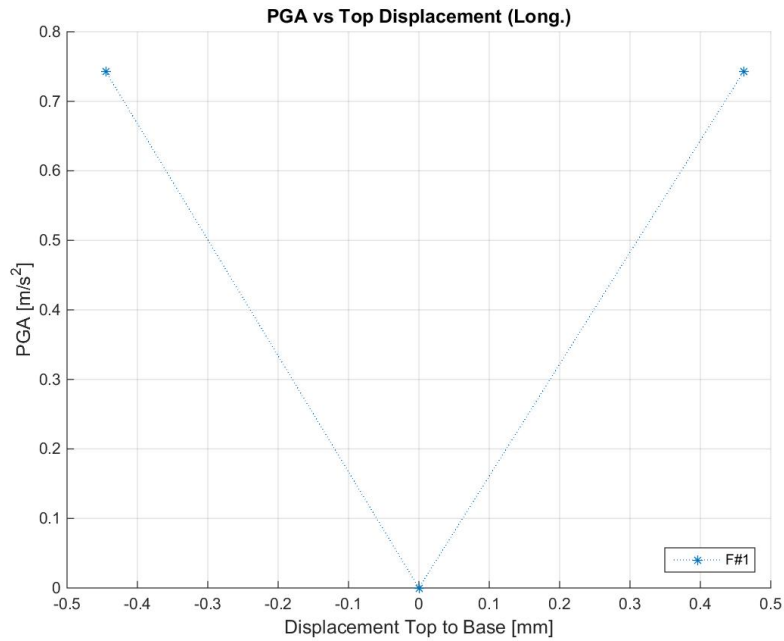
Figure 356. PGA vs. top-to-base displacement maxima – Positive and negative, Test run #1.

Figure 357 shows the PGA versus secant – positive and negative – stiffness relationship, the latter parameter being identified according to the linear approximation reported in Figure 351.
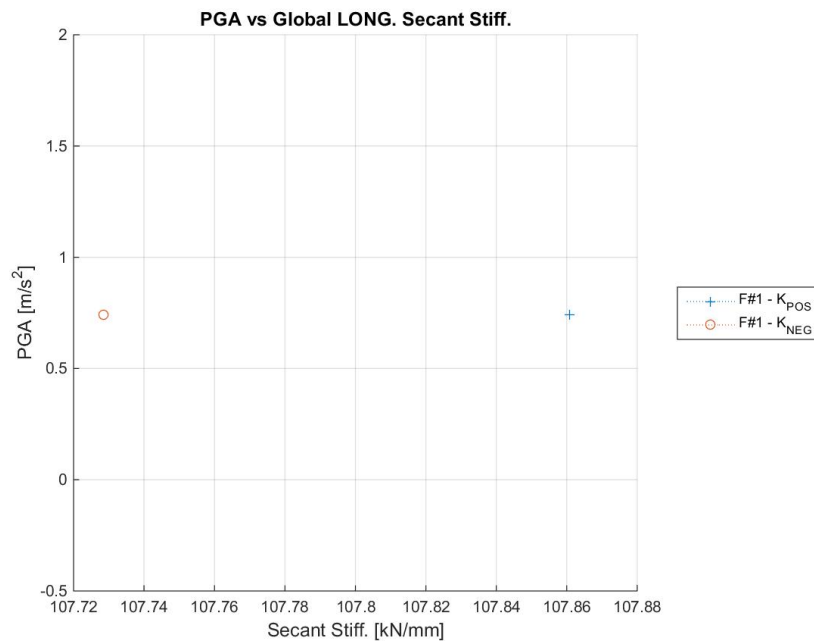

Figure 357. PGA-global secant stiffness relationships – Positive and negative directions, Test run #1.

Figure 358 shows the PGA versus maximum base shear relationship of the specimen at this stage of the testing sequence.
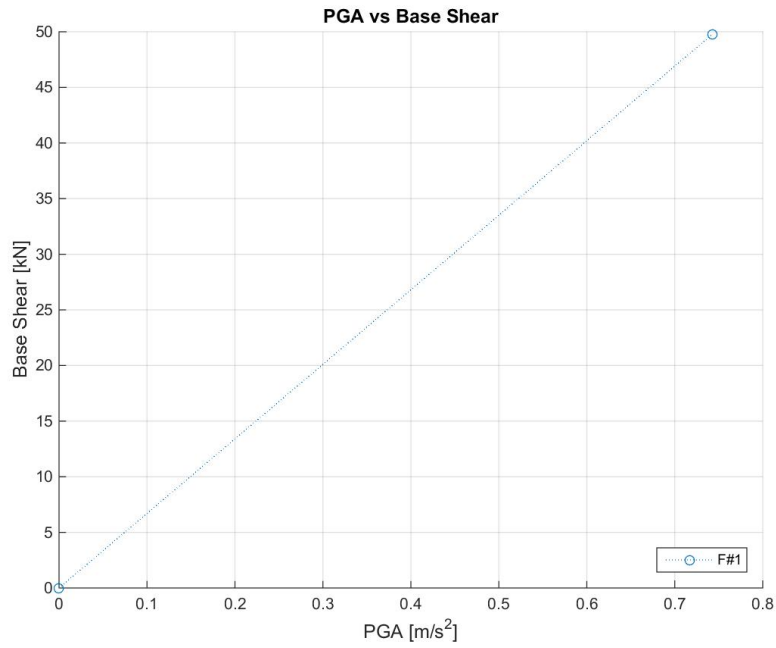
Figure 358. Maximum base shear vs. peak ground acceleration – Test run #1.

Figure 359 shows the arias intensity versus maximum base shear relationship of the specimen at this stage of the testing sequence.
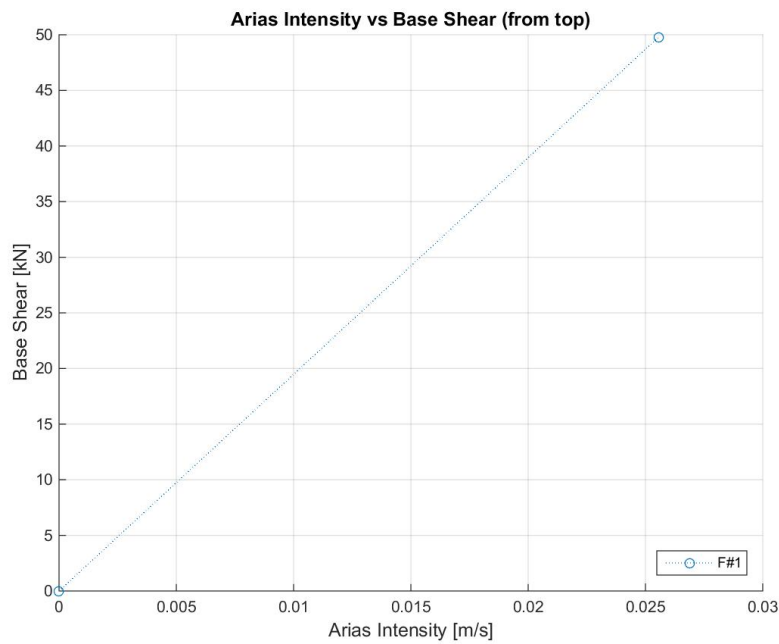
Figure 359. Maximum base shear vs. arias intensity – Test run #1.

6.6.2 Test run #2 – SF = 50% – Test at 50%

Figure 360 shows the comparison between the acceleration spectra from time-histories at reference and feedback (as recorded by the shake-table controller). The experimental acceleration time-history used for the spectrum comparison is the average of the recorded accelerations on the foundation of EUC-BUILD5 specimen (accelerometers #139 and #140). Furthermore, Figure 361 shows the discrepancy in percentage.
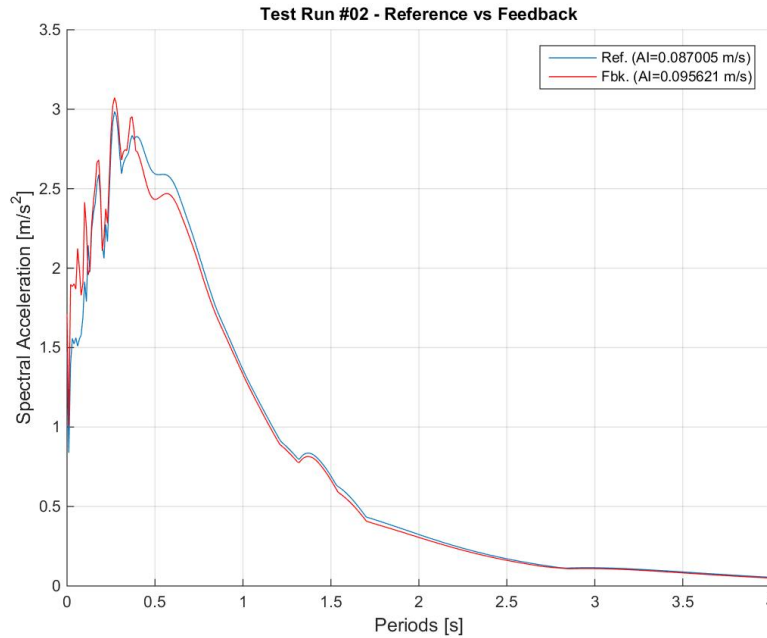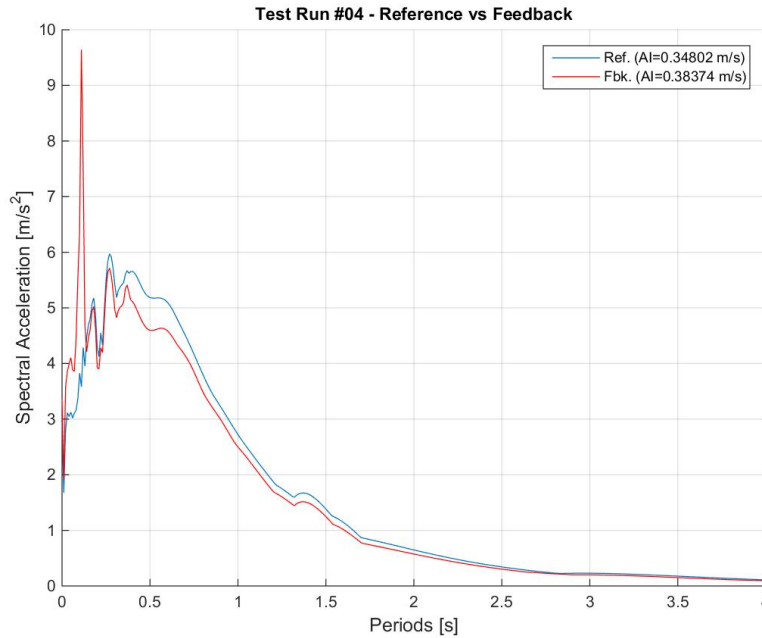

Figure 360. Comparison between acceleration spectra from time-histories at reference and feedback.
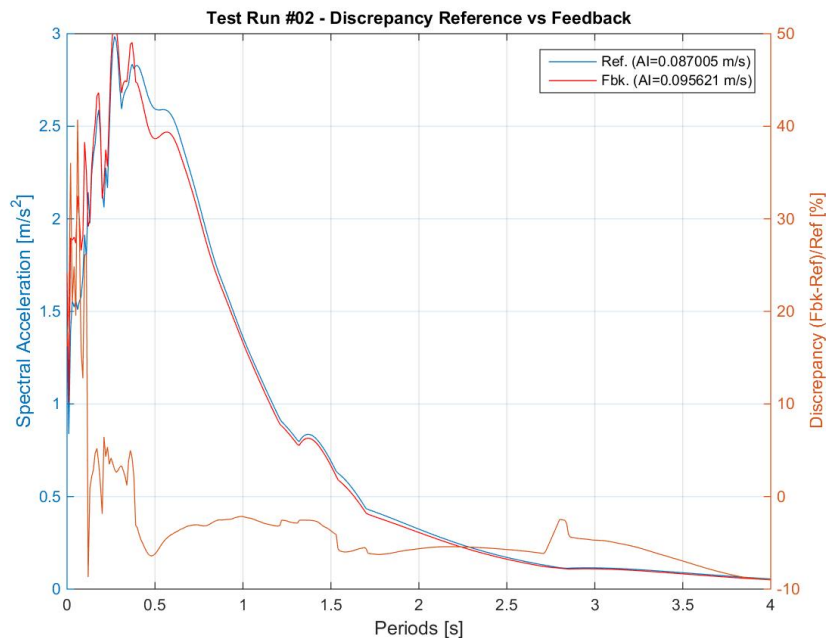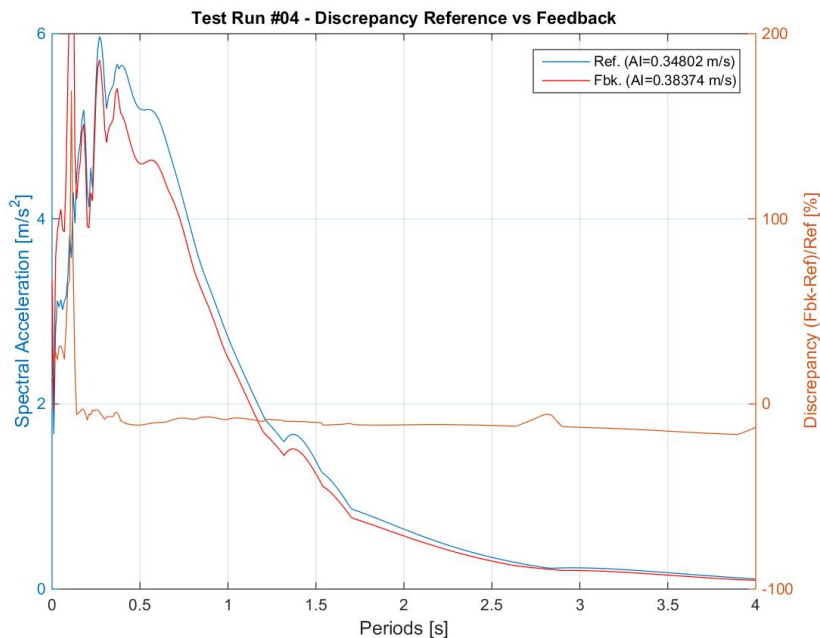

Figure 361. Discrepancy between acceleration spectra from time-histories at reference and feedback.

Figure 362 shows the acceleration time-histories recorded at the foundation level (accelerometers #139 and #140) and the average of the accelerations recorded by the two accelerometers.
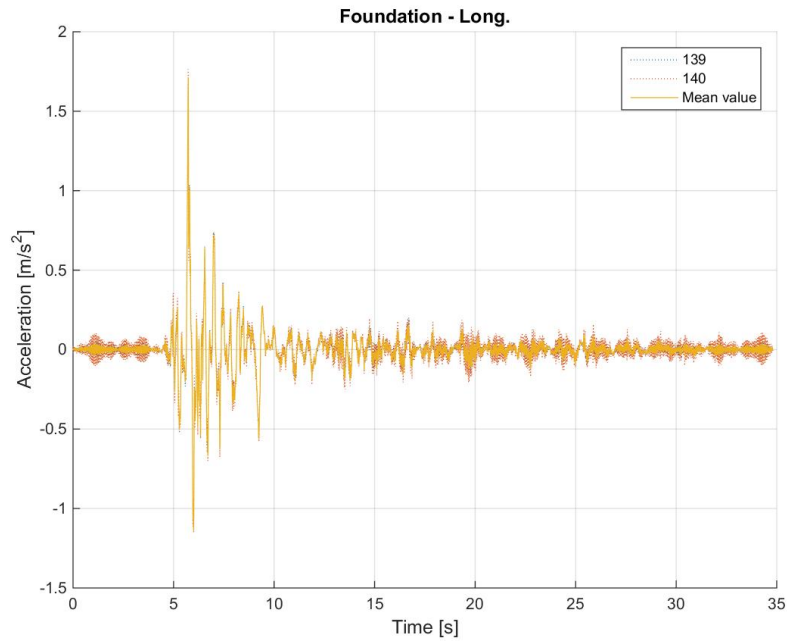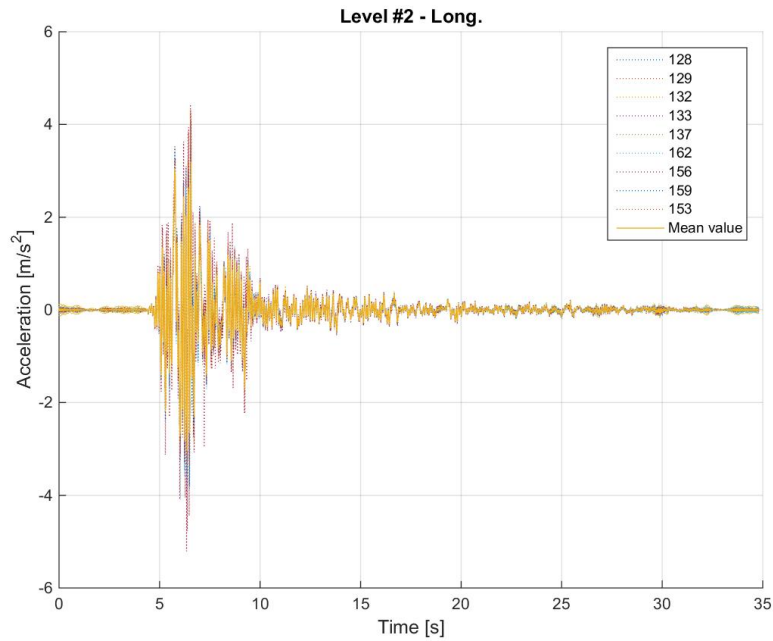

Figure 362. Acceleration time-histories at the foundation level – Individual and average of accelerometers.

Figure 363 shows the acceleration time-histories recorded at the first floor of the specimen and the average of the accelerations recorded by all the accelerometers installed at this level.
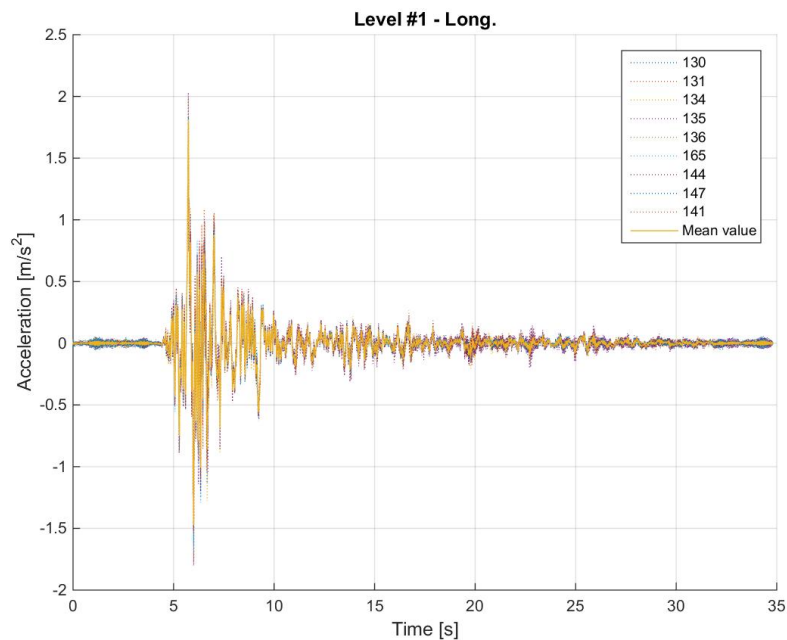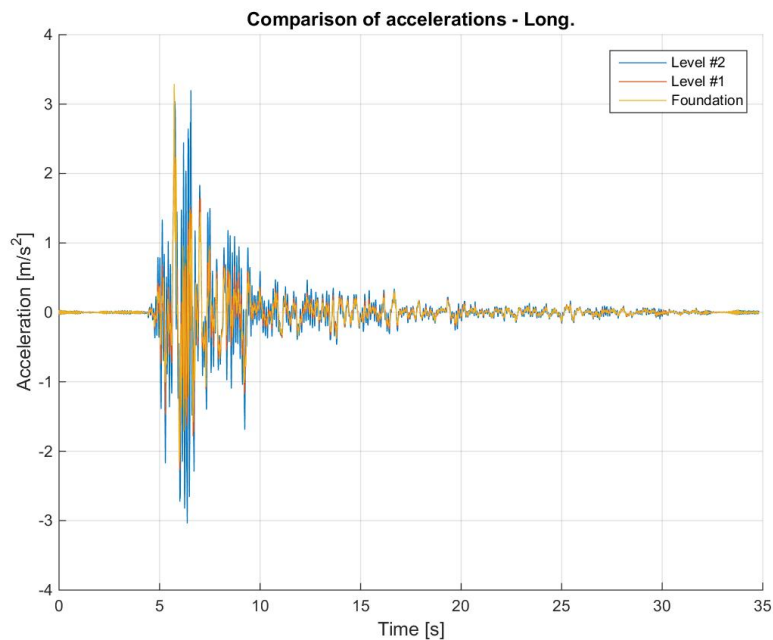

Figure 363. Acceleration time-histories at the first floor – Individual and average of accelerometers.

Figure 364 shows the acceleration time-histories recorded at the second floor and the average of the accelerations recorded by all the accelerometers installed at this level.
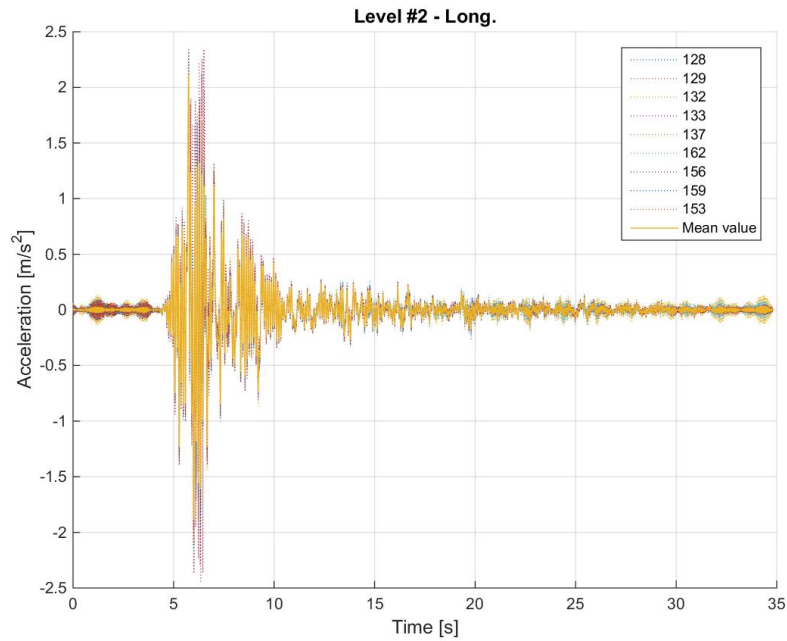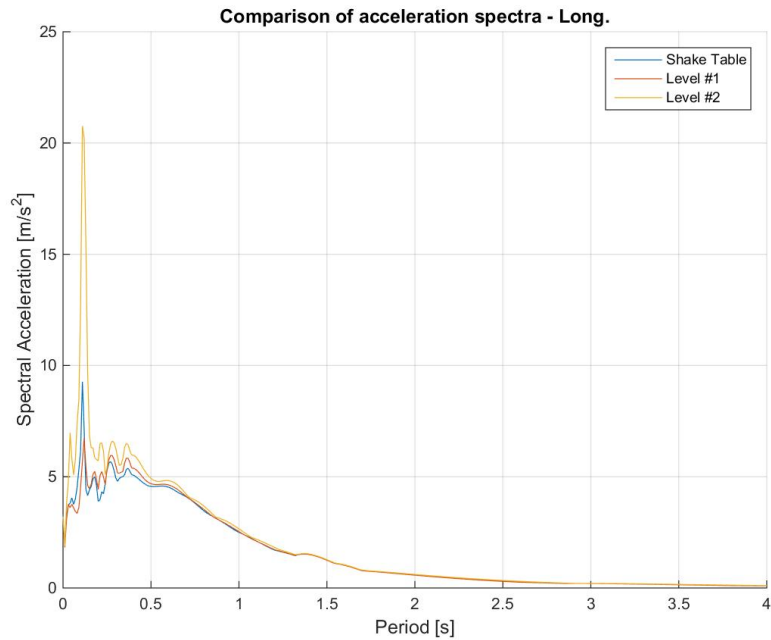

Figure 364. Acceleration time-histories at the second floor – Individual and average of accelerometers.

Figure 365 shows a comparison between the average acceleration time-history at the foundation, the first floor and the second floor of the specimen.
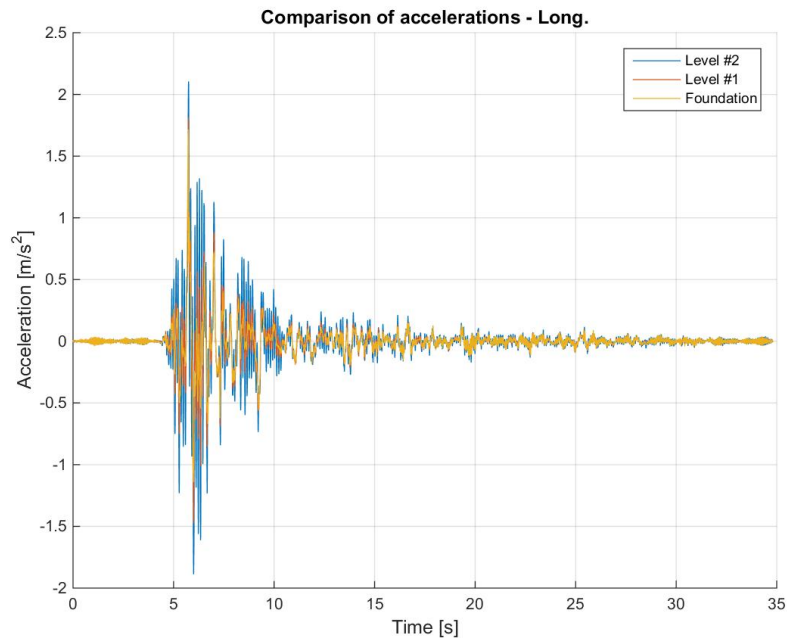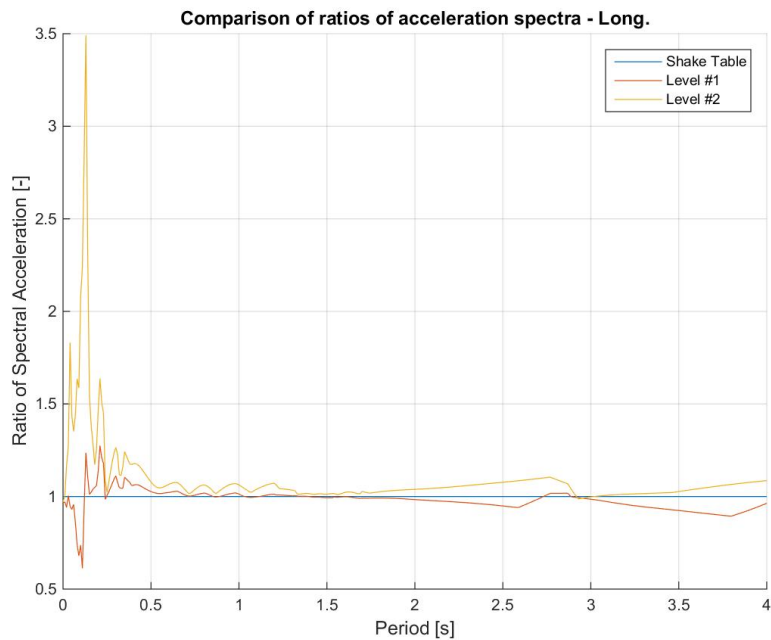

Figure 365. Comparison between average acceleration time-histories – Foundation, first and second storeys.

Figure 366 shows a comparison between the acceleration spectra at the base, the first storey and the second storey, which were computed using the average acceleration time-history at the foundation, the first floor and the second floor of the specimen. The spectral accelerations were also normalised with respect to the one at the base and the obtained spectral acceleration ratios are plotted together in Figure 367. Obviously, the curve obtained for the base is the horizontal blue line, which is plotted since it serves as reference for the two floors (and their amplification).
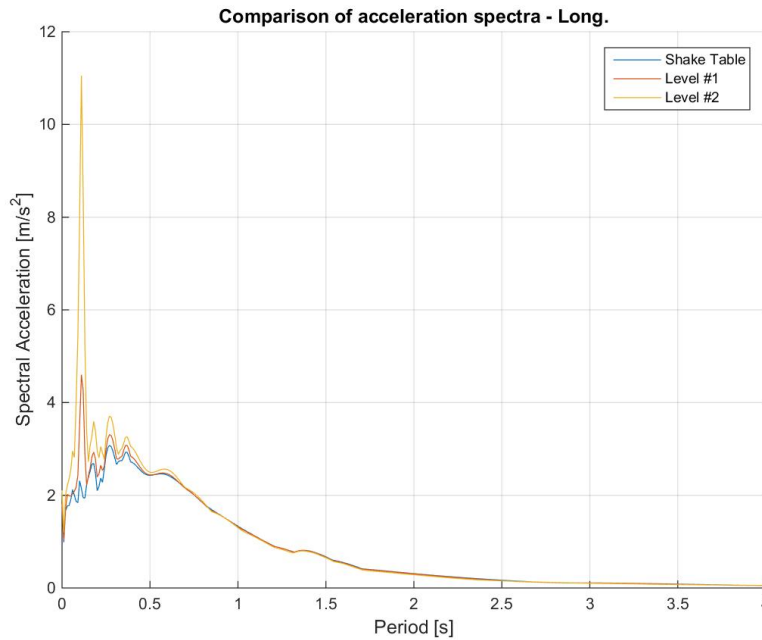

Figure 366. Acceleration spectra from average time-histories at the foundation, first and second floors.
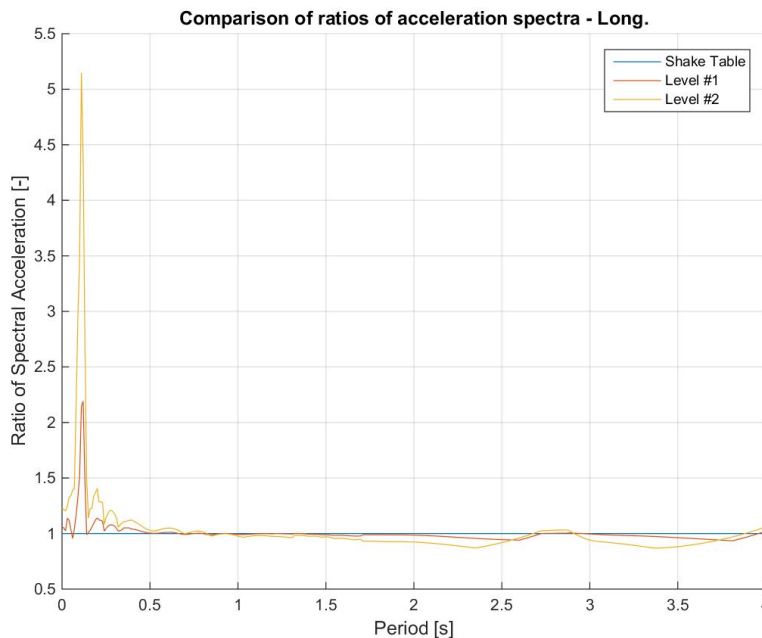

Figure 367. Spectral acceleration ratios: first floor-to-foundation and second floor-to-foundation.

Figure 368 shows a comparison between the displacement time-histories at the foundation, the first floor and the second floor of the specimen.
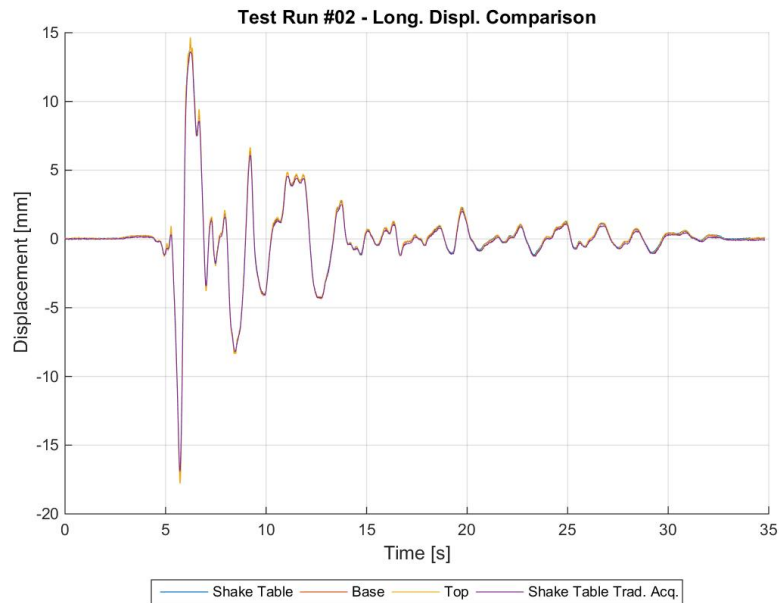

Figure 368. Comparison between average displacement time-histories – Foundation, first and second storeys.

Figure 369 shows a comparison between the imposed base shear time-history and the recorded base shear time-history, the former one being the force applied by the actuators of the shake-table.
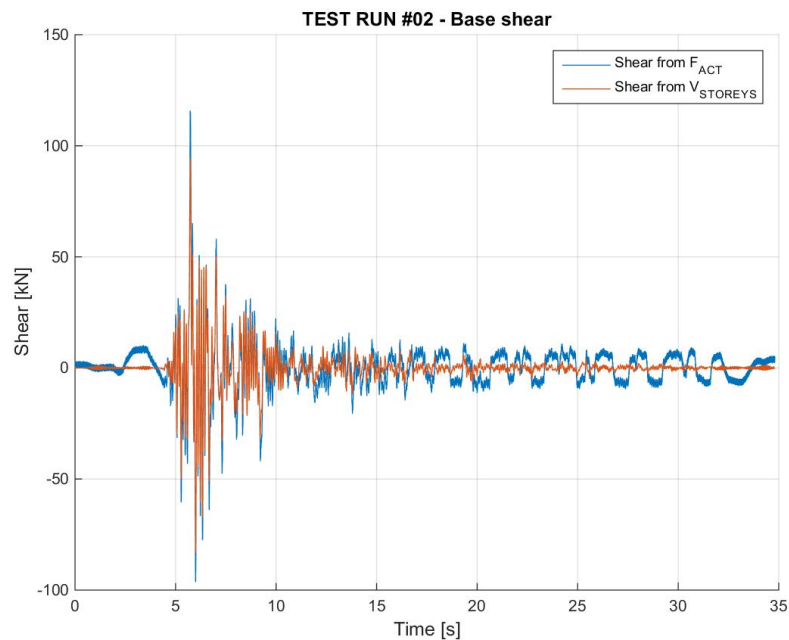

Figure 369. Imposed base shear vs. measured base shear – Comparison through time.

Figure 370 shows the hysteretic base shear-top displacement response of the specimen. For the sake of clarity, it is noted that the total base shear is plotted against the top-to-base displacement of EUC-BUILD5 specimen. Hysteresis loops were also processed to obtain a linear approximation that takes into account both Northward and Southward (i.e. positive and negative) motion and identifies, in an equivalent manner, the corresponding base shear-displacement couples. The hysteretic response and the linear approximation are superimposed in Figure 371.
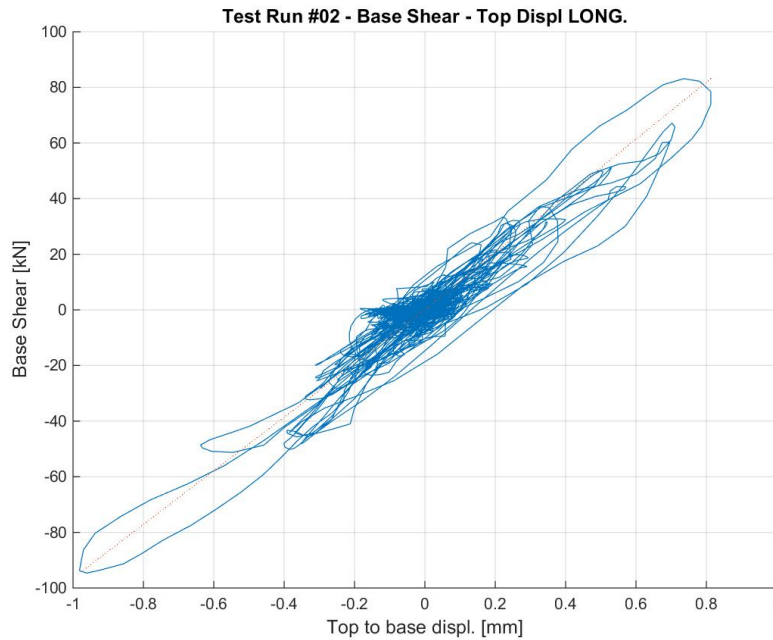
Figure 370. Base shear-top displacement response of EUC-BUILD5 – Test run #2, top-to-base displacement.
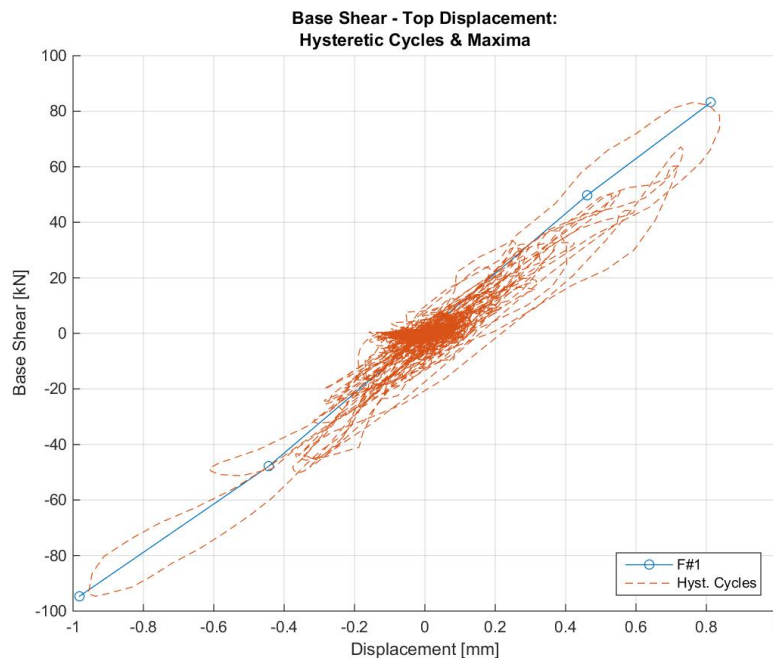
Figure 371. Base shear vs. top-to-base displacement – Hysteretic response and maxima (positive and negative).

Figure 372 shows the absolute maxima – positive or negative – top displacement-base shear couples that were obtained from the hysteresis loops of the specimen.
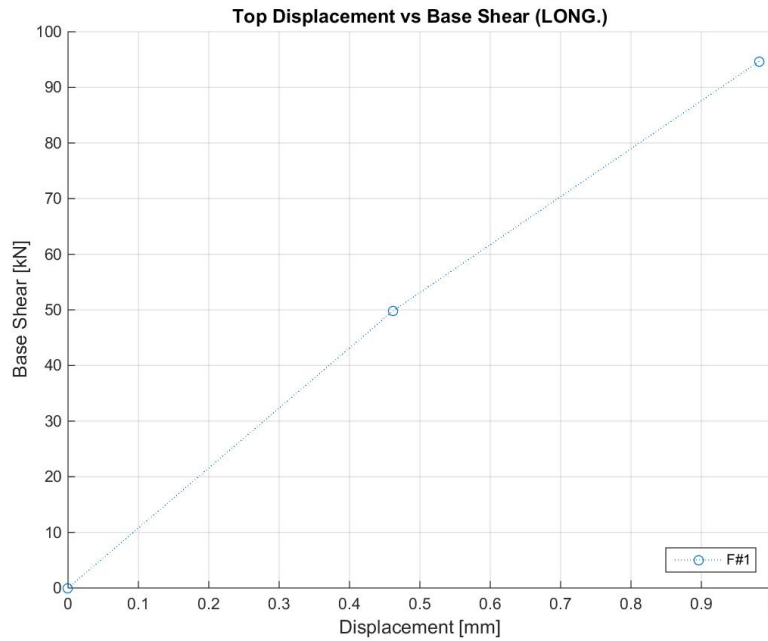
Figure 372. Base shear vs. top-to-base displacement maxima – Test run #2.

Figure 373 shows the maxima – positive and negative – top displacement-base shear couples that were obtained from the linear approximation of the specimen response (see Figure 371).
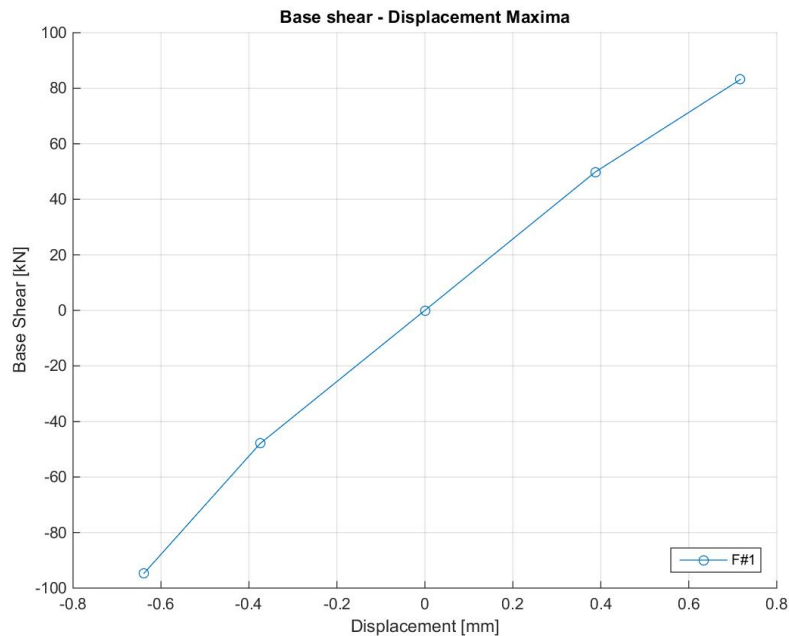
Figure 373. Base shear vs. top-to-base displacement maxima – Positive and negative, Test run #2.

Figure 374 shows the hysteretic response of the first storey of the specimen, which is illustrated in terms of storey shear versus inter-storey displacement relationship.
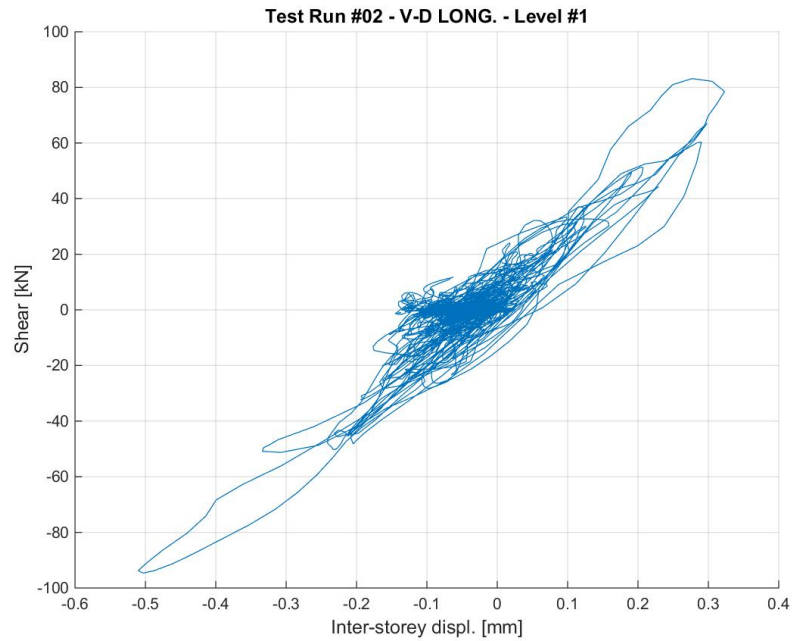
Figure 374. Storey shear vs. inter-storey displacement response – First storey, Test run #2.

Figure 375 shows the hysteretic response of the second storey of the specimen, which is illustrated in terms of storey shear versus inter-storey displacement relationship.
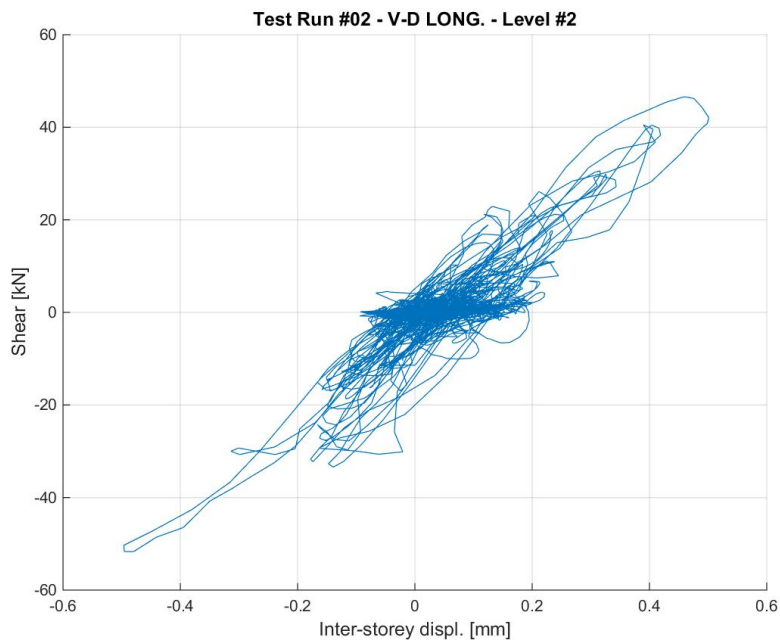
Figure 375. Storey shear vs. inter-storey displacement response – Second storey, Test run #2.

Figure 376 shows the PGA versus maxima – positive and negative – top displacement relationship, the latter parameter being identified according to the linear approximation reported in Figure 371.
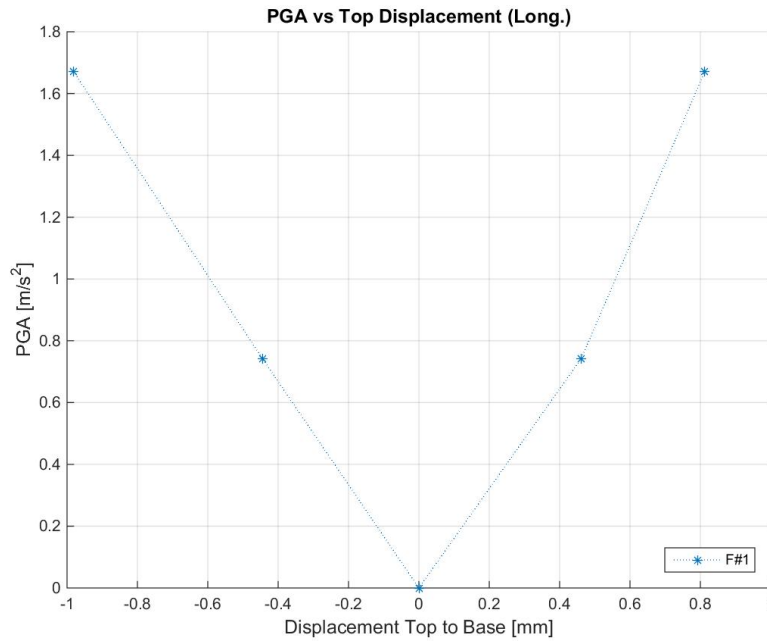
Figure 376. PGA vs. top-to-base displacement maxima – Positive and negative, Test run #2.

Figure 377 shows the PGA versus secant – positive and negative – stiffness relationship, the latter parameter being identified according to the linear approximation reported in Figure 371.
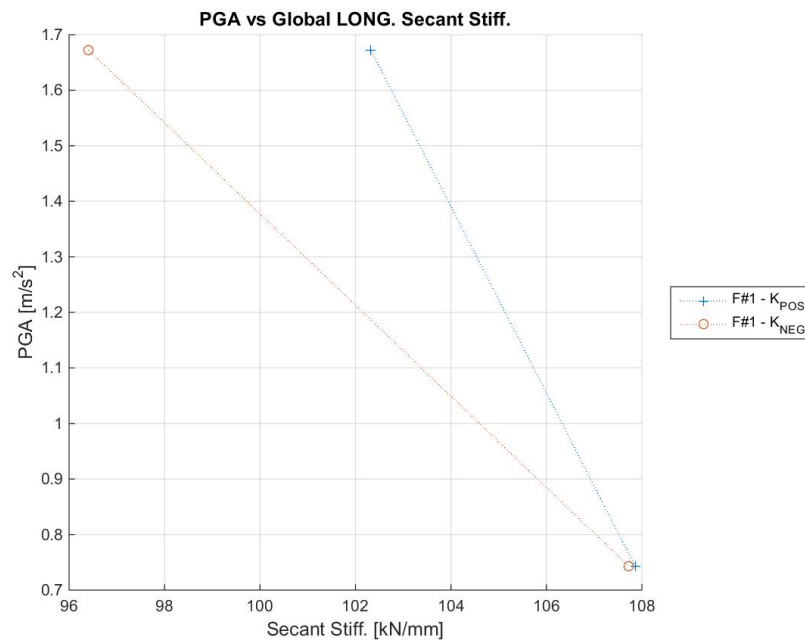
Figure 377. PGA-global secant stiffness relationships – Positive and negative directions, Test run #2.

Figure 378 shows the PGA versus maximum base shear relationship of the specimen at this stage of the testing sequence.
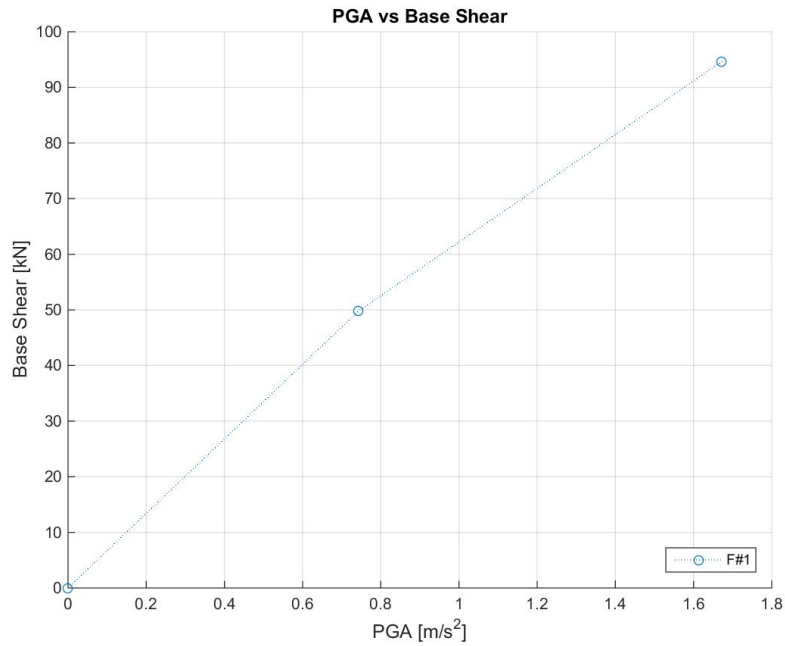
Figure 378. Maximum base shear vs. peak ground acceleration – Test run #2.

Figure 379 shows the arias intensity versus maximum base shear relationship of the specimen at this stage of the testing sequence.
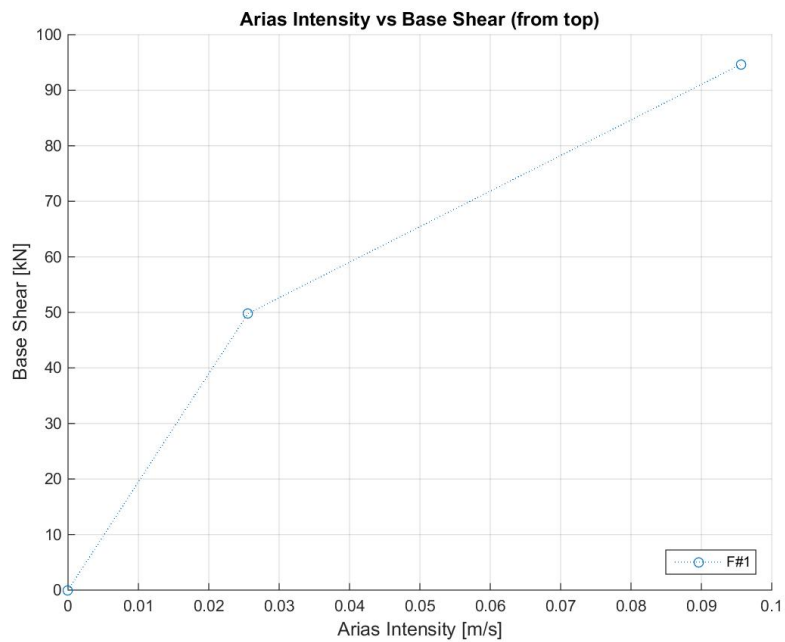
Figure 379. Maximum base shear vs. arias intensity – Test run #2.

6.6.3 Test run #3 – SF = 34% – Controller compensation

Figure 380 shows the comparison between the acceleration spectra from time-histories at reference and feedback (as recorded by the shake-table controller). The experimental acceleration time-history used for the spectrum comparison is the average of the recorded accelerations on the foundation of EUC-BUILD5 specimen (accelerometers #139 and #140). Furthermore, Figure 381 shows the discrepancy in percentage.

Figure 380. Comparison between acceleration spectra from time-histories at reference and feedback.

Figure 381. Discrepancy between acceleration spectra from time-histories at reference and feedback.

Figure 382 shows the acceleration time-histories recorded at the foundation level (accelerometers #139 and #140) and the average of the accelerations recorded by the two accelerometers.
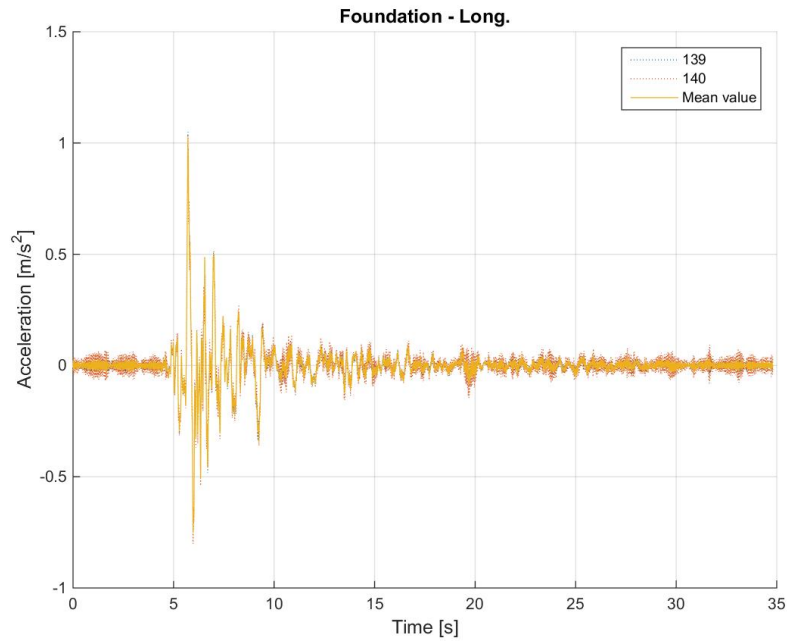
Figure 382. Acceleration time-histories at the foundation level – Individual and average of accelerometers.

Figure 383 shows the acceleration time-histories recorded at the first floor of the specimen and the average of the accelerations recorded by all the accelerometers installed at this level.
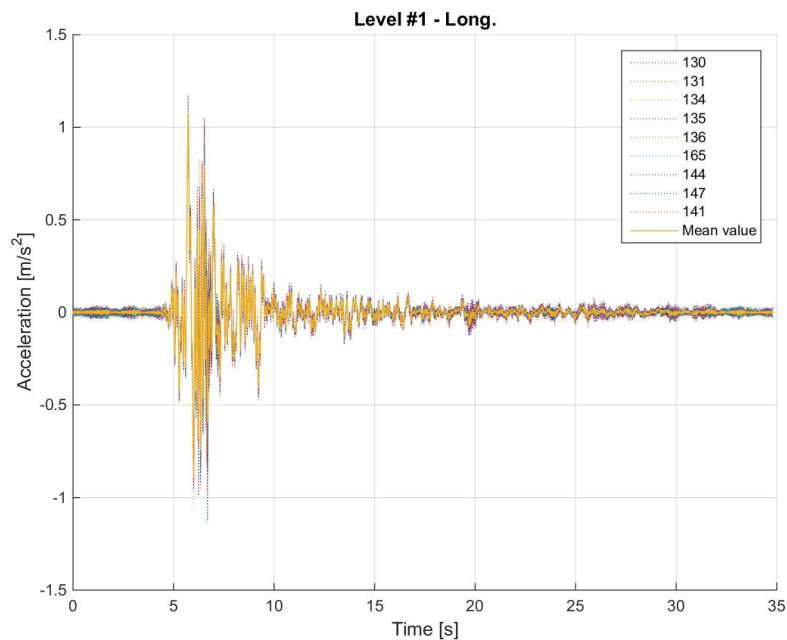
Figure 383. Acceleration time-histories at the first floor – Individual and average of accelerometers.

Figure 384 shows the acceleration time-histories recorded at the second floor and the average of the accelerations recorded by all the accelerometers installed at this level.

Figure 384. Acceleration time-histories at the second floor – Individual and average of accelerometers.

Figure 385 shows a comparison between the average acceleration time-history at the foundation, the first floor and the second floor of the specimen.
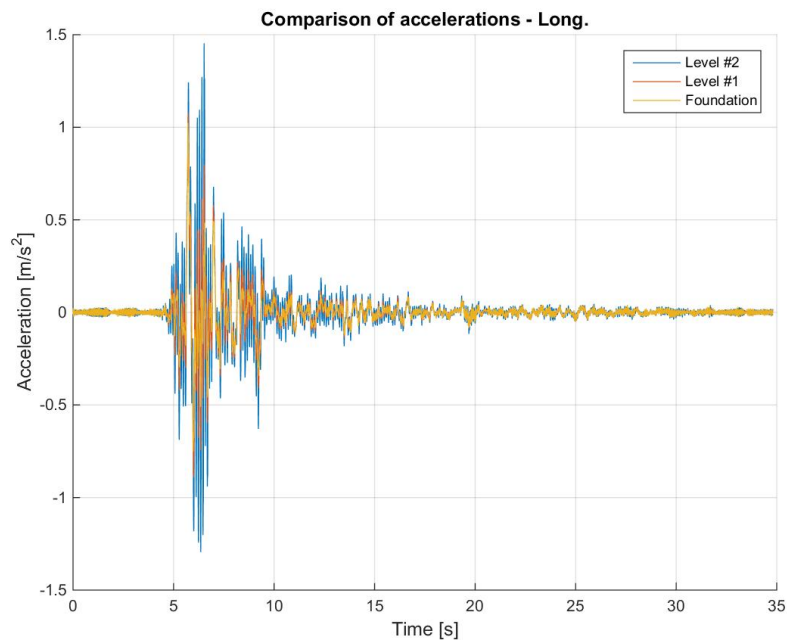
Figure 385. Comparison between average acceleration time-histories – Foundation, first and second storeys.

Figure 386 shows a comparison between the acceleration spectra at the base, the first storey and the second storey, which were computed using the average acceleration time-history at the foundation, the first floor and the second floor of the specimen. The spectral accelerations were also normalised with respect to the one at the base and the obtained spectral acceleration ratios are plotted together in Figure 387. Obviously, the curve obtained for the base is the horizontal blue line, which is plotted since it serves as reference for the two floors (and their amplification).
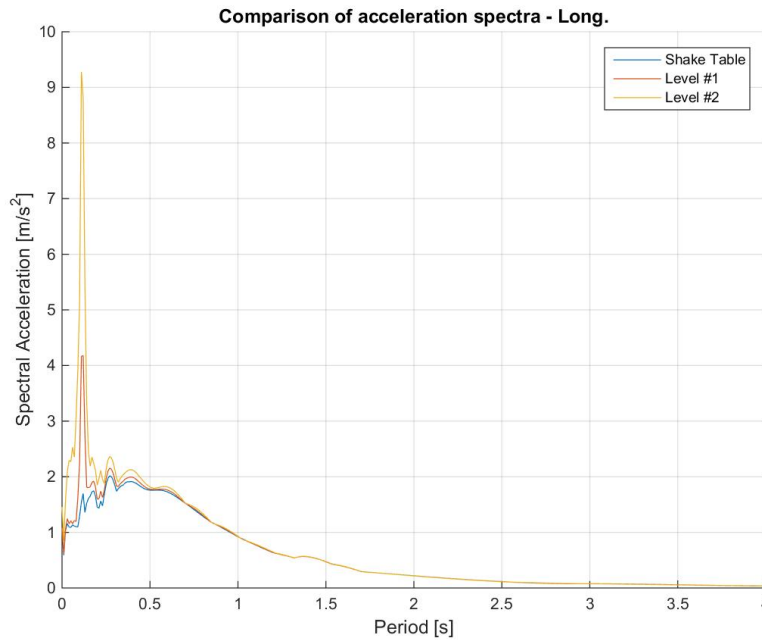
Figure 386. Acceleration spectra from average time-histories at the foundation, first and second floors.
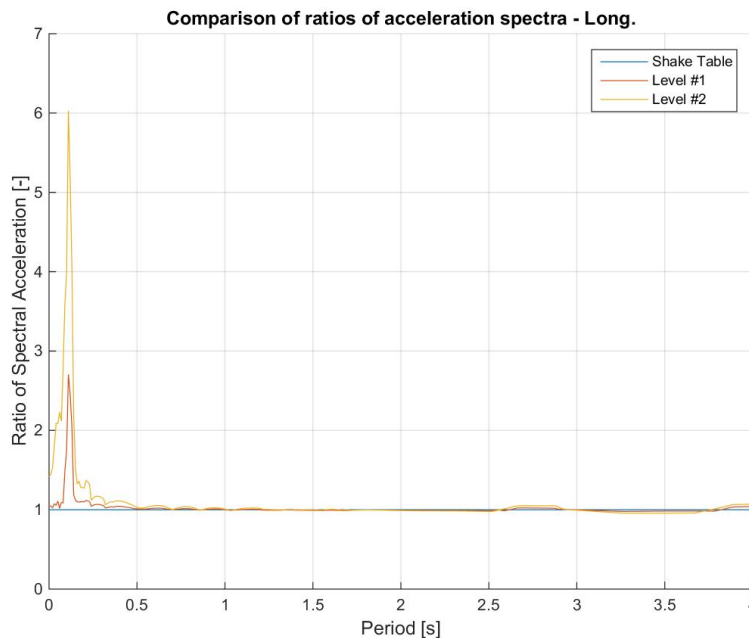
Figure 387. Spectral acceleration ratios: first floor-to-foundation and second floor-to-foundation.

Figure 388 shows a comparison between the displacement time-histories at the foundation, the first floor and the second floor of the specimen.
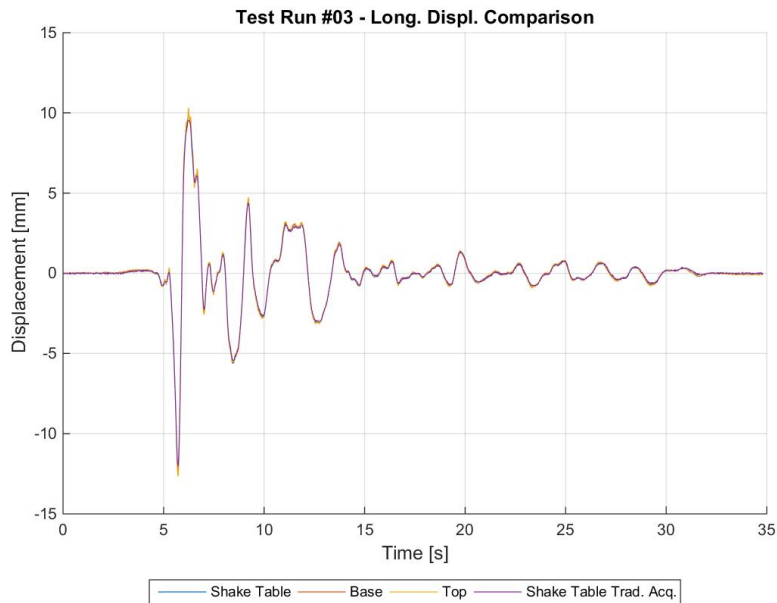
Figure 388. Comparison between average displacement time-histories – Foundation, first and second storeys.

Figure 389 shows a comparison between the imposed base shear time-history and the recorded base shear time-history, the former one being the force applied by the actuators of the shake-table.
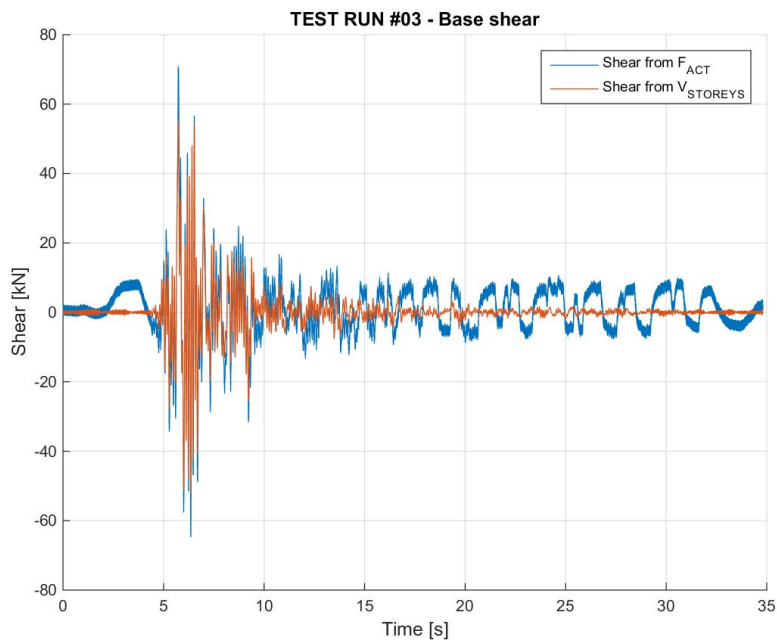
Figure 389. Imposed base shear vs. measured base shear – Comparison through time.

Figure 390 shows the hysteretic base shear-top displacement response of the specimen. For the sake of clarity, it is noted that the total base shear is plotted against the top-to-base displacement of EUC-BUILD5 specimen. Hysteresis loops were also processed to obtain a linear approximation that takes into account both Northward and Southward (i.e. positive and negative) motion and identifies, in an equivalent manner, the corresponding base shear-displacement couples. The hysteretic response and the linear approximation are superimposed in Figure 391.
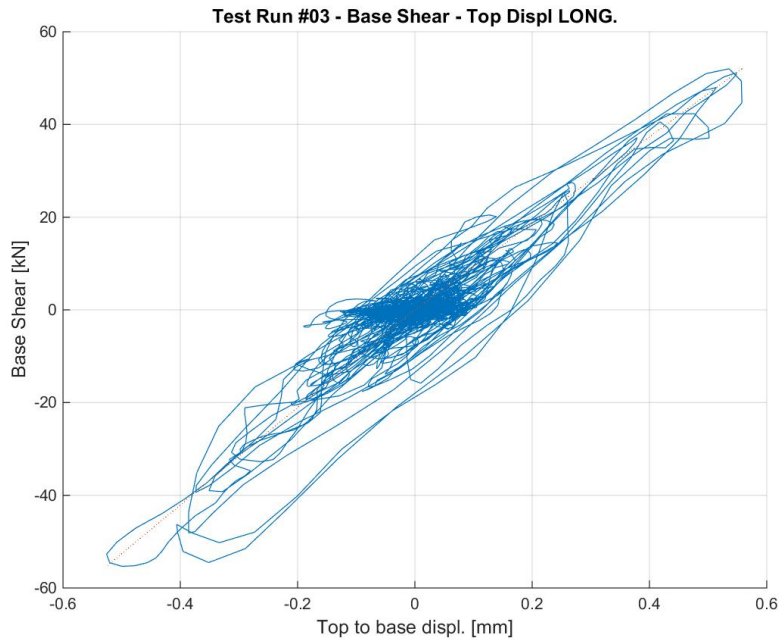
Figure 390. Base shear-top displacement response of EUC-BUILD5 – Test run #3, top-to-base displacement.
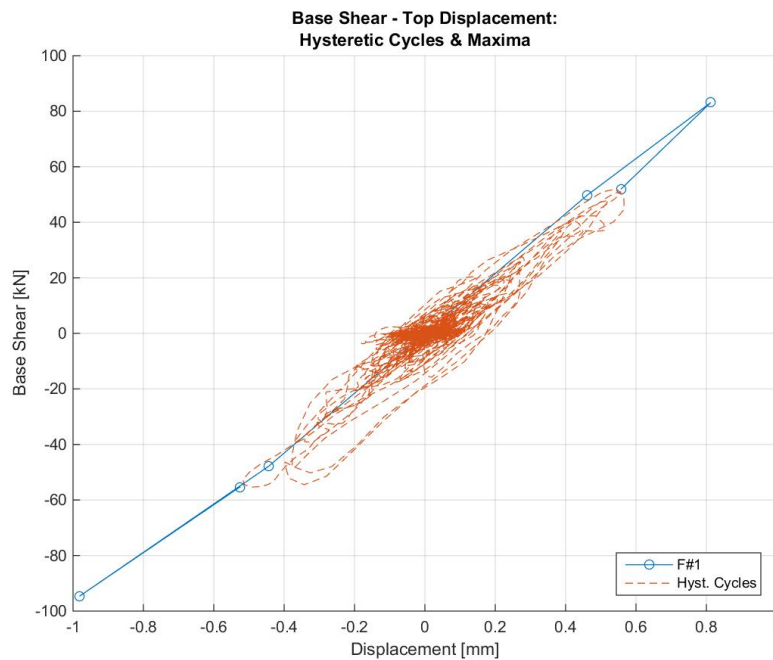
Figure 391. Base shear vs. top-to-base displacement – Hysteretic response and maxima (positive and negative).

Figure 392 shows the absolute maxima – positive or negative – top displacement-base shear couples that were obtained from the hysteresis loops of the specimen.
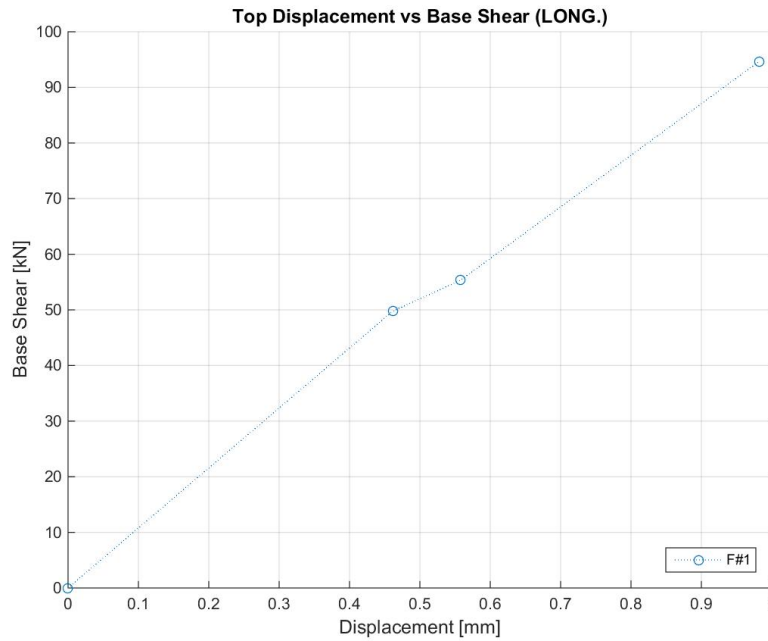
Figure 392. Base shear vs. top-to-base displacement maxima – Test run #3.

Figure 393 shows the maxima – positive and negative – top displacement-base shear couples that were obtained from the linear approximation of the specimen response (see Figure 391).

Figure 393. Base shear vs. top-to-base displacement maxima – Positive and negative, Test run #3.

Figure 394 shows the hysteretic response of the first storey of the specimen, which is illustrated in terms of storey shear versus inter-storey displacement relationship.
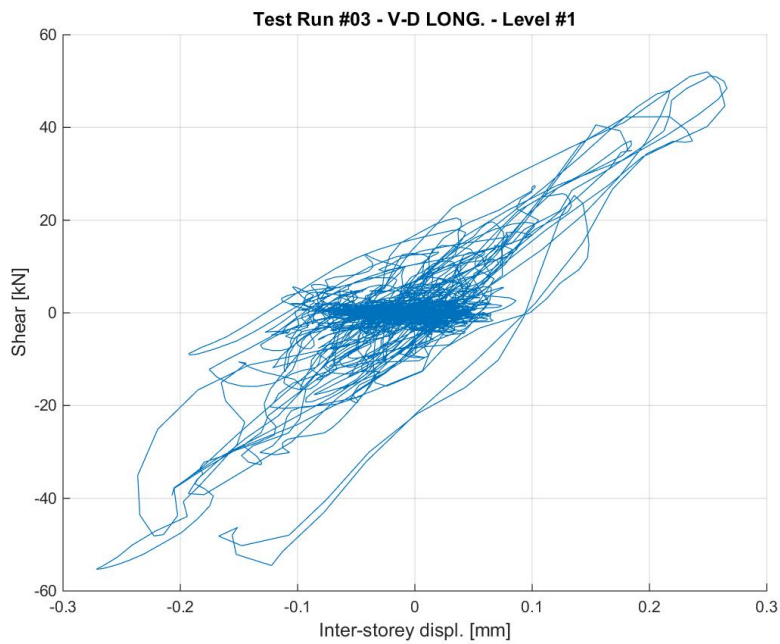
Figure 394. Storey shear vs. inter-storey displacement response – First storey, Test run #3.

Figure 395 shows the hysteretic response of the second storey of the specimen, which is illustrated in terms of storey shear versus inter-storey displacement relationship.
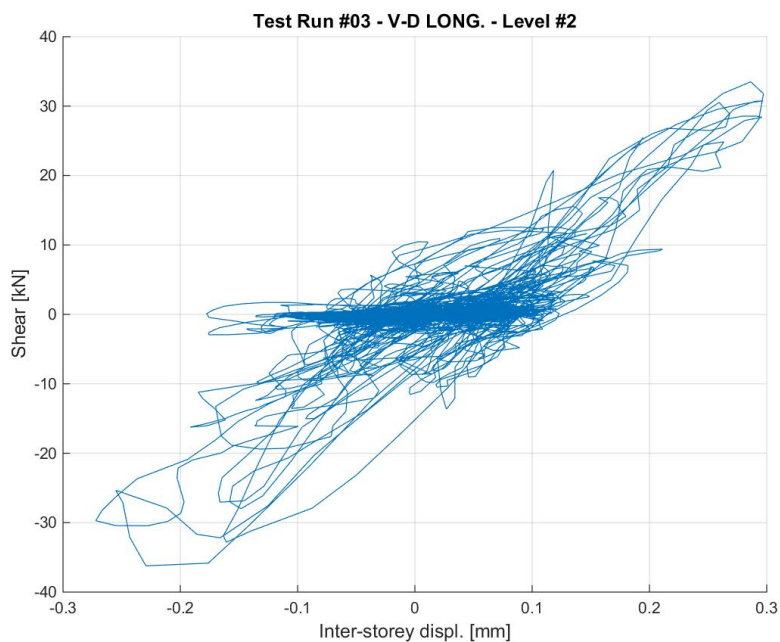
Figure 395. Storey shear vs. inter-storey displacement response – Second storey, Test run #3.

Figure 396 shows the PGA versus maxima – positive and negative – top displacement relationship, the latter parameter being identified according to the linear approximation reported in Figure 391.
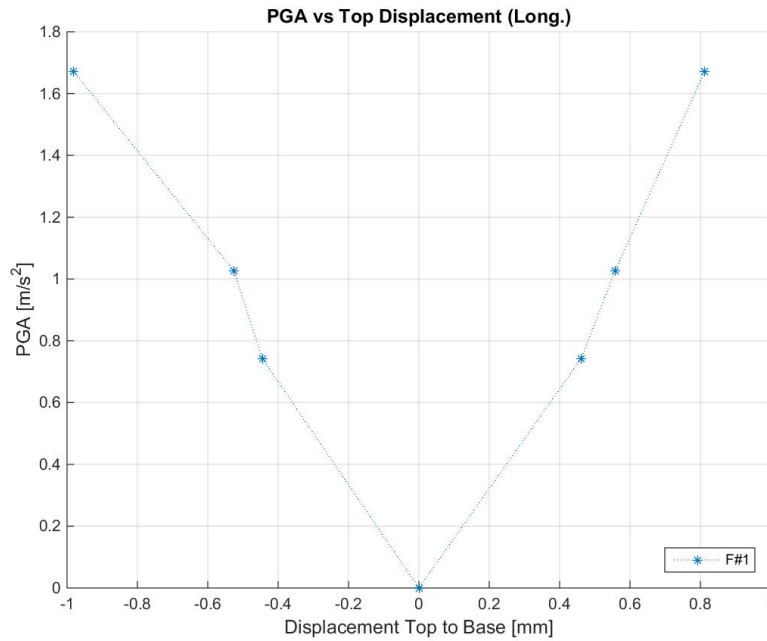
Figure 396. PGA vs. top-to-base displacement maxima – Positive and negative, Test run #3.

Figure 397 shows the PGA versus secant – positive and negative – stiffness relationship, the latter parameter being identified according to the linear approximation reported in Figure 391.
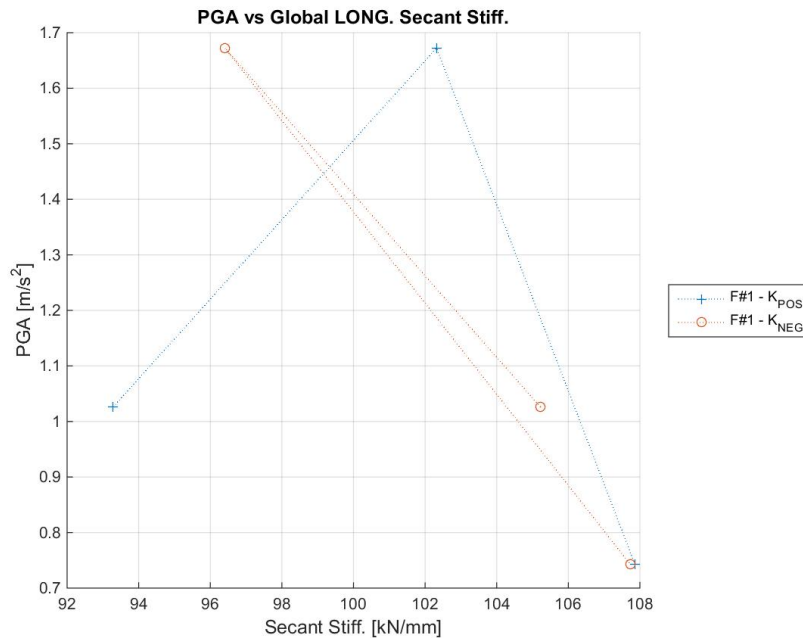
Figure 397. PGA-global secant stiffness relationships – Positive and negative directions, Test run #3.

Figure 398 shows the PGA versus maximum base shear relationship of the specimen at this stage of the testing sequence.
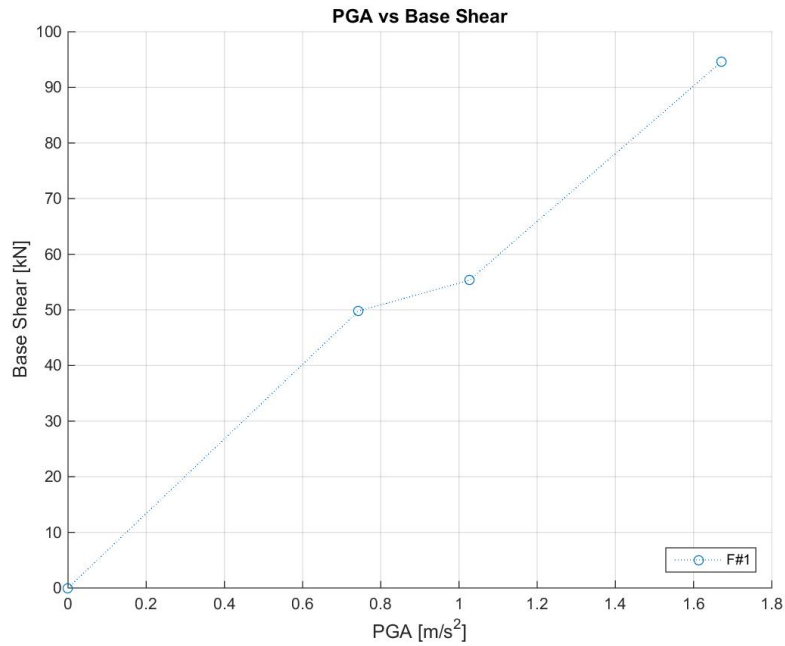
Figure 398. Maximum base shear vs. peak ground acceleration – Test run #3.

Figure 399 shows the arias intensity versus maximum base shear relationship of the specimen at this stage of the testing sequence.
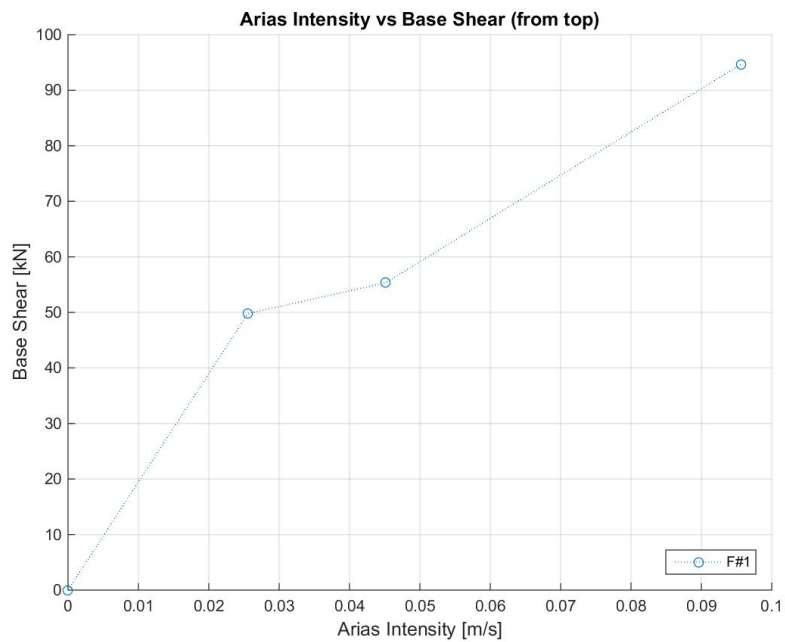
Figure 399. Maximum base shear vs. arias intensity – Test run #3.

6.6.4 Test run #4 – SF = 100% – Test at 100%

Figure 400 shows the comparison between the acceleration spectra from time-histories at reference and feedback (as recorded by the shake-table controller). The experimental acceleration time-history used for the spectrum comparison is the average of the recorded accelerations on the foundation of EUC-BUILD5 specimen (accelerometers #139 and #140). Furthermore, Figure 401 shows the discrepancy in percentage.

Figure 400. Comparison between acceleration spectra from time-histories at reference and feedback.

Figure 401. Discrepancy between acceleration spectra from time-histories at reference and feedback.

Figure 402 shows the acceleration time-histories recorded at the foundation level (accelerometers #139 and #140) and the average of the accelerations recorded by the two accelerometers.
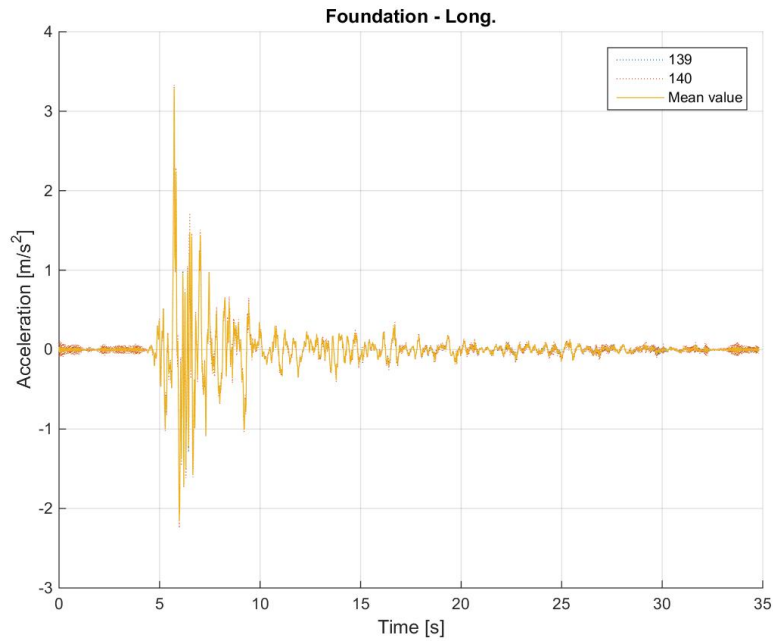
Figure 402. Acceleration time-histories at the foundation level – Individual and average of accelerometers.

Figure 403 shows the acceleration time-histories recorded at the first floor of the specimen and the average of the accelerations recorded by all the accelerometers installed at this level.
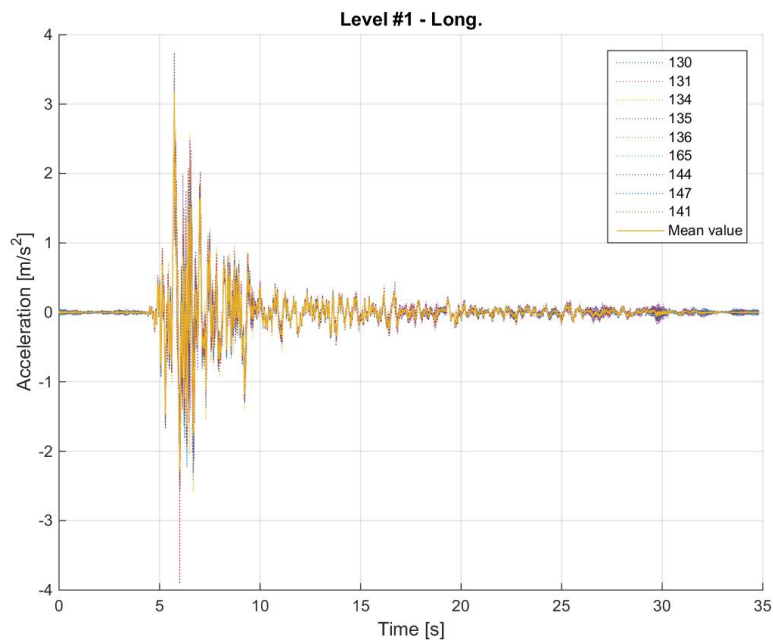
Figure 403. Acceleration time-histories at the first floor – Individual and average of accelerometers.

Figure 404 shows the acceleration time-histories recorded at the second floor and the average of the accelerations recorded by all the accelerometers installed at this level.

Figure 404. Acceleration time-histories at the second floor – Individual and average of accelerometers.

Figure 405 shows a comparison between the average acceleration time-history at the foundation, the first floor and the second floor of the specimen.

Figure 405. Comparison between average acceleration time-histories – Foundation, first and second storeys.

Figure 406 shows a comparison between the acceleration spectra at the base, the first storey and the second storey, which were computed using the average acceleration time-history at the foundation, the first floor and the second floor of the specimen. The spectral accelerations were also normalised with respect to the one at the base and the obtained spectral acceleration ratios are plotted together in Figure 407. Obviously, the curve obtained for the base is the horizontal blue line, which is plotted since it serves as reference for the two floors (and their amplification).

Figure 406. Acceleration spectra from average time-histories at the foundation, first and second floors.

Figure 407. Spectral acceleration ratios: first floor-to-foundation and second floor-to-foundation.

Figure 408 shows a comparison between the displacement time-histories at the foundation, the first floor and the second floor of the specimen.
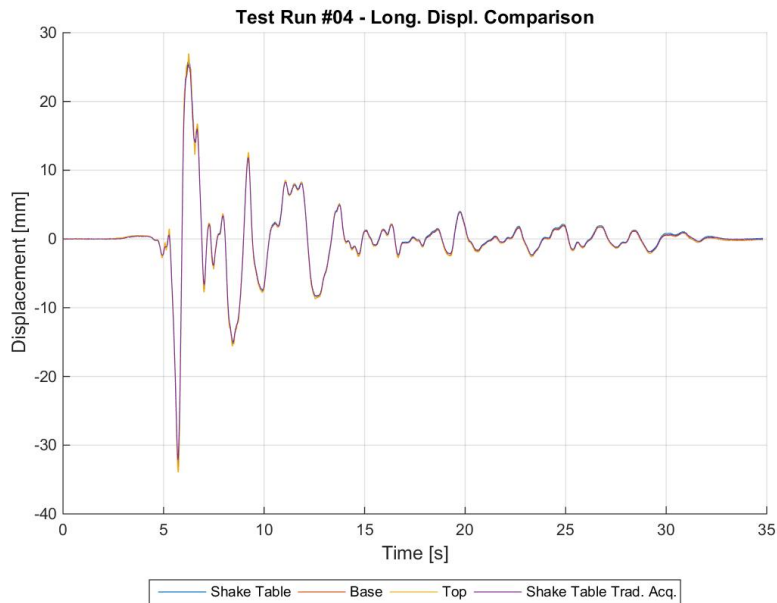
Figure 408. Comparison between average displacement time-histories – Foundation, first and second storeys.

Figure 409 shows a comparison between the imposed base shear time-history and the recorded base shear time-history, the former one being the force applied by the actuators of the shake-table.
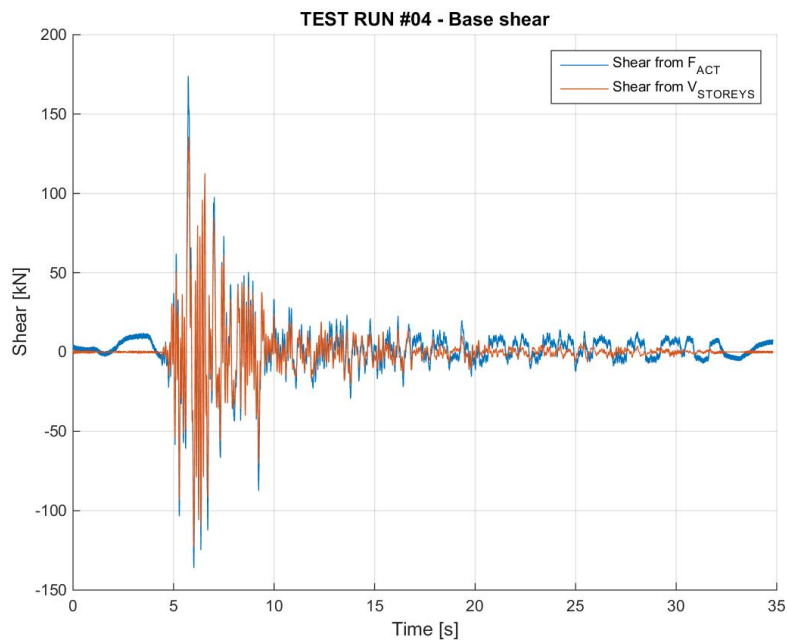
Figure 409. Imposed base shear vs. measured base shear – Comparison through time.

Figure 410 shows the hysteretic base shear-top displacement response of the specimen. For the sake of clarity, it is noted that the total base shear is plotted against the top-to-base displacement of EUC-BUILD5 specimen. Hysteresis loops were also processed to obtain a linear approximation that takes into account both Northward and Southward (i.e. positive and negative) motion and identifies, in an equivalent manner, the corresponding base shear-displacement couples. The hysteretic response and the linear approximation are superimposed in Figure 411.
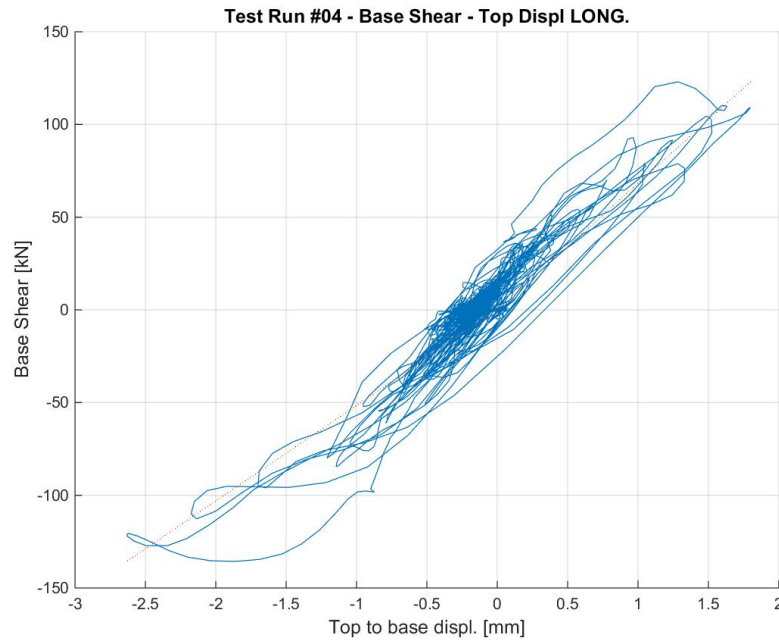
Figure 410. Base shear-top displacement response of EUC-BUILD5 – Test run #4, top-to-base displacement.
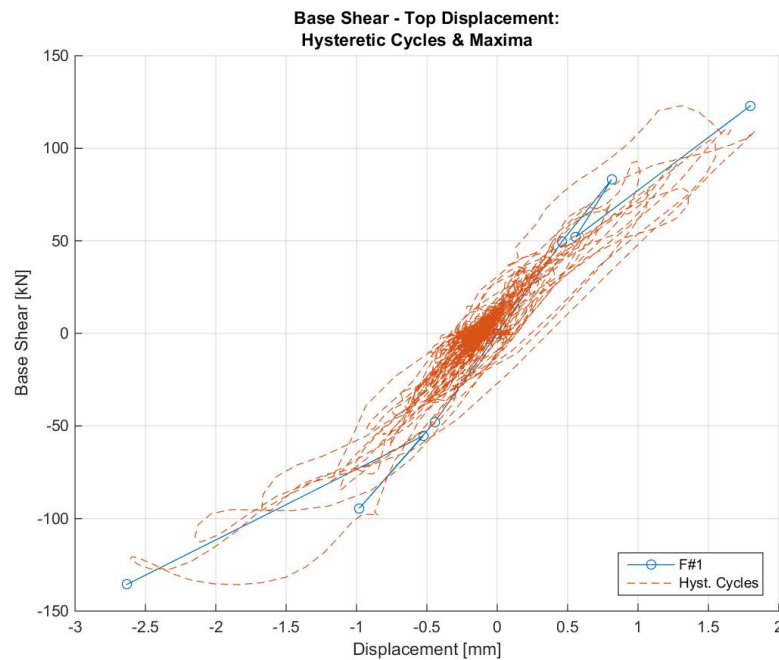
Figure 411. Base shear vs. top-to-base displacement – Hysteretic response and maxima (positive and negative).

Figure 412 shows the absolute maxima – positive or negative – top displacement-base shear couples that were obtained from the hysteresis loops of the specimen.
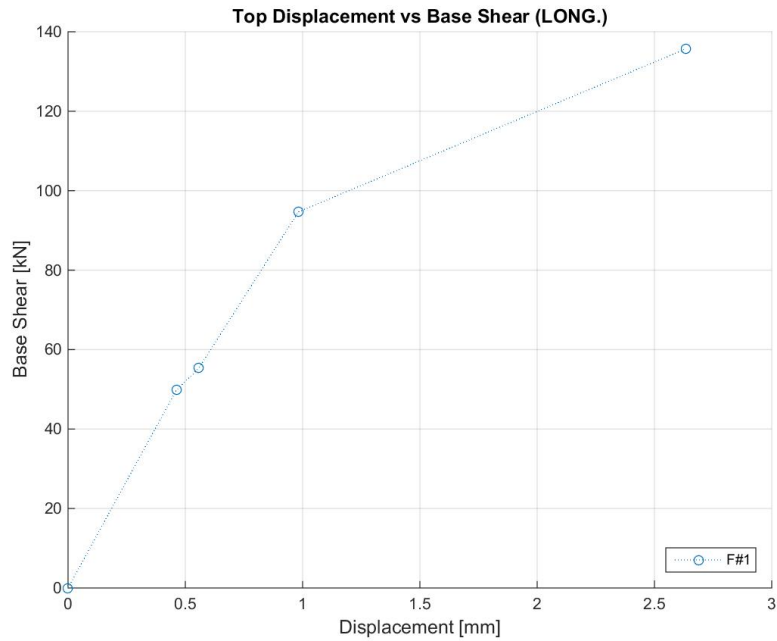
Figure 412. Base shear vs. top-to-base displacement maxima – Test run #4.

Figure 413 shows the maxima – positive and negative – top displacement-base shear couples that were obtained from the linear approximation of the specimen response (see Figure 411).
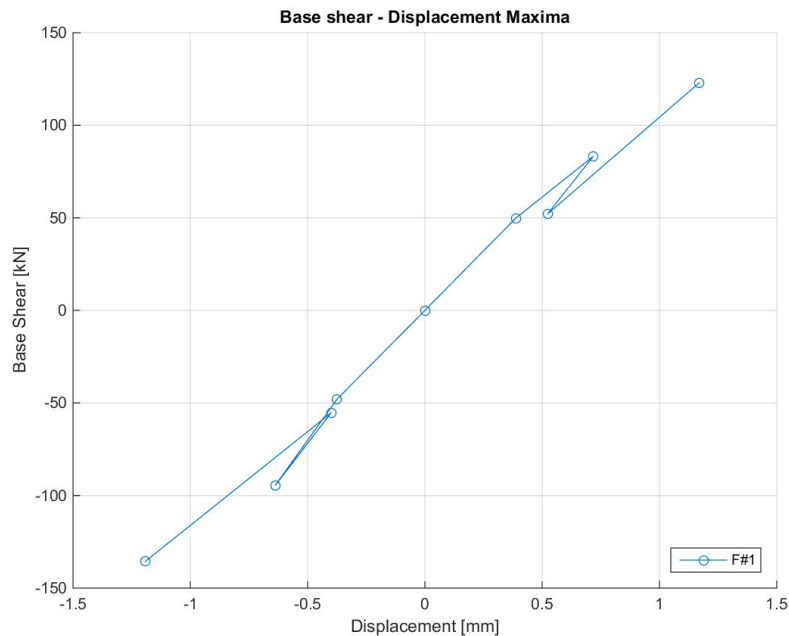
Figure 413. Base shear vs. top-to-base displacement maxima – Positive and negative, Test run #4.

Figure 414 shows the hysteretic response of the first storey of the specimen, which is illustrated in terms of storey shear versus inter-storey displacement relationship.
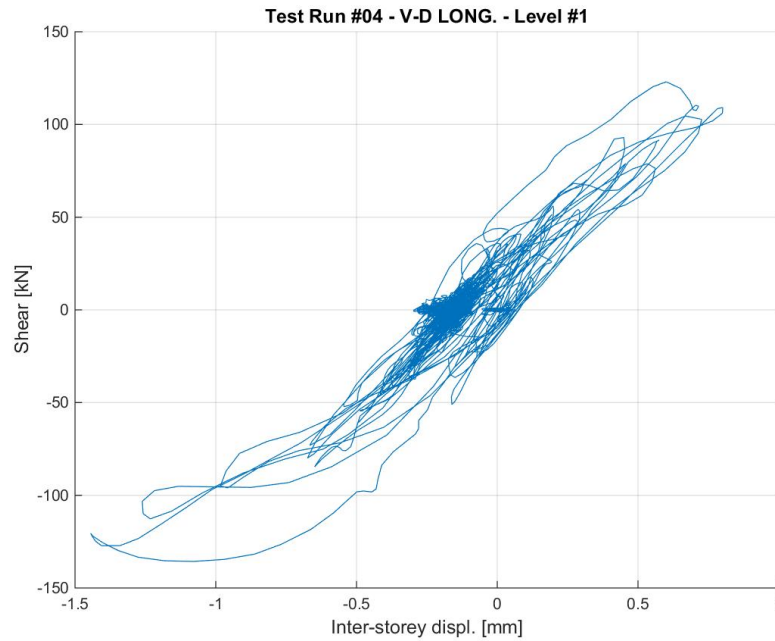
Figure 414. Storey shear vs. inter-storey displacement response – First storey, Test run #4.

Figure 415 shows the hysteretic response of the second storey of the specimen, which is illustrated in terms of storey shear versus inter-storey displacement relationship.
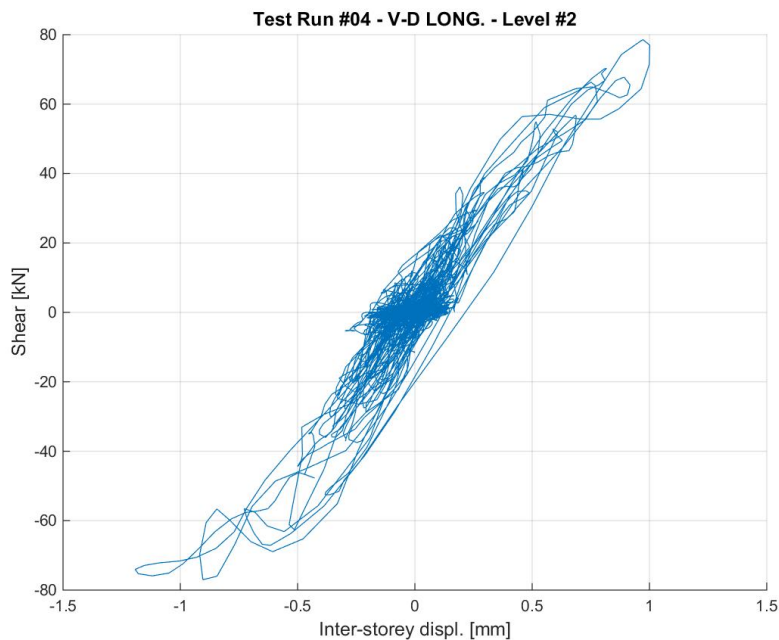
Figure 415. Storey shear vs. inter-storey displacement response – Second storey, Test run #4.

Figure 416 shows the PGA versus maxima – positive and negative – top displacement relationship, the latter parameter being identified according to the linear approximation reported in Figure 411.
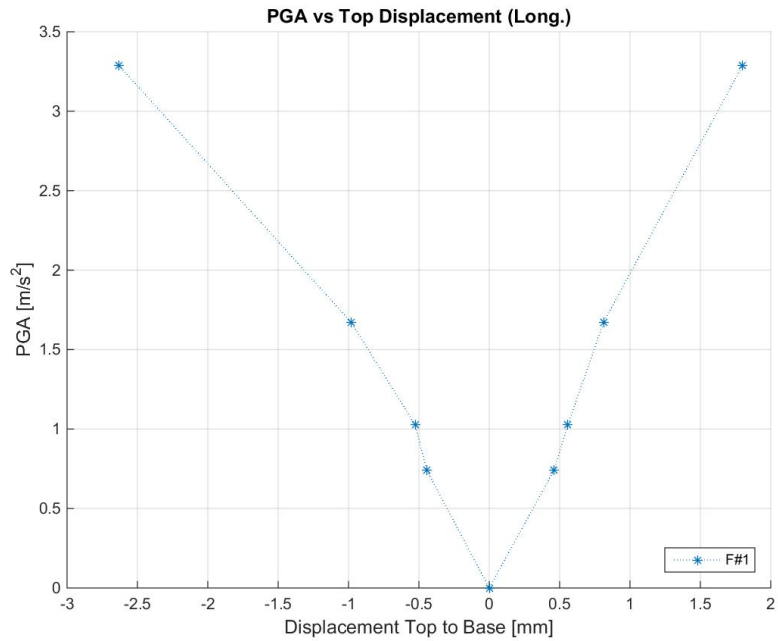
Figure 416. PGA vs. top-to-base displacement maxima – Positive and negative, Test run #4.

Figure 417 shows the PGA versus secant – positive and negative – stiffness relationship, the latter parameter being identified according to the linear approximation reported in Figure 411.
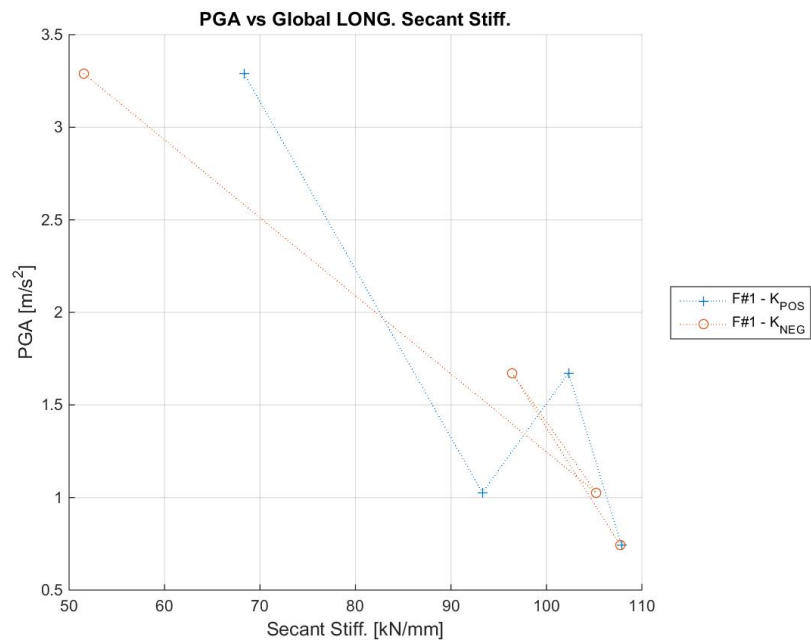
Figure 417. PGA-global secant stiffness relationships – Positive and negative directions, Test run #4.

Figure 418 shows the PGA versus maximum base shear relationship of the specimen at this stage of the testing sequence.
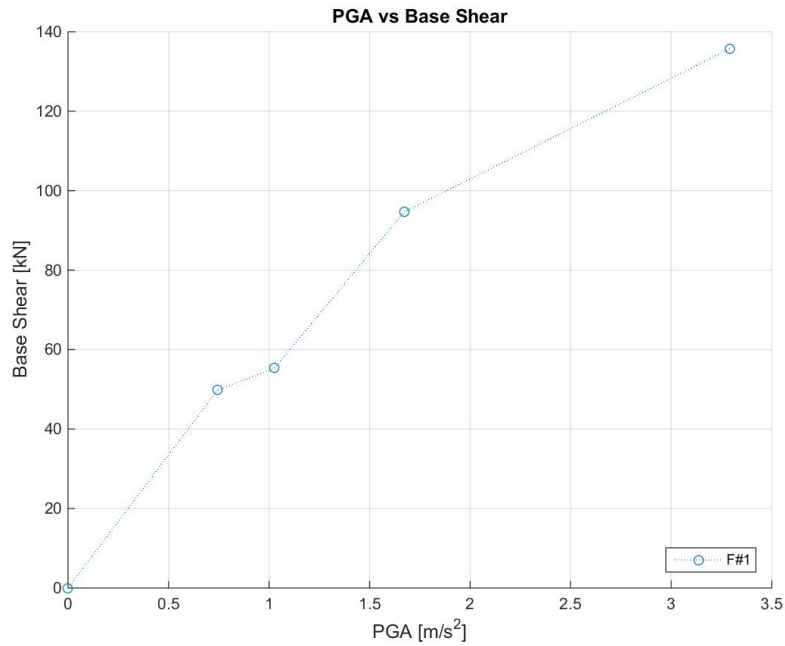
Figure 418. Maximum base shear vs. peak ground acceleration – Test run #4.

Figure 419 shows the arias intensity versus maximum base shear relationship of the specimen at this stage of the testing sequence.
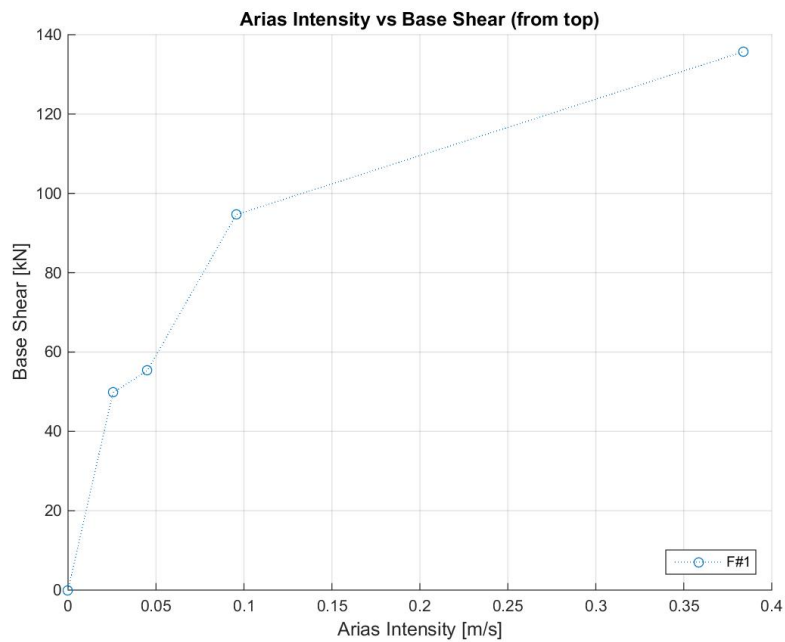
Figure 419. Maximum base shear vs. arias intensity – Test run #4.

6.6.5 Test run #5 – SF = 34% – Controller compensation

Figure 420 shows the comparison between the acceleration spectra from time-histories at reference and feedback (as recorded by the shake-table controller). The experimental acceleration time-history used for the spectrum comparison is the average of the recorded accelerations on the foundation of EUC-BUILD5 specimen (accelerometers #139 and #140). Furthermore, Figure 421 shows the discrepancy in percentage.
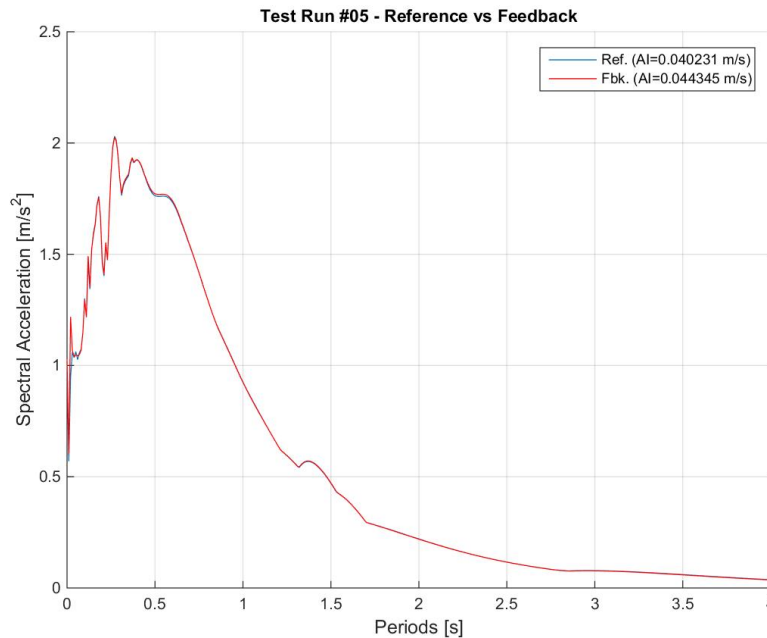
Figure 420. Comparison between acceleration spectra from time-histories at reference and feedback.
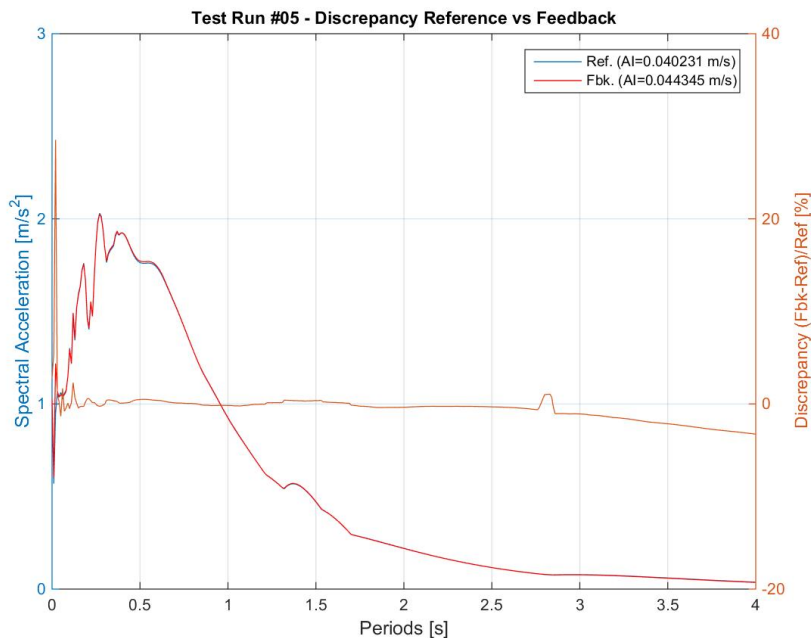
Figure 421. Discrepancy between acceleration spectra from time-histories at reference and feedback.

Figure 422 shows the acceleration time-histories recorded at the foundation level (accelerometers #139 and #140) and the average of the accelerations recorded by the two accelerometers.
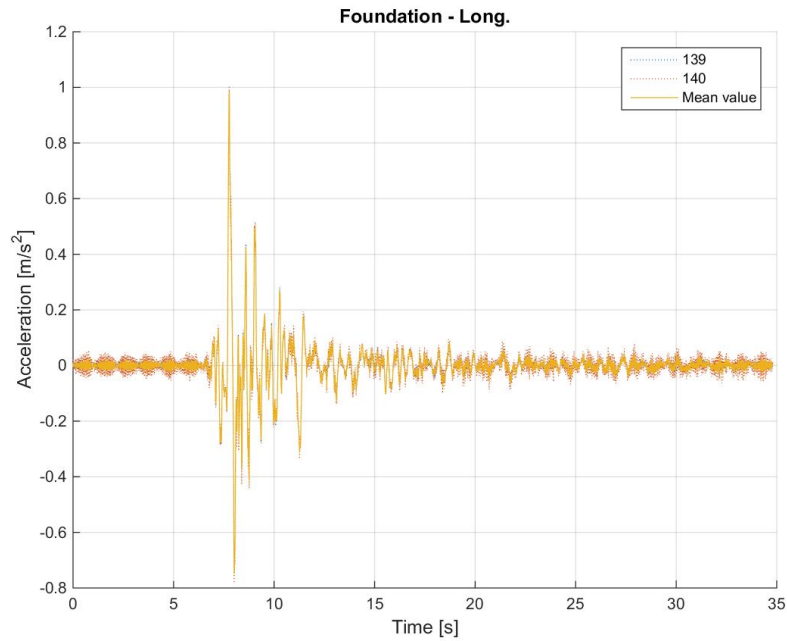
Figure 422. Acceleration time-histories at the foundation level – Individual and average of accelerometers.

Figure 423 shows the acceleration time-histories recorded at the first floor of the specimen and the average of the accelerations recorded by all the accelerometers installed at this level.
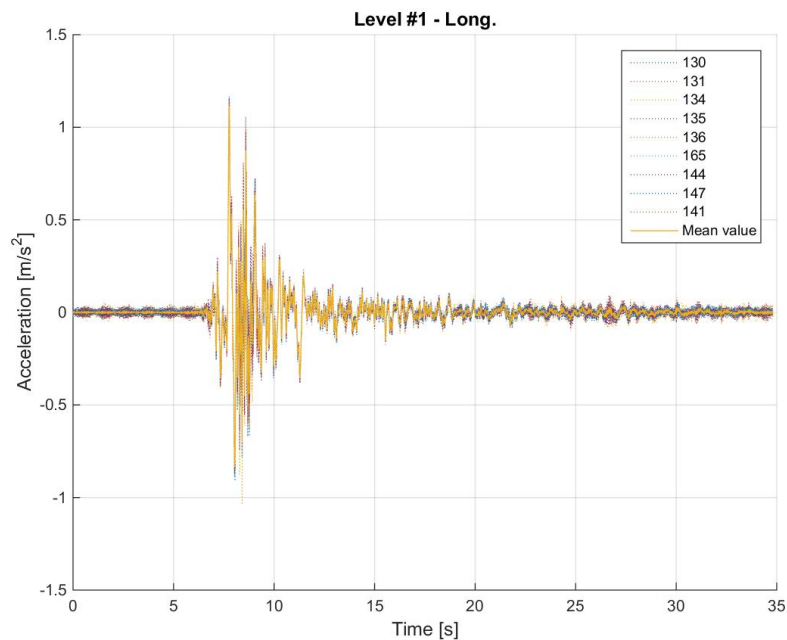
Figure 423. Acceleration time-histories at the first floor – Individual and average of accelerometers.

Figure 424 shows the acceleration time-histories recorded at the second floor and the average of the accelerations recorded by all the accelerometers installed at this level.
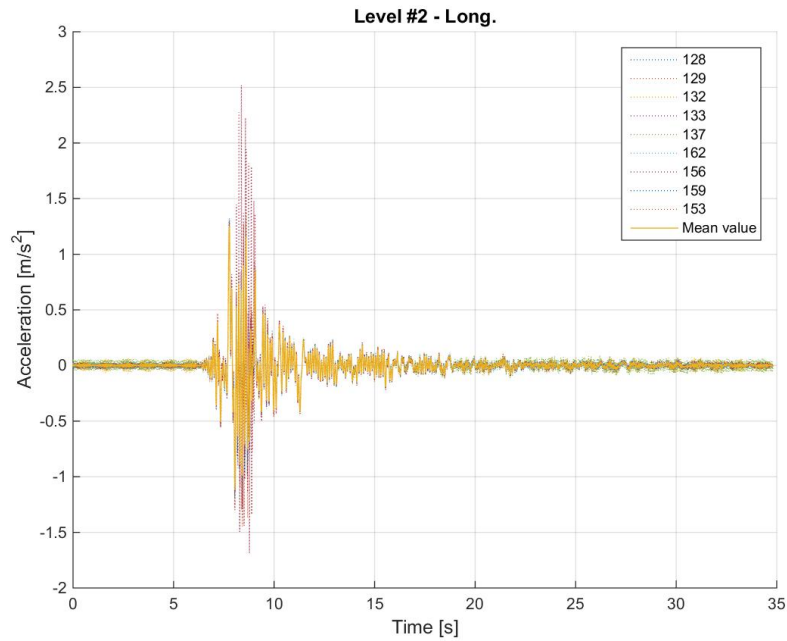
Figure 424. Acceleration time-histories at the second floor – Individual and average of accelerometers.

Figure 425 shows a comparison between the average acceleration time-history at the foundation, the first floor and the second floor of the specimen.
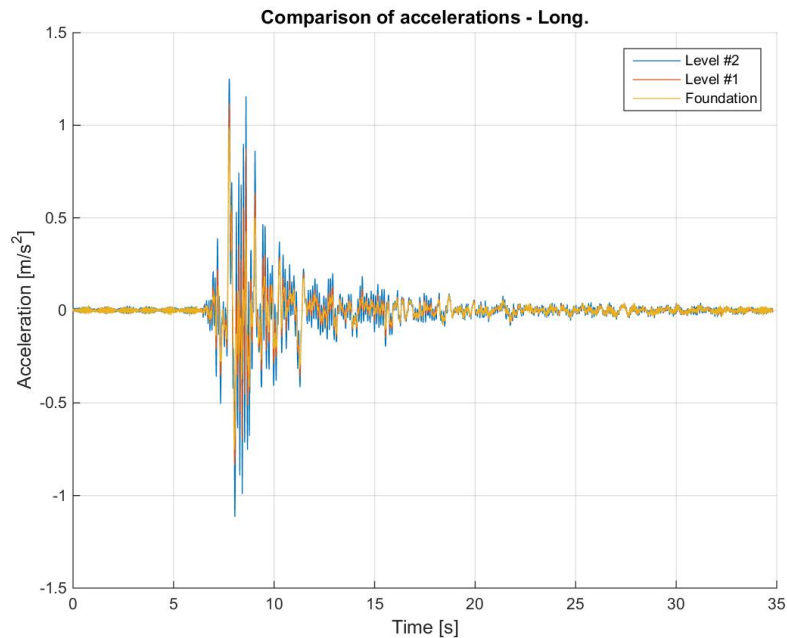

Figure 425. Comparison between average acceleration time-histories – Foundation, first and second storeys.

Figure 426 shows a comparison between the acceleration spectra at the base, the first storey and the second storey, which were computed using the average acceleration time-history at the foundation, the first floor and the second floor of the specimen. The spectral accelerations were also normalised with respect to the one at the base and the obtained spectral acceleration ratios are plotted together in Figure 427. Obviously, the curve obtained for the base is the horizontal blue line, which is plotted since it serves as reference for the two floors (and their amplification).
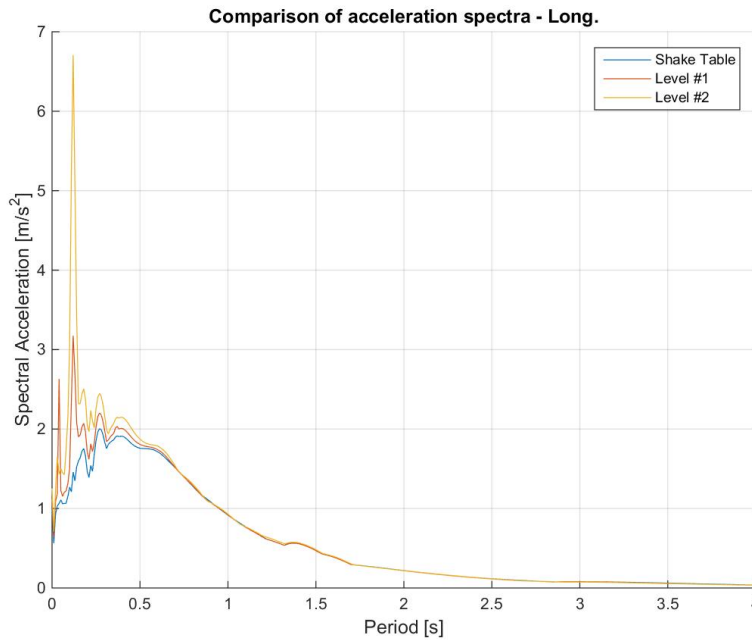
Figure 426. Acceleration spectra from average time-histories at the foundation, first and second floors.
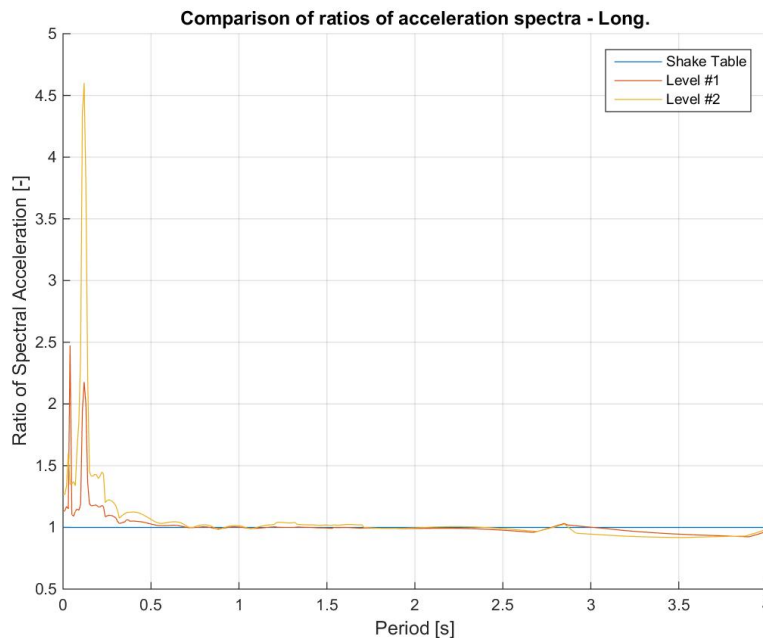
Figure 427. Spectral acceleration ratios: first floor-to-foundation and second floor-to-foundation.

Figure 428 shows a comparison between the displacement time-histories at the foundation, the first floor and the second floor of the specimen.
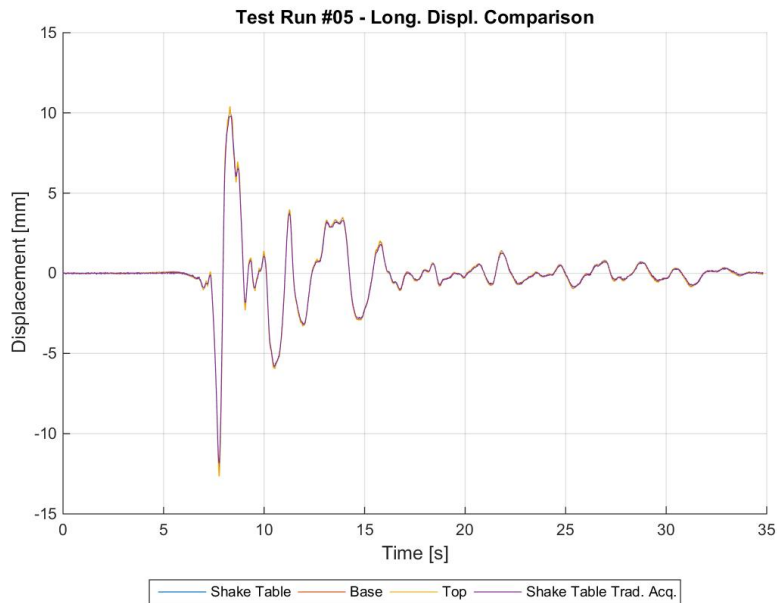
Figure 428. Comparison between average displacement time-histories – Foundation, first and second storeys.

Figure 429 shows a comparison between the imposed base shear time-history and the recorded base shear time-history, the former one being the force applied by the actuators of the shake-table.
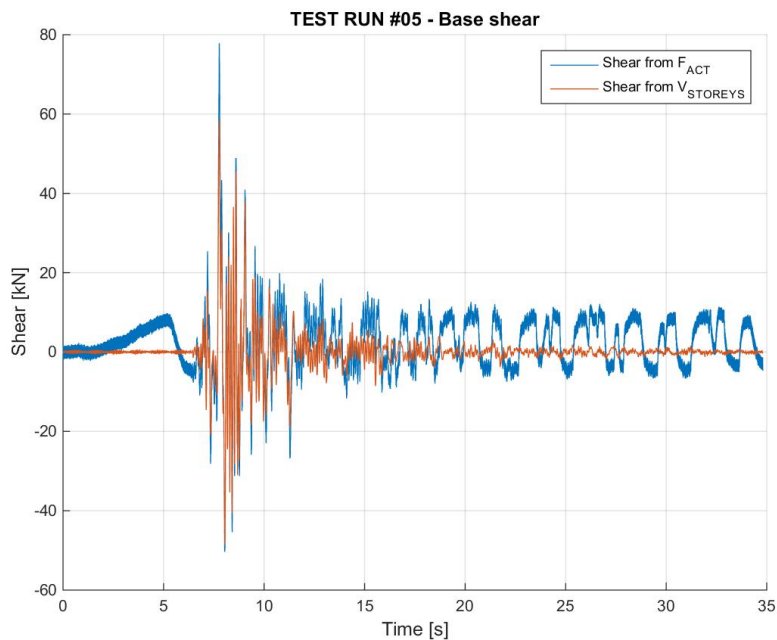
Figure 429. Imposed base shear vs. measured base shear – Comparison through time.

Figure 430 shows the hysteretic base shear-top displacement response of the specimen. For the sake of clarity, it is noted that the total base shear is plotted against the top-to-base displacement of EUC-BUILD5 specimen. Hysteresis loops were also processed to obtain a linear approximation that takes into account both Northward and Southward (i.e. positive and negative) motion and identifies, in an equivalent manner, the corresponding base shear-displacement couples. The hysteretic response and the linear approximation are superimposed in Figure 431.
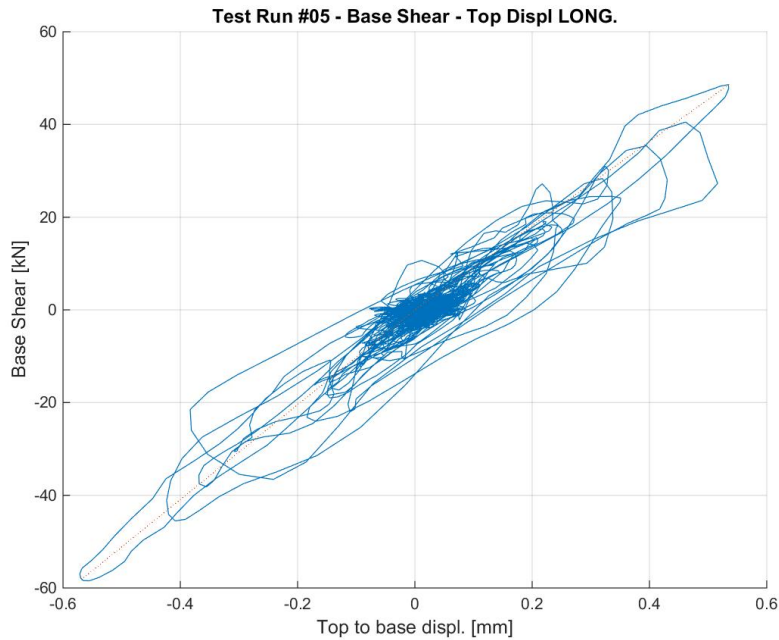
Figure 430. Base shear-top displacement response of EUC-BUILD5 – Test run #5, top-to-base displacement.
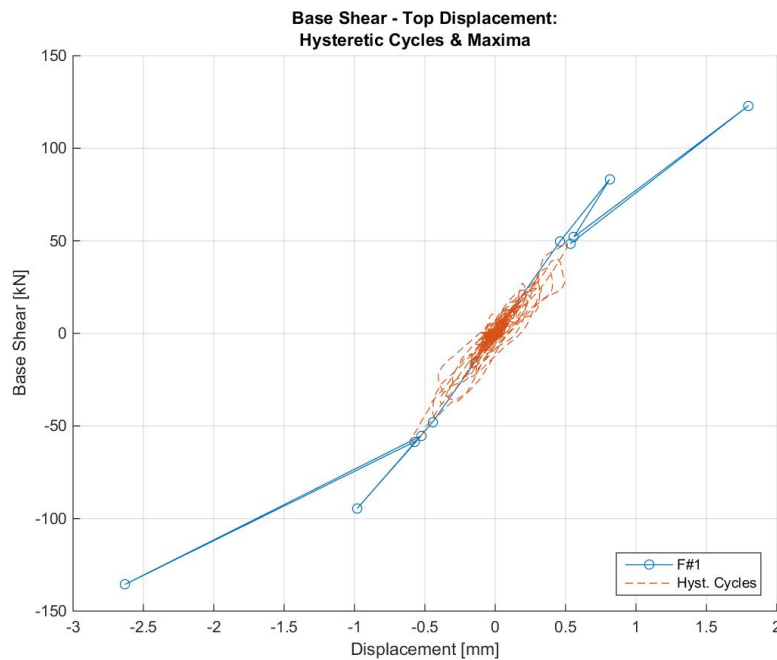
Figure 431. Base shear vs. top-to-base displacement – Hysteretic response and maxima (positive and negative).

Figure 432 shows the absolute maxima – positive or negative – top displacement-base shear couples that were obtained from the hysteresis loops of the specimen.
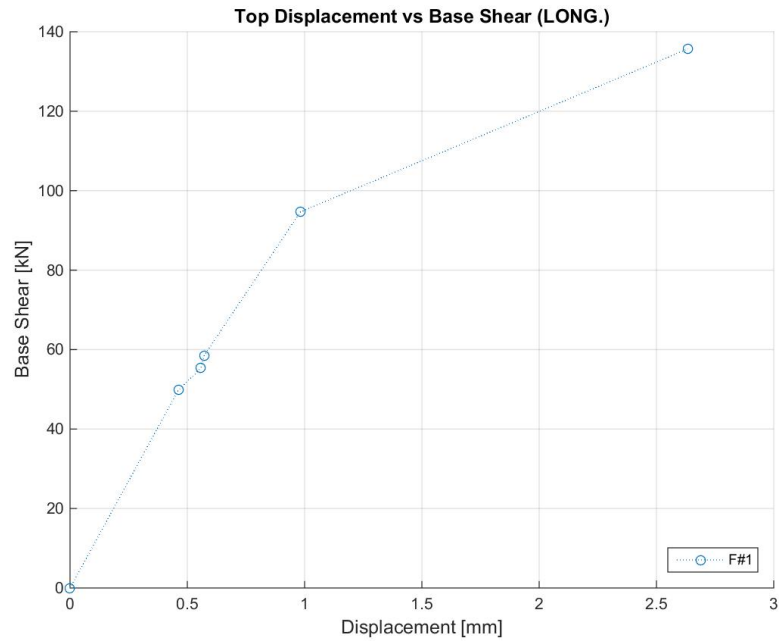
Figure 432. Base shear vs. top-to-base displacement maxima – Test run #5.

Figure 433 shows the maxima – positive and negative – top displacement-base shear couples that were obtained from the linear approximation of the specimen response (see Figure 431).
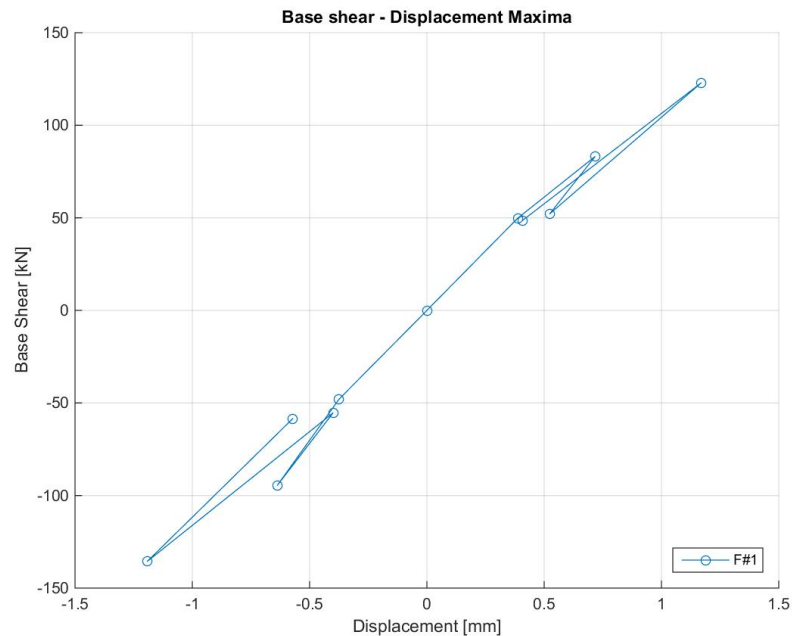
Figure 433. Base shear vs. top-to-base displacement maxima – Positive and negative, Test run #5.

Figure 434 shows the hysteretic response of the first storey of the specimen, which is illustrated in terms of storey shear versus inter-storey displacement relationship.
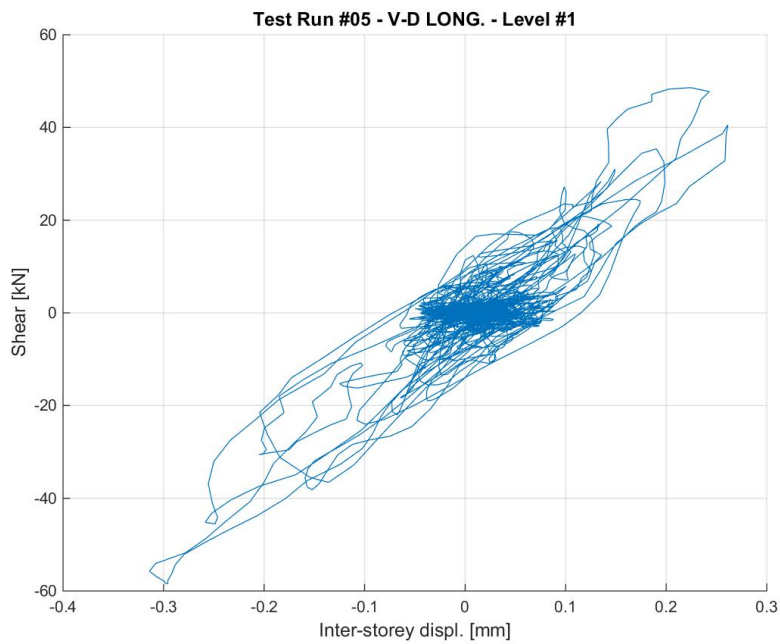
Figure 434. Storey shear vs. inter-storey displacement response – First storey, Test run #5.

Figure 435 shows the hysteretic response of the second storey of the specimen, which is illustrated in terms of storey shear versus inter-storey displacement relationship.
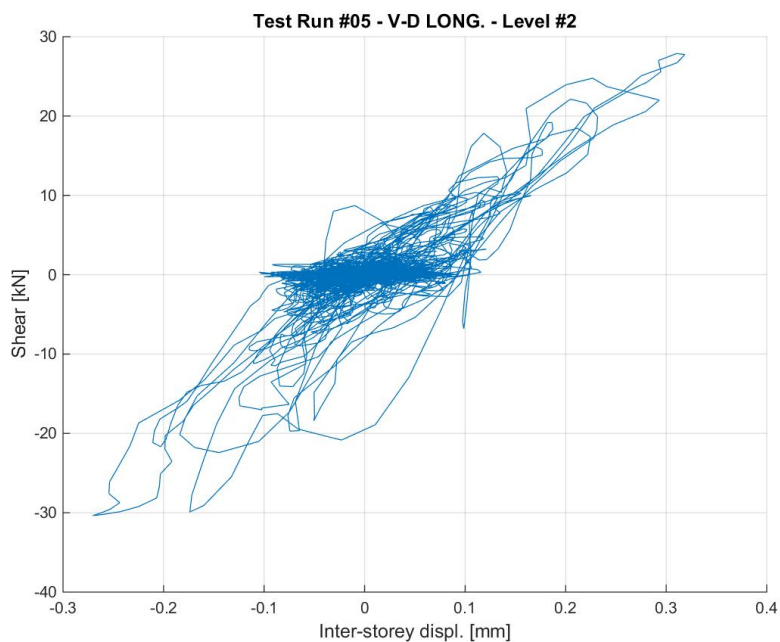
Figure 435. Storey shear vs. inter-storey displacement response – Second storey, Test run #5.

Figure 436 shows the PGA versus maxima – positive and negative – top displacement relationship, the latter parameter being identified according to the linear approximation reported in Figure 431.
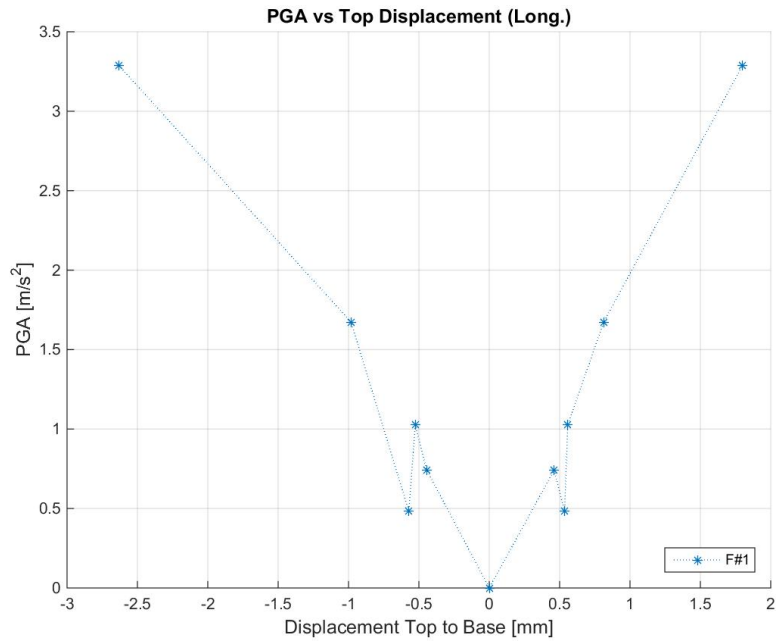

Figure 436. PGA vs. top-to-base displacement maxima – Positive and negative, Test run #5.

Figure 437 shows the PGA versus secant – positive and negative – stiffness relationship, the latter parameter being identified according to the linear approximation reported in Figure 431.
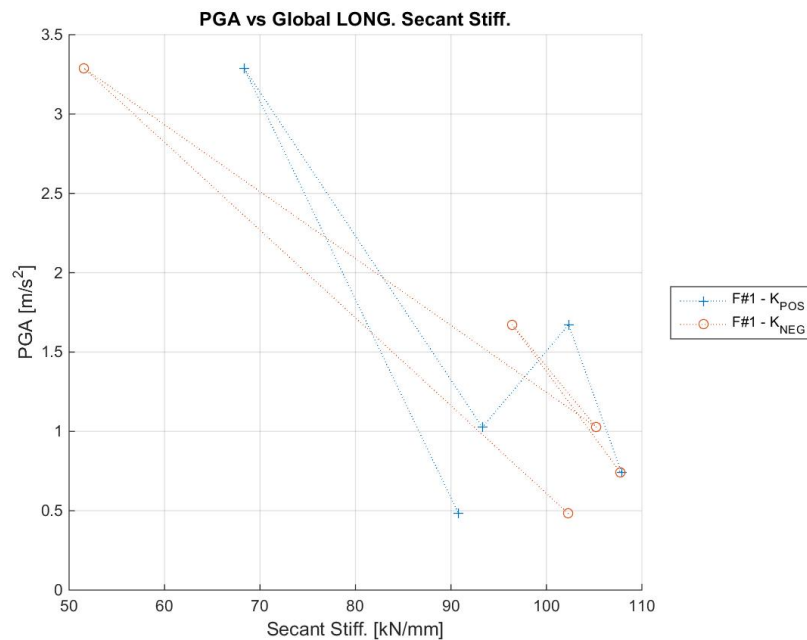
Figure 437. PGA-global secant stiffness relationships – Positive and negative directions, Test run #5.

Figure 438 shows the PGA versus maximum base shear relationship of the specimen at this stage of the testing sequence.
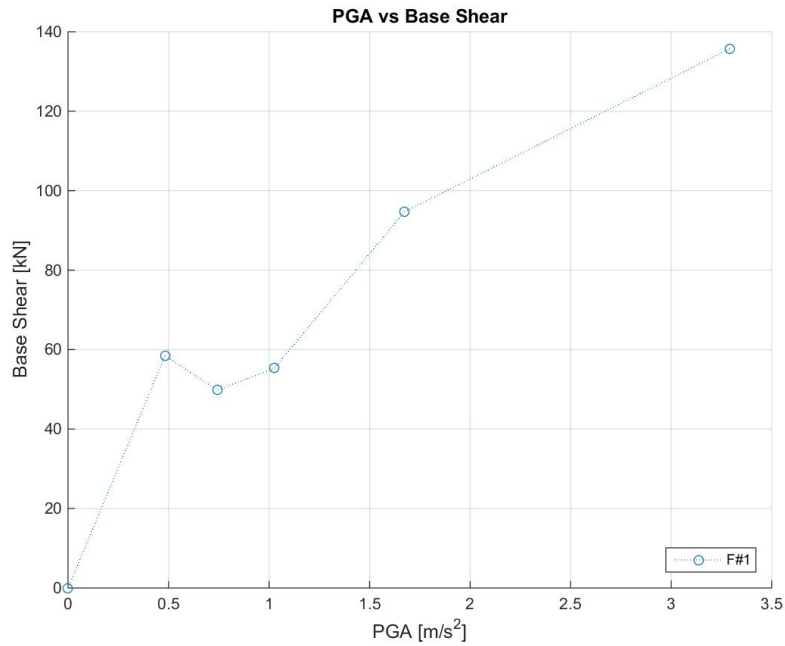
Figure 438. Maximum base shear vs. peak ground acceleration – Test run #5.

Figure 439 shows the arias intensity versus maximum base shear relationship of the specimen at this stage of the testing sequence.
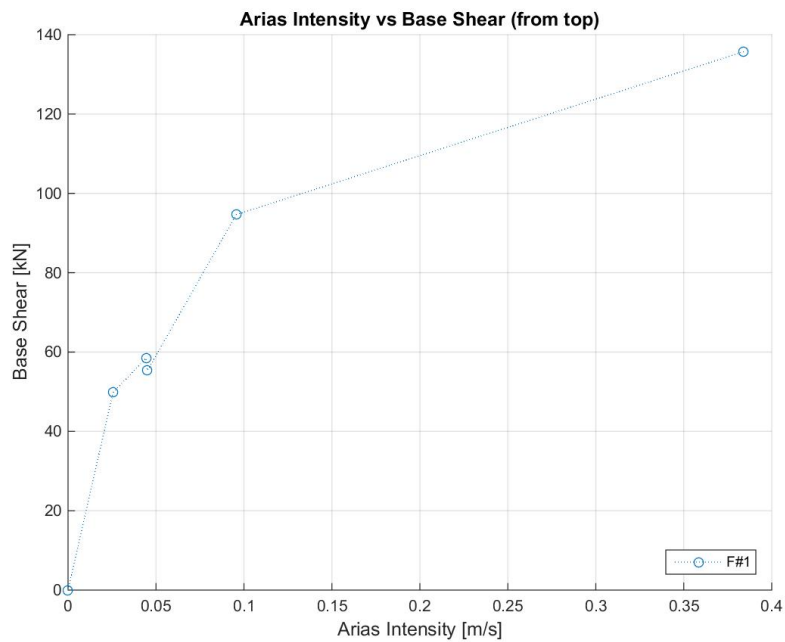
Figure 439. Maximum base shear vs. arias intensity – Test run #5.

6.6.6 Test run #6 – SF = 150% – Test at 150%

Figure 440 shows the comparison between the acceleration spectra from time-histories at reference and feedback (as recorded by the shake-table controller). The experimental acceleration time-history used for the spectrum comparison is the average of the recorded accelerations on the foundation of EUC-BUILD5 specimen (accelerometers #139 and #140). Furthermore, Figure 441 shows the discrepancy in percentage.
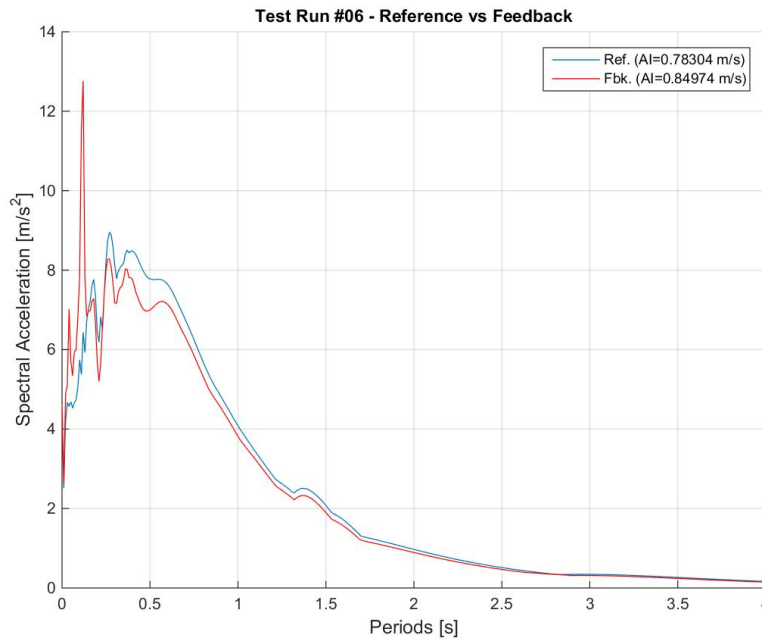
Figure 440. Comparison between acceleration spectra from time-histories at reference and feedback.
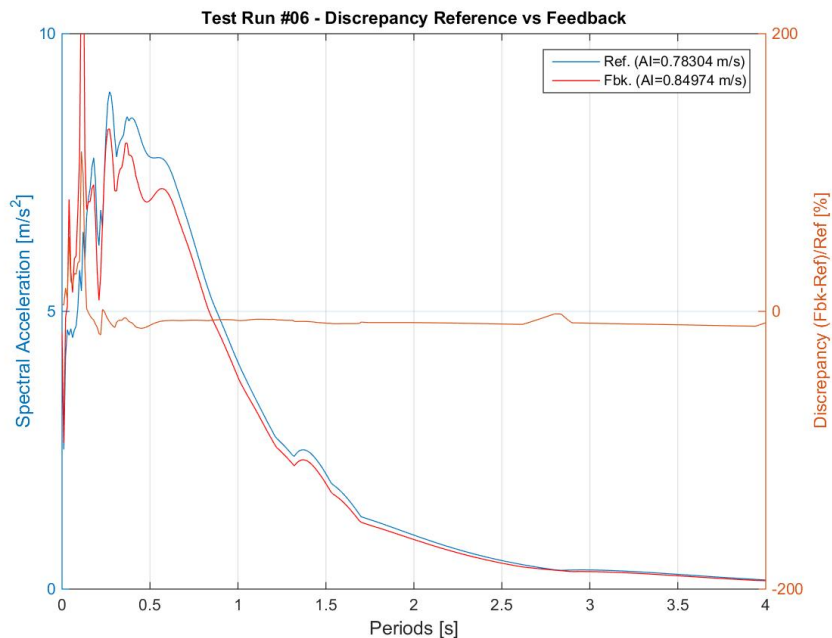

Figure 441. Discrepancy between acceleration spectra from time-histories at reference and feedback.

Figure 442 shows the acceleration time-histories recorded at the foundation level (accelerometers #139 and #140) and the average of the accelerations recorded by the two accelerometers.
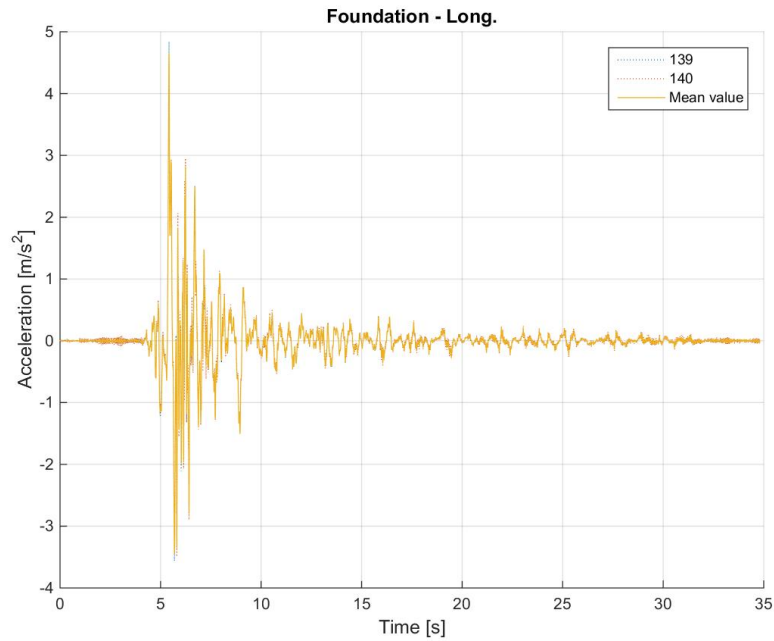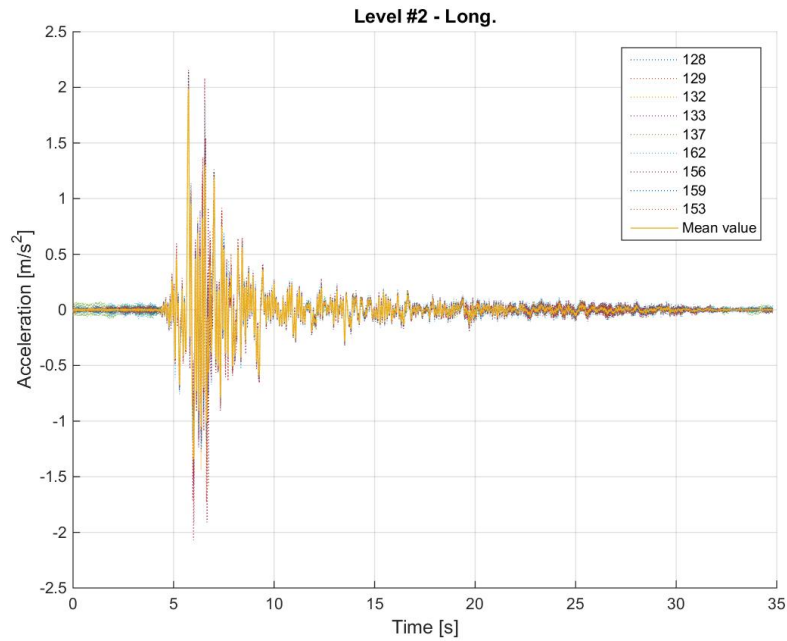

Figure 442. Acceleration time-histories at the foundation level – Individual and average of accelerometers.

Figure 443 shows the acceleration time-histories recorded at the first floor of the specimen and the average of the accelerations recorded by all the accelerometers installed at this level.
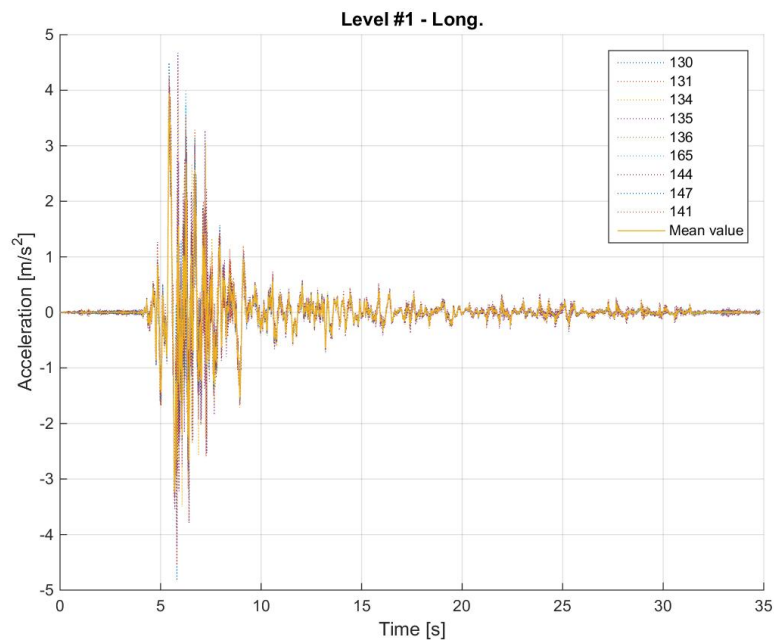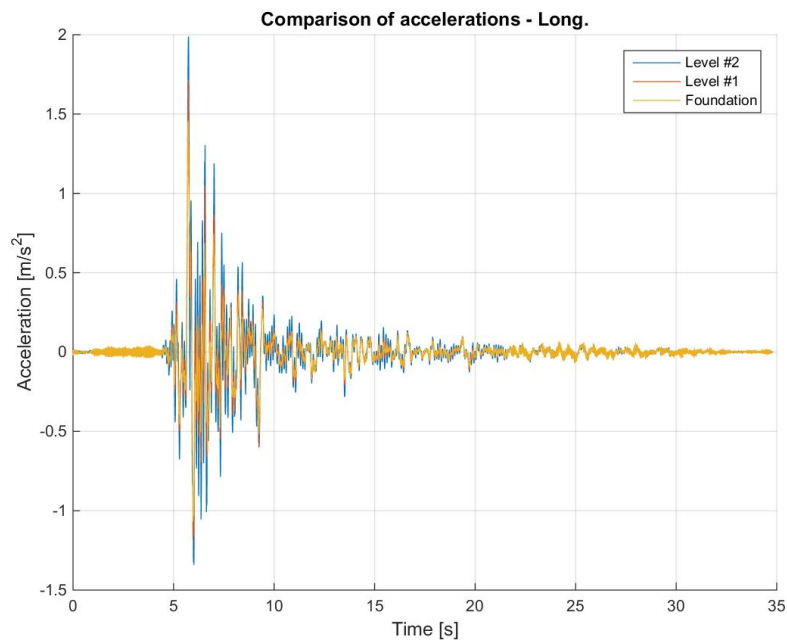

Figure 443. Acceleration time-histories at the first floor – Individual and average of accelerometers.

Figure 444 shows the acceleration time-histories recorded at the second floor and the average of the accelerations recorded by all the accelerometers installed at this level.
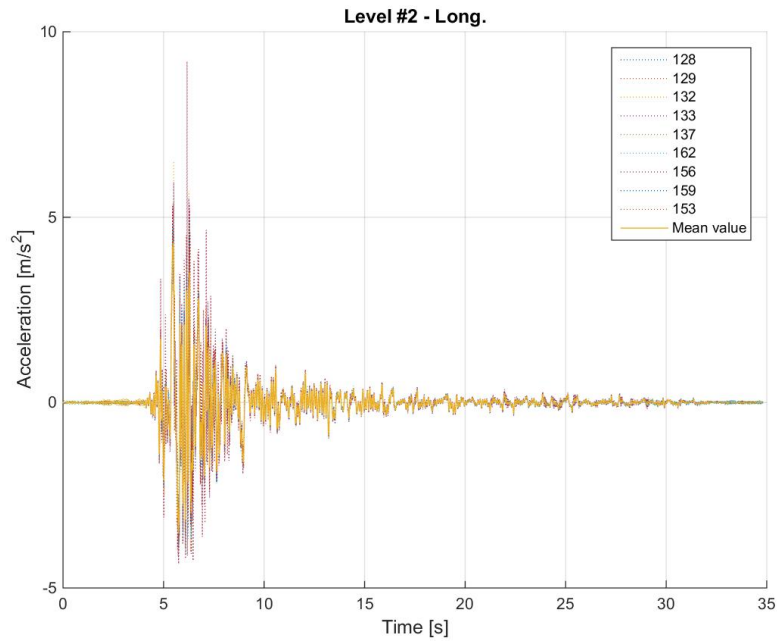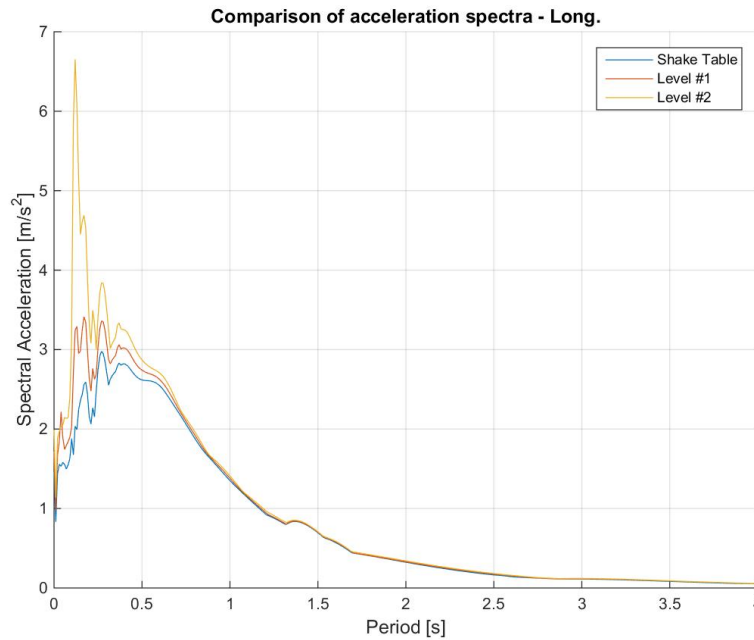

Figure 444. Acceleration time-histories at the second floor – Individual and average of accelerometers.

Figure 445 shows a comparison between the average acceleration time-history at the foundation, the first floor and the second floor of the specimen.
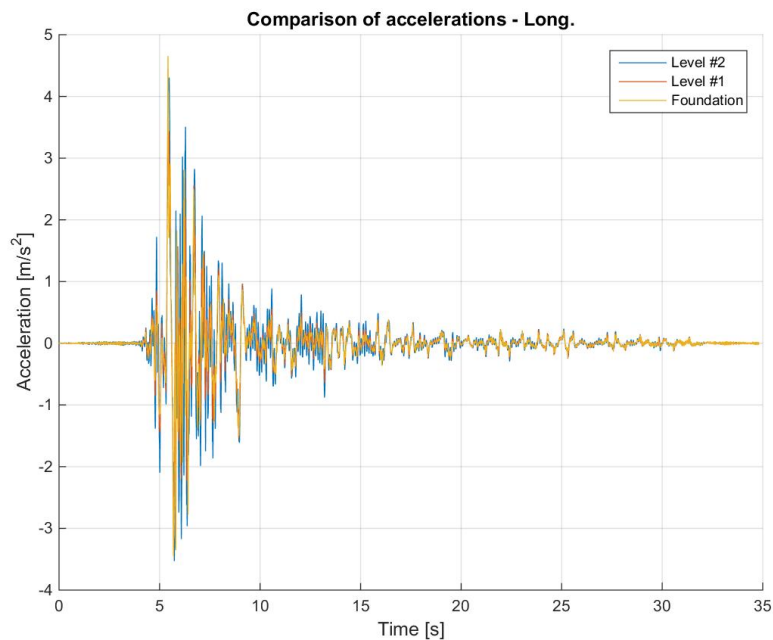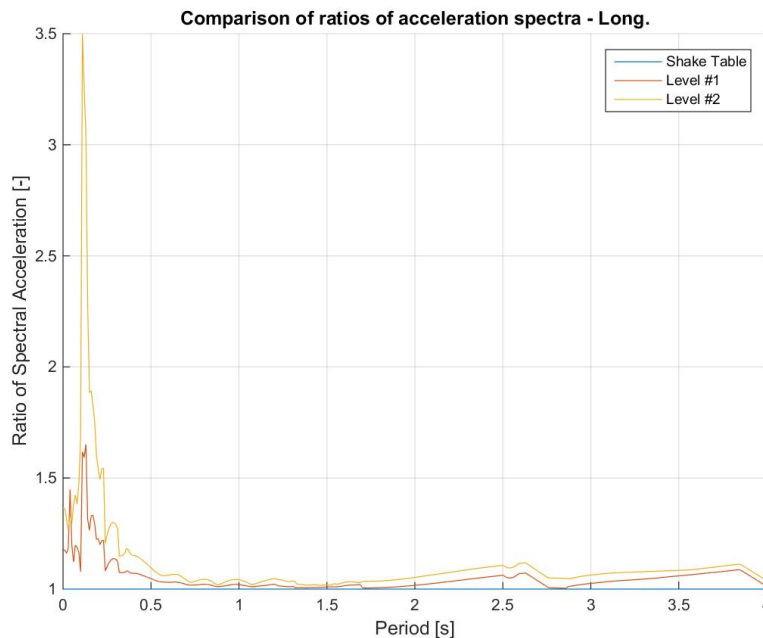

Figure 445. Comparison between average acceleration time-histories – Foundation, first and second storeys.

Figure 446 shows a comparison between the acceleration spectra at the base, the first storey and the second storey, which were computed using the average acceleration time-history at the foundation, the first floor and the second floor of the specimen. The spectral accelerations were also normalised with respect to the one at the base and the obtained spectral acceleration ratios are plotted together in Figure 447. Obviously, the curve obtained for the base is the horizontal blue line, which is plotted since it serves as reference for the two floors (and their amplification).
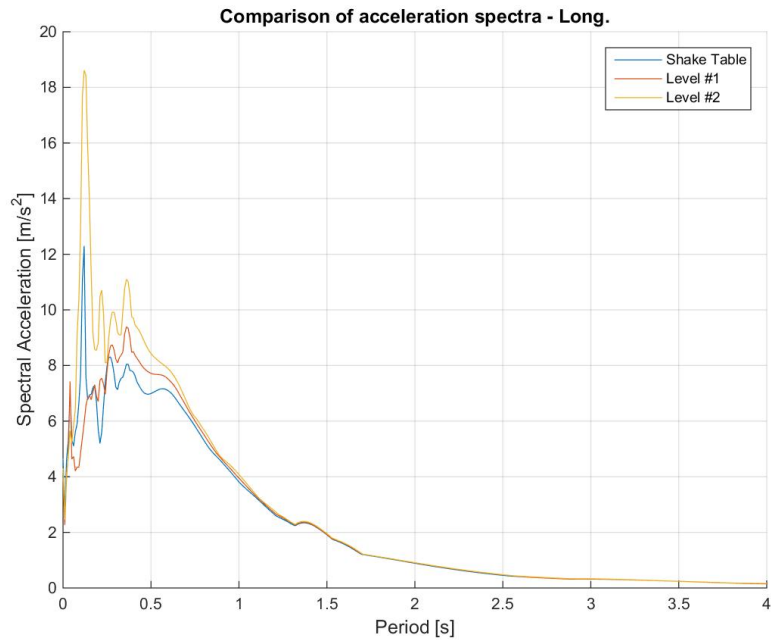

Figure 446. Acceleration spectra from average time-histories at the foundation, first and second floors.
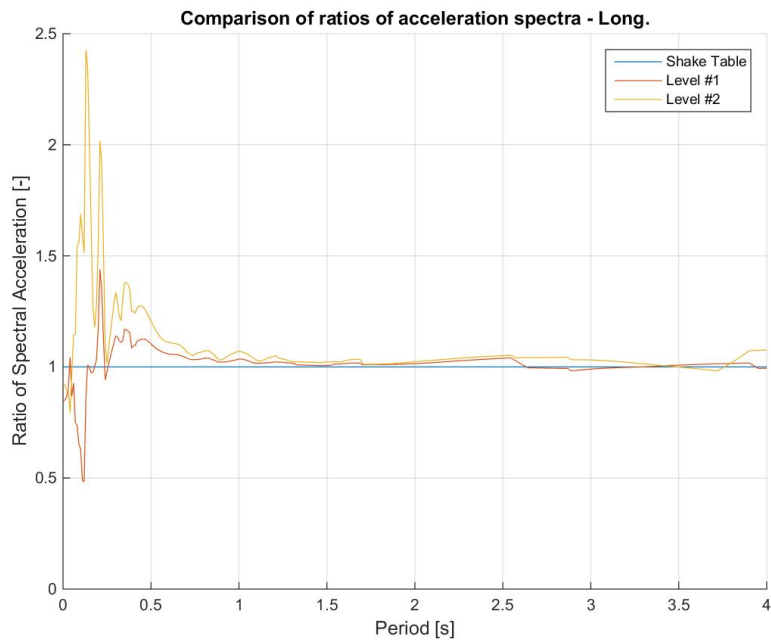

Figure 447. Spectral acceleration ratios: first floor-to-foundation and second floor-to-foundation.

Figure 448 shows a comparison between the displacement time-histories at the foundation, the first floor and the second floor of the specimen.
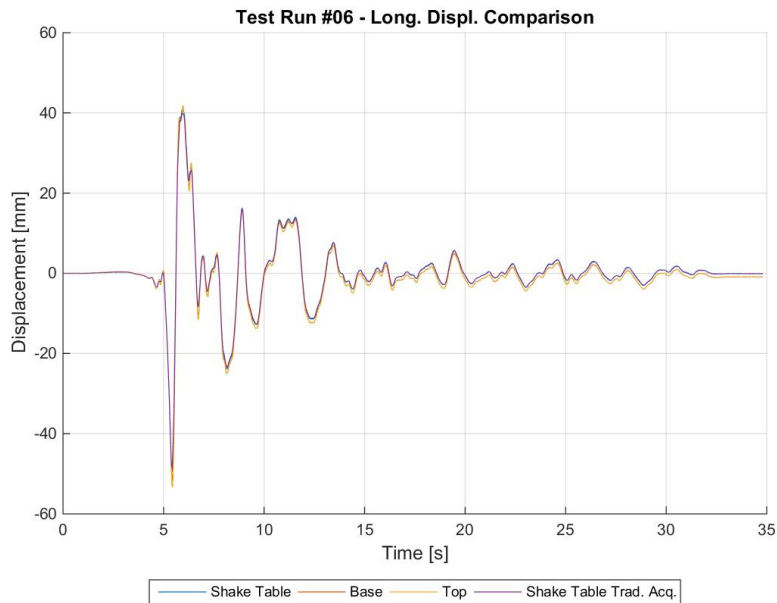

Figure 448. Comparison between average displacement time-histories – Foundation, first and second storeys.

Figure 449 shows a comparison between the imposed base shear time-history and the recorded base shear time-history, the former one being the force applied by the actuators of the shake-table.
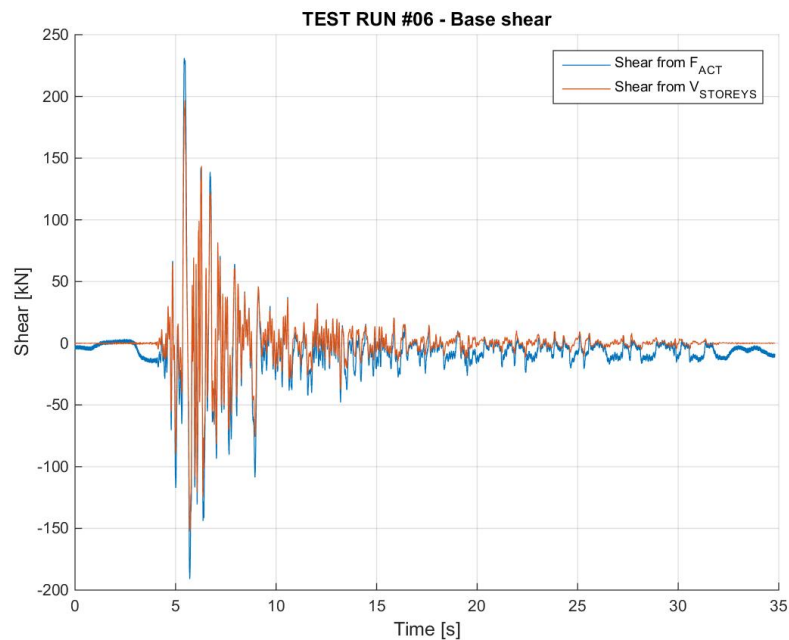

Figure 449. Imposed base shear vs. measured base shear – Comparison through time.

Figure 450 shows the hysteretic base shear-top displacement response of the specimen. For the sake of clarity, it is noted that the total base shear is plotted against the top-to-base displacement of EUC-BUILD5 specimen. Hysteresis loops were also processed to obtain a linear approximation that takes into account both Northward and Southward (i.e. positive and negative) motion and identifies, in an equivalent manner, the corresponding base shear-displacement couples. The hysteretic response and the linear approximation are superimposed in Figure 451.
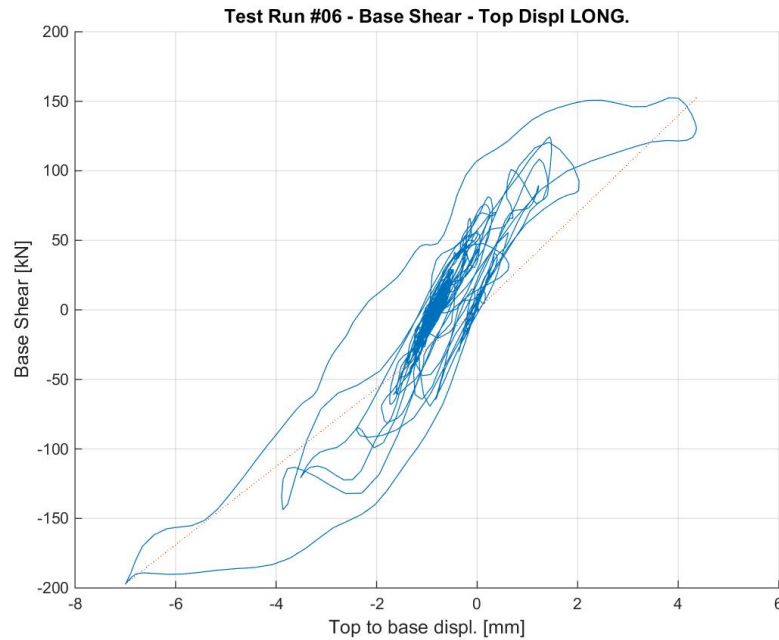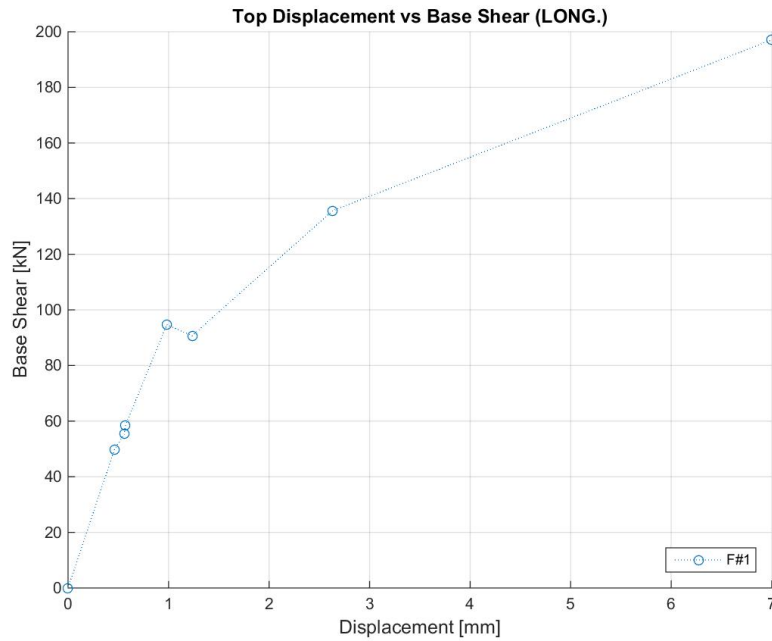

Figure 450. Base shear-top displacement response of EUC-BUILD5 – Test run #6, top-to-base displacement.
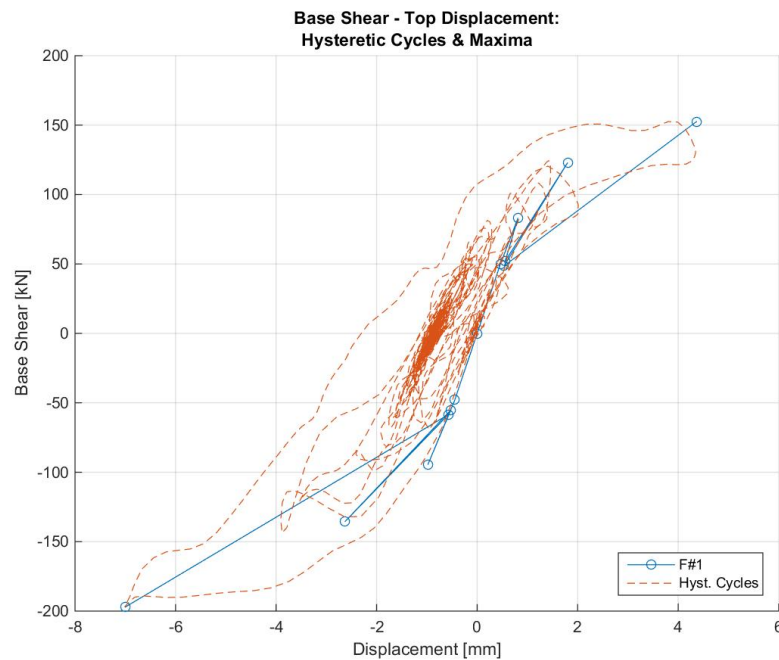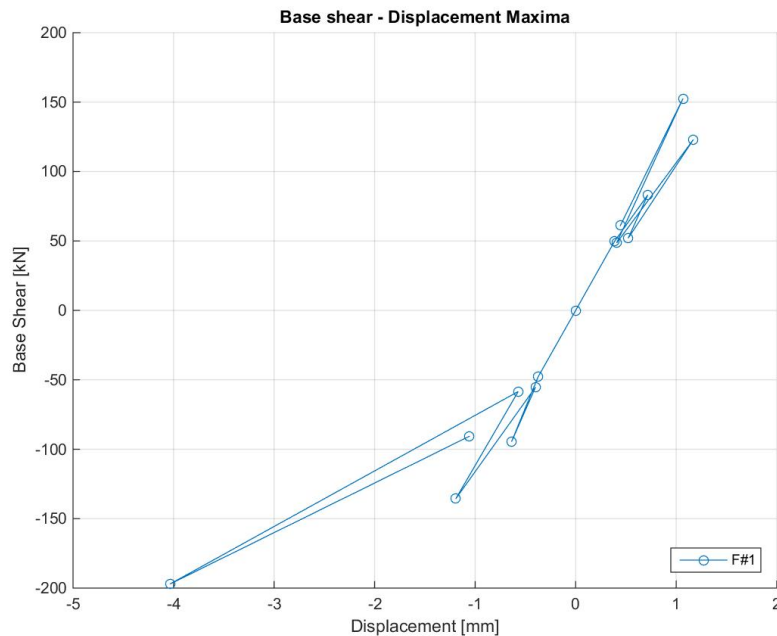

Figure 451. Base shear vs. top-to-base displacement – Hysteretic response and maxima (positive and negative).

Figure 452 shows the absolute maxima – positive or negative – top displacement-base shear couples that were obtained from the hysteresis loops of the specimen.
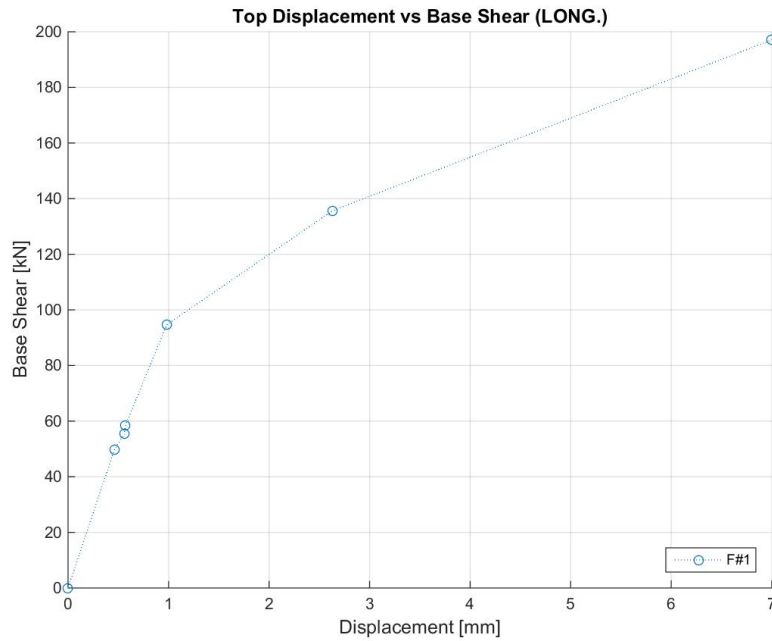

Figure 452. Base shear vs. top-to-base displacement maxima – Test run #6.

Figure 453 shows the maxima – positive and negative – top displacement-base shear couples that were obtained from the linear approximation of the specimen response (see Figure 288).
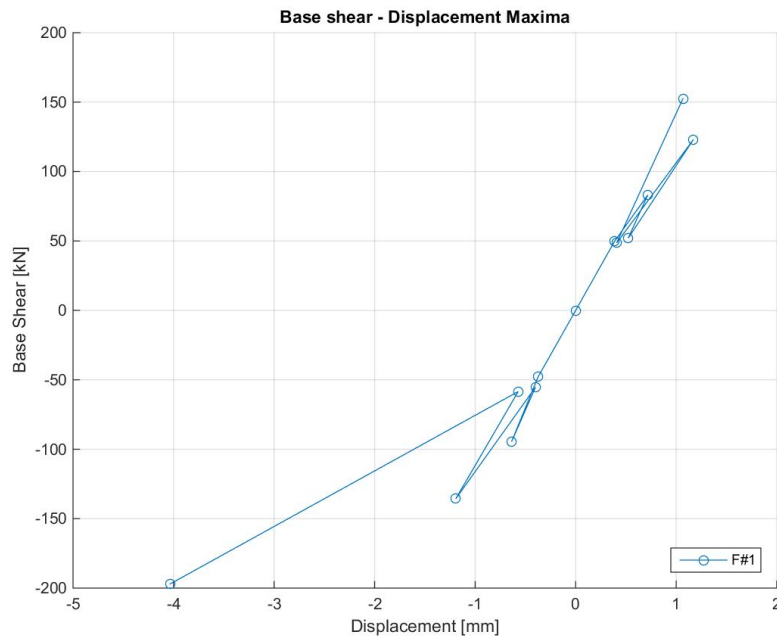

Figure 453. Base shear vs. top-to-base displacement maxima – Positive and negative, Test run #6.

Figure 454 shows the hysteretic response of the first storey of the specimen, which is illustrated in terms of storey shear versus inter-storey displacement relationship.
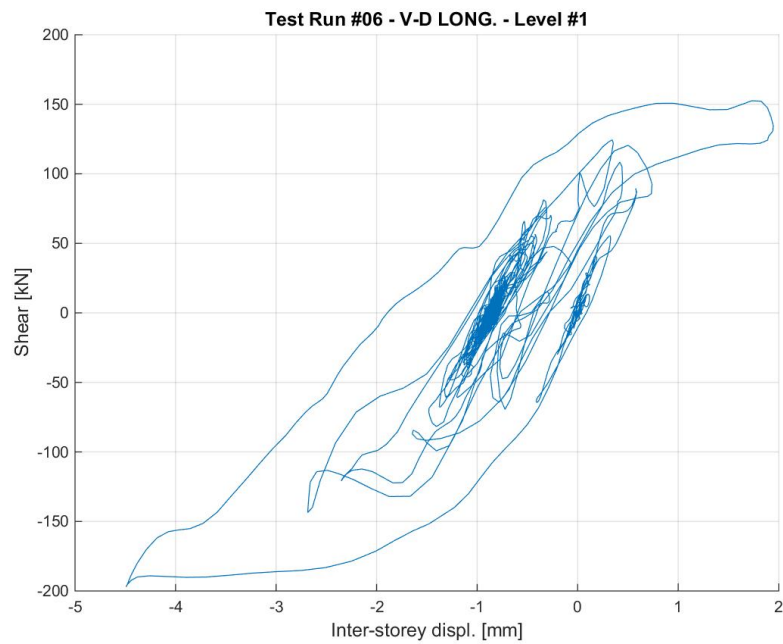
Figure 454. Storey shear vs. inter-storey displacement response – First storey, Test run #6.

Figure 455 shows the hysteretic response of the second storey of the specimen, which is illustrated in terms of storey shear versus inter-storey displacement relationship.
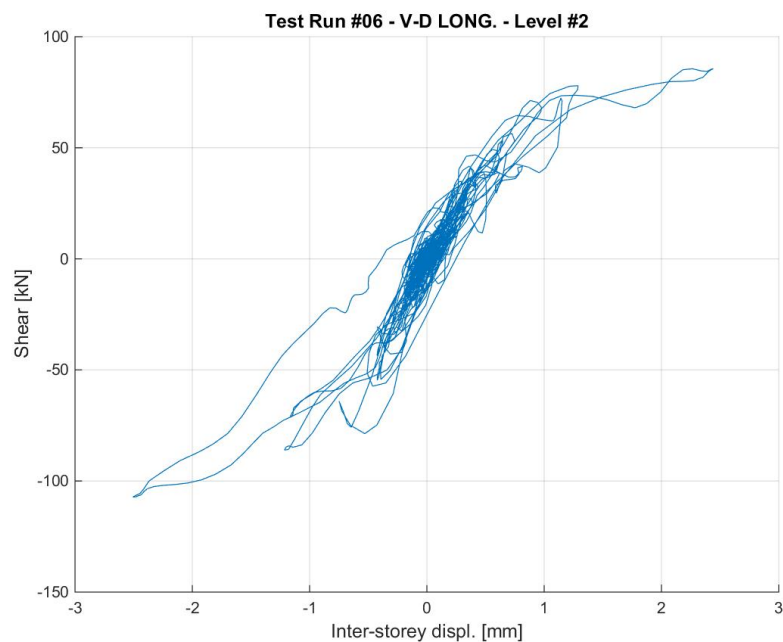
Figure 455. Storey shear vs. inter-storey displacement response – Second storey, Test run #6.

Figure 456 shows the PGA versus maxima – positive and negative – top displacement relationship, the latter parameter being identified according to the linear approximation reported in Figure 288.
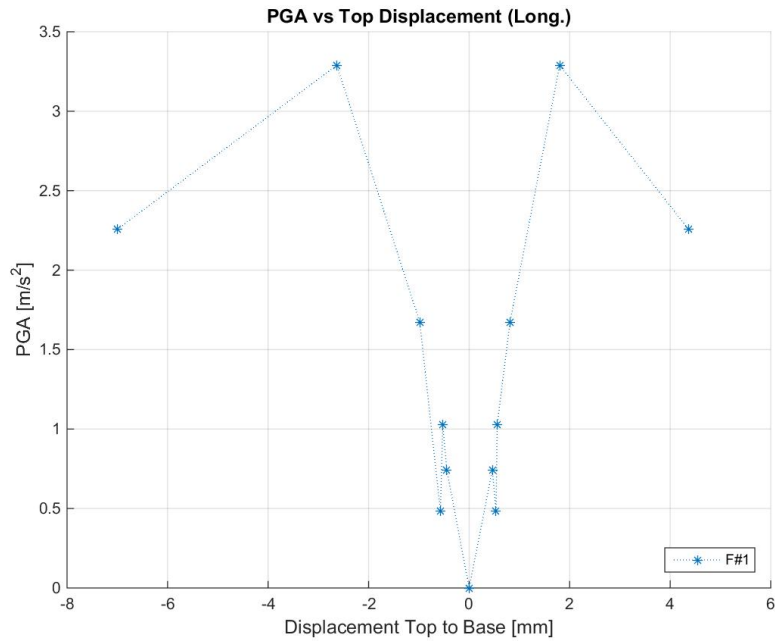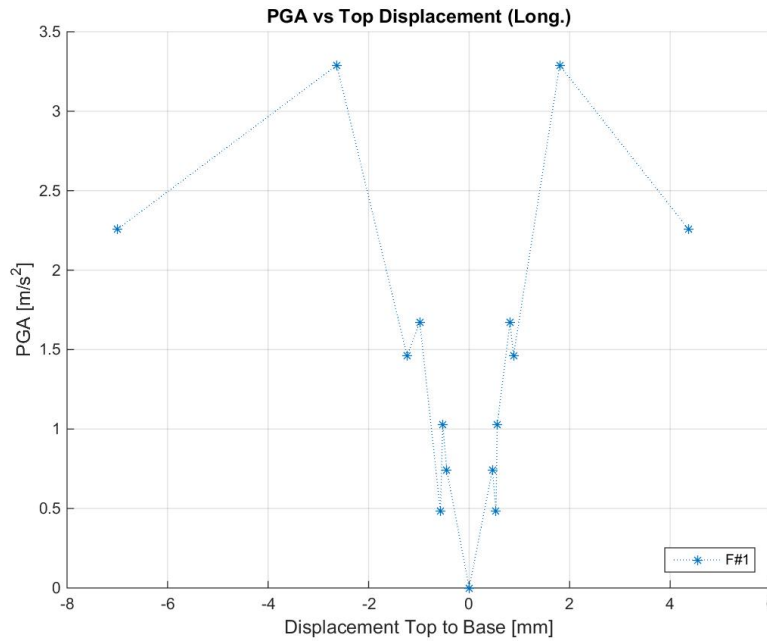

Figure 456. PGA vs. top-to-base displacement maxima – Positive and negative, Test run #6.

Figure 457 shows the PGA versus secant – positive and negative – stiffness relationship, the latter parameter being identified according to the linear approximation reported in Figure 288.
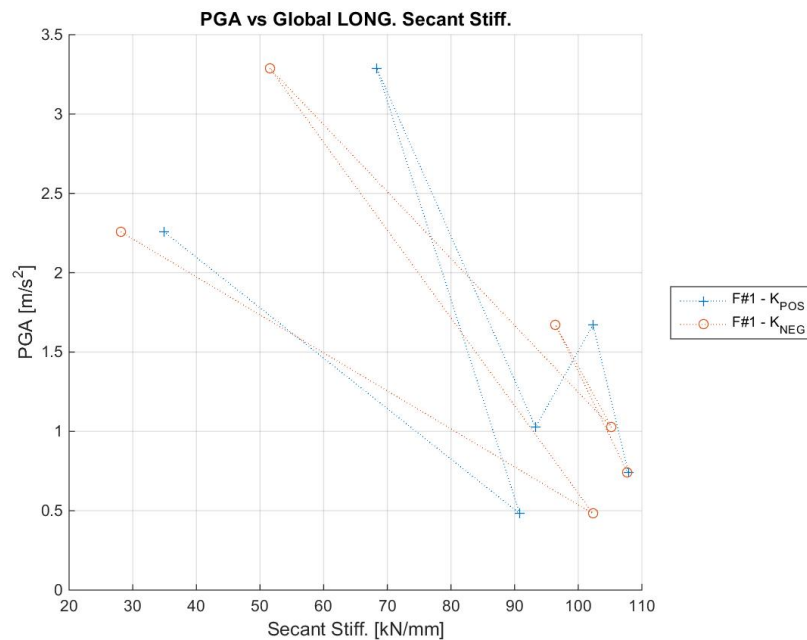
Figure 457. PGA-global secant stiffness relationships – Positive and negative directions, Test run #6.

Figure 458 shows the PGA versus maximum base shear relationship of the specimen at this stage of the testing sequence.
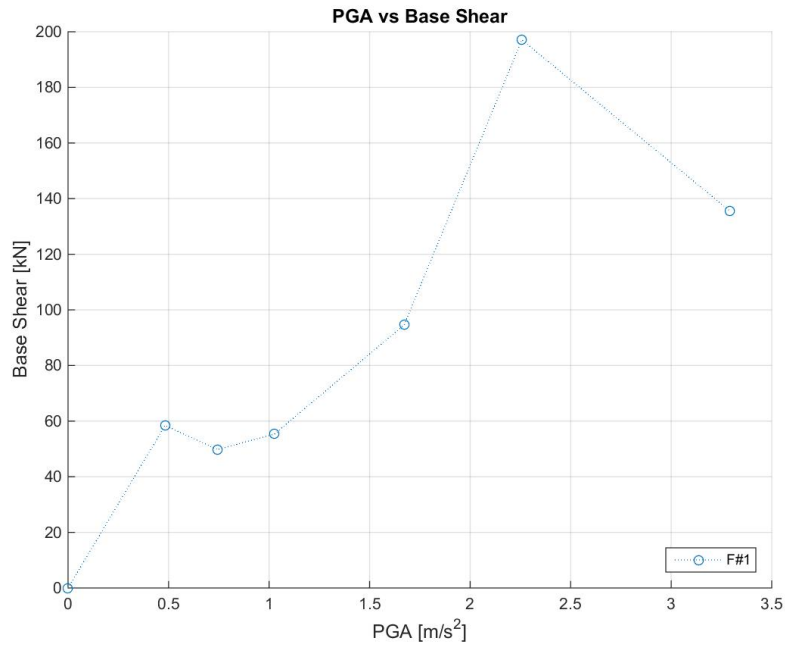
Figure 458. Maximum base shear vs. peak ground acceleration – Test run #6.

Figure 459 shows the arias intensity versus maximum base shear relationship of the specimen at this stage of the testing sequence.
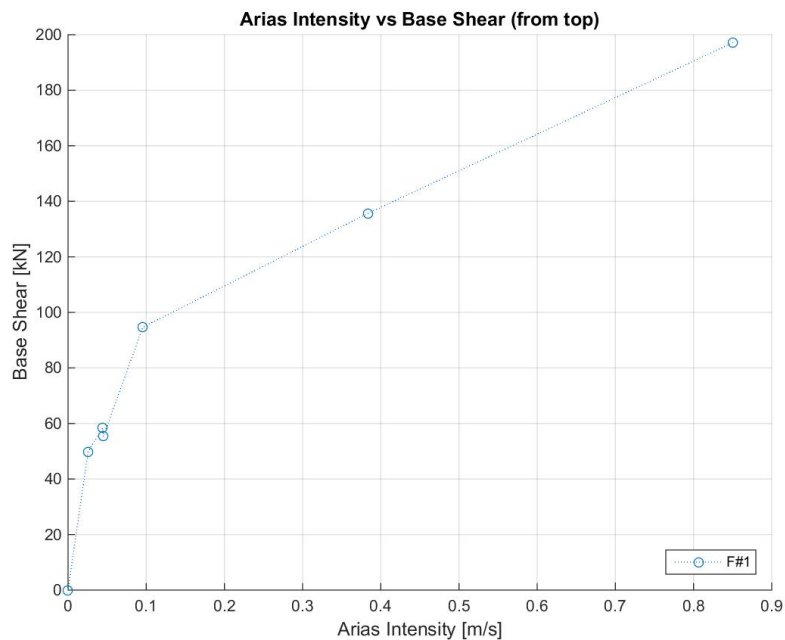
Figure 459. Maximum base shear vs. arias intensity – Test run #6.

6.6.7 Test run #7 – SF = 50% – Controller compensation

Figure 460 shows the comparison between the acceleration spectra from time-histories at reference and feedback (as recorded by the shake-table controller). The experimental acceleration time-history used for the spectrum comparison is the average of the recorded accelerations on the foundation of EUC-BUILD5 specimen (accelerometers #139 and #140). Furthermore, Figure 461 shows the discrepancy in percentage.
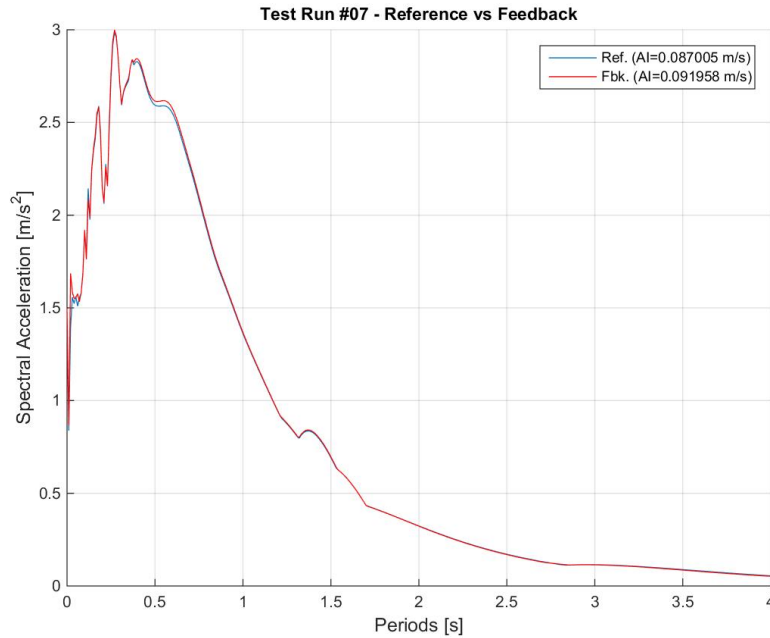
Figure 460. Comparison between acceleration spectra from time-histories at reference and feedback.
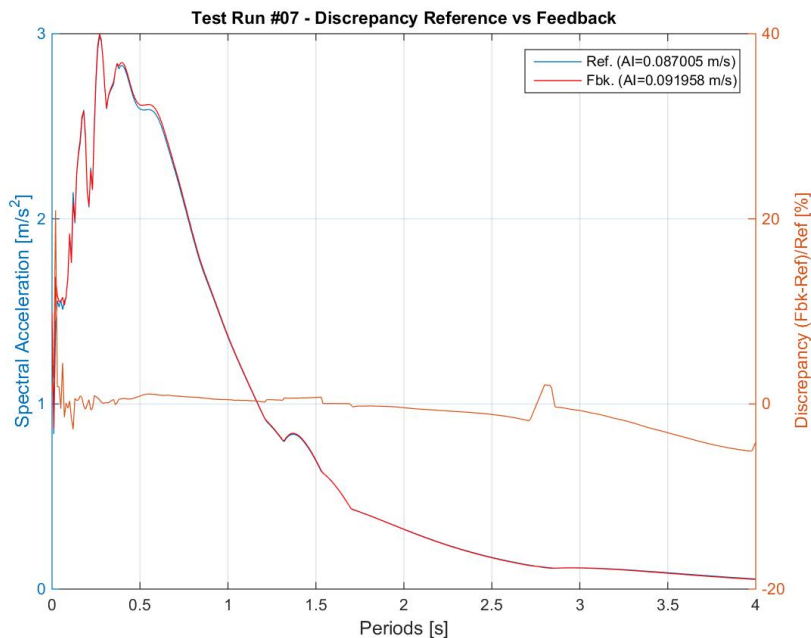
Figure 461. Discrepancy between acceleration spectra from time-histories at reference and feedback.

Figure 462 shows the acceleration time-histories recorded at the foundation level (accelerometers #139 and #140) and the average of the accelerations recorded by the two accelerometers.
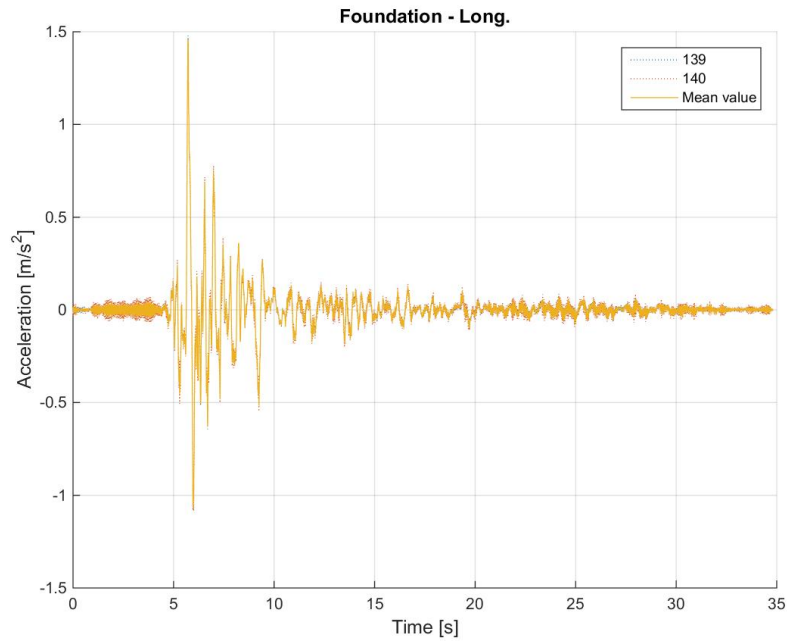
Figure 462. Acceleration time-histories at the foundation level – Individual and average of accelerometers.

Figure 463 shows the acceleration time-histories recorded at the first floor of the specimen and the average of the accelerations recorded by all the accelerometers installed at this level.
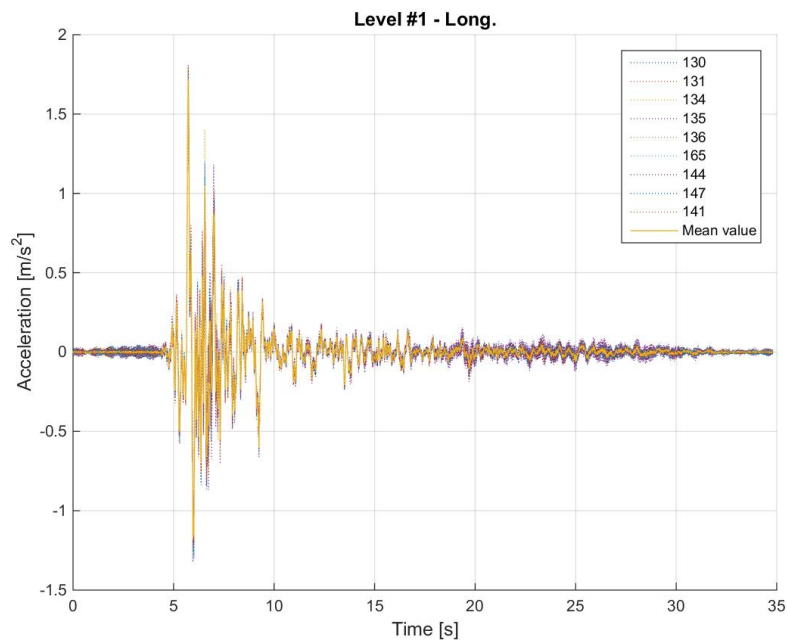
Figure 463. Acceleration time-histories at the first floor – Individual and average of accelerometers.

Figure 464 shows the acceleration time-histories recorded at the second floor and the average of the accelerations recorded by all the accelerometers installed at this level.

Figure 464. Acceleration time-histories at the second floor – Individual and average of accelerometers.

Figure 465 shows a comparison between the average acceleration time-history at the foundation, the first floor and the second floor of the specimen.

Figure 465. Comparison between average acceleration time-histories – Foundation, first and second storeys.
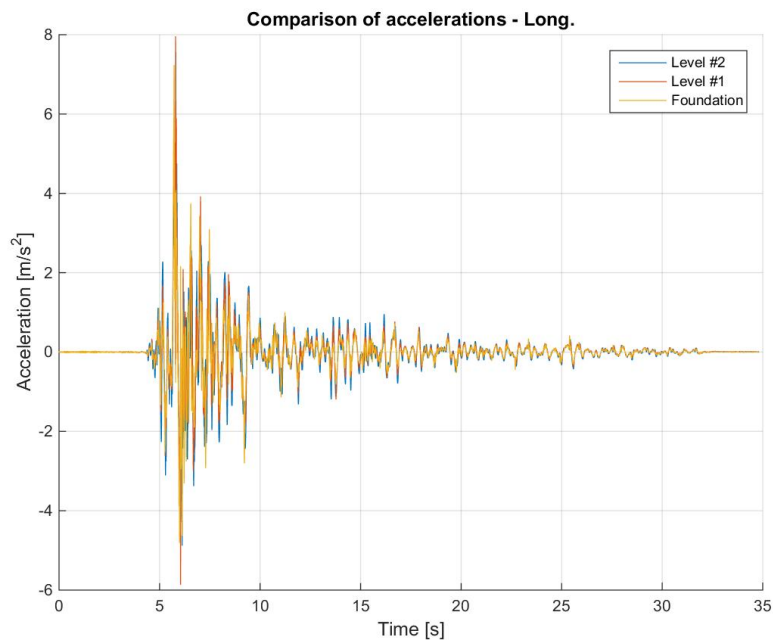
Figure 466 shows a comparison between the acceleration spectra at the base, the first storey and the second storey, which were computed using the average acceleration time-history at the foundation, the first floor and the second floor of the specimen. The spectral accelerations were also normalised with respect to the one at the base and the obtained spectral acceleration ratios are plotted together in Figure 467. Obviously, the curve obtained for the base is the horizontal blue line, which is plotted since it serves as reference for the two floors (and their amplification).

Figure 466. Acceleration spectra from average time-histories at the foundation, first and second floors.

Figure 467. Spectral acceleration ratios: first floor-to-foundation and second floor-to-foundation.

Figure 468 shows a comparison between the displacement time-histories at the foundation, the first floor and the second floor of the specimen.
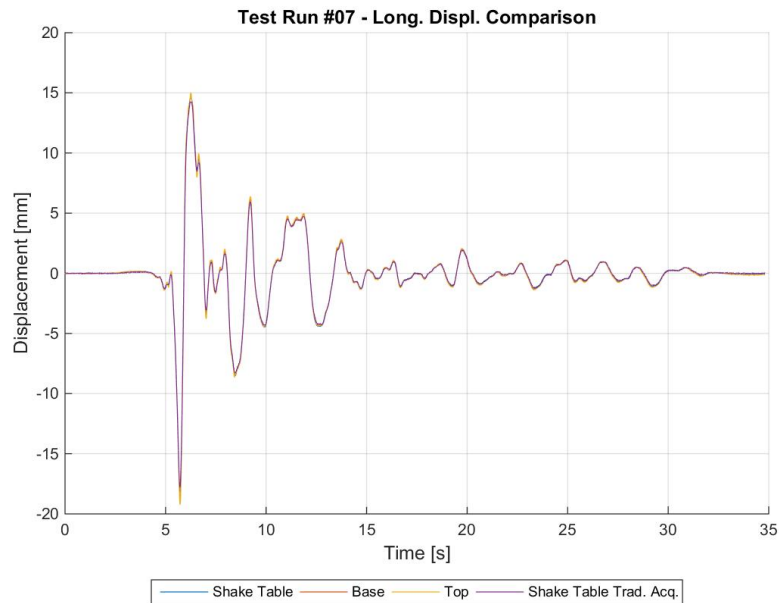
Figure 468. Comparison between average displacement time-histories – Foundation, first and second storeys.

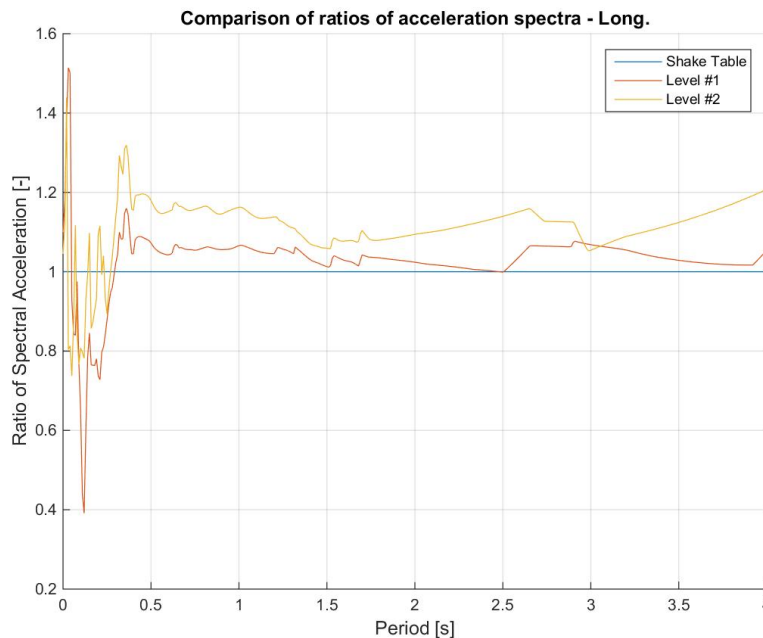Figure 469 shows a comparison between the imposed base shear time-history and the recorded base shear time-history, the former one being the force applied by the actuators of the shake-table.
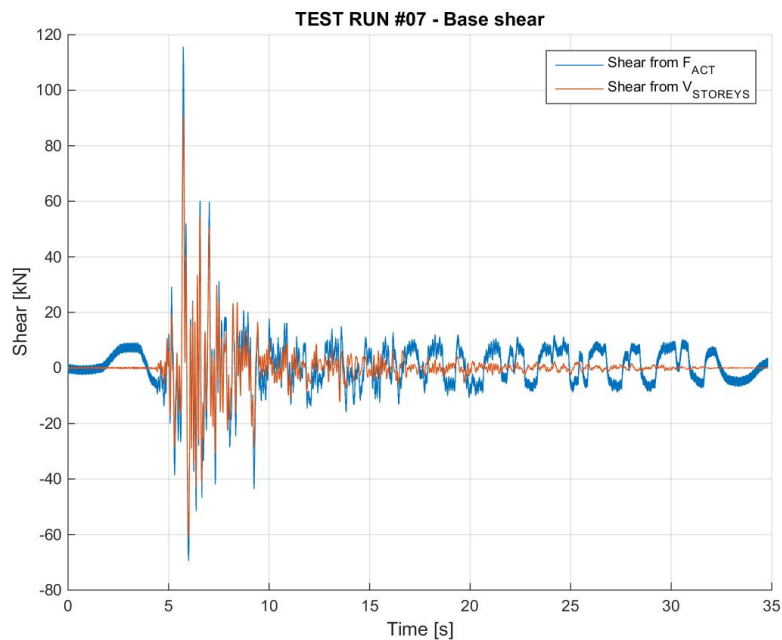
Figure 469. Imposed base shear vs. measured base shear – Comparison through time.

Figure 470 shows the hysteretic base shear-top displacement response of the specimen. For the sake of clarity, it is noted that the total base shear is plotted against the top-to-base displacement of EUC-BUILD5 specimen. Hysteresis loops were also processed to obtain a linear approximation that takes into account both Northward and Southward (i.e. positive and negative) motion and identifies, in an equivalent manner, the corresponding base shear-displacement couples. The hysteretic response and the linear approximation are superimposed in Figure 471.
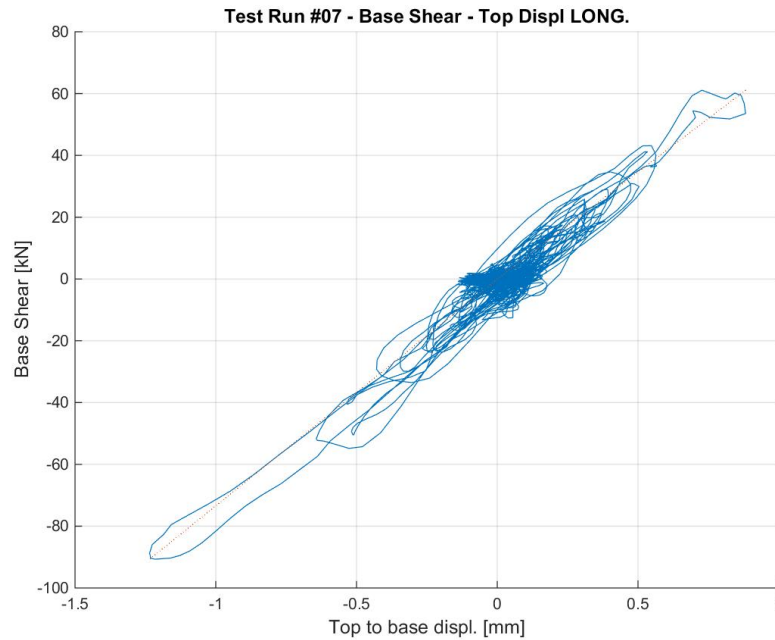
Figure 470. Base shear-top displacement response of EUC-BUILD5 – Test run #7, top-to-base displacement.
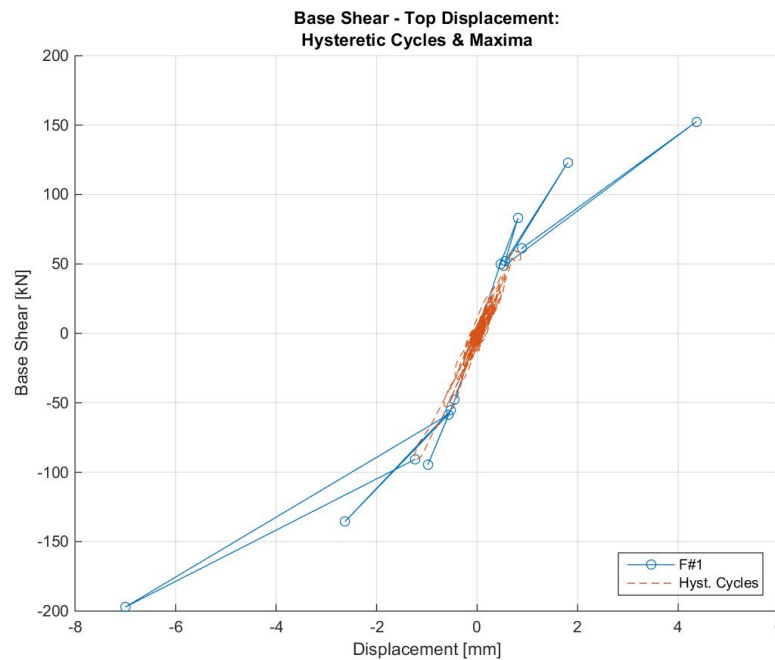
Figure 471. Base shear vs. top-to-base displacement – Hysteretic response and maxima (positive and negative).

Figure 472 shows the absolute maxima – positive or negative – top displacement-base shear couples that were obtained from the hysteresis loops of the specimen.

Figure 472. Base shear vs. top-to-base displacement maxima – Test run #7.

Figure 473 shows the maxima – positive and negative – top displacement-base shear couples that were obtained from the linear approximation of the specimen response (see Figure 471).

Figure 473. Base shear vs. top-to-base displacement maxima – Positive and negative, Test run #7.

Figure 474 shows the hysteretic response of the first storey of the specimen, which is illustrated in terms of storey shear versus inter-storey displacement relationship.
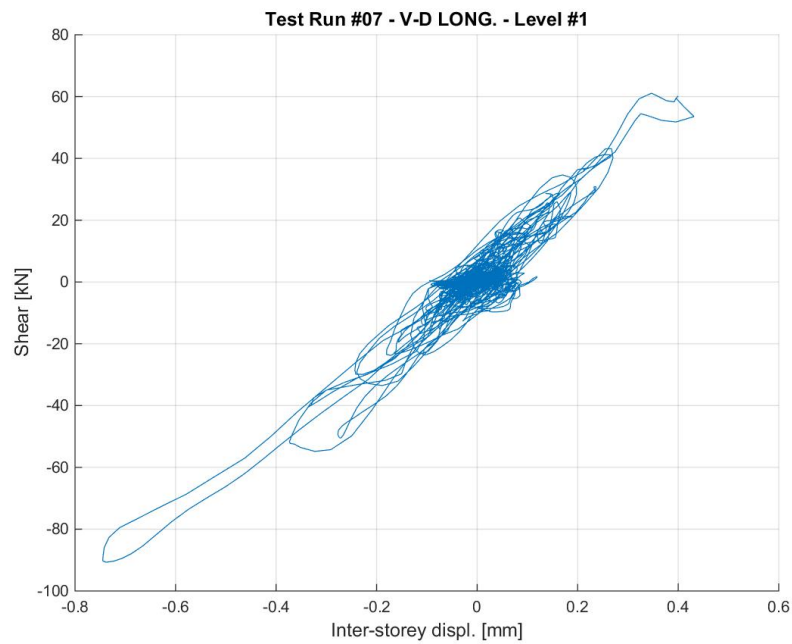
Figure 474. Storey shear vs. inter-storey displacement response – First storey, Test run #7.

Figure 475 shows the hysteretic response of the second storey of the specimen, which is illustrated in terms of storey shear versus inter-storey displacement relationship.
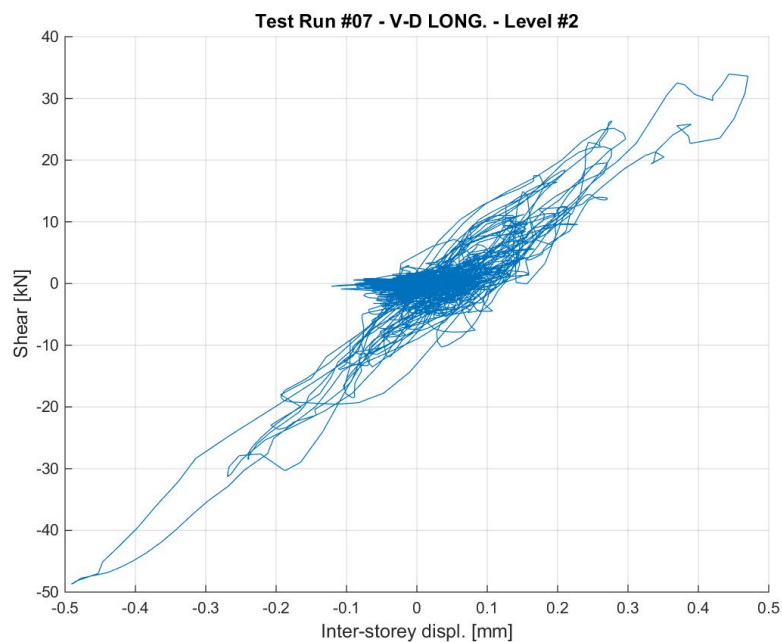
Figure 475. Storey shear vs. inter-storey displacement response – Second storey, Test run #7.

Figure 476 shows the PGA versus maxima – positive and negative – top displacement relationship, the latter parameter being identified according to the linear approximation reported in Figure 471.

Figure 476. PGA vs. top-to-base displacement maxima – Positive and negative, Test run #7.

Figure 477 shows the PGA versus secant – positive and negative – stiffness relationship, the latter parameter being identified according to the linear approximation reported in Figure 471.
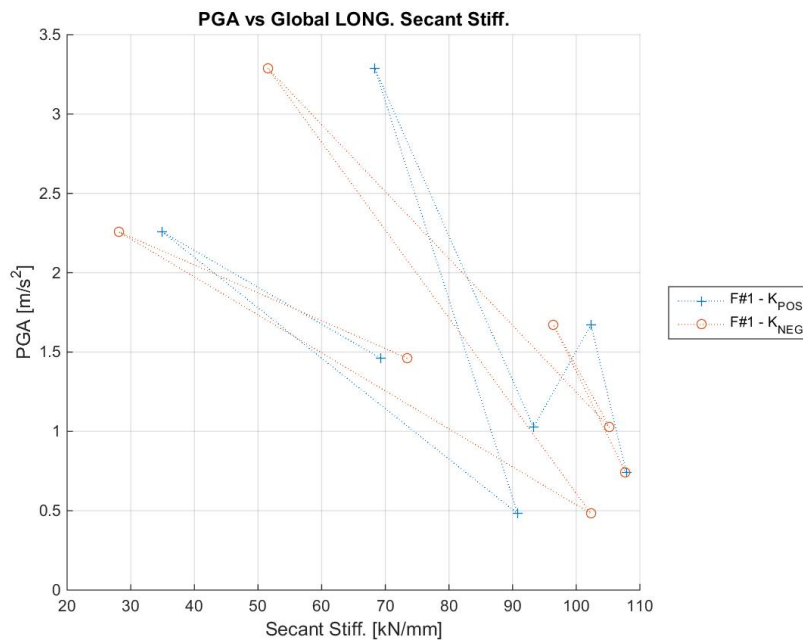
Figure 477. PGA-global secant stiffness relationships – Positive and negative directions, Test run #7.

Figure 478 shows the PGA versus maximum base shear relationship of the specimen at this stage of the testing sequence.
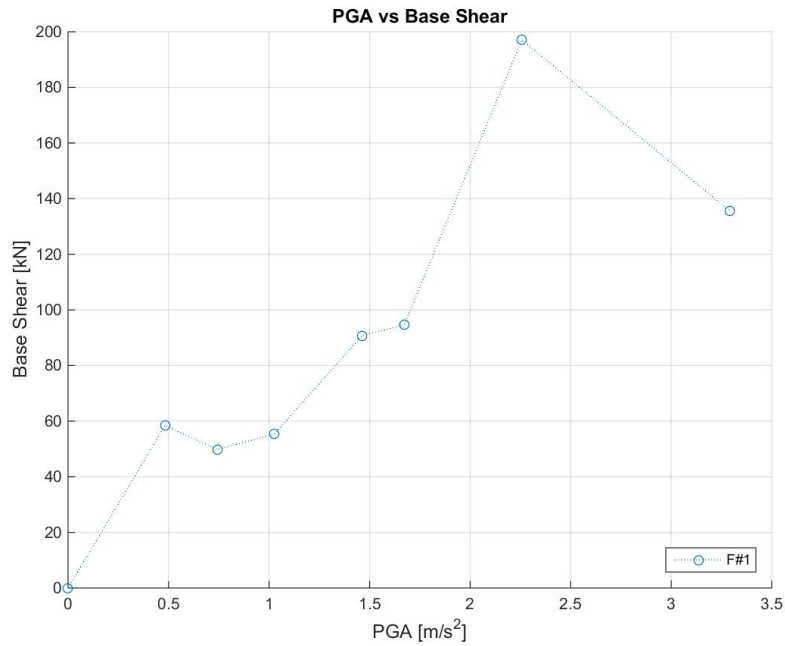
Figure 478. Maximum base shear vs. peak ground acceleration – Test run #7.

Figure 479 shows the arias intensity versus maximum base shear relationship of the specimen at this stage of the testing sequence.
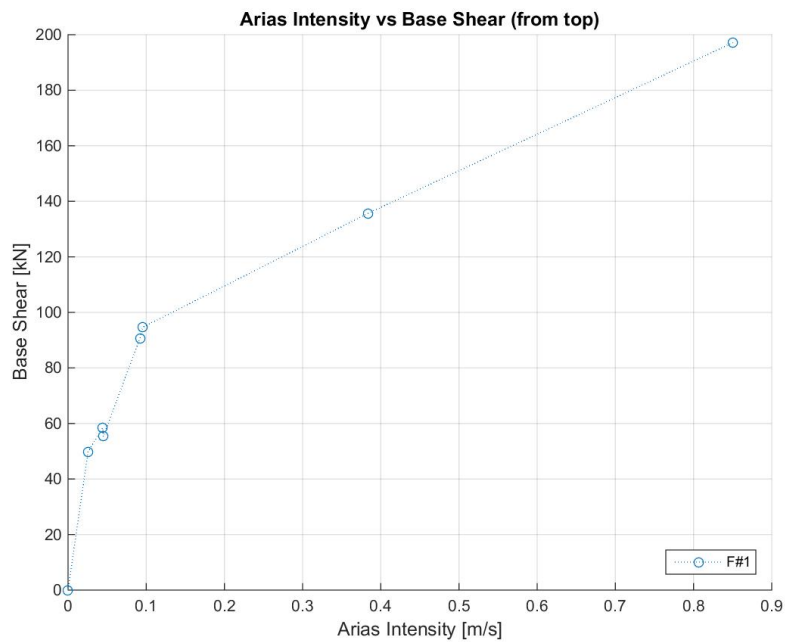
Figure 479. Maximum base shear vs. arias intensity – Test run #7.

6.6.8 Test run #8 – SF = 200% – Test at 200%

Figure 480 shows the comparison between the acceleration spectra from time-histories at reference and feedback (as recorded by the shake-table controller). The experimental acceleration time-history used for the spectrum comparison is the average of the recorded accelerations on the foundation of EUC-BUILD5 specimen (accelerometers #139 and #140). Furthermore, Figure 481 shows the discrepancy in percentage.
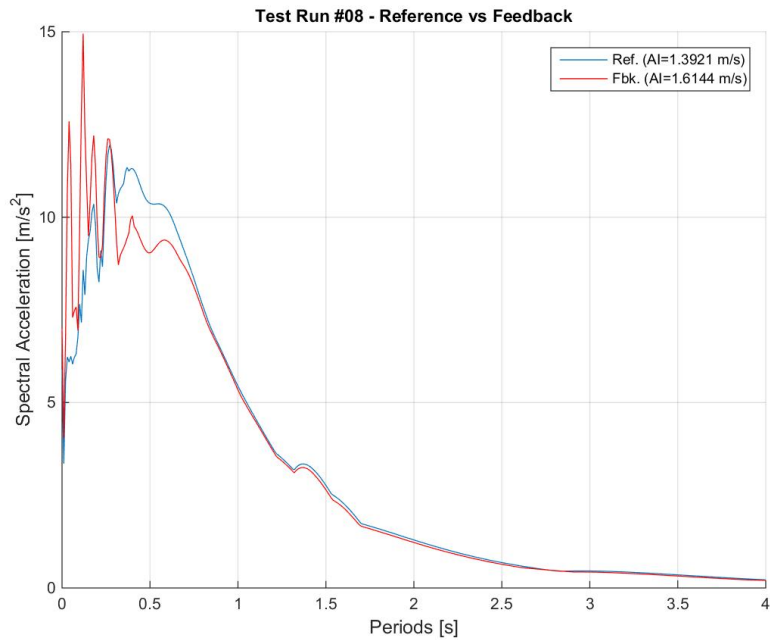
Figure 480. Comparison between acceleration spectra from time-histories at reference and feedback.
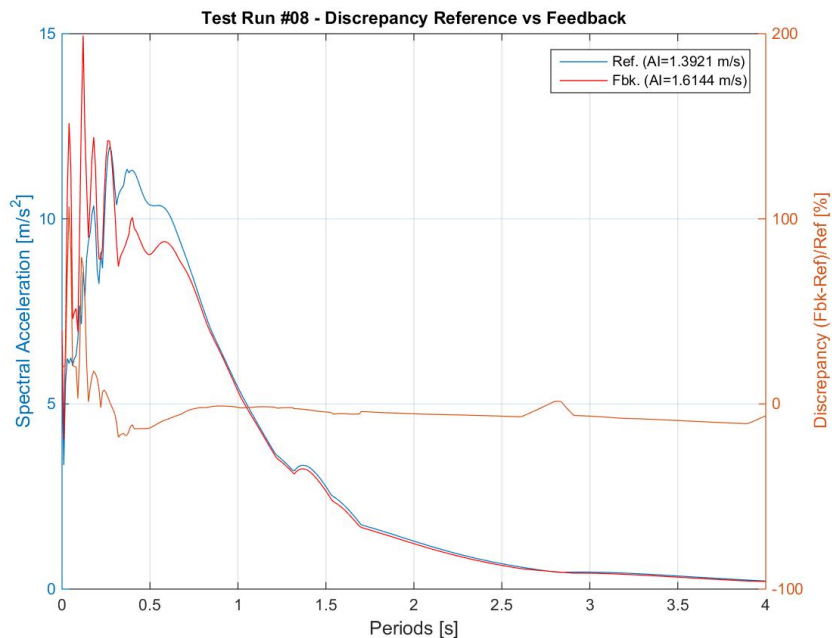
Figure 481. Discrepancy between acceleration spectra from time-histories at reference and feedback.

Figure 482 shows the acceleration time-histories recorded at the foundation level (accelerometers #139 and #140) and the average of the accelerations recorded by the two accelerometers.
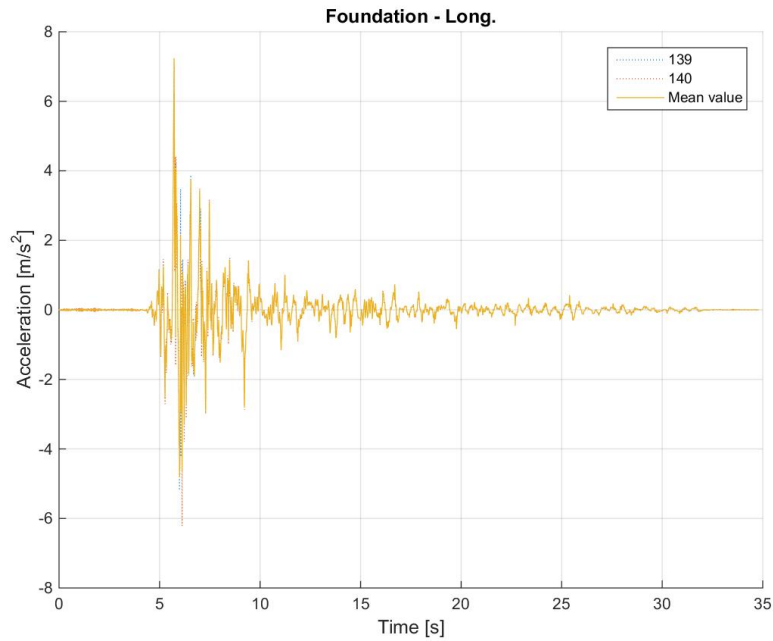
Figure 482. Acceleration time-histories at the foundation level – Individual and average of accelerometers.

Figure 483 shows the acceleration time-histories recorded at the first floor of the specimen and the average of the accelerations recorded by all the accelerometers installed at this level.
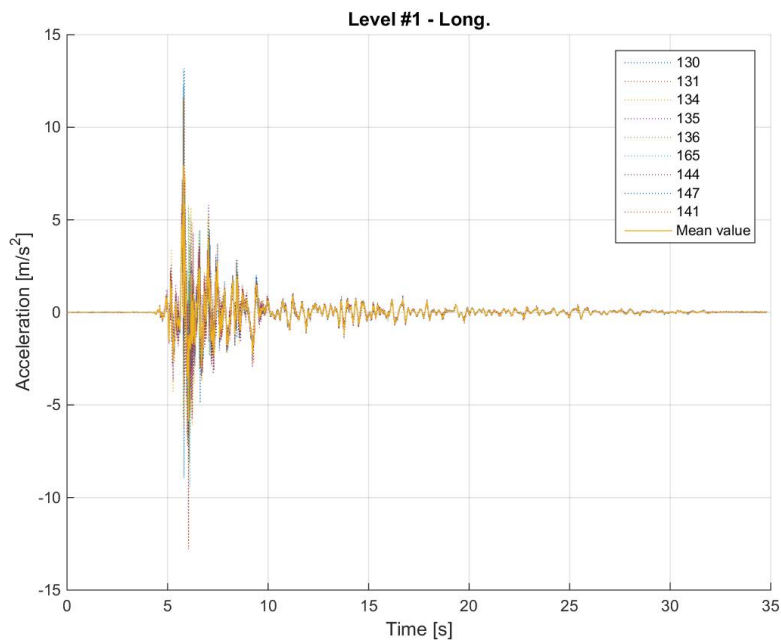
Figure 483. Acceleration time-histories at the first floor – Individual and average of accelerometers.

Figure 484 shows the acceleration time-histories recorded at the second floor and the average of the accelerations recorded by all the accelerometers installed at this level.
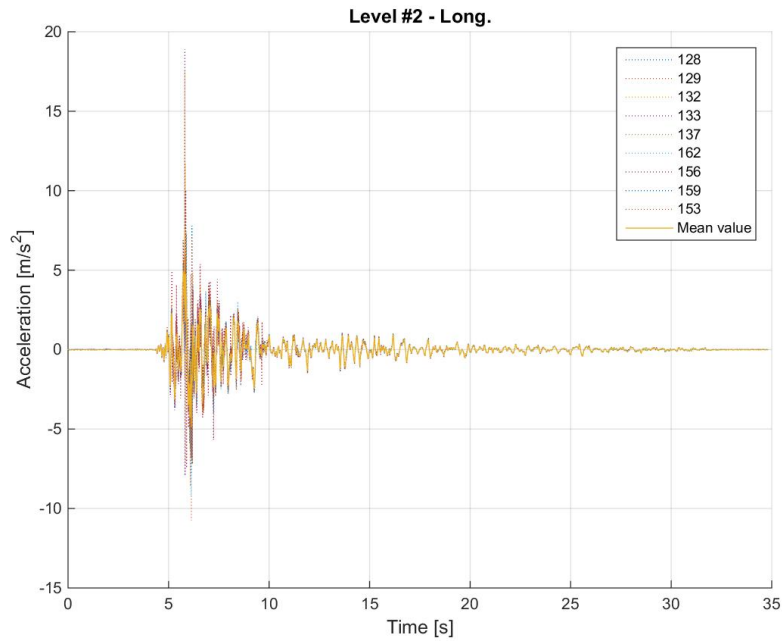
Figure 484. Acceleration time-histories at the second floor – Individual and average of accelerometers.

Figure 485 shows a comparison between the average acceleration time-history at the foundation, the first floor and the second floor of the specimen.

Figure 485. Comparison between average acceleration time-histories – Foundation, first and second storeys.

Figure 486 shows a comparison between the acceleration spectra at the base, the first storey and the second storey, which were computed using the average acceleration time-history at the foundation, the first floor and the second floor of the specimen. The spectral accelerations were also normalised with respect to the one at the base and the obtained spectral acceleration ratios are plotted together in Figure 487. Obviously, the curve obtained for the base is the horizontal blue line, which is plotted since it serves as reference for the two floors (and their amplification).
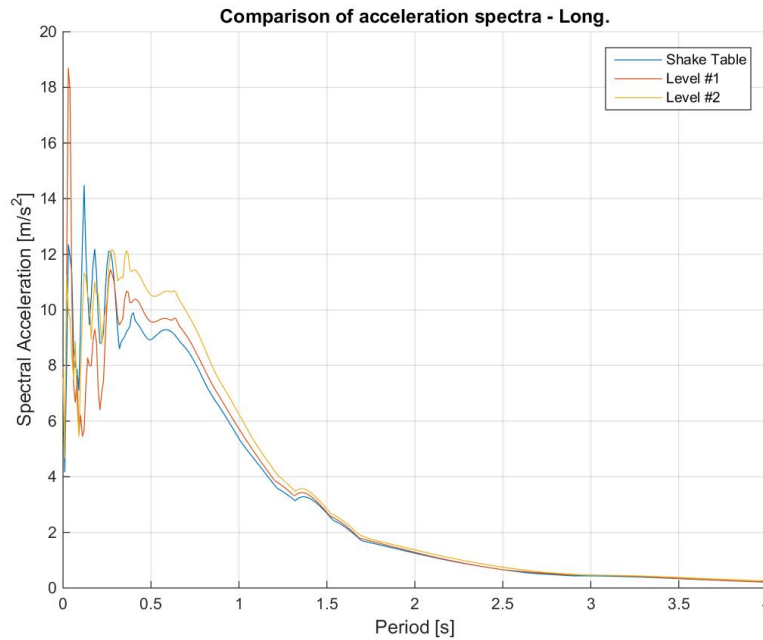
Figure 486. Acceleration spectra from average time-histories at the foundation, first and second floors.

Figure 487. Spectral acceleration ratios: first floor-to-foundation and second floor-to-foundation.

Figure 488 shows a comparison between the displacement time-histories at the foundation, the first floor and the second floor of the specimen.
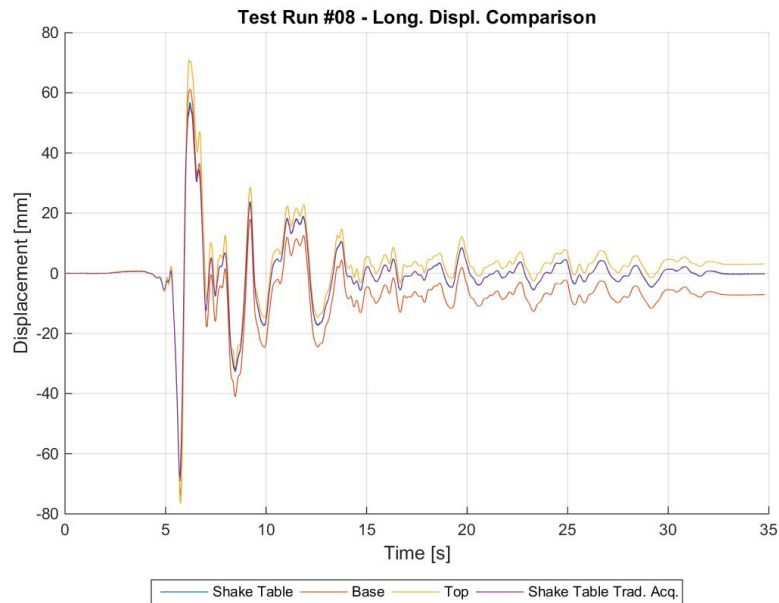
Figure 488. Comparison between average displacement time-histories – Foundation, first and second storeys.

Figure 489 shows a comparison between the imposed base shear time-history and the recorded base shear time-history, the former one being the force applied by the actuators of the shake-table.
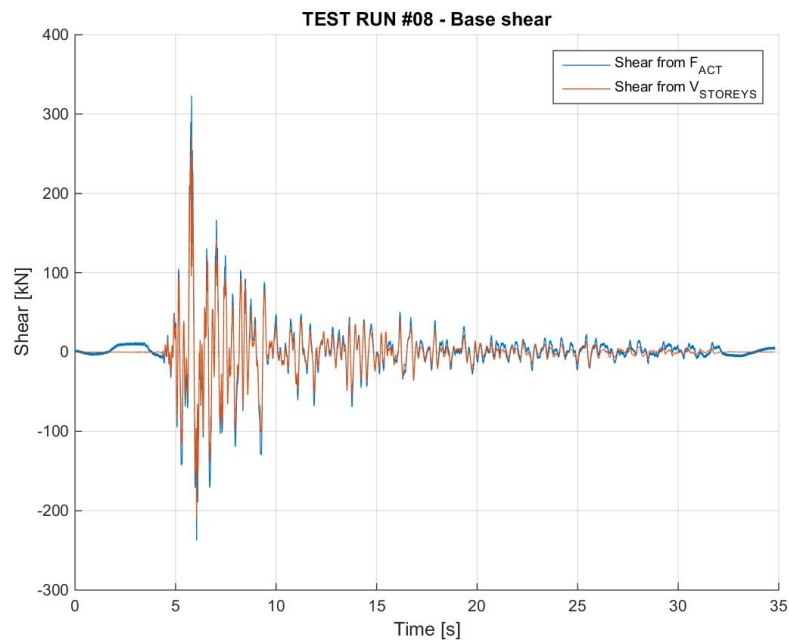
Figure 489. Imposed base shear vs. measured base shear – Comparison through time.

Figure 490 shows the hysteretic base shear-top displacement response of the specimen. For the sake of clarity, it is noted that the total base shear is plotted against the top-to-base displacement of EUC-BUILD5 specimen. Hysteresis loops were also processed to obtain a linear approximation that takes into account both Northward and Southward (i.e. positive and negative) motion and identifies, in an equivalent manner, the corresponding base shear-displacement couples. The hysteretic response and the linear approximation are superimposed in Figure 491.
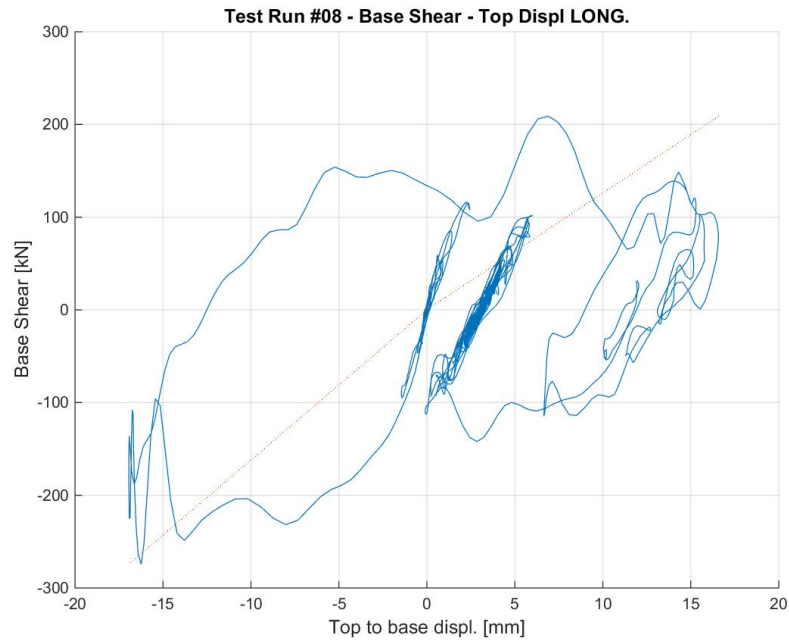
Figure 490. Base shear-top displacement response of EUC-BUILD5 – Test run #8, top-to-base displacement.
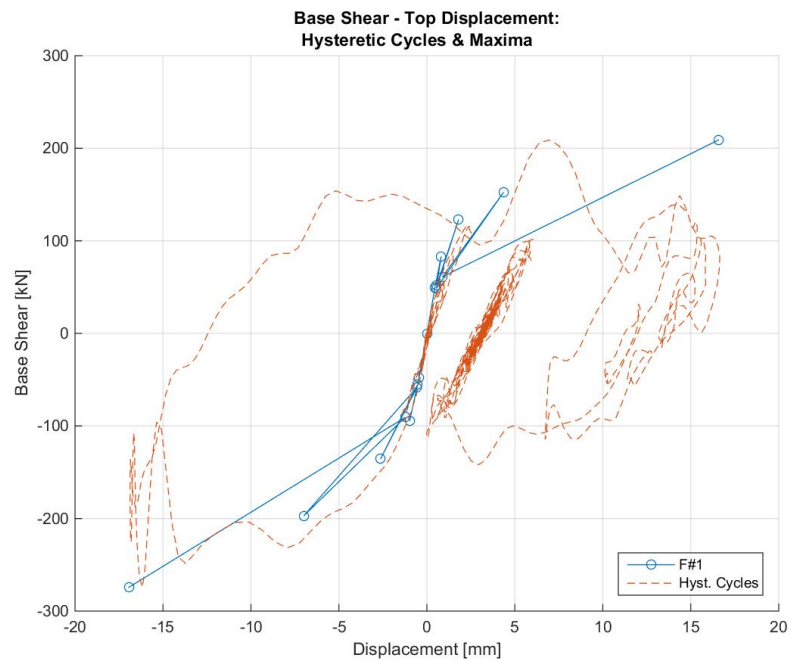
Figure 491. Base shear vs. top-to-base displacement – Hysteretic response and maxima (positive and negative).

Figure 492 shows the absolute maxima – positive or negative – top displacement-base shear couples that were obtained from the hysteresis loops of the specimen.
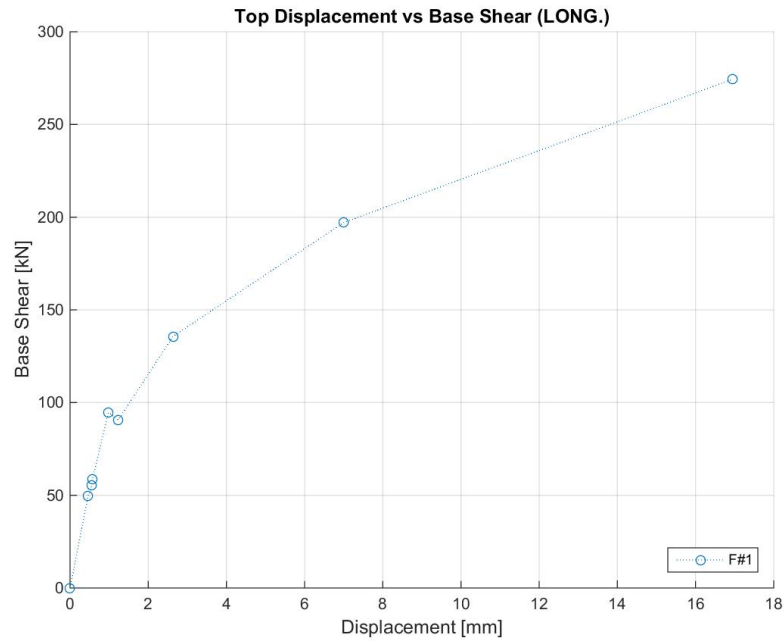
Figure 492. Base shear vs. top-to-base displacement maxima – Test run #8.

Figure 493 shows the maxima – positive and negative – top displacement-base shear couples that were obtained from the linear approximation of the specimen response (see Figure 491).
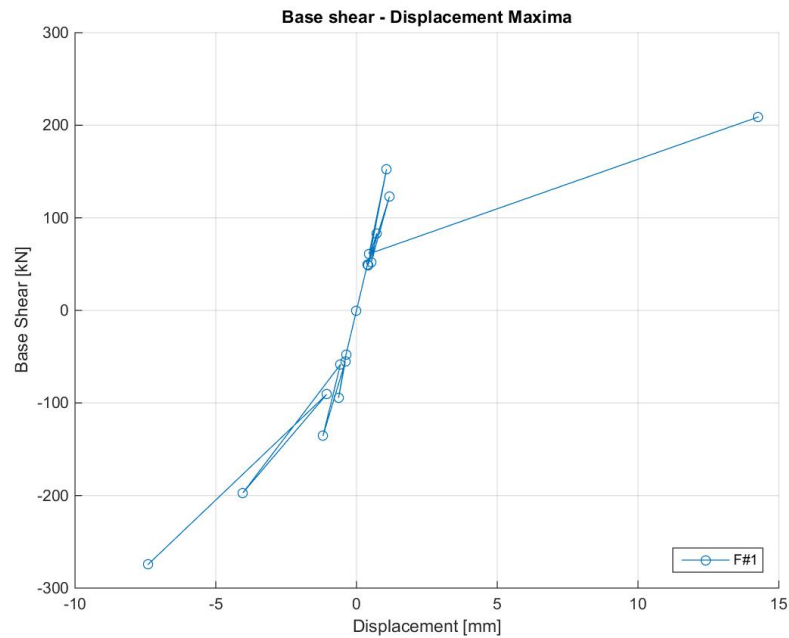
Figure 493. Base shear vs. top-to-base displacement maxima – Positive and negative, Test run #8.

Figure 494 shows the hysteretic response of the first storey of the specimen, which is illustrated in terms of storey shear versus inter-storey displacement relationship.
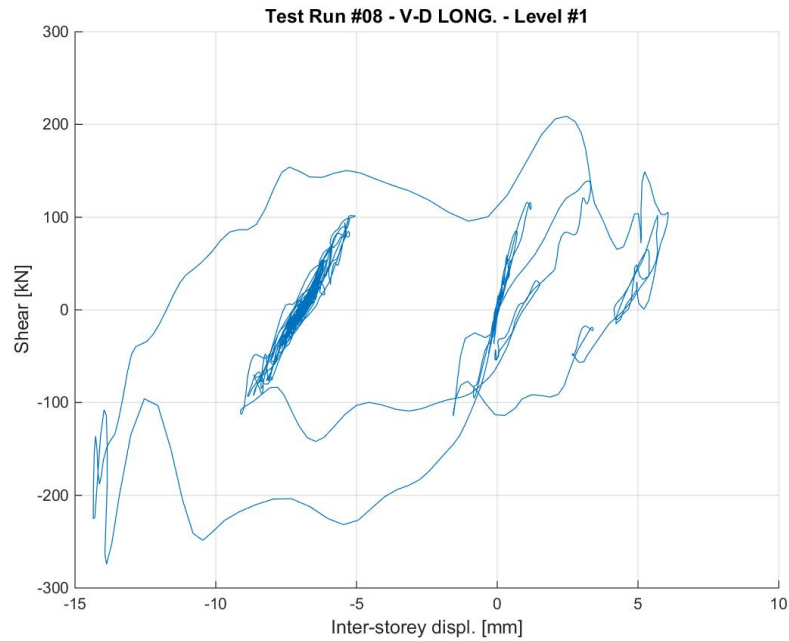
Figure 494. Storey shear vs. inter-storey displacement response – First storey, Test run #8.

Figure 495 shows the hysteretic response of the second storey of the specimen, which is illustrated in terms of storey shear versus inter-storey displacement relationship.
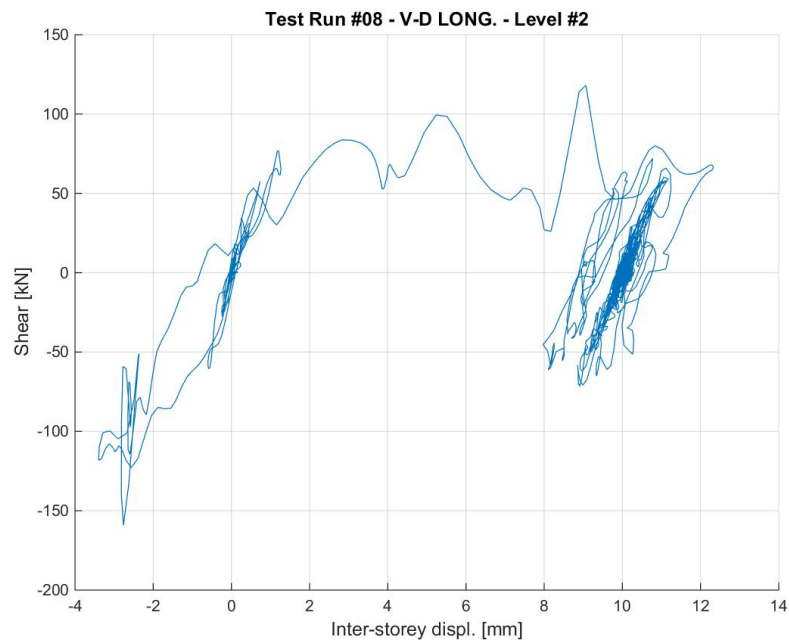
Figure 495. Storey shear vs. inter-storey displacement response – Second storey, Test run #8.

Figure 496 shows the PGA versus maxima – positive and negative – top displacement relationship, the latter parameter being identified according to the linear approximation reported in Figure 491.
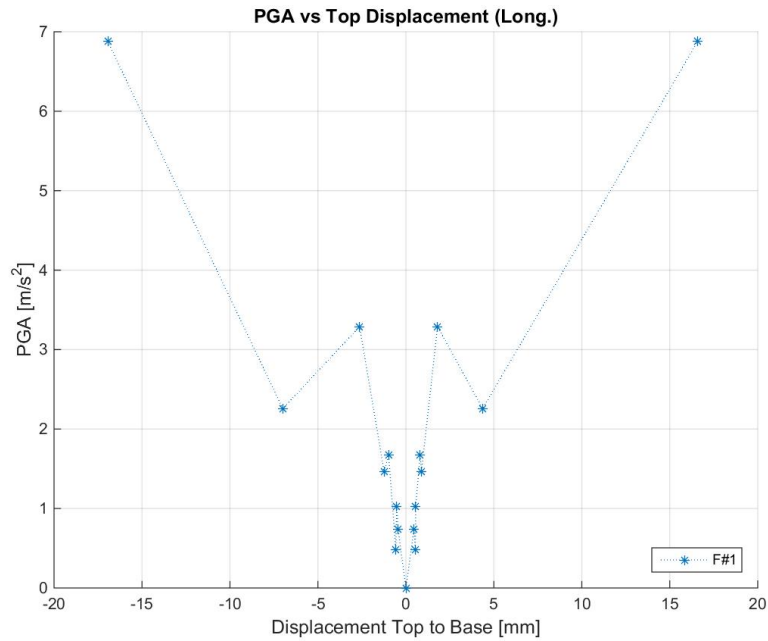
Figure 496. PGA vs. top-to-base displacement maxima – Positive and negative, Test run #8.

Figure 497 shows the PGA versus secant – positive and negative – stiffness relationship, the latter parameter being identified according to the linear approximation reported in Figure 491.
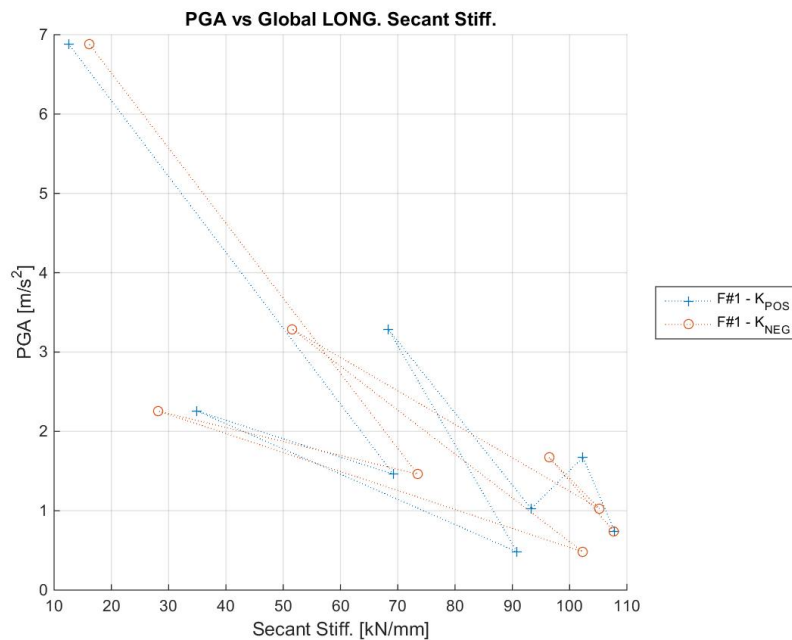
Figure 497. PGA-global secant stiffness relationships – Positive and negative directions, Test run #8.

Figure 498 shows the PGA versus maximum base shear relationship of the specimen at this stage of the testing sequence.
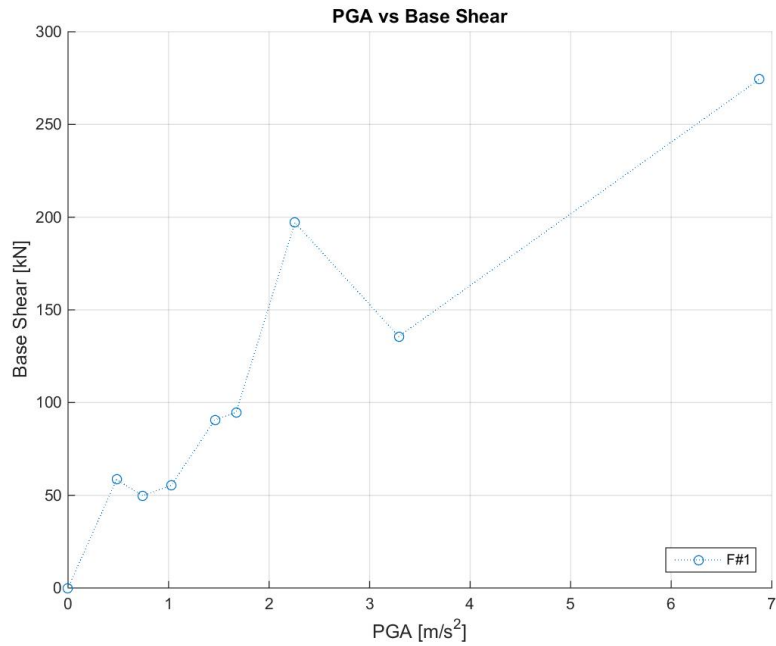
Figure 498. Maximum base shear vs. peak ground acceleration – Test run #8.

Figure 499 shows the arias intensity versus maximum base shear relationship of the specimen at this stage of the testing sequence.
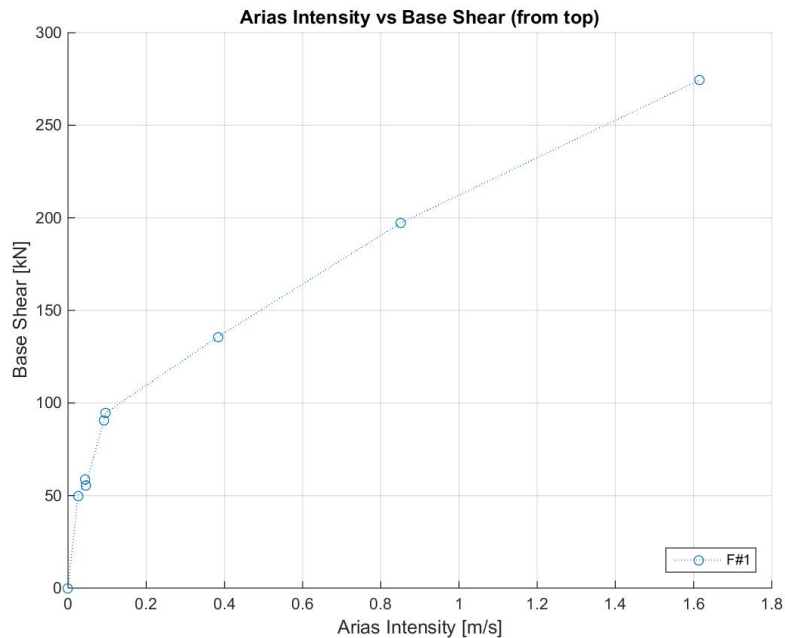
Figure 499. Maximum base shear vs. arias intensity – Test run #8.

6.6.9 Test run #9 – SF = 50% – Controller compensation

Figure 500 shows the comparison between the acceleration spectra from time-histories at reference and feedback (as recorded by the shake-table controller). The experimental acceleration time-history used for the spectrum comparison is the average of the recorded accelerations on the foundation of EUC-BUILD5 specimen (accelerometers #139 and #140). Furthermore, Figure 501 shows the discrepancy in percentage.
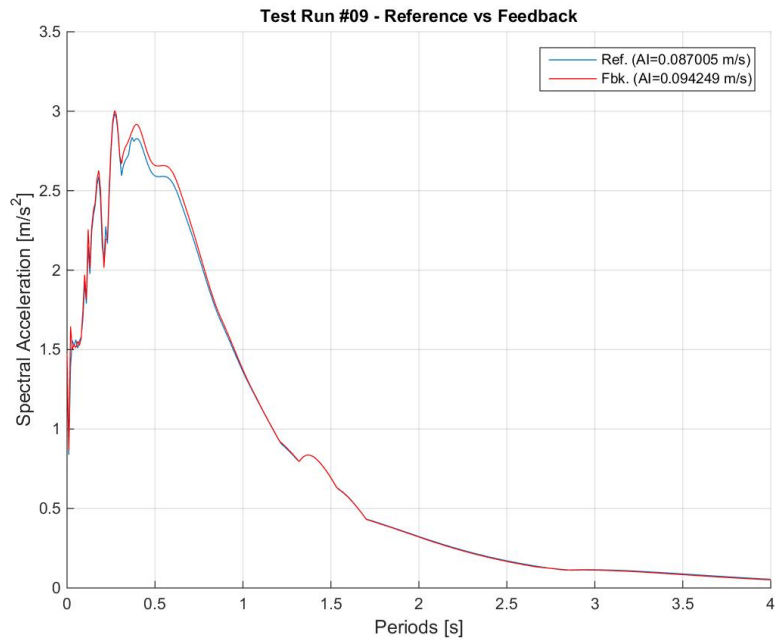
Figure 500. Comparison between acceleration spectra from time-histories at reference and feedback.
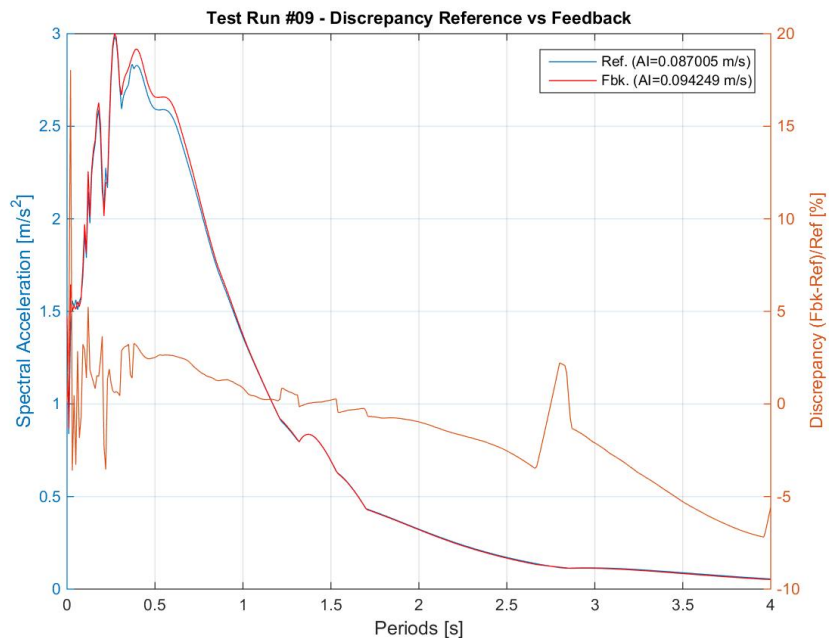
Figure 501. Discrepancy between acceleration spectra from time-histories at reference and feedback.

Figure 502 shows the acceleration time-histories recorded at the foundation level (accelerometers #139 and #140) and the average of the accelerations recorded by the two accelerometers.
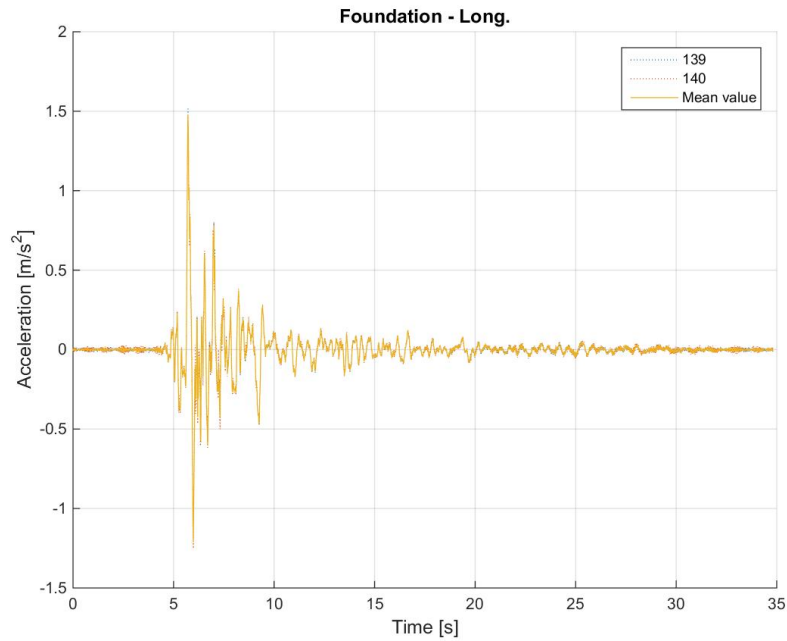
Figure 502. Acceleration time-histories at the foundation level – Individual and average of accelerometers.

Figure 503 shows the acceleration time-histories recorded at the first floor of the specimen and the average of the accelerations recorded by all the accelerometers installed at this level.
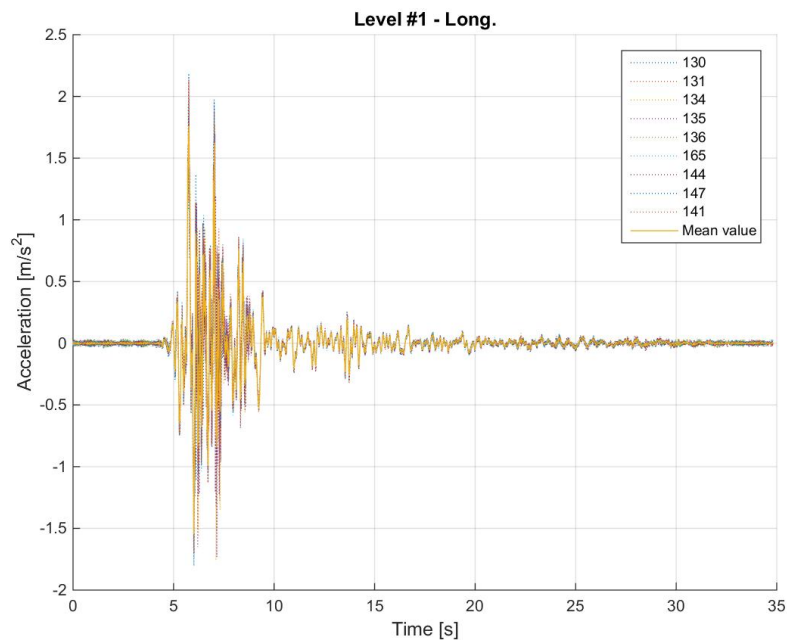
Figure 503. Acceleration time-histories at the first floor – Individual and average of accelerometers.

Figure 504 shows the acceleration time-histories recorded at the second floor and the average of the accelerations recorded by all the accelerometers installed at this level.
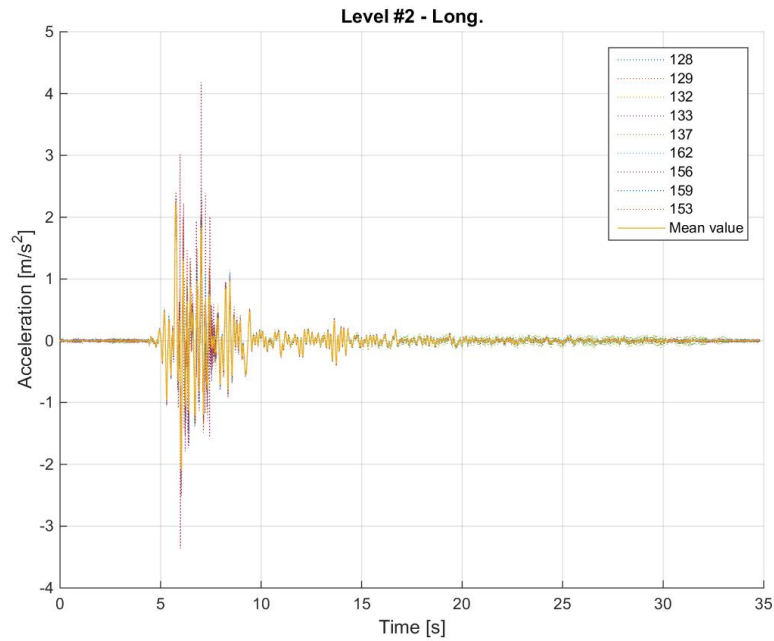
Figure 504. Acceleration time-histories at the second floor – Individual and average of accelerometers.

Figure 505 shows a comparison between the average acceleration time-history at the foundation, the first floor and the second floor of the specimen.
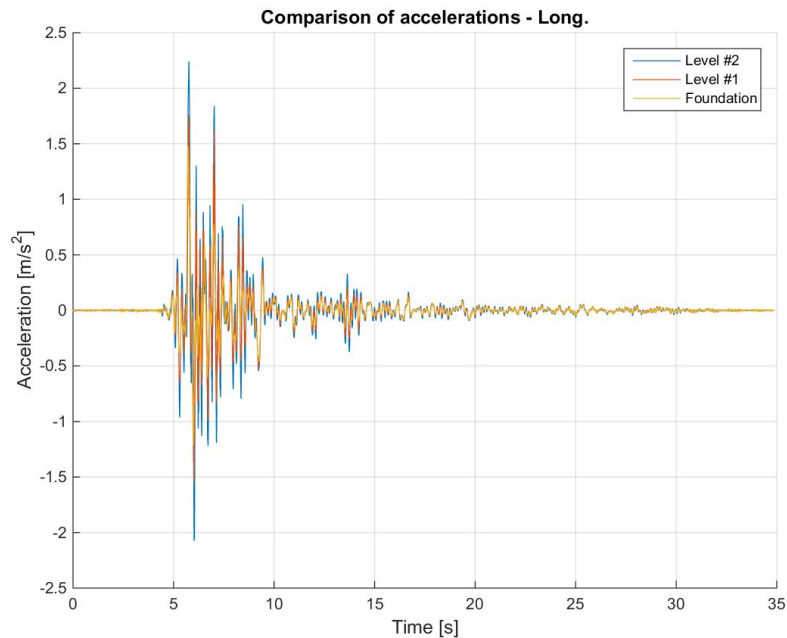
Figure 505. Comparison between average acceleration time-histories – Foundation, first and second storeys.

Figure 506 shows a comparison between the acceleration spectra at the base, the first storey and the second storey, which were computed using the average acceleration time-history at the foundation, the first floor and the second floor of the specimen. The spectral accelerations were also normalised with respect to the one at the base and the obtained spectral acceleration ratios are plotted together in Figure 507. Obviously, the curve obtained for the base is the horizontal blue line, which is plotted since it serves as reference for the two floors (and their amplification).
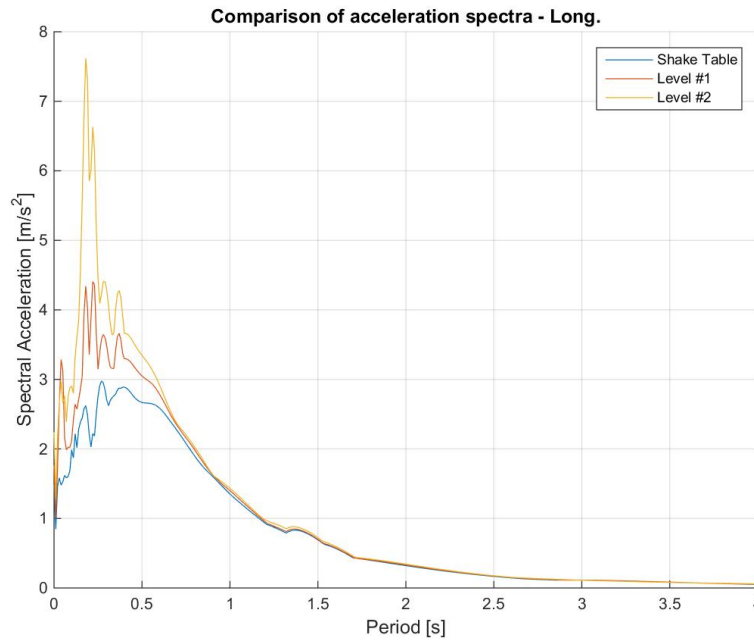
Figure 506. Acceleration spectra from average time-histories at the foundation, first and second floors.
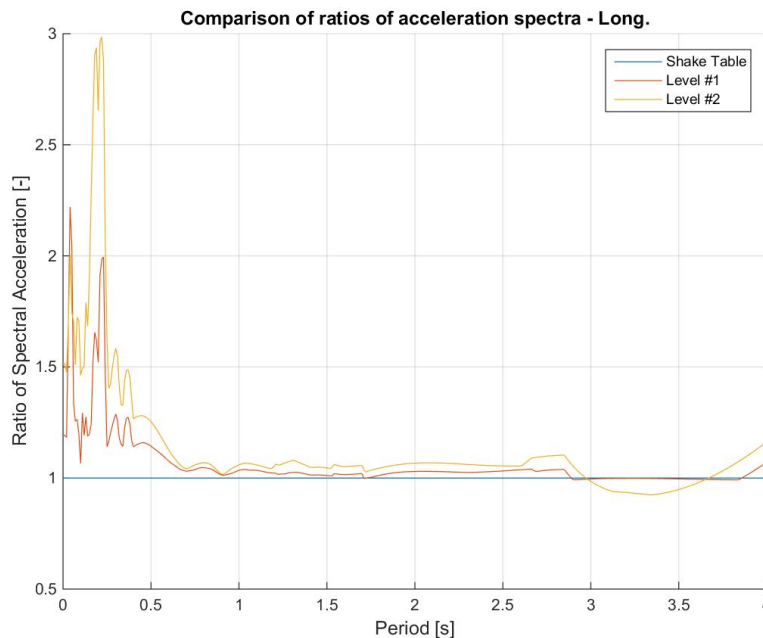
Figure 507. Spectral acceleration ratios: first floor-to-foundation and second floor-to-foundation.

Figure 508 shows a comparison between the displacement time-histories at the foundation, the first floor and the second floor of the specimen.
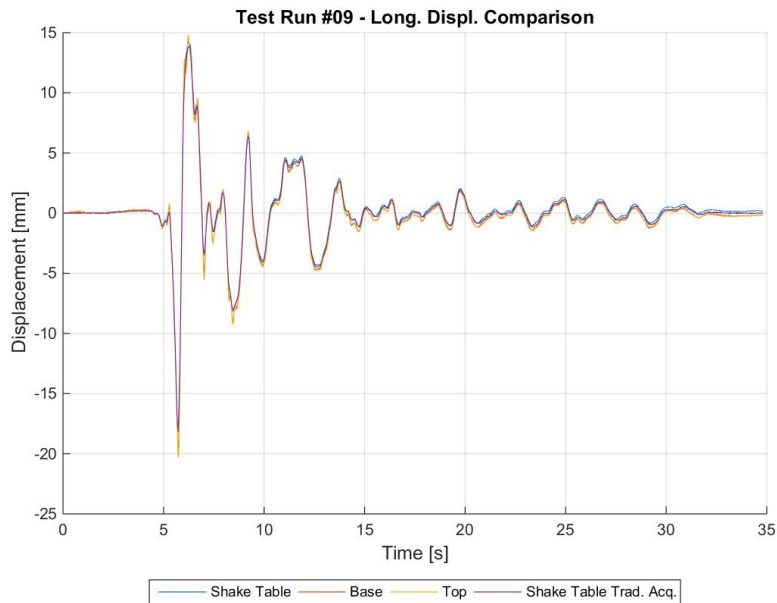
Figure 508. Comparison between average displacement time-histories – Foundation, first and second storeys.

Figure 509 shows a comparison between the imposed base shear time-history and the recorded base shear time-history, the former one being the force applied by the actuators of the shake-table.
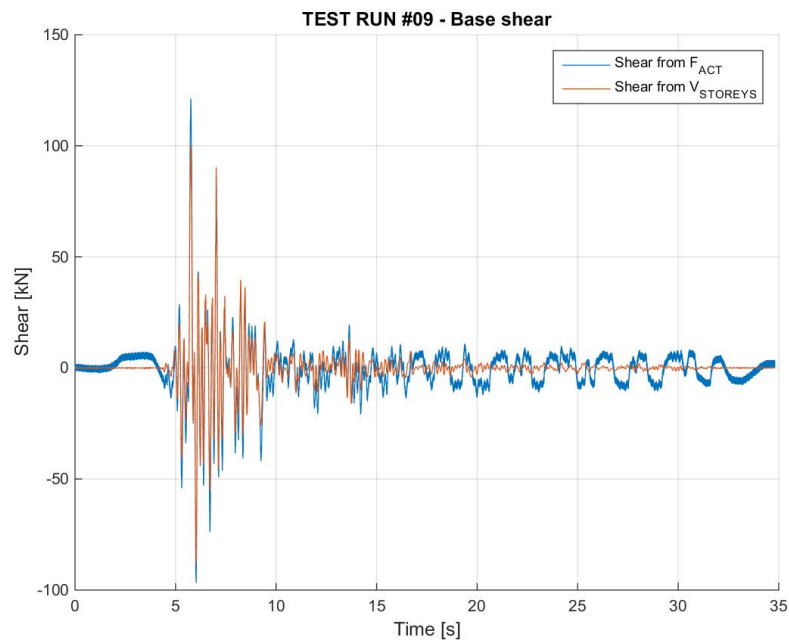
Figure 509. Imposed base shear vs. measured base shear – Comparison through time.

Figure 510 shows the hysteretic base shear-top displacement response of the specimen. For the sake of clarity, it is noted that the total base shear is plotted against the top-to-base displacement of EUC-BUILD5 specimen. Hysteresis loops were also processed to obtain a linear approximation that takes into account both Northward and Southward (i.e. positive and negative) motion and identifies, in an equivalent manner, the corresponding base shear-displacement couples. The hysteretic response and the linear approximation are superimposed in Figure 511.
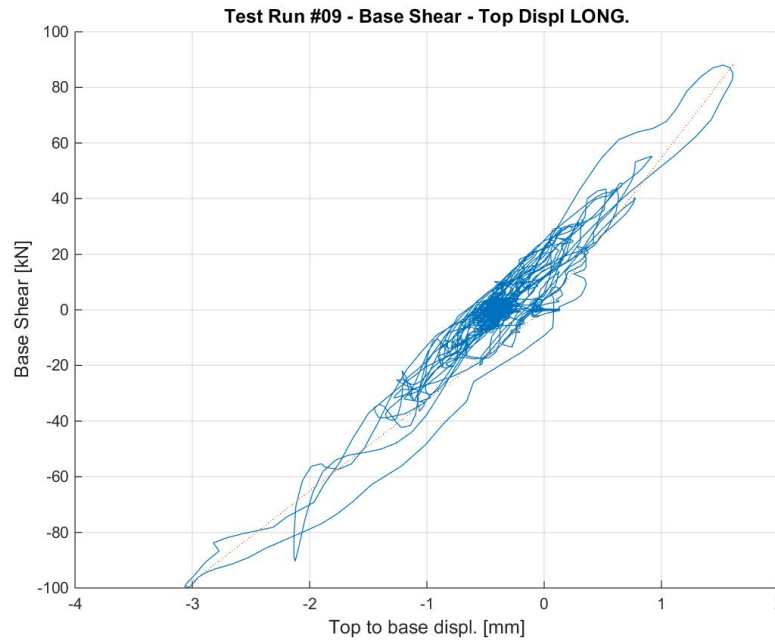
Figure 510. Base shear-top displacement response of EUC-BUILD5 – Test run #9, top-to-base displacement.
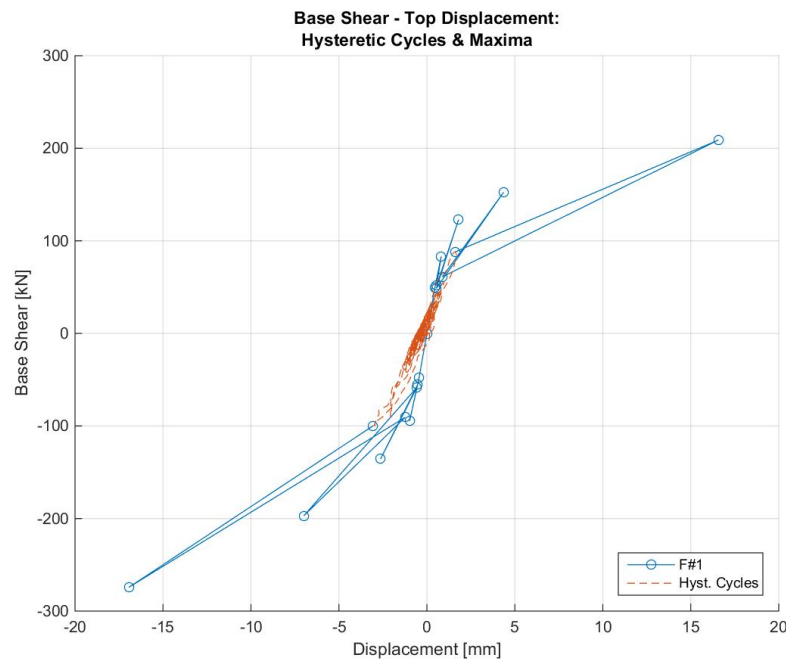
Figure 511. Base shear vs. top-to-base displacement – Hysteretic response and maxima (positive and negative).

Figure 512 shows the absolute maxima – positive or negative – top displacement-base shear couples that were obtained from the hysteresis loops of the specimen.
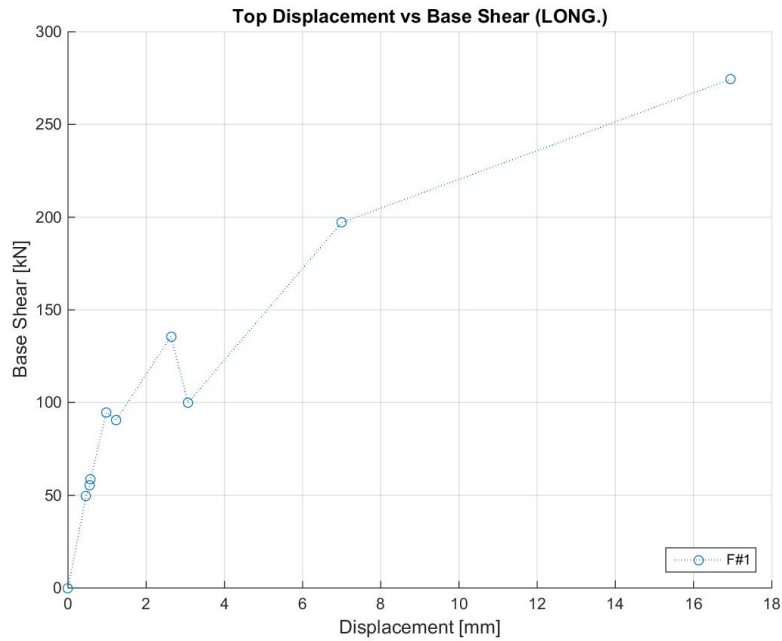
Figure 512. Base shear vs. top-to-base displacement maxima – Test run #9.

Figure 513 shows the maxima – positive and negative – top displacement-base shear couples that were obtained from the linear approximation of the specimen response (see Figure 511).
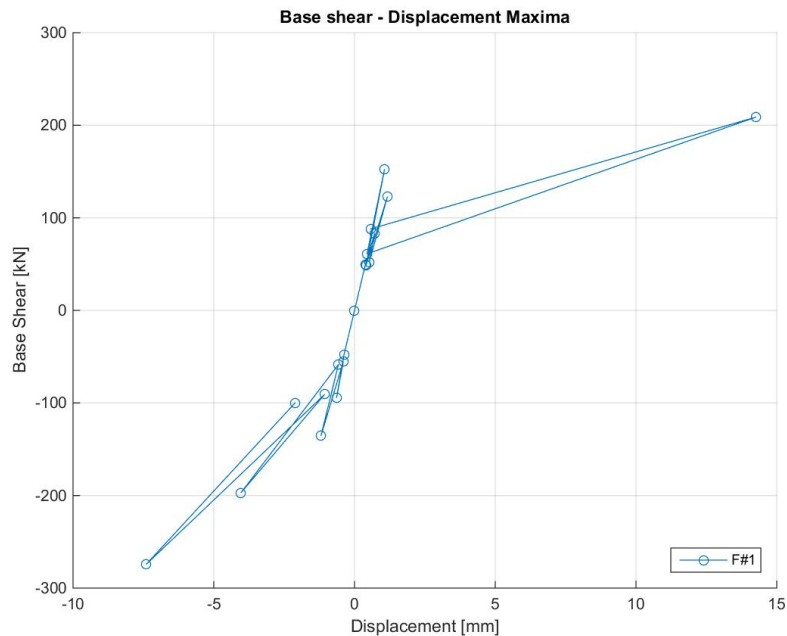
Figure 513. Base shear vs. top-to-base displacement maxima – Positive and negative, Test run #9.

Figure 514 shows the hysteretic response of the first storey of the specimen, which is illustrated in terms of storey shear versus inter-storey displacement relationship.
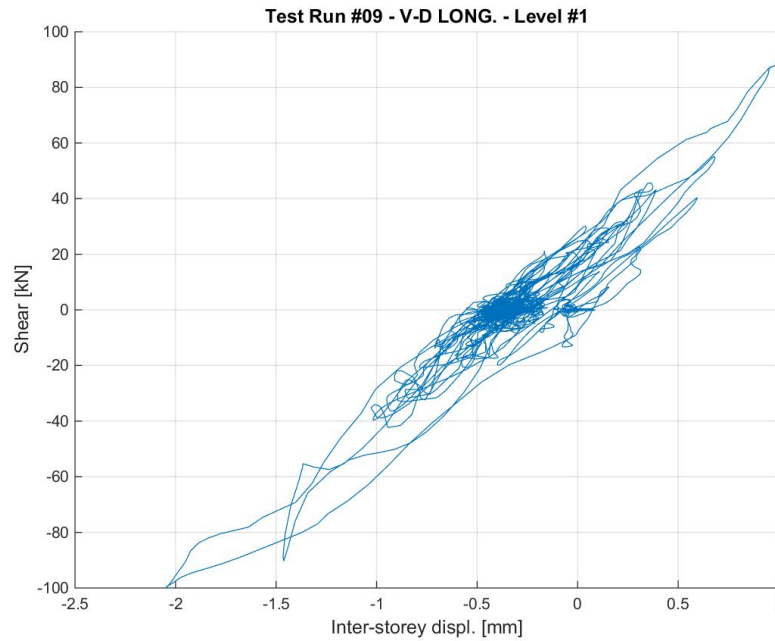
Figure 514. Storey shear vs. inter-storey displacement response – First storey, Test run #9.

Figure 515 shows the hysteretic response of the second storey of the specimen, which is illustrated in terms of storey shear versus inter-storey displacement relationship.
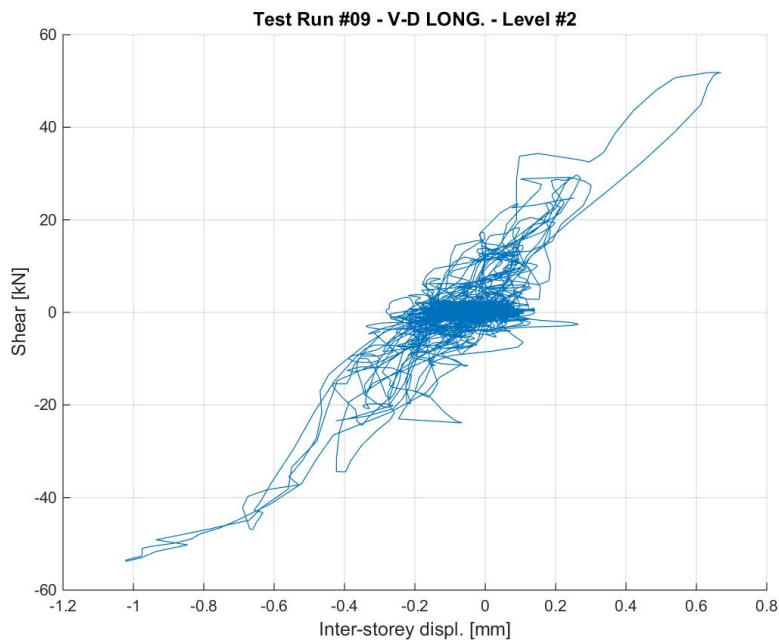
Figure 515. Storey shear vs. inter-storey displacement response – Second storey, Test run #9.

Figure 516 shows the PGA versus maxima – positive and negative – top displacement relationship, the latter parameter being identified according to the linear approximation reported in Figure 511.
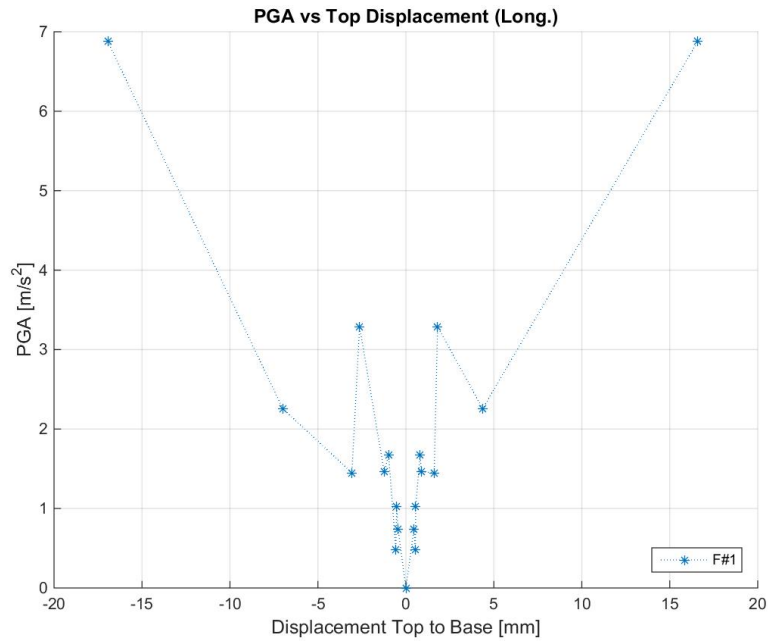
Figure 516. PGA vs. top-to-base displacement maxima – Positive and negative, Test run #9.

Figure 517 shows the PGA versus secant – positive and negative – stiffness relationship, the latter parameter being identified according to the linear approximation reported in Figure 511.
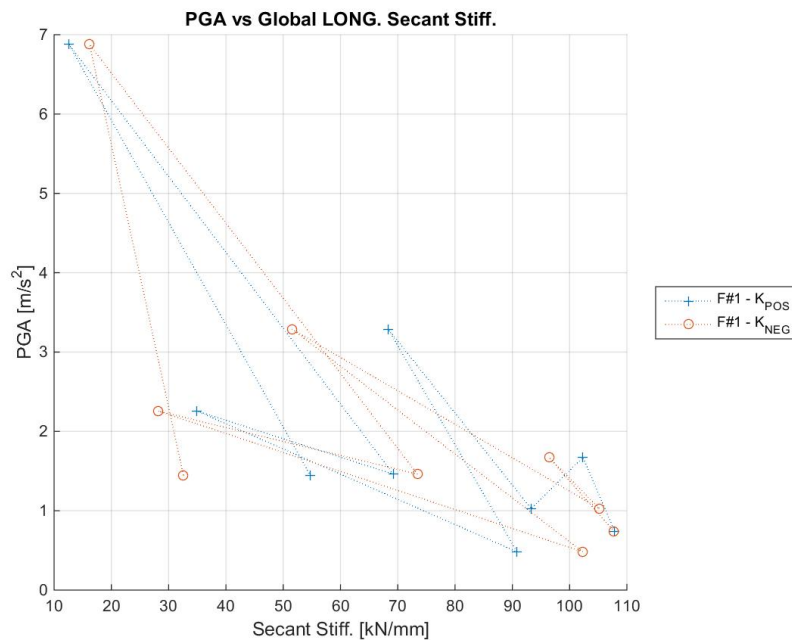
Figure 517. PGA-global secant stiffness relationships – Positive and negative directions, Test run #9.

Figure 518 shows the PGA versus maximum base shear relationship of the specimen at this stage of the testing sequence.
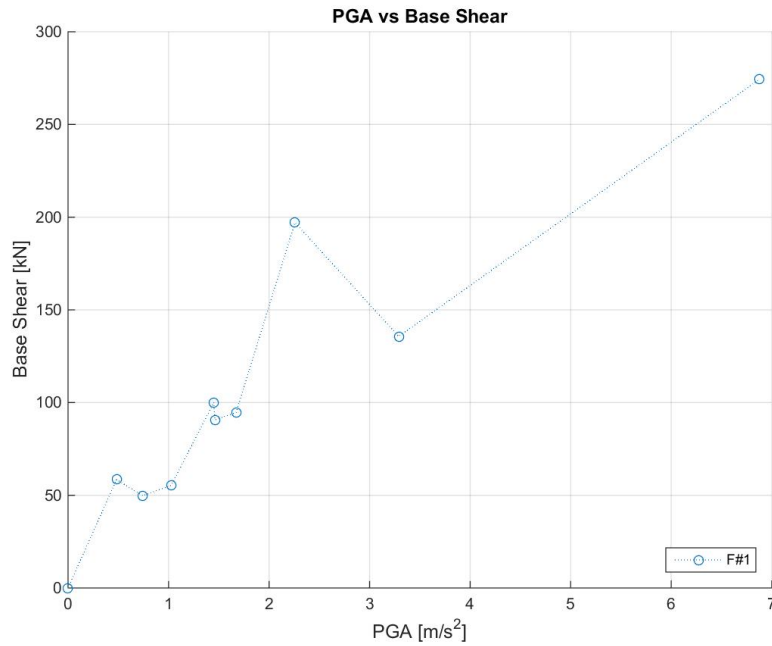
Figure 518. Maximum base shear vs. peak ground acceleration – Test run #9.

Figure 519 shows the arias intensity versus maximum base shear relationship of the specimen at this stage of the testing sequence.
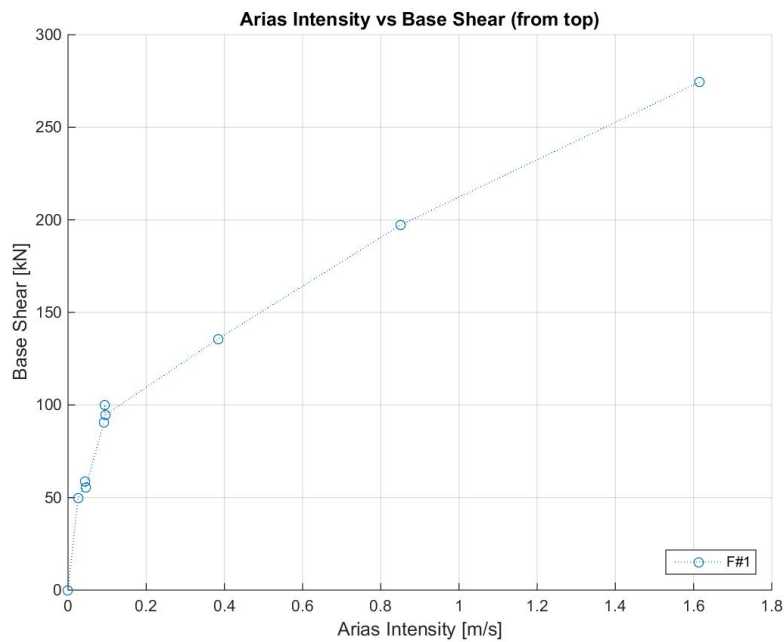
Figure 519. Maximum base shear vs. arias intensity – Test run #9.

6.6.10 Test run #10 – SF = 200% – Test at 200%(BIS)

Figure 520 shows the comparison between the acceleration spectra from time-histories at reference and feedback (as recorded by the shake-table controller). The experimental acceleration time-history used for the spectrum comparison is the average of the recorded accelerations on the foundation of EUC-BUILD5 specimen (accelerometers #139 and #140). Furthermore, Figure 521 shows the discrepancy in percentage.
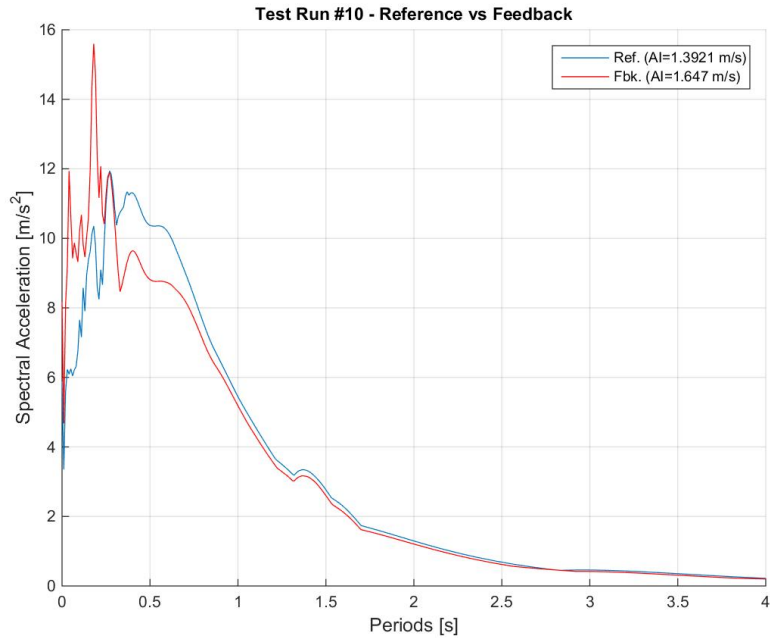
Figure 520. Comparison between acceleration spectra from time-histories at reference and feedback.
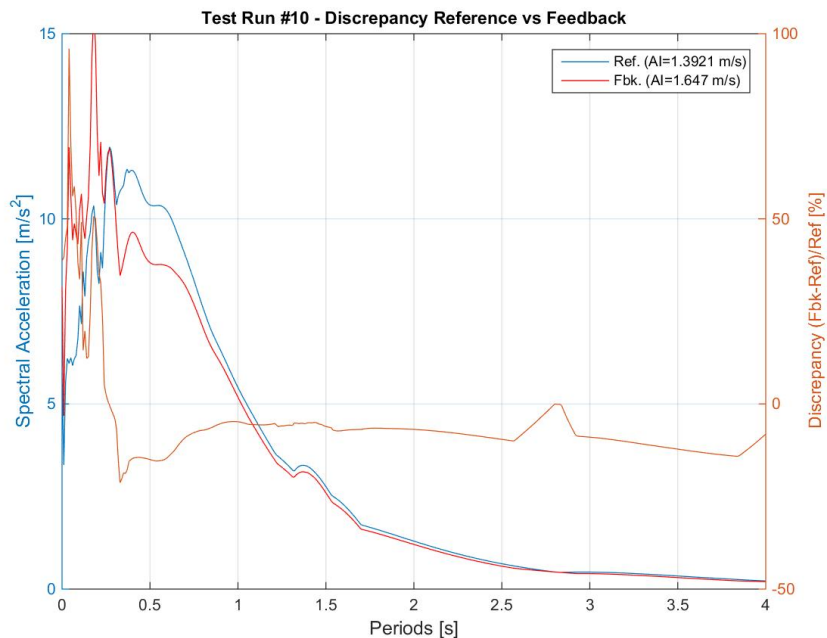
Figure 521. Discrepancy between acceleration spectra from time-histories at reference and feedback.

Figure 522 shows the acceleration time-histories recorded at the foundation level (accelerometers #139 and #140) and the average of the accelerations recorded by the two accelerometers.
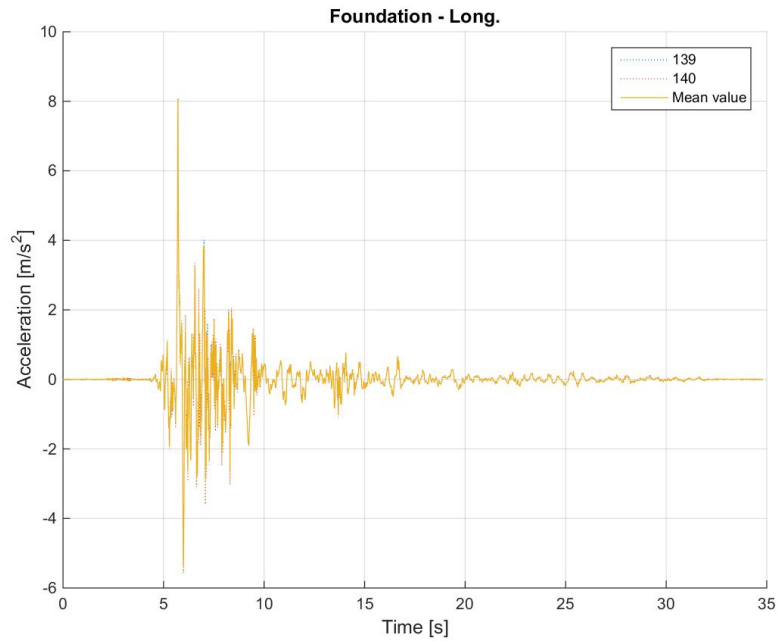
Figure 522. Acceleration time-histories at the foundation level – Individual and average of accelerometers.
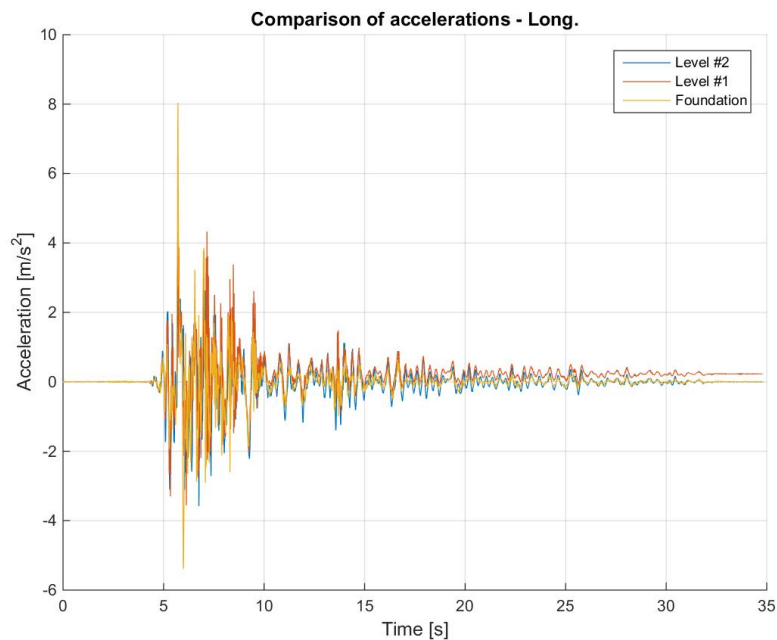
Figure 523 shows the acceleration time-histories recorded at the first floor of the specimen and the average of the accelerations recorded by all the accelerometers installed at this level.
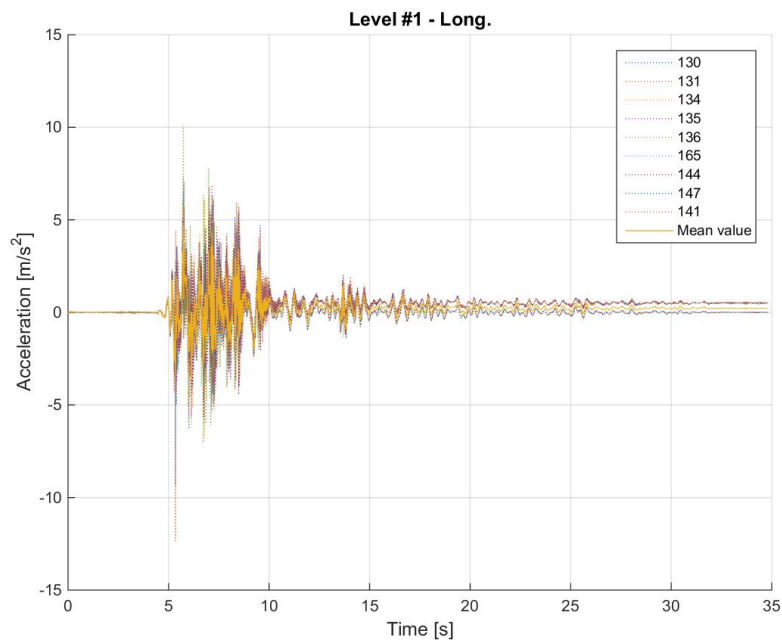
Figure 523. Acceleration time-histories at the first floor – Individual and average of accelerometers.

Figure 524 shows the acceleration time-histories recorded at the second floor and the average of the accelerations recorded by all the accelerometers installed at this level.
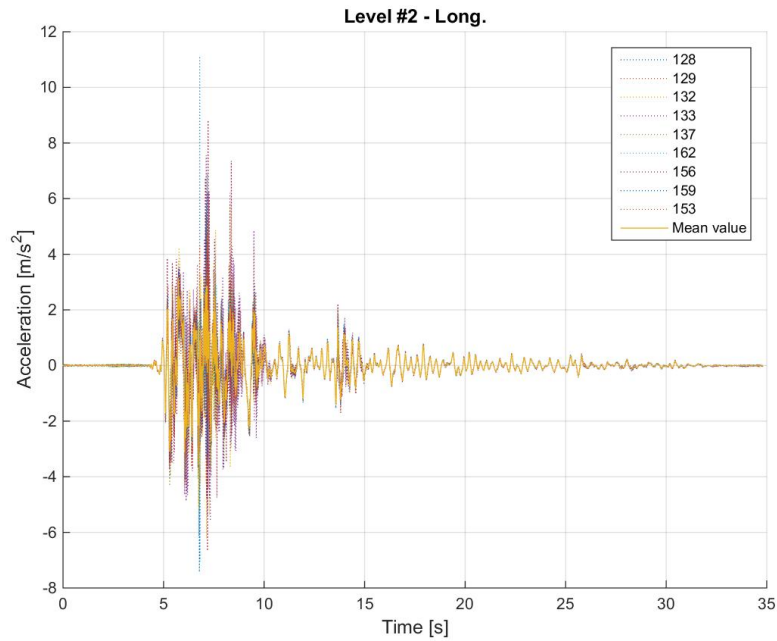
Figure 524. Acceleration time-histories at the second floor – Individual and average of accelerometers.

Figure 525 shows a comparison between the average acceleration time-history at the foundation, the first floor and the second floor of the specimen.
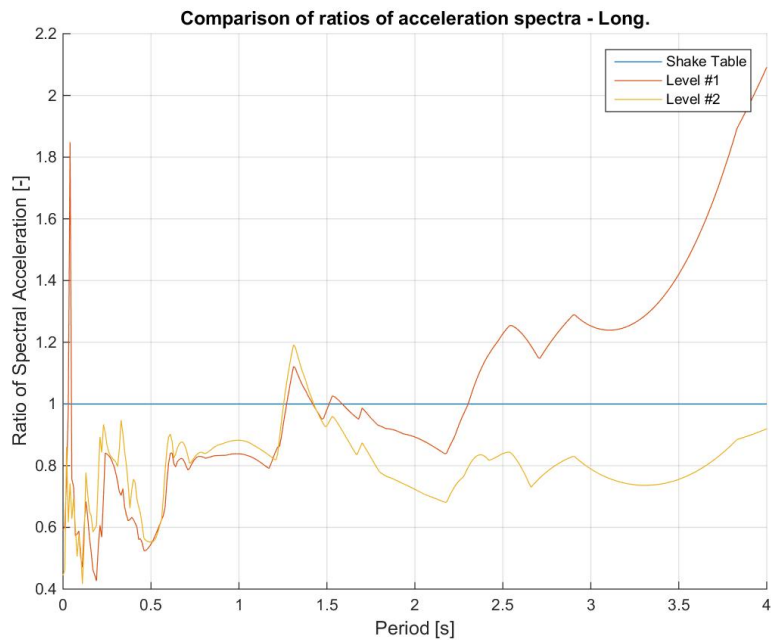

Figure 525. Comparison between average acceleration time-histories – Foundation, first and second storeys.

Figure 526 shows a comparison between the acceleration spectra at the base, the first storey and the second storey, which were computed using the average acceleration time-history at the foundation, the first floor and the second floor of the specimen. The spectral accelerations were also normalised with respect to the one at the base and the obtained spectral acceleration ratios are plotted together in Figure 527. Obviously, the curve obtained for the base is the horizontal blue line, which is plotted since it serves as reference for the two floors (and their amplification).
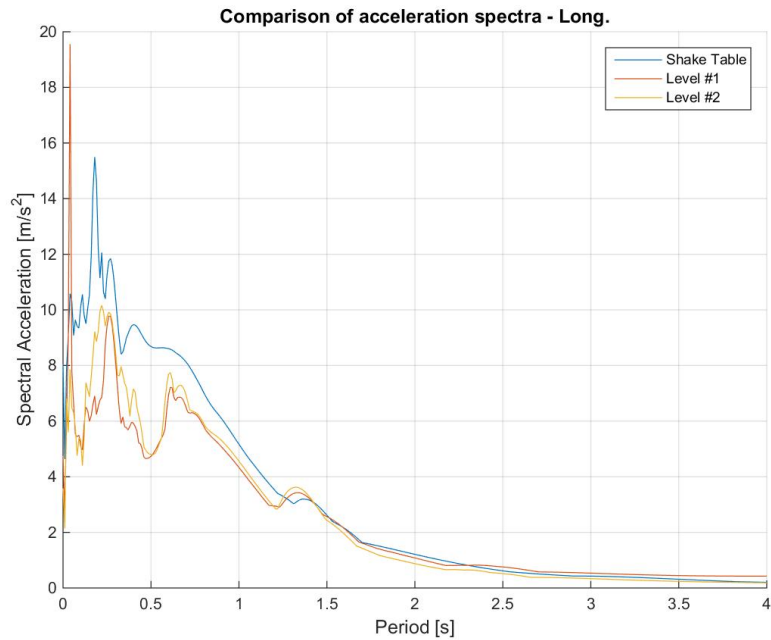
Figure 526. Acceleration spectra from average time-histories at the foundation, first and second floors.


Figure 527. Spectral acceleration ratios: first floor-to-foundation and second floor-to-foundation.

Figure 528 shows a comparison between the displacement time-histories at the foundation, the first floor and the second floor of the specimen.
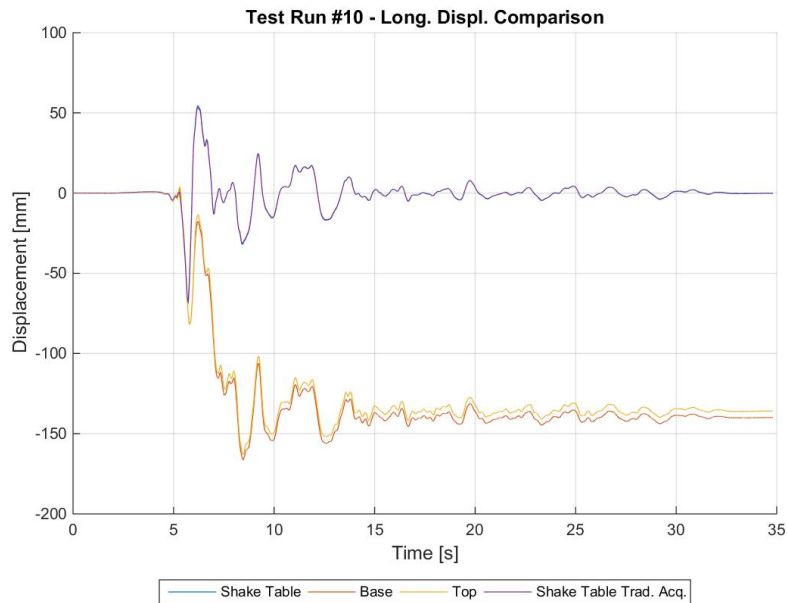

Figure 528. Comparison between average displacement time-histories – Foundation, first and second storeys.

Figure 529 shows a comparison between the imposed base shear time-history and the recorded base shear time-history, the former one being the force applied by the actuators of the shake-table.
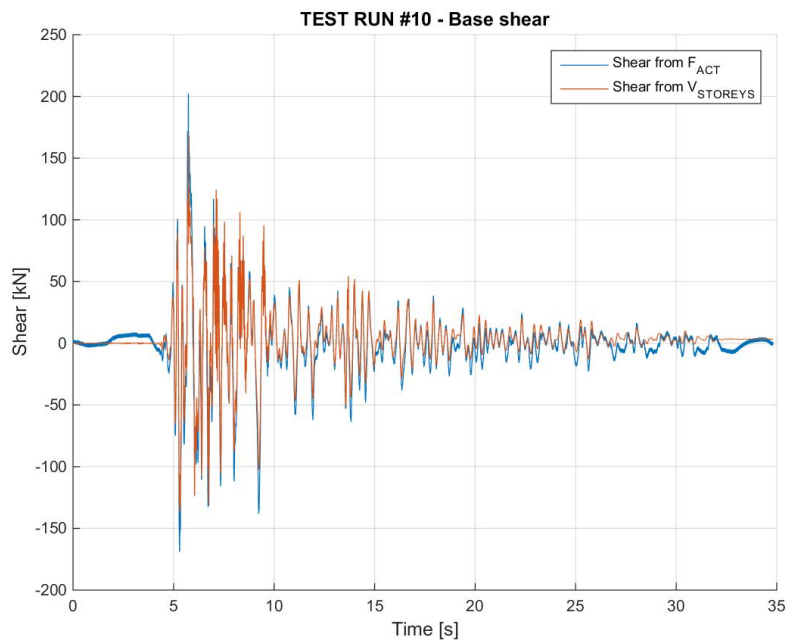

Figure 529. Imposed base shear vs. measured base shear – Comparison through time.

Figure 530 shows the hysteretic base shear-top displacement response of the specimen. For the sake of clarity, it is noted that the total base shear is plotted against the top-to-base displacement of EUC-BUILD5 specimen. Hysteresis loops were also processed to obtain a linear approximation that takes into account both Northward and Southward (i.e. positive and negative) motion and identifies, in an equivalent manner, the corresponding base shear-displacement couples. The hysteretic response and the linear approximation are superimposed in Figure 531.
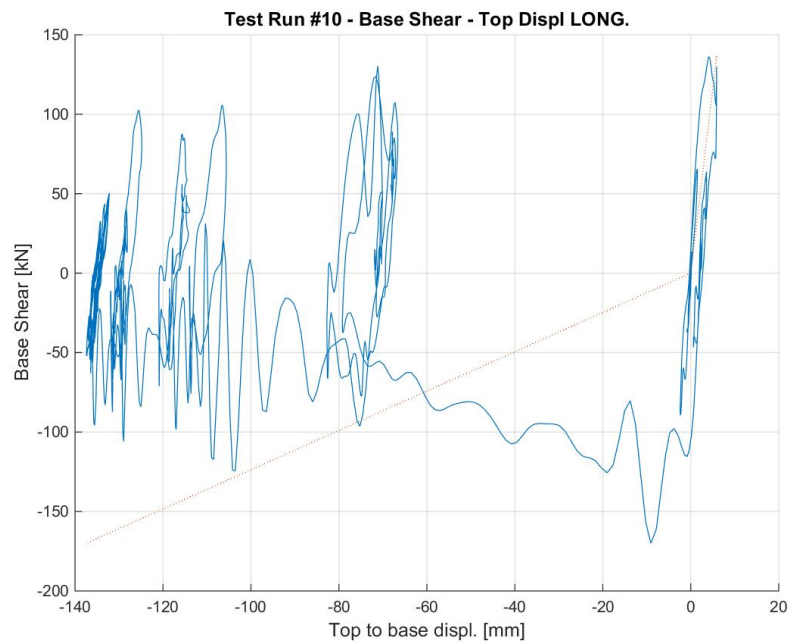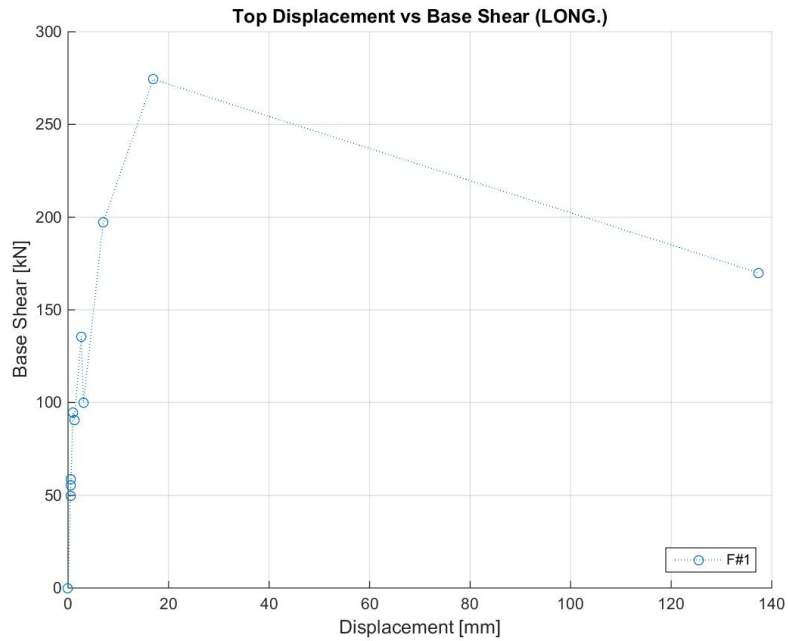

Figure 530. Base shear-top displacement response of EUC-BUILD5 – Test run #10, top-to-base displacement.
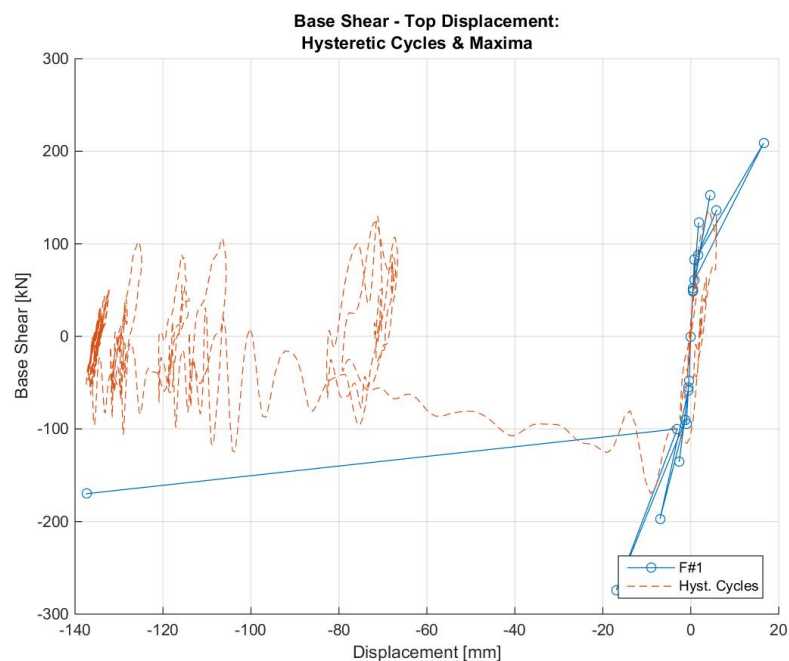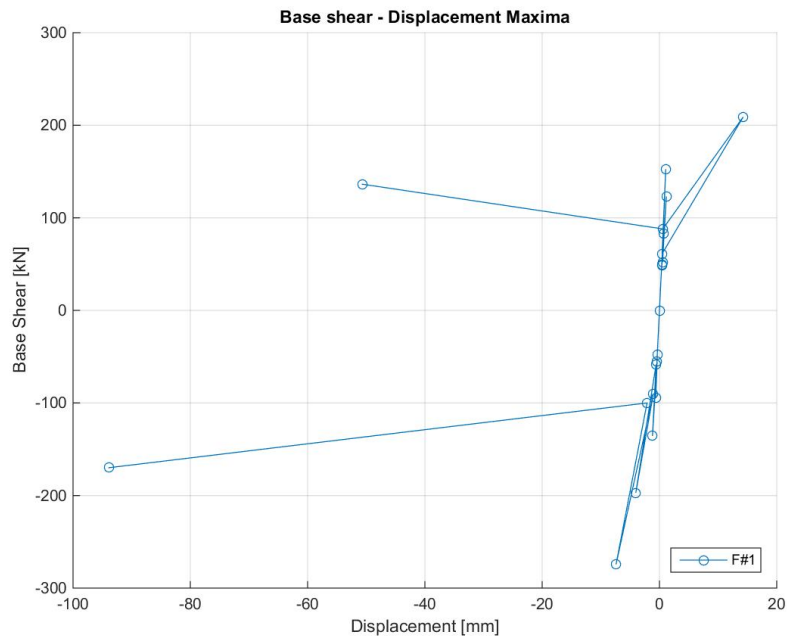

Figure 531. Base shear vs. top-to-base displacement – Hysteretic response and maxima (positive and negative).

Figure 532 shows the absolute maxima – positive or negative – top displacement-base shear couples that were obtained from the hysteresis loops of the specimen.


Figure 532. Base shear vs. top-to-base displacement maxima – Test run #10.

Figure 533 shows the maxima – positive and negative – top displacement-base shear couples that were obtained from the linear approximation of the specimen response (see Figure 531).


Figure 533. Base shear vs. top-to-base displacement maxima – Positive and negative, Test run #10.

Figure 534 shows the hysteretic response of the first storey of the specimen, which is illustrated in terms of storey shear versus inter-storey displacement relationship.
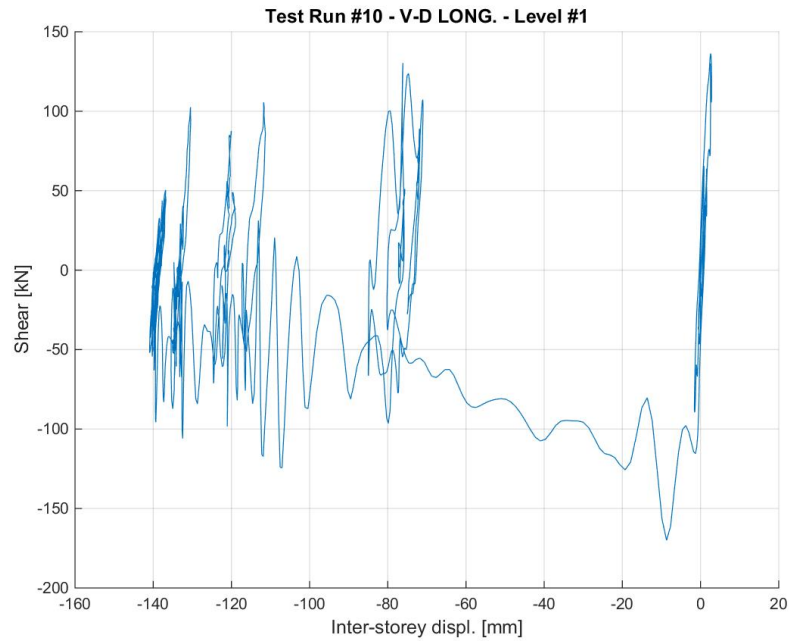
Figure 534. Storey shear vs. inter-storey displacement response – First storey, Test run #10.

Figure 535 shows the hysteretic response of the second storey of the specimen, which is illustrated in terms of storey shear versus inter-storey displacement relationship.
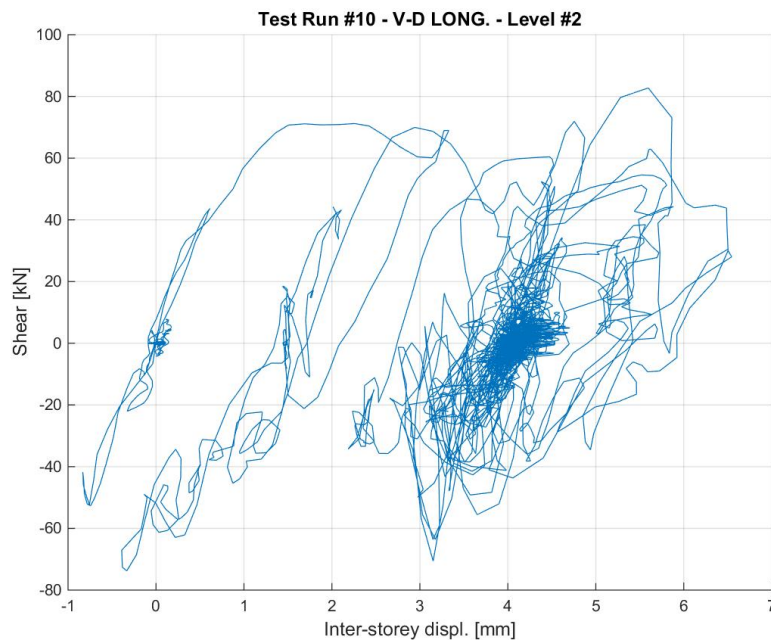
Figure 535. Storey shear vs. inter-storey displacement response – Second storey, Test run #10.

Figure 536 shows the PGA versus maxima – positive and negative – top displacement relationship, the latter parameter being identified according to the linear approximation reported in Figure 531.
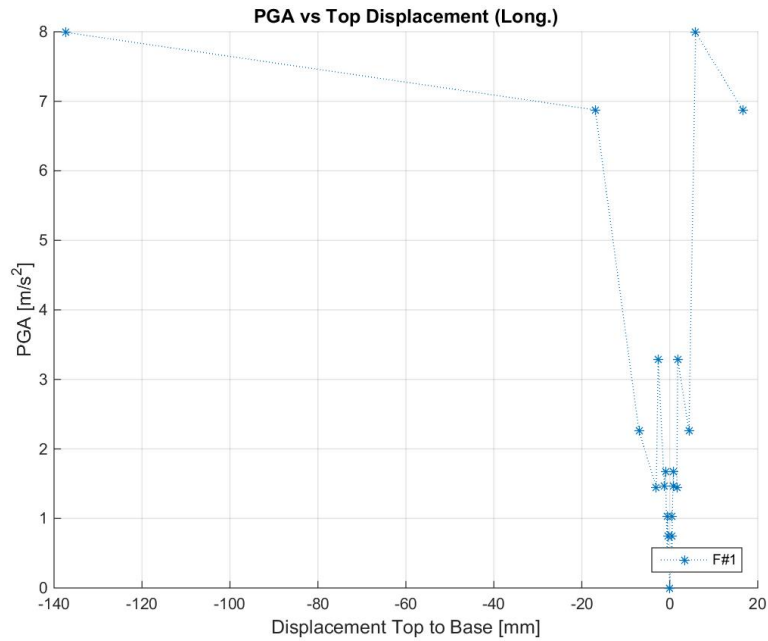

Figure 536. PGA vs. top-to-base displacement maxima – Positive and negative, Test run #10.

Figure 537 shows the PGA versus secant – positive and negative – stiffness relationship, the latter parameter being identified according to the linear approximation reported in Figure 531.
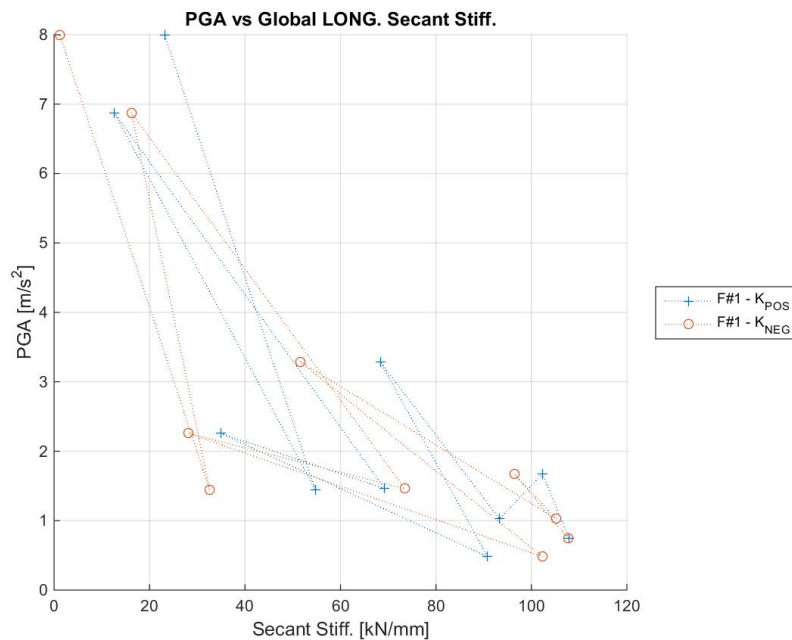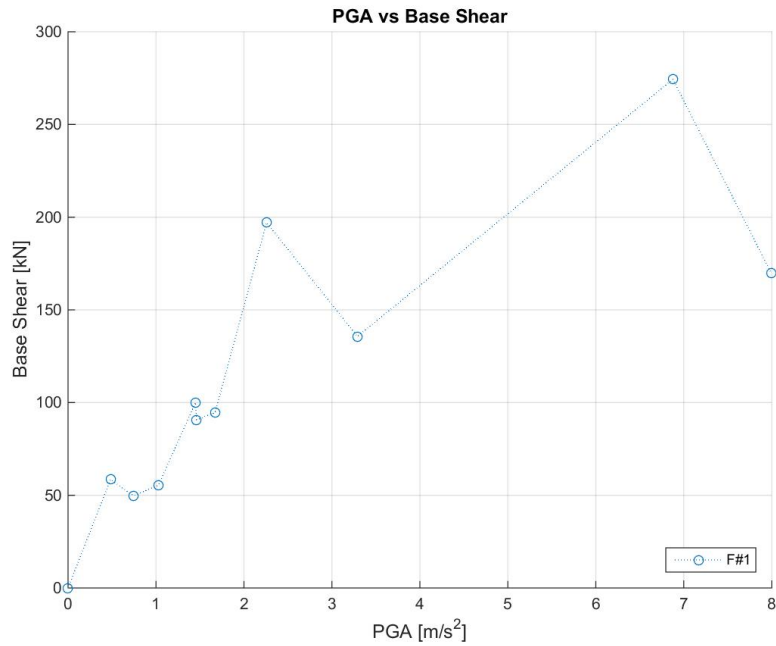

Figure 537. PGA-global secant stiffness relationships – Positive and negative directions, Test run #10.

Figure 538 shows the PGA versus maximum base shear relationship of the specimen at this stage of the testing sequence.

Figure 538. Maximum base shear vs. peak ground acceleration – Test run #10.

Figure 539 shows the arias intensity versus maximum base shear relationship of the specimen at this stage of the testing sequence.
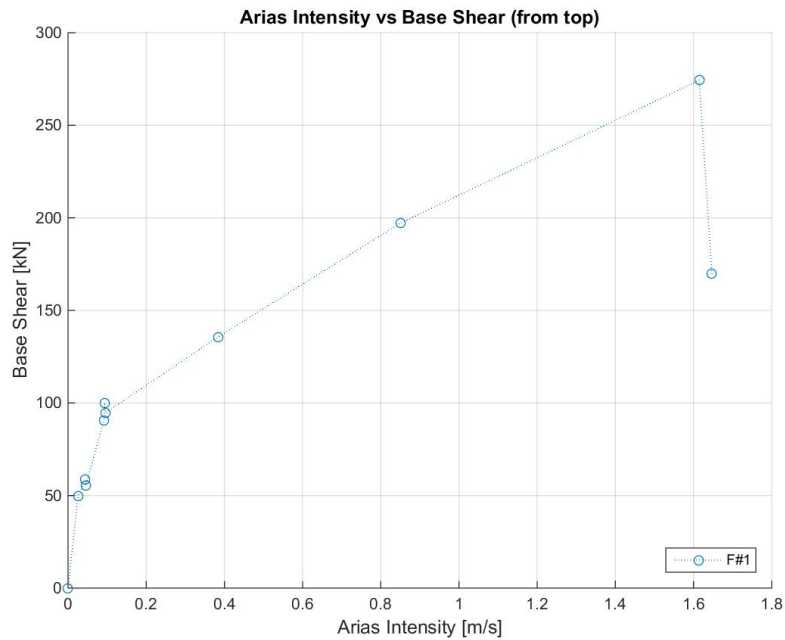
Figure 539. Maximum base shear vs. arias intensity – Test run #10.

7   Dismantling of EUC-BUILD5 specimen

Apart from minor issues that will be discussed in what follows, the process of dismantling of EUC-BUILD5 specimen was essentially based on the same approach that was followed for the dismantling of the EUC-BUILD4 specimen. As such, a detailed photographic sequence of the operations was omitted for the sake of brevity, and interested readers may refer instead to the companion report *Cyclic testing of a full-scale two-storey RC precast wall-slab-wall structure representative of the Groningen building stock*.

The primary phases of dismantling are, in any case, briefly reported and several photos of the three-way connection between the first-storey stability and lateral walls are presented, with a view to further point out aspects related to the response/failure mechanism of the steel connectors and the battered state of the specimen after the test. Figure 540 to Figure 555 are provided to summarise the prevailing observations collected for this purpose.

It is worth recalling that, in the very first minutes after the test, EUC-BUILD5 specimen had to be urgently propped-up, in face of what appeared to be a very precarious stability of the structure. To this end, use was made of temporary steel vertical and diagonal members, the latter ones being the same adopted in the erection of the specimen. Props were first installed and then it was possible to pull the first floor up from the precast walls underneath, as done for the case of EUC-BUILD4. It is clear that, in that case, steel plates and prestressed tendons mounted on the structure for installation of the actuators had contributed to prevent any type of disassemblage of the flooring system. On the other hand, such an effect was ensured in this case by a post-tensioned steel beam.

Thus, when dismantling the test specimen, the flooring system composed of hollow core slab panels and concrete topping was carefully lifted without disassemblage of precast elements and concrete screed on top of them. Once this operation had been completed, the second-storey stability wall was dismantled, by simply removing the grout in the niches and cutting the hooked anchors embedded into them. Use was then made of a similar approach for dismantling the transversal walls. Each wall was dismantled and lifted up by means of the same anchoring hooks used to erect the specimen.

Dismantling of the first storey started with the uplift of the flooring system that was carried out like before, without ruining the concrete topping and separating the slab panels apart. This also allowed inspection of the top edge of the ground-floor walls; details of the fabric felt underneath the first-floor slab, in correspondence to the stability wall, are reported in Figure 540 (it is recalled that close to the south edge of the stability wall the post-construction gap between the stability wall and the precast slabs was not large enough to allow the removal of the layer of felt).

As far as dismantling of the ground-floor walls is concerned, the process started with the North-sided transversal walls and then moved on with the South-sided walls. Figure 541 shows overall and enlarged views of both the stability wall and the SouthEast-sided transversal wall. As pointed out by Figure 542 to Figure 555, each one of the four three-way joints was surveyed with great care and detailed enlarged views of the permanently-bent connectors were collected before dismantling of these wall panels. Finally, the stability wall and the two South-sided transversal walls were dismantled by simply lifting them up, one by one. Although the stability wall and the two lateral walls were completely disconnected, there was some grout still remaining in the niches, which was thus removed so as to separate the two lateral walls apart.

Figure 540. Top view of stability and transversal walls after dismantling of the first-storey slab.

Figure 541. Diagonal props for lateral stability and detail of the damage state of steel connectors.

It was hence possible to inspect the damaged anchors embedded in the South transversal walls of the first storey. A few photos of them are collected in Figure 542 to Figure 555, and corroborate previous considerations regarding their failure mechanism. As also shown either in Section 6.5.4 or by the testing of EUC-BUILD4 (please refer to Eucentre report EUC173/2017U), permanent bending of connectors was caused by the orthogonal ones embedded in the stability wall. However, whilst the steel connectors of the first-storey stability wall remained intact in the case of EUC-BUILD4, the dynamic loading exerted by the last test run (i.e. Test run #10) was strong enough to damage also these. The end zone of the hook, which is in contact with the connector between the transversal walls, opened up, when pulling, and the three-way anchorage got entirely disconnected. The hook itself became straight and the inner part bent upwards conspicuously. Noteworthy is that, although this mechanism was more pronounced in the top two three-way connections, all four joints exhibited damage/failure of fairly similar type and extent.

To confirm such a consideration, interested readers may inpect the photographic sequence reported below. Details of the top three-way connection (i.e. the fourth one starting from the base) are shown in Figure 544 and Figure 545, whereas those pertaining to the third joint can be observed in Figure 546 to Figure 548. Furthermore, Figure 549 to Figure 551 present few photos of the steel connectors of the second three-way connection, and Figure 552 to Figure 554 report on the main observations for the bottom three-way joint. Finally, Figure 555 provides a further and even more enlarged view of the top three-way joint, the latter being the one that featured the widest gap between the first-storey stability and lateral walls.

Figure 542. Permanenlty-bent steel connectors embedded in the sockets of the stability wall.

Figure 543. Permanenlty-bent steel connectors embedded in the stability wall – West-side view.

Figure 544. Outwardly-bent and upwardly-bent steel hooks in lateral and stability walls – Top connection.
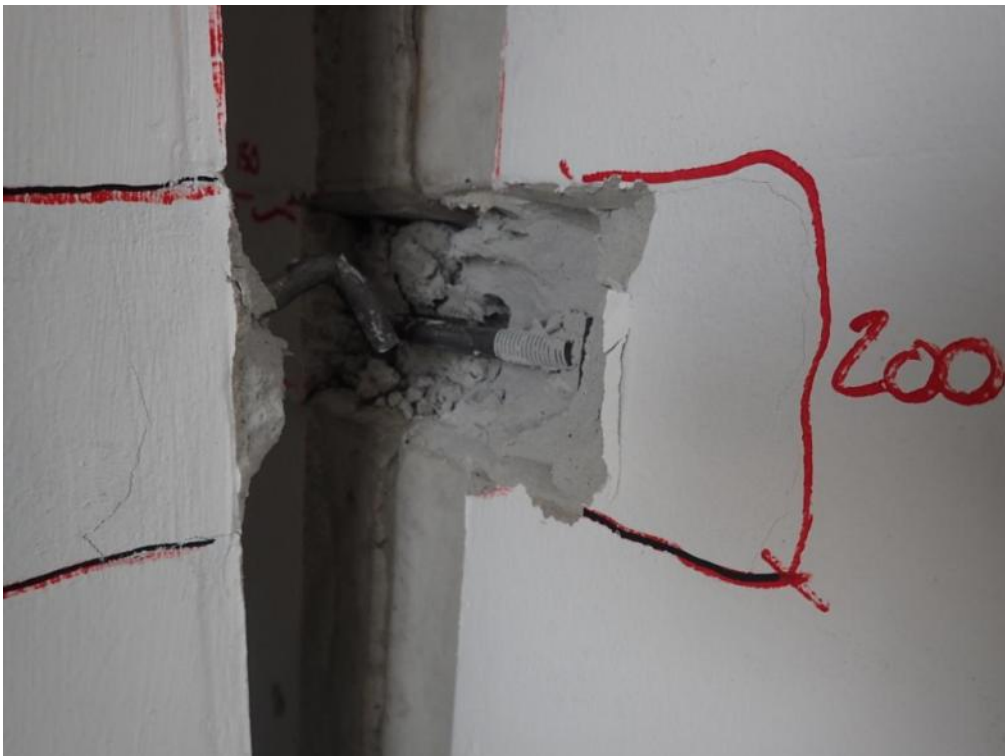
Figure 545. Enlarged view of steel hooks embedded in lateral and stability walls – Top connection.

Figure 546. Permanently-bent steel hooks in lateral and stability walls – Third panel joint from the base.

Figure 547. Enlarged view of steel hooks in lateral and stability walls – Third panel joint from the base.

Figure 548. Outwardly-bent and upwardly-bent steel hooks of the third panel joint from the base.

Figure 549. Damage of steel connectors between stability and lateral walls – Second joint from the base.

Figure 550. Enlarged view of failed steel connectors in the second panel joint from the base.

Figure 551. Outwardly-bent and upwardly-bent steel hooks of the second panel joint (from the base).

Figure 552. Damage pattern of the bottom three-way connection between stability and lateral walls.

Figure 553. Detailed view of the bottom three-way connection between the stability and lateral walls.

Figure 554. Side view of the bottom three-way connection between stability and lateral walls.

Figure 555. Bottom view of bent steel connectors between lateral and stability walls – Top connection.

8 References

1. Arup [2017] 229746_031_NOT2008_Rev0.05_Issue EUC-BUILD-4 Prototype building description

2. Arup [2017] 229746_031.0_DRW2007_Rev0.05_Issue_EUC-BUILD-4_5 SWb Specimen drawings

3. Brunesi, E., Peloso, S., Pinho, R., Nascimbene, R. (2017a). *Cyclic testing of a full-scale two-storey RC precast wall-slab-wall structure representative of the Groningen building stock*. Report EUC173/2017U, European Centre for Training and Research in Earthquake Engineering (EUCENTRE), Pavia, Italy.

4. Brunesi, E., Peloso, S., Pinho, R., Nascimbene, R. (2017b). *Cyclic testing of a full-scale cast-in-place reinforced concrete wall-slab-wall structure representative of the Groningen building stock*. Report EUC095/2017U, European Centre for Training and Research in Earthquake Engineering (EUCENTRE), Pavia, Italy.

Appendix A

Appendix A1: test runs for controller compensation

The aim of this Appendix is to provide additional data/information regarding the shake-table test of specimen EUC-BUILD5, which was subjected to incremental dynamic test runs that consisted of a series of shake-table motions of increasing intensity. As reported in Table 14 of this report, a run for controller compensation had preceded each one of them. Needless to say that, during these auxiliary runs of minor relevance, track was taken of displacements and accelerations measured, as reported in Section 6.6.

Response plots are thus provided here, in addition to those presented therein, with the aim of clarifying even furher that test runs for controller compensation had negligible impact on the specimen. Separate sub-sections, one per each run, present response time-histories of measured displacements and computed forces. Hysteretic response curves are also provided using the procedure that was followed for test runs of relevance, as shown and extensively discussed in Section 6.2. By the same token, plots of the same type of those collected in Section 6.3 are herein presented, so as to illustrate the deformed shape of EUC-BUILD5 specimen at key time instants. Lastly, it is worth mentioning that these auxiliary/complementary plots may help further understanding the data collected in Section 6.6.

Test run #1 – SF = 25% – Controller compensation

Figure A1 shows response time-histories obtained for Test run #1. The horizontal forces exerted at the two floor levels and the corresponding horizontal displacements are collected therein, together with hysteretic curves presenting the storey force-storey displacement response and the storey shear versus inter-storey displacement response. Furthermore, Figure A2 shows the deformed shapes at positive and negative displacement peaks reached during Test run #1.
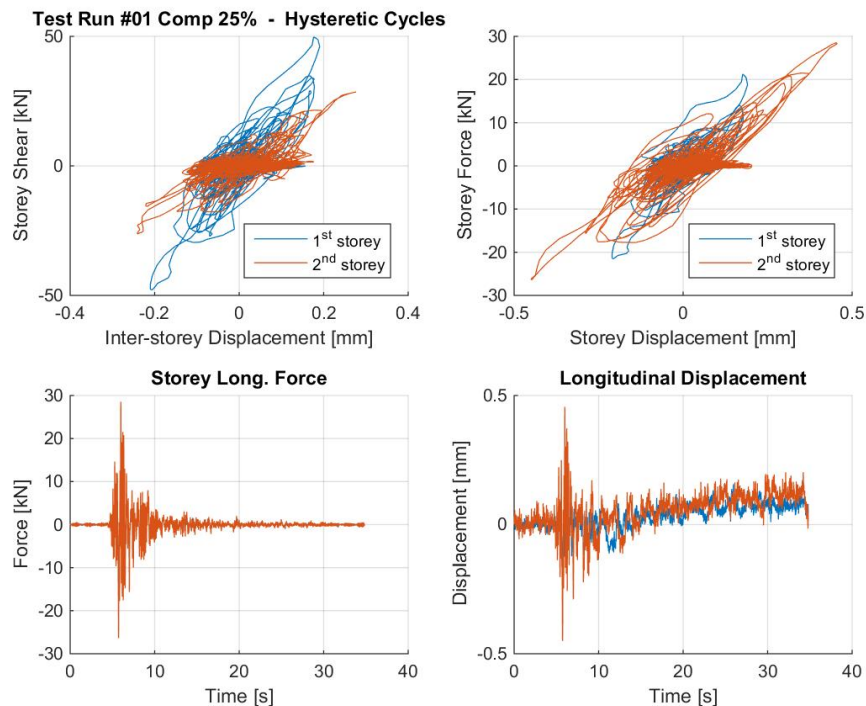

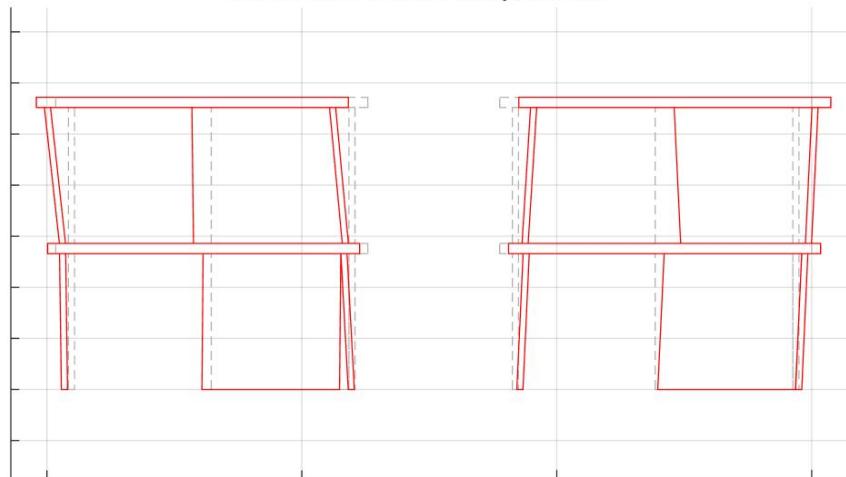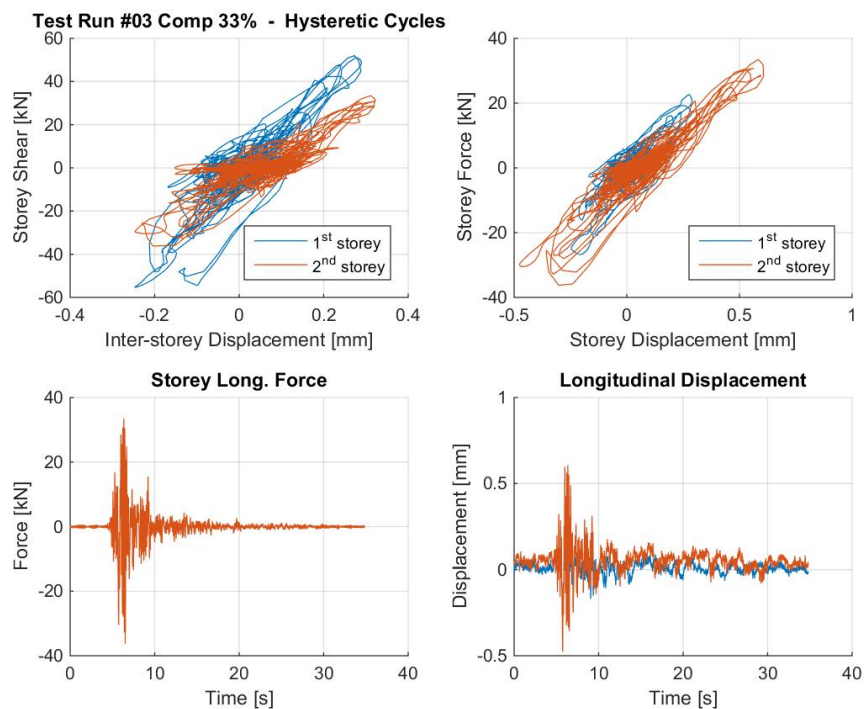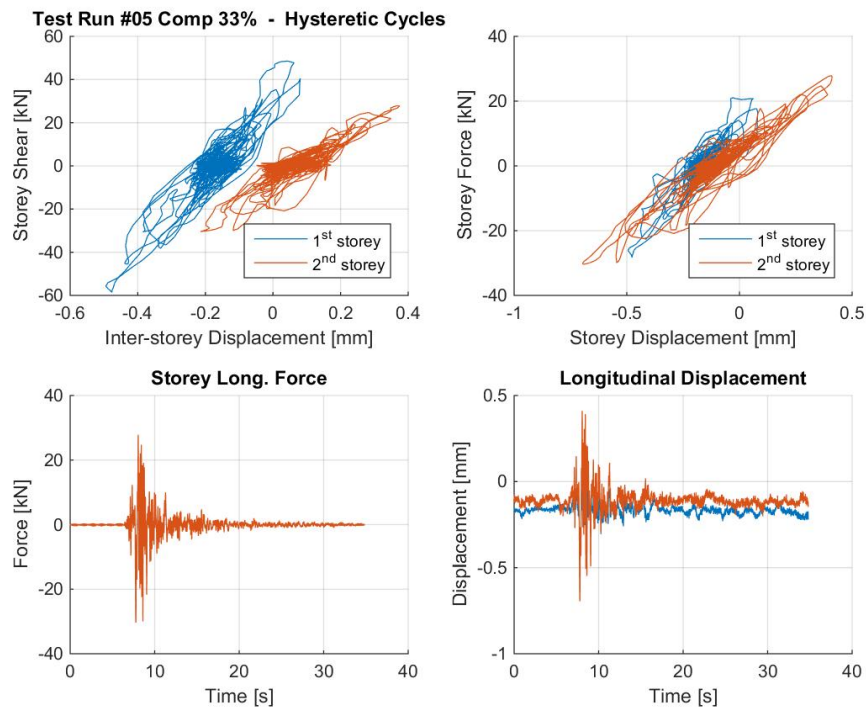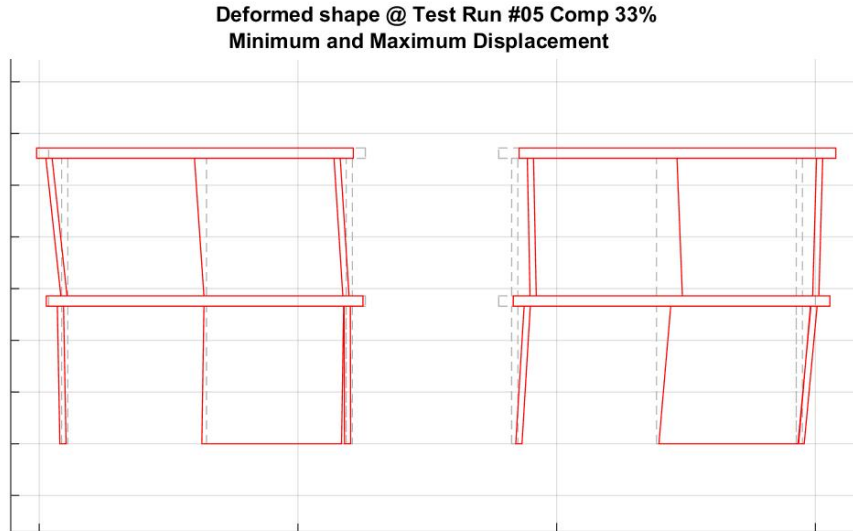**Figure A1. Response time-histories: displacement, storey force and storey shear – Test run #1.**

Figure A2. Deformed shape of EUC-BUILD5 specimen (max and min) – Test run #1.

Test run #3 – SF = 34% – Controller compensation

Figure A3 shows response time-histories obtained for Test run #3. The horizontal forces exerted at the two floor levels and the corresponding horizontal displacements are collected therein, together with hysteretic curves presenting the storey force-storey displacement response and the storey shear versus inter-storey displacement response. Furthermore, Figure A4 shows the deformed shapes at positive and negative displacement peaks reached during Test run #3.
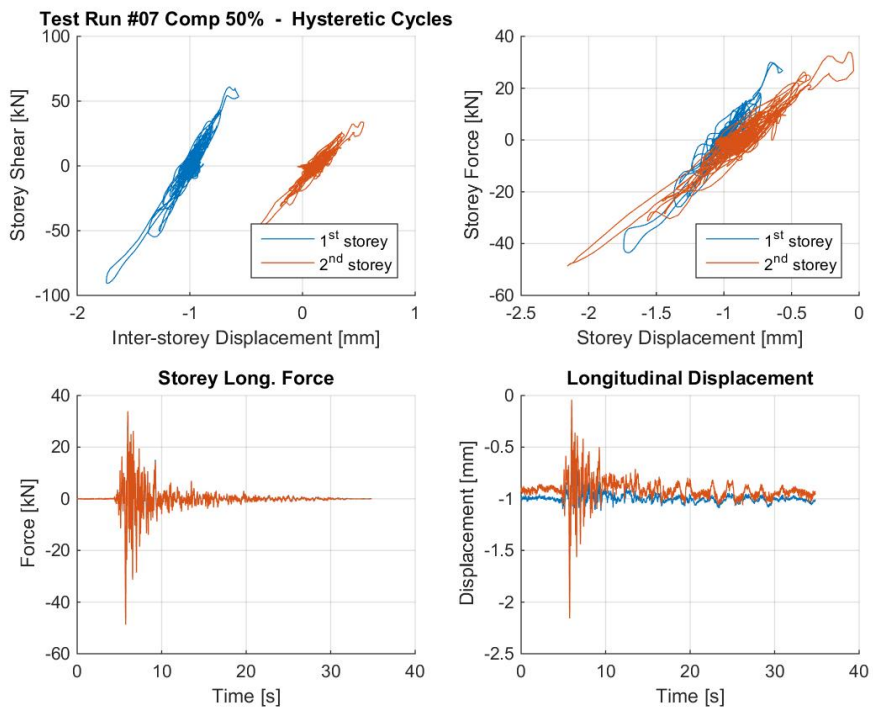

Figure A3. Response time-histories: displacement, storey force and storey shear – Test run #3.

Figure A4. Deformed shape of EUC-BUILD5 specimen (max and min) – Test run #3.
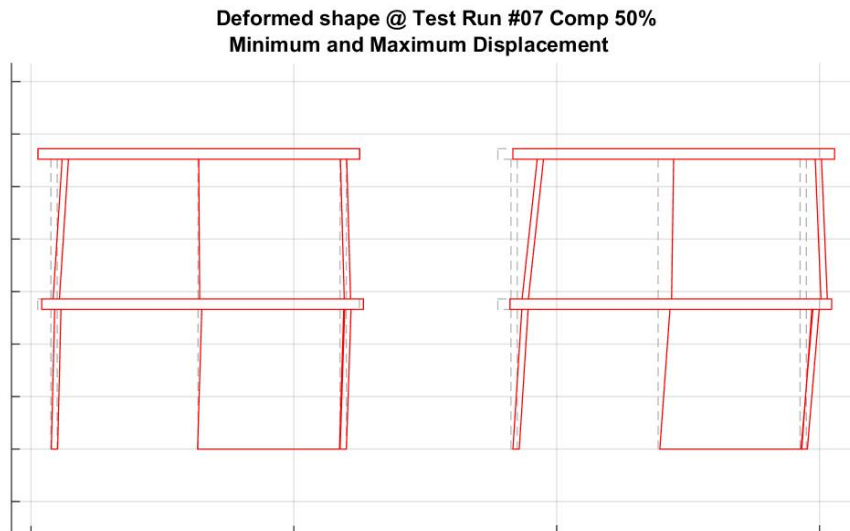
Test run #5 – SF = 34% – Controller compensation

Figure A5 shows response time-histories obtained for Test run #5. The horizontal forces exerted at the two floor levels and the corresponding horizontal displacements are collected therein, together with hysteretic curves presenting the storey force-storey displacement response and the storey shear versus inter-storey displacement response. Furthermore, Figure A6 shows the deformed shapes at positive and negative displacement peaks reached during Test run #5.

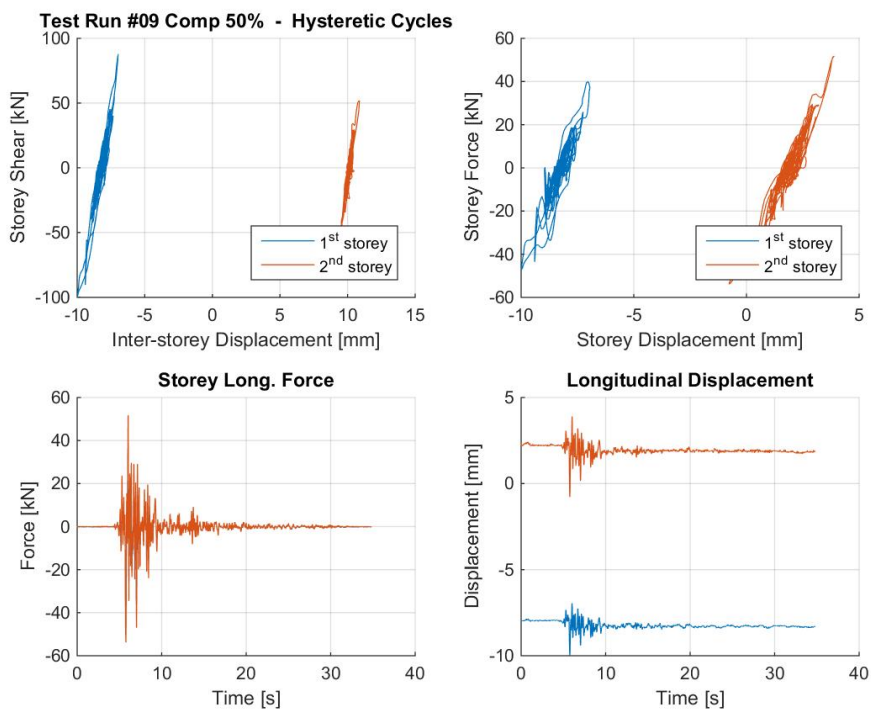**Figure A5. Response time-histories: displacement, storey force and storey shear – Test run #5.**

Figure A6. Deformed shape of EUC-BUILD5 specimen (max and min) – Test run #5.

Test run #7 – SF = 50% – Controller compensation

Figure A7 shows response time-histories obtained for Test run #7. The horizontal forces exerted at the two floor levels and the corresponding horizontal displacements are collected therein, together with hysteretic curves presenting the storey force-storey displacement response and the storey shear versus inter-storey displacement response. Furthermore, Figure A8 shows the deformed shapes at positive and negative displacement peaks reached during Test run #7.

Figure A7. Response time-histories: displacement, storey force and storey shear – Test run #7.

Figure A8. Deformed shape of EUC-BUILD5 specimen (max and min) – Test run #7.

Test run #9 – SF = 50% – Controller compensation

Figure A9 shows response time-histories obtained for Test run #9. The horizontal forces exerted at the two floor levels and the corresponding horizontal displacements are collected therein, together with hysteretic curves presenting the storey force-storey displacement response and the storey shear versus inter-storey displacement response. Furthermore, Figure A10 shows the deformed shapes at positive and negative displacement peaks reached during Test run #9.

Figure A9. Response time-histories: displacement, storey force and storey shear – Test run #9.

Deformed shape @ Test Run #09 Comp 50%
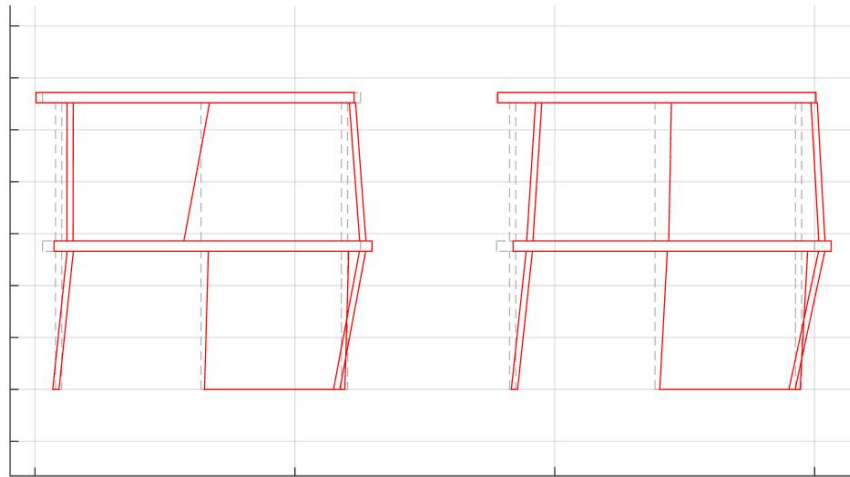**Minimum and Maximum Displacement**

Figure A10. Deformed shape of EUC-BUILD5 specimen (max and min) – Test run #9.

Appendix A2: response including test runs for controller compensation

In what follows, the experimental response of EUC-BUILD5 specimen was analysed even further in order to provide interested readers with a series of complementary plots of the hysteretic curves of both the specimen and key parts of it. Therein, data pertaining to test runs for structural assessment purposes are superimposed to those of runs for controller compensation.

As extensively shown in Section 6.6 and also in Appendix A1, the series of test runs carried out for controller compensation had minor influence on both structural response and evolution of dynamic properties of specimen EUC-BUILD5. Despite this, for the sake of completeness and transparency, global and local response plots including test runs for controller compensation are presented in the following sections, one per each type of data examined.

Global response

Figure A11 and Figure A12 show the base shear versus top-to-base displacement response curve of the specimen, explicitly accounting for the response of test runs executed for purposes of controller compensation (see Table 14 of this report). Consistently to the approach that has been considered in Section 6.2, the former figure distinguishes the response of each single run, whereas the latter figure permits to distinguish the backbone curve from the corresponding hysteresis loops. Furthermore, it is clear, from Figure A13 to Figure A16, that the same scheme has been adopted for the storey shear versus inter-storey displacement response of the first and second floors. Also in this case, it can be concluded that test runs for controller compensation neither affect the behaviour of the building nor alter test results and the corresponding trends obtained.
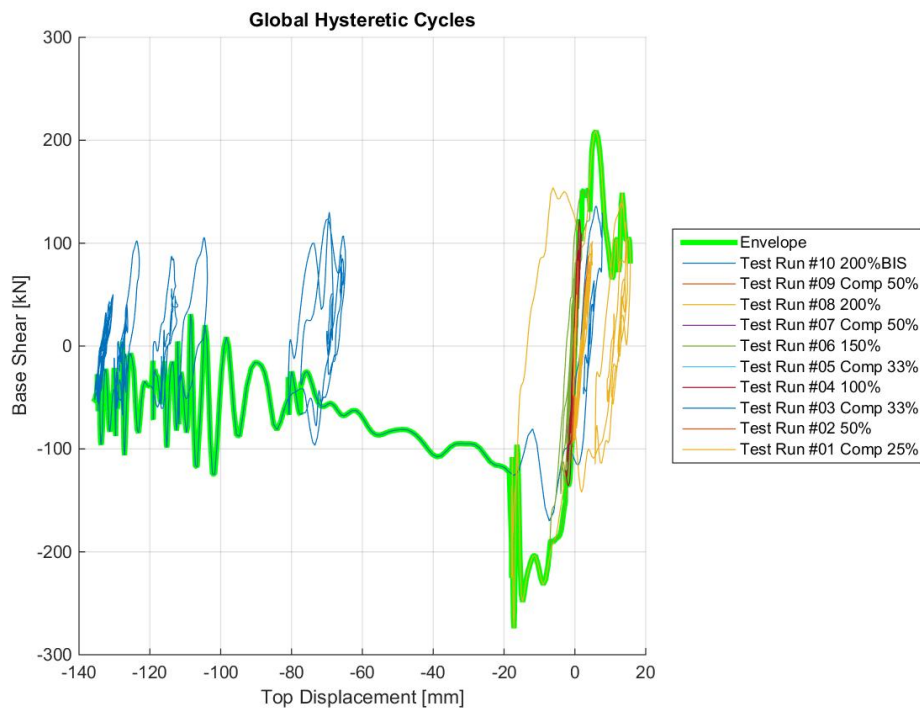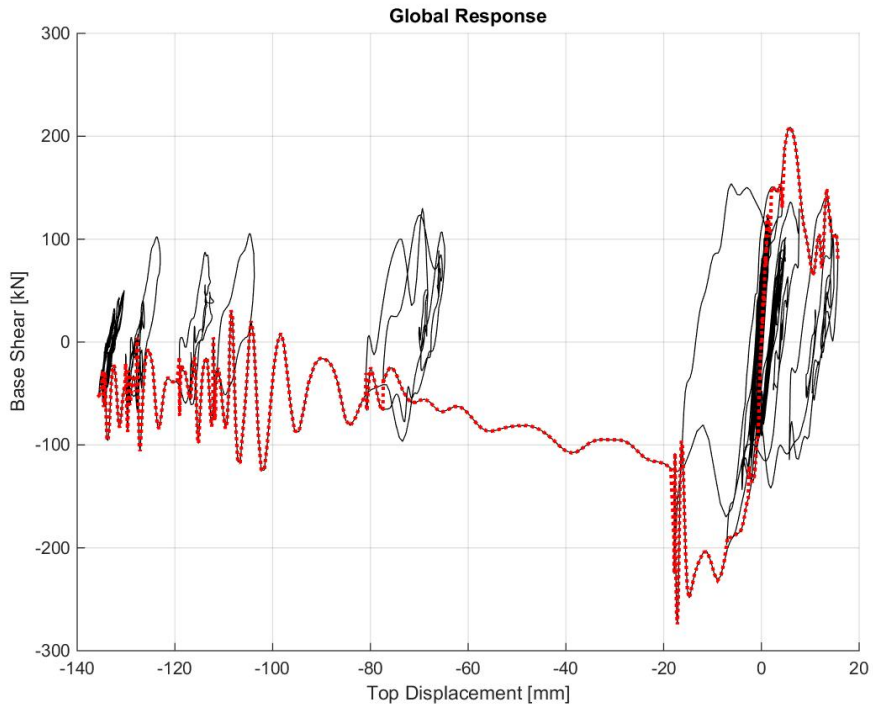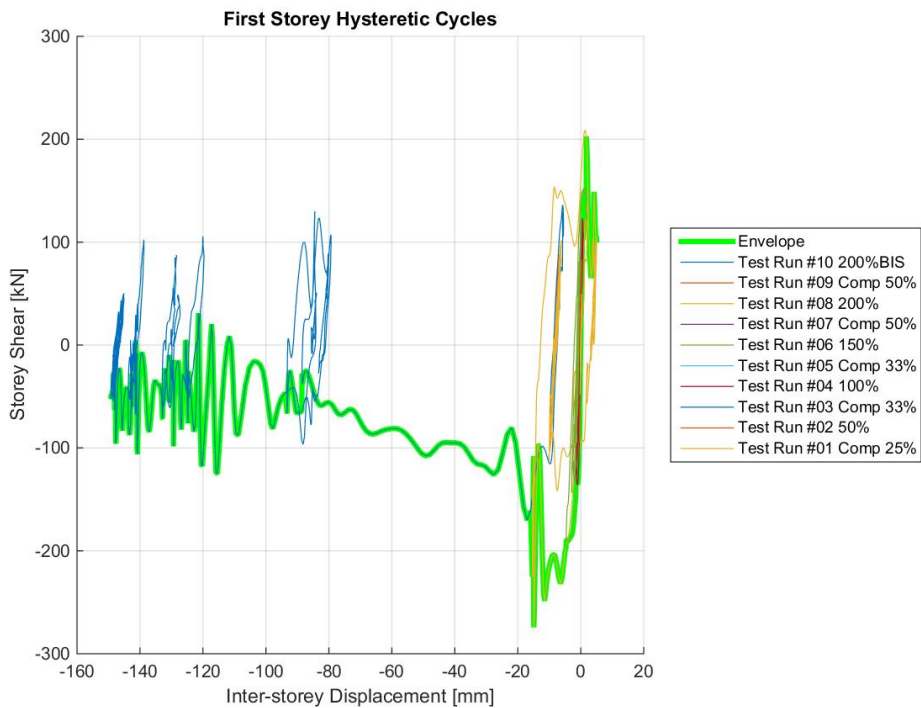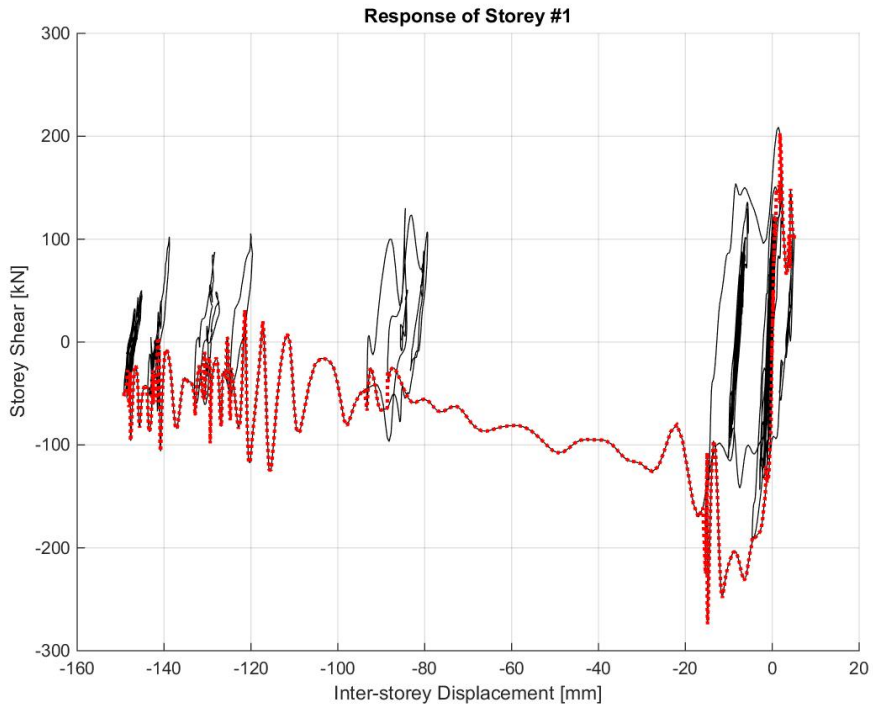

Figure A11. Base shear-top displacement response considering test runs for controller compensation.
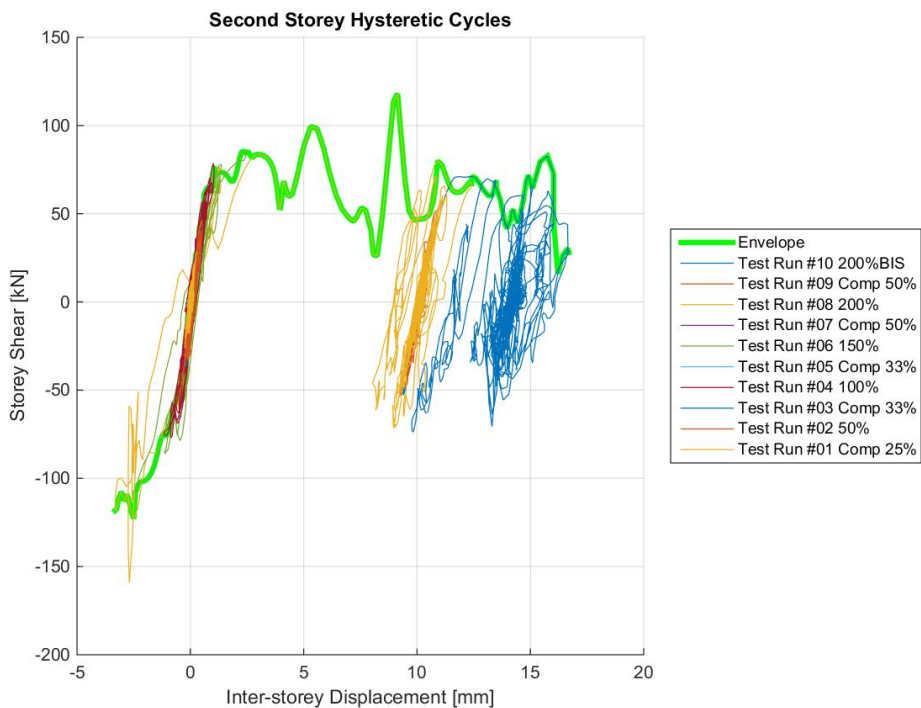
Figure A12. Base shear-top displacement response considering test runs for controller compensation – Envelope.
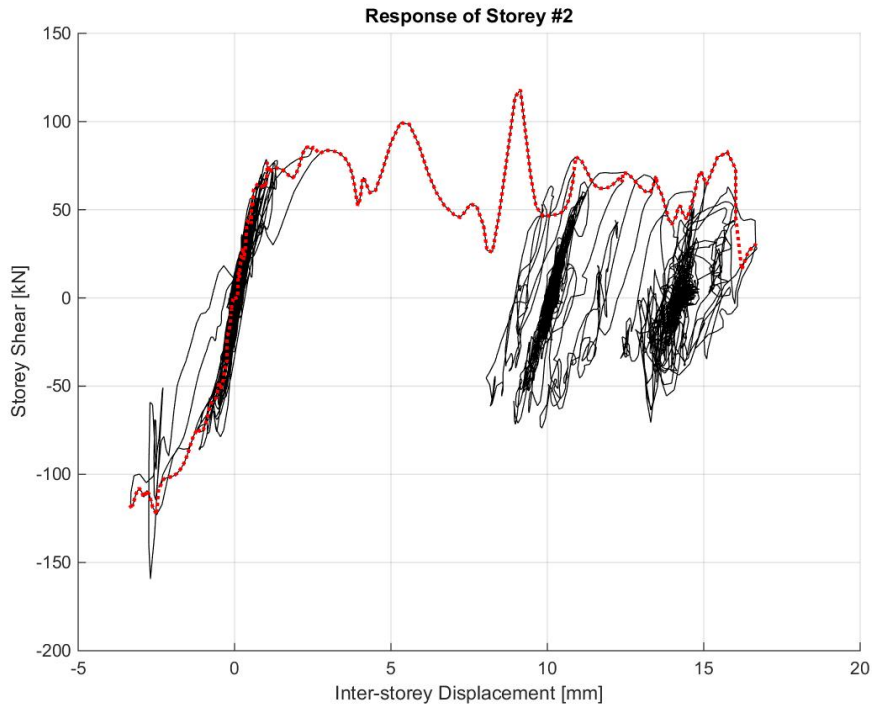

Figure A13. Storey shear vs. inter-storey displacement response considering test runs for controller compensation – First storey.

Figure A14. Storey shear vs. inter-storey displacement response considering test runs for controller compensation – First storey, envelope.

Figure A15. Storey shear vs. inter-storey displacement response considering test runs for controller compensation – Second storey.

Figure A16. Storey shear vs. inter-storey displacement response considering test runs for controller compensation – Second storey, envelope.

Local response

Rotation response data are also herein further processed to present plots of local mechanisms (such as rocking and sliding of the stability walls) that include test runs for controller compensation. To this end, a set of response graphs that resemble those presented in Section 6.4 of this report are collected hereafter.

In particular, Figure A17 and Figure A18 show the base rotation due to rocking of the ground-floor stability wall, whereas the vertical sliding of this structural wall element with respect to the adjacent transversal wall panels is provided in Figure A19 and Figure A20. It is worth recalling that the plots given below were created by means of the instrumentation placed on the West and East sides of the panel, their measurements being considered separately and also averaged, which results in a total of three response graph per each floor and mechanism of interest.

An additional six plots are also provided for the second-storey stability wall; three of them (Figure A21 and Figure A22) illustrate the base rotation due to rocking of the second-floor stability wall, whilst its vertical sliding on the counterpart lateral walls can be gathered from the other three plots (Figure A23 and Figure A24).

As previously observed in terms of global response data and also reaffirmed here with regards to the local response, test runs for controller compensation do not seem to have influenced the specimen seismic response in any shape or form.
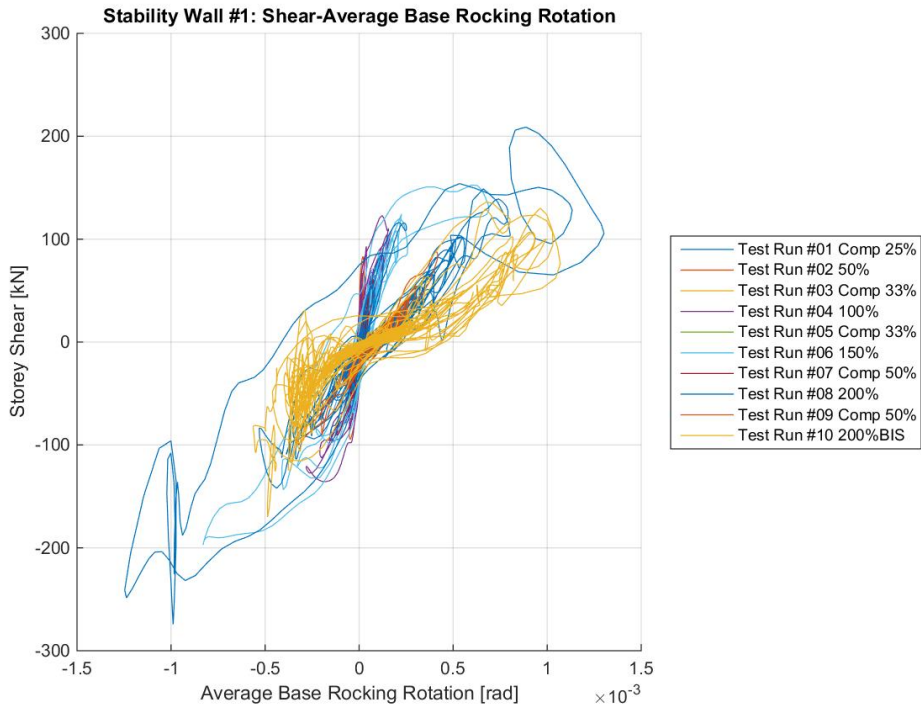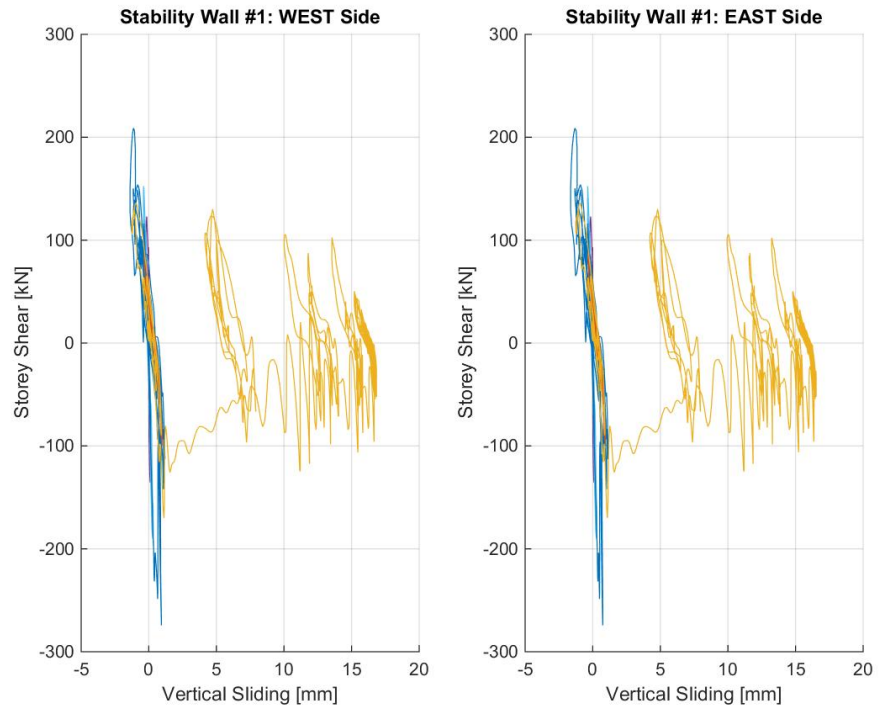
Figure A17. Base rotation due to rocking of the first-storey stability wall considering test runs for controller compensation – Average of West and East sides.
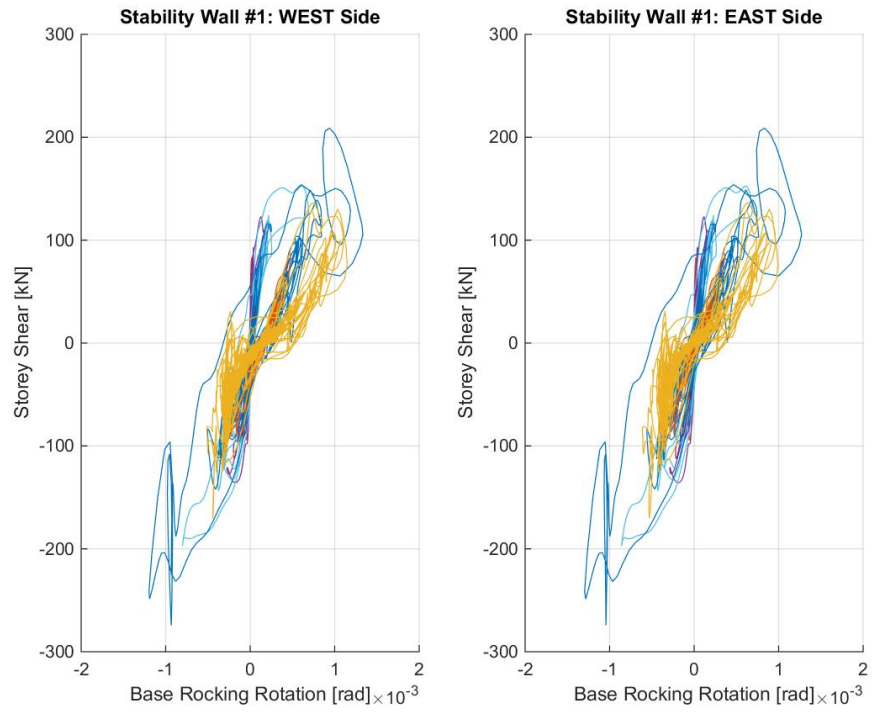
Figure A18. Base rotation due to rocking of the first-storey stability wall considering test runs for controller compensation – West and East sides.
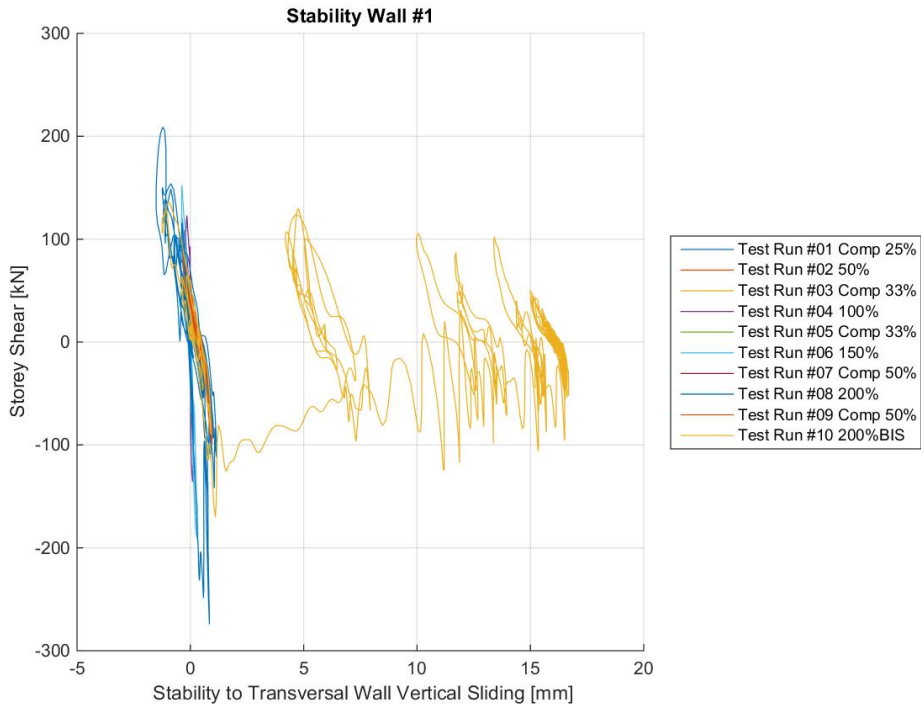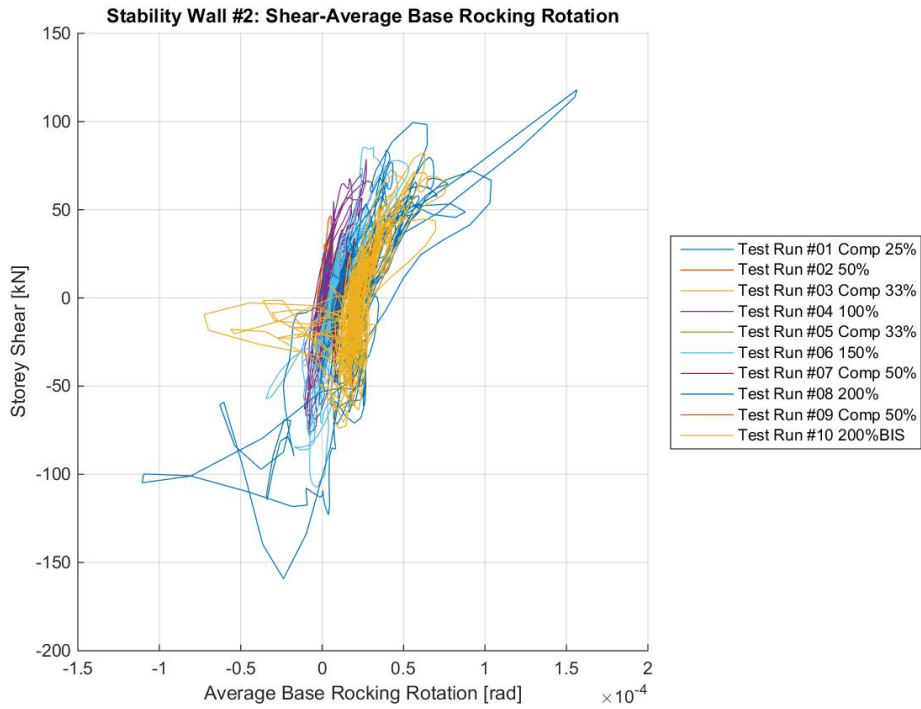
Figure A19. Vertical sliding of the first-storey stability wall considering test runs for controller compensation – Average of West and East sides.
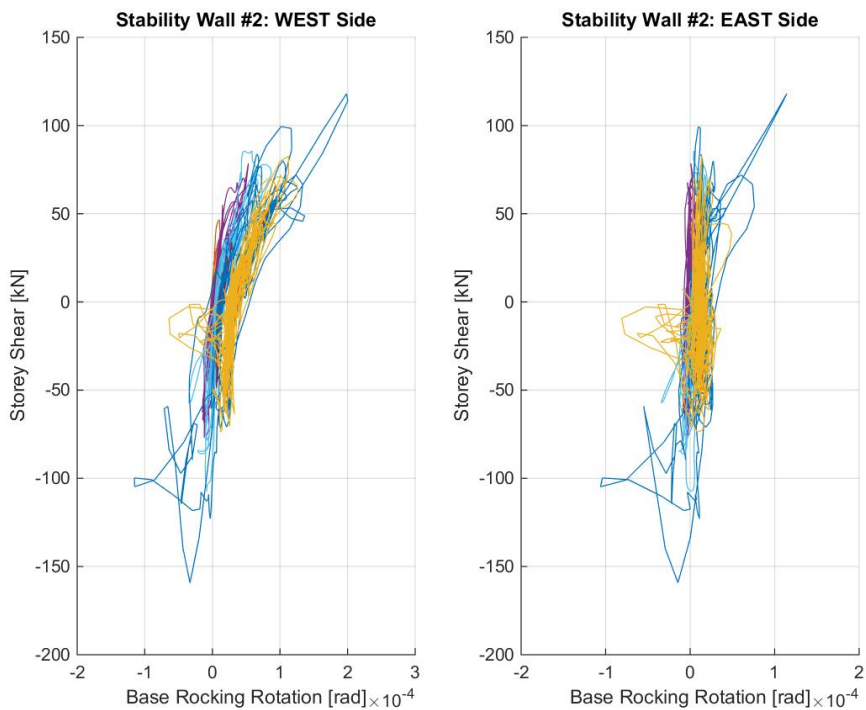

Figure A20. Vertical sliding of the first-storey stability wall considering test runs for controller compensation – West and East sides.
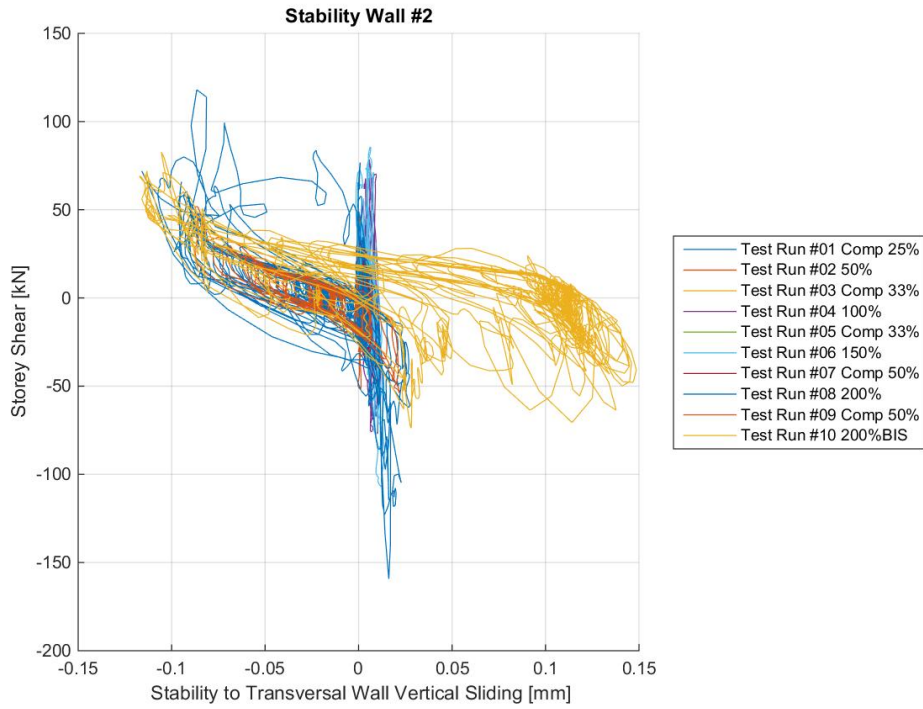
Figure A21. Base rotation due to rocking of the first-storey stability wall considering test runs for controller compensation – Average of West and East sides.

Figure A22. Base rotation due to rocking of the first-storey stability wall considering test runs for controller compensation – West and East sides.

Figure A23. Vertical sliding of the second-storey stability wall considering test runs for controller compensation – Average of West and East sides.
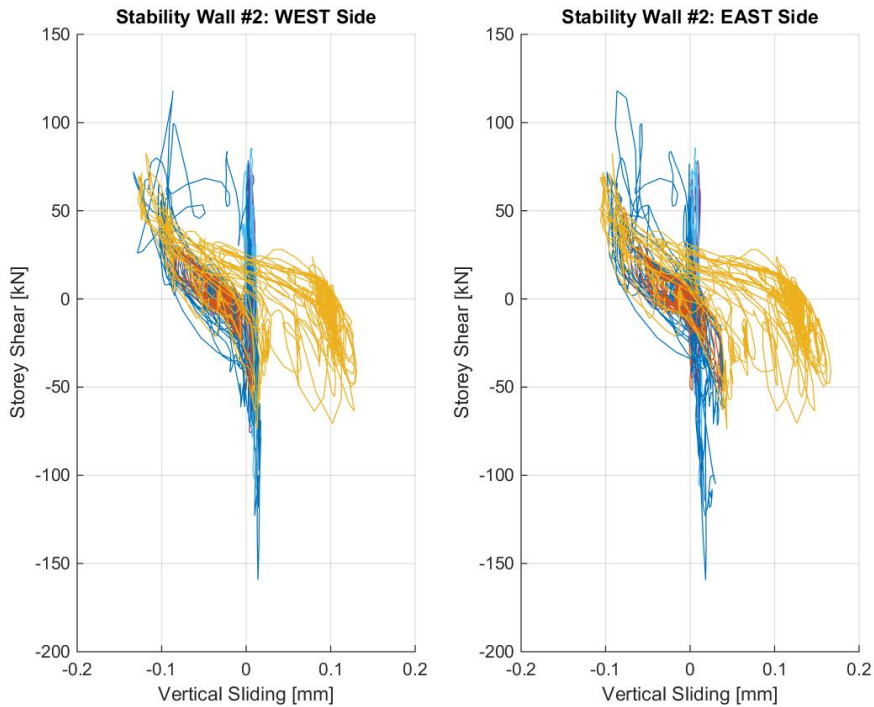
Figure A24. Vertical sliding of the second-storey stability wall considering test runs for controller compensation – West and East sides.

Appendix B

Selection of accelerogram for shake-table test of EUC-BUILD5 specimen

by Helen Crowley

20th April 2017

This short note describes the selection of the accelerogram proposed to be used for the shake-table test of the precast reinforced concrete specimen EUC-BUILD5.

The uniform hazard spectrum (UHS) for a return period of 2475 years from the v4 probabilistic seismic hazard assessment (PSHA) carried out by NAM has been used as the basis for selecting records, as it is expected that this spectrum will be used for seismic assessment (for the 'collapse prevention' limit state) in the NPR. The UHS at Ten Boer has been selected as this has the highest spectral ordinates (see Figure B1).
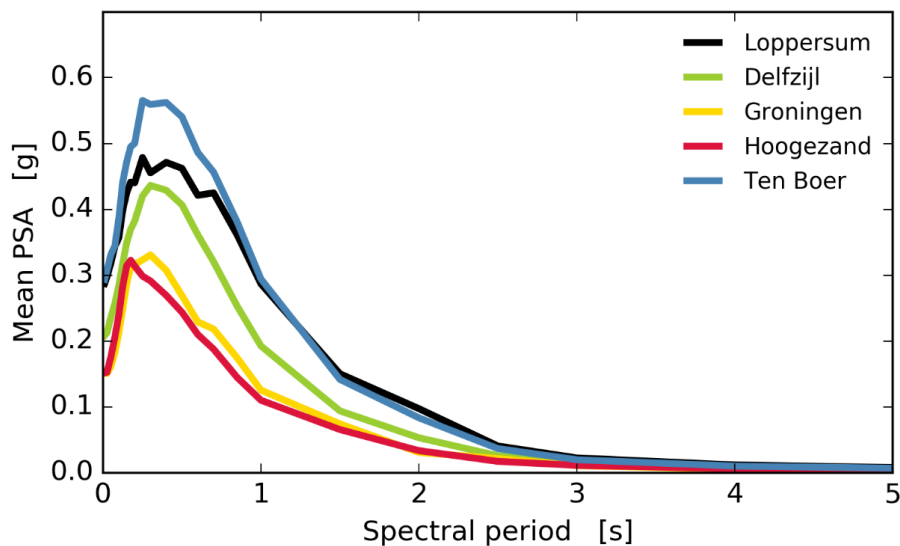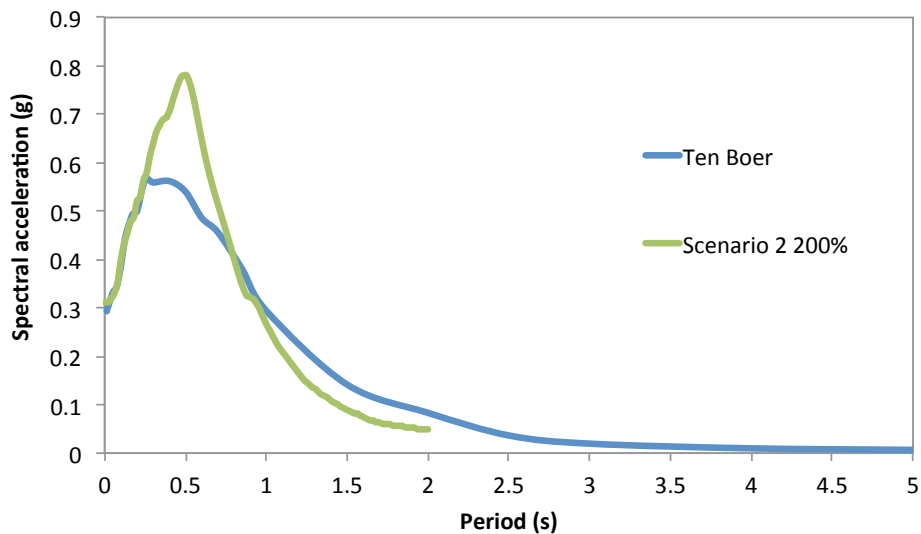

Figure B1. v4 uniform hazard spectra (UHS) for return period of 2475 years at various locations across the Groningen field.

Before selecting a new record for the shake-table test, the Ten Boer UHS has been compared with the spectrum of scenario 2 (at 200%) that was used in previous experiments. As can be seen in Figure B2, the latest developments in the PSHA for the Groningen field, and in particular those of the GMPE (Bommer et al., 2017), have changed quite significantly the shape of the uniform hazard spectrum, in particular for the low periods of vibration. For this reason, it was felt to be timely to select a new record for the EUC-BUILD5 shake-table test.

For the previous dynamic tests carried out for NAM, a scenario spectrum has been calculated using the modal event from PSHA disaggregation, and records have been matched to that spectrum. Disaggregation results from the v4 PSHA are not currently available. However, a scenario spectrum (based on the v4 GMPE, with upper central logic tree branch) for magnitude 4.5 at a rupture distance of 3km (i.e. the minimum distance) with a total sigma of 1.1 has been found to match closely the UHS at Ten Boer (see Figure B3). Given its similarly with a scenario spectrum (meaning that it is a reasonable spectral shape to match individual records to), the Ten Boer UHS

has been used as the target spectrum for the selection and matching of records for the EUC-BUILD5 shake-table test.

Figure B2. Comparison between spectrum of scenario 2 used in previous shake-table tests and the latest UHS (at 2475 year return period for Ten Boer).
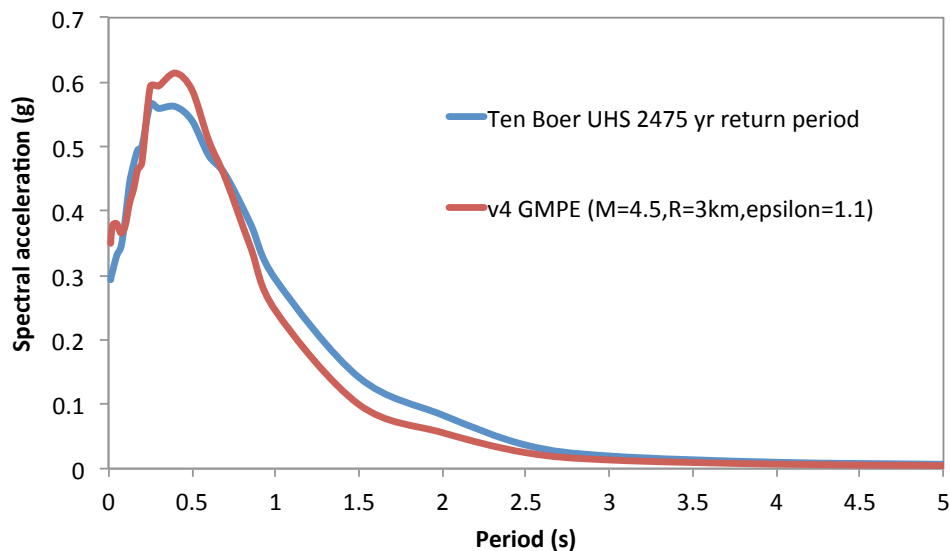
Figure B3. v4 uniform hazard spectra (UHS) for return period of 2475 years at Ten Boer compared with a scenario spectrum.

The central upper logic tree branch of the v4 duration GMPE (together with the characteristics of the scenario described above) has been used to estimate the conditional significant duration (5-75%). The correlation coefficient according to Bradley (2011) between spectral ordinates at 0.05s (selected as a representative period, given the high stiffness of the pre-cast specimen) and 5-75% significant duration has been used.

Table B1. Conditional 5-75% significant duration calculation.

Median D_{s5-75} (s)	$\rho[D_{s5-75}, Sa(0.05)]$	$\varepsilon_{Sa(0.05)}$	ε_{Ds5-75}	σ_{Ds5-75}	Conditional mean D_{s5-75} (s)
1.85	-0.45	1.1	-0.5	0.64	1.35

A pre-selection of candidate records from the NGA database[1] has been undertaken and then SeismoMatch (Seismosoft, 2017) has been used to match them to the target spectrum. The final selected record (see Table B2) only required a few iterations to match the target spectrum (with a tolerance of 0.3) and the matched record had a 5-75% significant duration of 1.65 seconds, which is only slightly higher than the target duration. This is felt to be appropriate, given that the dominating scenario of the UHS is not yet available from disaggregation, and could be higher than 4.5 (which would mean higher durations).

Table B2. Characteristics of selected record.

Waveform N_0.	Database	EQ Name	EQ Date	Mw	Repi (km)
NGA_145_H2	NGA	Coyote Lake	06-08-1979	5.74	7.95
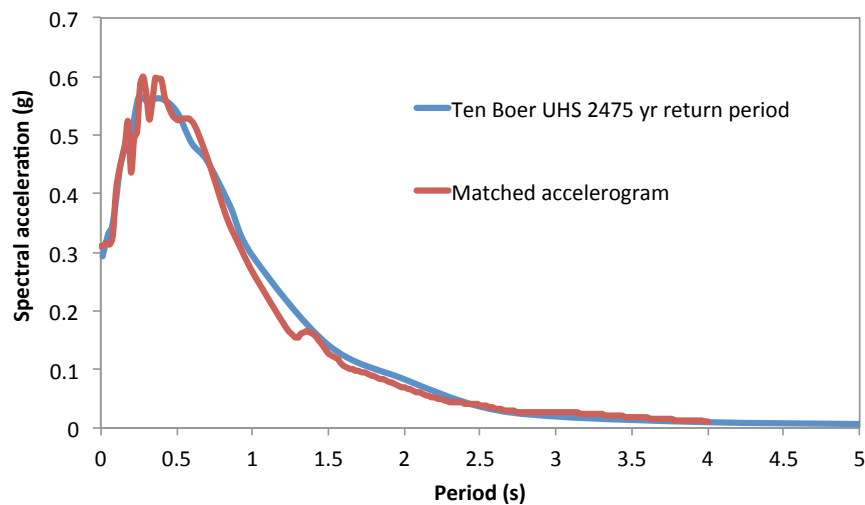
Figure B4. Comparison of target spectrum (Ten Boer UHS) and spectrum of matched accelerogram.

References

Bommer JJ, Dost B, Edwards B, Kruiver PP, Meijers P, Ntinalexis M, Rodriguez-Marek A, Ruigrok E, Spetzler J, Stafford PJ (2017) "V4 Ground-Motion Model (GMM) for Response Spectral Accelerations, Peak Ground Velocity, and Significant Durations in the Groningen Field," Report submitted to NAM.

Bradley, B.A. (2011). Correlation of significant duration with amplitude and cumulative intensity measures and its use in ground motion selection. Journal of Earthquake Engineering 15(6), 809-832.

---

[1] http://ngawest2.berkeley.edu

Seismosoft (2017) SeismoMatch, a computer program for spectrum matching of earthquake records. Available from URL: http://www.seismosoft.com/downloads

Appendix C

Initial friction testing attempts for characterisation of felt material

For the sake of clarity and completeness, some of the first cyclic testing attempts were documented with the support of a photographic sequence (see Figure C1 to Figure C4). In particular, Figure C1 shows a non-symmetric configuration of test, which was based on the use of gypsum and one layer of felt per each one of the three points of contact between the top and bottom concrete blocks.

Figure C1. First cyclic friction testing attempts – Asymmetric configuration, one felt layer plus gypsum.

Details of the three pieces of felt material after the cyclic testing can be observed in Figure C2. It is worth specifying that these first test runs were carried out by imposing a maximum displacement of 100 mm in pulling and pushing direction. It is believed that the pressure distribution imposed by the additional vertical loads was far from being uniform (and uniformly distributed on the three pieces of felt) and also that concrete-on-concrete contact occurred during testing for such displacements. It was thus decided (i) to reduce the maximum displacement to 30 mm, and (ii) to change number and position of the points of contact (from three to four symmetrically arranged contact points). Figure C3 shows one of the four pieces of felt during one of the new testing attempts, which were carried out by using layers of felt material taken out from the samples that have been already tested. In this case, four layers of felt per each pile were used, resulting in an excessive deformation in the vertical and horizontal directions. Figure C4 presents an example of disintegrated felt stack after the testing.

Figure C2. First cyclic friction testing attempts – Felt layers after testing.

All these first cyclic testing attempts were instrumented and data were anyway processed to have a measure of the frictional force transfer mobilised between the two concrete blocks. In Figure C5 and Figure C6, the reader may find exemplificative plots of the results of these cyclic testing of the felt material. Much higher variability than what had been shown before can be observed in this case due to the fact that the collected results pertain to testing configurations that are very different in type. As far as the very first testing attempts are concerned, the static friction coefficients are in close agreement with those obtained from triplet tests, whilst the values derived by using the results of progressively refined testing attempts tend to progressively decrease. The last trial shown in Figure C5 and Figure C6 confirms static and dynamic friction coefficients that closely match with the statistics reported in Table 11 (see Section 4.4.3).

Figure C3. First cyclic friction testing attempts – Symmetric configuration, four layers of exhausted felt.

Figure C4. First cyclic friction testing attempts – Disintegrated felt stack after testing.
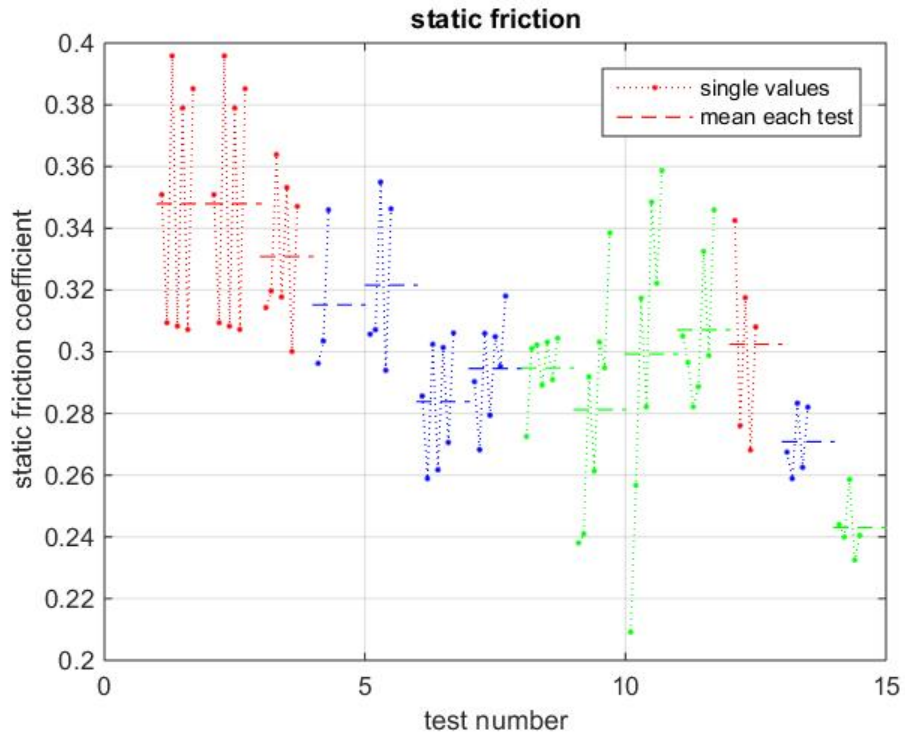
Figure C5. First cyclic friction testing attempts – Estimate of static friction coefficient.
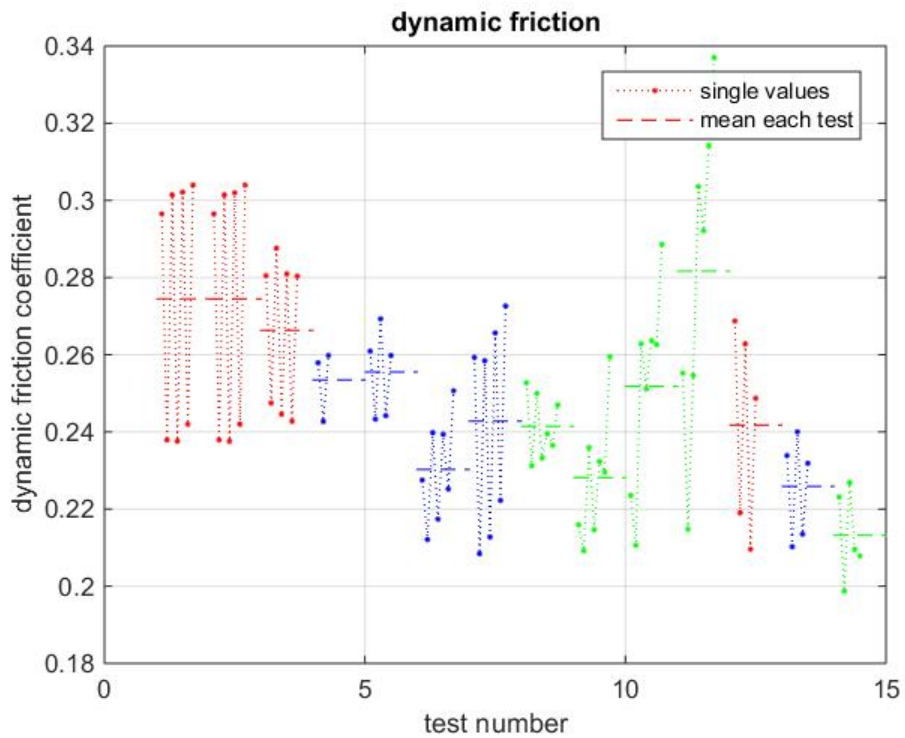

Figure C6. First cyclic friction testing attempts – Estimate of dynamic friction coefficient.